Institute for Theoretical Particle Physics and Cosmology

RWTH AACHEN UNIVERSITY

Suppressed Diffusion Around Cosmic Ray Sources and Impact on Galactic Propagation

Von der Fakultät für Mathematik, Informatik und Naturwissenschaften der RWTH Aachen University zur Erlangung des akademischen Grades eines Doktors der Naturwissenschaften genehmigte Dissertation

vorgelegt von

Hanno Jacobs M.Sc.

aus

Neuss

Berichter: Prof. Dr. Philipp Mertsch
Prof. Dr. Christopher Wiebusch

Tag der mündlichen Prüfung: 14.06.2024

Diese Dissertation ist auf den Internetseiten der Universitätsbibliothek verfügbar.

Abstract

Suppressed Diffusion Around Cosmic Ray Sources and Impact on Galactic Propagation

by Hanno Jacobs

At the beginning of the 20th century a variety of observations found that the Earth is constantly bombarded by charged high energy particles from space. These cosmic rays mainly consist of protons, but also contain heavier elements. Over a large range in energy from MeV to EeV they resemble a power law. At GeV energies their arrival directions are nearly isotropic, since charged particles get deflected in the turbulent magnetic fields in the Galaxy. This prevents a direct tracking of the particles back to their sources. From the ratios of hadronic cosmic rays it is possible to deduce that particles must propagate diffusively throughout the Galaxy. Thereby, the parameters of models we fit to these data are galactic averages.

In contrast, high energy γ-rays are produced by cosmic rays and directly point back to their origin. With this it is possible to indirectly probe the distribution of comic rays within the Galaxy. Recent observations of γ-rays around pulsars and supernova remnants, both potential sources, indicate that diffusion in these regions is more than two orders of magnitude lower than in the galactic average. This indicates that the conditions within the Galaxy are far from homogeneous.

In this thesis, we investigate whether cosmic rays themselves can produce the suppressed diffusion. The basic idea is that in the vicinity of the source the strong spatial gradient of the cosmic ray density gives rise to the resonant streaming-instability. This produces magnetic waves upon which they scatter, a process called self-confinement. We make use of finite-difference codes to investigate the surroundings of supernova remnants. We extend existing models below 10 GeV and show that suppressed diffusion can exist for up to 1 Myr after the supernova. The same mechanism was proposed to explain TeV-γ-ray-halos around pulsars. We implement the cascade of turbulence in existing models and show that the effectivity of the streaming-instability crucially depends on the large scale magnetic field. Our calculations indicate, that the streaming instability alone is not able to explain the observations around the pulsar Geminga.

Additionally, we investigate the effects of suppressed diffusion in the galactic disk on hadronic cosmic ray ratios. The basic idea is that unstable particles are confined within the disk for longer if the diffusion coefficient is smaller. Then, the ratio of unstable to stable nuclei is increased compared to standard predictions. We develop a semi-analytical two-zone model of the Galaxy with a reduced diffusion coefficient in the galactic disk compared to the galactic halo and show that this model can be constrained by recent AMS-02 ^{10}Be/^{9}Be data. For the case that the diffusion coefficient in the disk represents an average over zones of low and high diffusion, we investigate the filling fraction of the suppression zones with stochastic differential equations. Finally, we highlight the impact of different spallation cross-section parametrisations on our findings.

Zusammenfassung

Unterdrückte Diffusion um Quellen Kosmischer Strahlung und Auswirkungen auf die Galaktische Propagation

von Hanno Jacobs

Zu Beginn des 20. Jahrhunderts wurden Beobachtungen unternommen die zeigen, dass die Erde von hoch energetischen, geladenen Teilchen aus dem Weltall bombardiert wird. Der Großteil besteht aus Protonen, aber auch schwereren Elemente und Anti-Teilchen. Das Spectrum entspricht über viele Größenordnungen von GeV bis EeV einem Potenzgesetz. Bei GeV Energien ist die Ankunftsrichtung nahezu isotrop, da geladene Teilchen durch die turbulenten Magnetfelder abgelenkt werden. Daher ist es nicht möglich aus der Ankunftsrichtung der Teilchen auf deren Ursprung zu schließen. Durch die relativen Häufigkeiten verschiedener Atome ist es möglich zu zeigen, dass die Teilchen sich diffusiv durch die Galaxy bewegen müssen. Die Parameter aus den Modellen, die den Transport in der Galaxy beschreiben, sind daher ein galaktischer Durchschnitt.

Zusätzlich zu diesen geladenen Teilchen werden γ-Strahlung gemessen. Diese werden durch kosmische Strahlung in der Galaxie produziert und propagieren danach ballistisch zu uns. Damit lassen sich ortsabhängige Teilchendichten in der Galaxie messen. Beobachtungen in der Nähe potenzieller Quellen weisen auf reduzierte Diffusion in diesen Regionen hin. Dies ist ein Hinweis für nicht homogene Bedingungen in der Galaxie.

In dieser Arbeit untersuchen wir, ob die Teilchen selber reduzierte Diffusion verursachen. Die grundlegende Idee dahinter ist, dass der räumliche Gradient der Teilchendichte in der Nähe der Quellen die resonante Strömungsinstabilität hervorruft, die magnetische Turbulenz produziert, an der die Teilchen abgelenkt werden. Wir untersuchen diesen Prozess um Supernovaüberreste herum, indem wir existierende Modelle zu Energien unterhalb von 10 GeV erweitern und die Kaskade der Turbulenz berücksichtigen. Damit sind wir in der Lage zu zeigen, dass der Diffusionskoeffizient für 1 Myr unterdrückt ist. Um Beobachtungen in der Umgebung von Pulsaren zu erklären reproduzieren wir existierende Arbeiten und zeigen, dass die Effektivität der Strömungsinstabilität stark vom großskaligen Magnetfeld abhängt. Auch im optimistischsten Fall ist es nicht möglich die Morphologie der gemessenen γ-Strahlung so zu erklären. Daraus schließen wir, dass weitere Mechanismen eine Rolle spielen müssen.

Zusätzlich untersuchen wir den Einfluss der Zonen reduzierter Diffusion auf Messungen hadronischer Teilchen. Dazu entwickeln wir ein halbanalytisches Zwei-Zonen-Model der Galaxie mit reduzierter Diffusion in der galaktischen Scheibe verglichen mit dem Halo. Wenn instabile Teilchen länger in der Scheibe verweilen, wird das gemessene Verhältnis von instabilen zu stabilen Teilchen steigen. Wir zeigen, dass neue AMS-02 $^{10}\mathrm{Be}/^{9}\mathrm{Be}$ Daten unser Modell bestätigen können. Für den Fall, dass die unterdrückte Diffusion in der Scheibe durch einzelne Zonen verursacht wird, bestimmen wir den Volumenanteil mit stochastischen Differenzialgleichungen. Schlussendlich gehen wir noch auf den Einfluss verschiedener Parameterisierungen der Spallationswirkungsquerschnitte ein.

Contents

1. Introduction

In 1912, Victor Hess measured the amount of ionising radiation during several balloon flights up to 5300 m [99]. In contrast to previous expectations, which suggested the sources of ionising radiation to originate from radioactive elements in the Earth or radiation of the sun, the ionisation rate increased with altitude, even in darkness. Hence, he concluded that the radiation must have a cosmic origin and named them cosmic rays. In contrast to his expectations, the majority of this radiation consists not of photons, but of charged particles, mainly protons, but also electrons, heavier nuclei and further secondary particles. Unlike γ-rays or neutrinos, cosmic rays do not travel on straight trajectories from their sources to us. Instead, they are deflected by the turbulent interstellar magnetic fields due to their charge and execute a random walk. This makes it difficult to backtrack the particles and find their origin. The high energies observed in cosmic rays indicate that they must have been produced in the most extreme environments of our Universe, hence offering a unique window into these high-energy astrophysical phenomena and the underlying physics, which are not reachable by human-made devices. Additionally, their energy density is comparable to that of thermal gas and magnetic fields within our Galaxy, indicating that they play a major role in galactic dynamics. They are also the only known agent able to penetrate into dense molecular clouds where they ionise and heat up the material. This in turn influences the chemistry and coupling of magnetic fields to gas, and thereby the gravitational collapse into stars in these regions.

1.1. Cosmic Ray Observations

The observed quantity of cosmic rays is the intensity, denoted $J(E)$, which is the number of particles at a specific kinetic energy E per unit time, unit energy, unit area and unit solid angle. Observational techniques vary greatly, depending on the type of particle and the energy. Up to TeV, direct detection via satellite telescopes is possible and at higher energies larger ground based telescopes are used.

1.1.1. The Spectrum of Cosmic Rays

Cosmic rays are non-thermal particles, meaning they do not follow a Maxwellian energy distribution. Instead, observations ranging from GeV to EeV found a nearly perfect power law $J(E) \propto E^{\gamma}$ as shown in Fig. 1.1 [169]. In particular, between 40 GeV and 3 PeV, the spectral index is $\gamma \approx -2.7$ [59]. At energies below 40 GeV magnetised plasma emitted by the Sun influences the transport of cosmic rays [175]. This leads to a harder spectrum, meaning a larger γ. At around 3 PeV, the spectra softens to $\gamma \approx -3.1$, due to its shape this feature is called the cosmic ray knee [59]. Above 8 EeV the spectrum hardens again to $\gamma \approx -2.7$, called the ankle, before it is cut off at around 60 EeV [59].

The origin of the knee is believed to be either the cut-off energy of galactic sources for protons or a change in transport and the slope until the ankle is given by a change in the composition to heavier masses. The ankle is thought to be caused by the transition from galactic to extragalactic particles [20]. The reason is that the Larmor radius of particles of $p = 8$ EeV and charge q in the magnetic field of the Galaxy $B_{rms} = 4\,\mu$G [97] is $r_L = p/qB_{rms} = 2.2$ kpc which is of the order of the height of the galactic halo [216]. Hence, these particles cannot be confined by the Galaxy and escape from the Galaxy into the intergalactic medium.

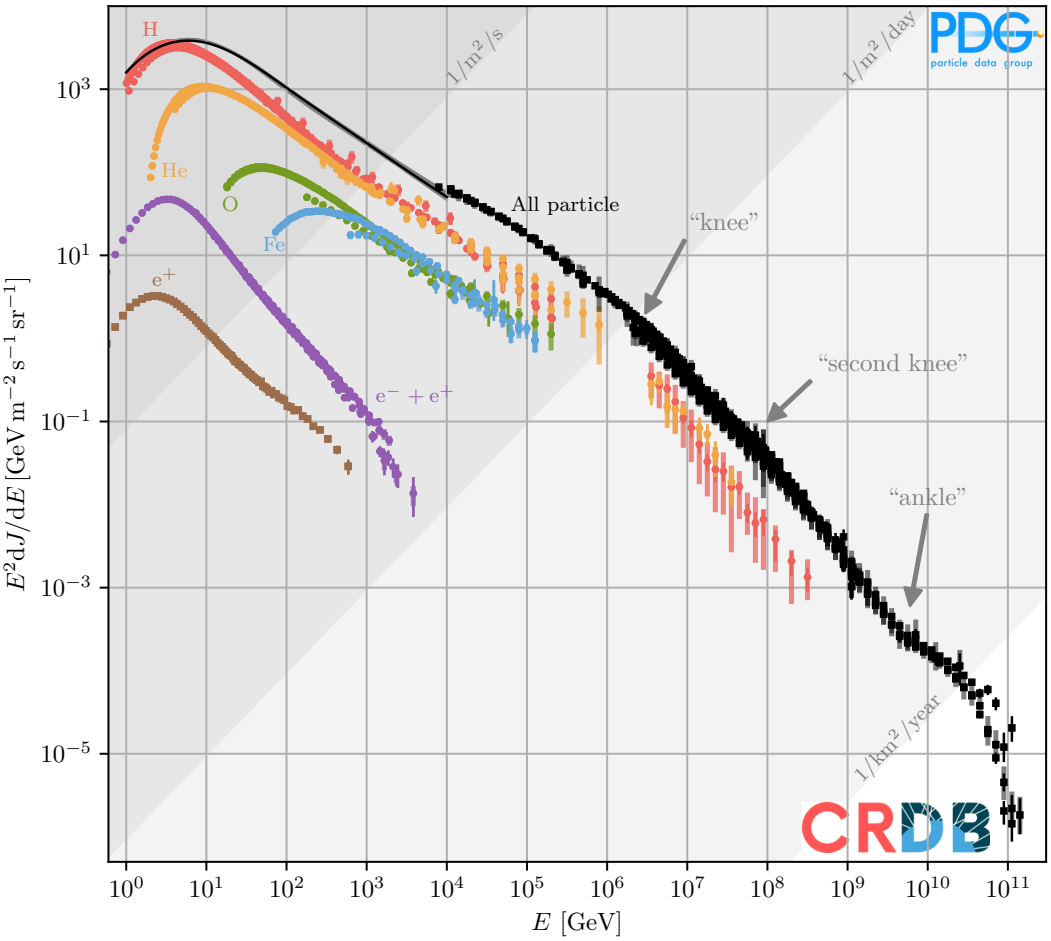

Figure 1.1: Spectrum of cosmic rays $E^2 \mathrm{d}J/\mathrm{d}E$ as a function of kinetic energy E as published in Mertsch [152] based on the Cosmic Ray Database [144, 147, 148]. The shaded grey areas mark the corresponding rate per area, indicating detectors of very different sizes are required to measure the observed spectra. In general the total spectrum of cosmic rays resembles a nearly uniform power law with spectral index $\gamma = -2.7$. The main features visible are a softening to $\gamma = -3.1$ at the knee at around 3 PeV, the hardening to $\gamma = -2.7$ at the ankle at 8 EeV and a high energy cut-off. Electrons and positrons are subabundant by 2 and 3 orders of magnitude.

1.1.2. Abundance of Cosmic Rays

In addition to the spectrum of cosmic rays, their composition also carries important information, both about their origin and their propagation. Due to the steeply falling spectrum, the number density, and hence the total relative abundances, are dominated by the intensities at GeV energies. The abundance in cosmic ray flux at $E_{\mathrm{kin}} = 20\,\mathrm{GeV}$ and the solar system are shown in Fig. 1.2, which is normalised to the abundance of silicon. All data and the figure are taken from the Cosmic Ray Database [144, 147, 148]. Generally, elements with even atomic numbers are more abundant than odd ones. This is caused by the pairing effect in the nucleus, which leads to favourable energetics of these elements. Therefore, they are produced more frequently. H and He are produced during big bang nucleosynthesis and dominate the total number count. Elements up to Fe are produced in stellar fusion reactions and supernovae explosions. Be, Li and B have low abundances, since these elements get destroyed by reactions in the star. Finally, at larger atomic numbers than Fe, an energy input is needed to create these elements, leading to strong suppression. In contrast to the solar system, several elements are overabundant in cosmic rays. The most notable ones are Be, Li and B. Since the composition within the solar system and the sources of cosmic rays should be nearly identical, and the acceleration mechanism only depends on rigidity, these particles must be produced during the propagation by spallation reactions with the interstellar medium [89]. Hence, they are referred to as secondaries, as opposed to primaries, which are accelerated from the thermal background in the sources of cosmic rays. The flux of secondary cosmic rays therefore measures the matter that is traversed on average during their propagation, called grammage and defined as $\chi = \int_{\mathrm{Source}}^{\mathrm{Earth}} \mathrm{d}s m_{\mathrm{gas}} n_{\mathrm{gas}}(s)$, where n_{gas} is the gas density, m_{gas} the gas mass and s the propagation length.

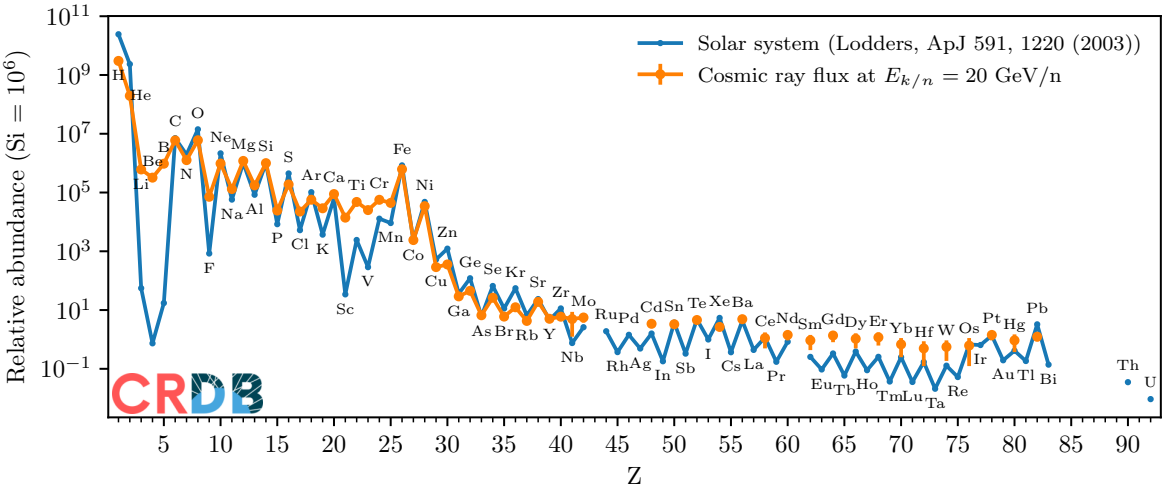

Figure 1.2: Abundances of elements in cosmic rays and solar system normalised to Si = 10^6. The figure is based on code and data provided by the Cosmic Ray Database [144, 147, 148].

1.1.3. Cosmic Ray Ratios

In the most simplistic setup, also known as the leaky box approximation, cosmic rays are considered to be homogeneously distributed in the Galaxy [42]. After being injected by sources at a rate Q_i they undergo spallation reactions during their propagation or decay and can escape the considered region at a rate Γ_{esc}. The governing equation for the cosmic ray number per unit energy N_i of species i can then be written as

$$\frac{\partial N_i}{\partial t} = Q_i - \Gamma_{\text{esc}} N_i - c\beta n_{\text{gas}} \sigma_i N_i + \sum_{k>i} c\beta n_{\text{gas}} \sigma_{k\to i} N_k - \frac{N_i}{\gamma \tau_i}, \tag{1.1}$$

where σ are the respective cross-sections, $\beta = v/c$, $\gamma = (1-\beta^2)^{-1/2}$ and τ the decay time. In the steady state assumption the left-hand side of Eq. 1.1 vanishes. With the escape time defined as $\tau_{\text{esc}} = 1/\Gamma_{\text{esc}}$ the number density of matter traversed before escape is then given by $\lambda_{\text{esc}} = c\beta n_{\text{gas}} \tau_{\text{esc}}$. The cross-sections can be obtained by collider experiments, which is straight forward for the total inelastic cross-section [204, 205], but for spallation cross-sections the necessary identification of the spallation fragments makes measurements significantly harder. Hence, several rough parametrisations exist, which sometimes differ by more than a factor of two [67, 84, 86]. Now, in case one species is purely primary and another produced solely in spalation reactions of this primary, the secondary to primary ratio is given by

$$\frac{N_{\text{sec.}}}{N_{\text{prim.}}} = \frac{\sigma_{\text{prim.}\to\text{sec.}}}{\sigma_{\text{prim.}} + \frac{1}{\lambda_{\text{esc}}}}, \tag{1.2}$$

where it was also assumed that both particles are stable. The most prominent example is the B/C ratio, which is shown in Fig. 1.3. It results in $\chi = \lambda_{\text{esc}} m_{\text{gas}} \approx 10\,\text{gcm}^{-2}$ at GeV energies. For a typical scale height of the disk $h \approx 100\,\text{pc}$ and a typical gas density of $n_{\text{gas,disk}} = 1\,\text{cm}^{-3}$ [76], the grammage accumulated in one crossing of the disk is $m_{\text{gas}} n_{\text{gas,disk}} h \approx 1 \times 10^{-3}\,\text{gcm}^{-2}$. Hence, the particles must cross the disk many times, which indicates that they do not travel ballistically, but rather diffusively. This is supported by the energy dependence of the grammage which is given by $\lambda_{\text{esc}} = \lambda_0 (E/E_0)^{-\delta}$ with $\delta \approx 0.33$. This is expected for resonant pitch-angle scattering upon magnetic turbulence with a Kolmogorov power spectrum [17], as is shown in Sec. 1.4.3. The grammage, which determines the B/C ratio, only depends on the product of n_{gas} and τ_{esc} and hence, these quantities are degenerate.

In order to break the degeneracy between the confinement time in the Galaxy τ_{esc} and the gas density n_{gas}, unstable secondary to stable secondary ratios are used. The most suited one is $^{10}\text{Be}/^{9}\text{Be}$, due to the half life-time of $\tau_{\text{Be}} \approx 1.4\,\text{Myr}$, which is of the same order as the expected τ_{esc}.

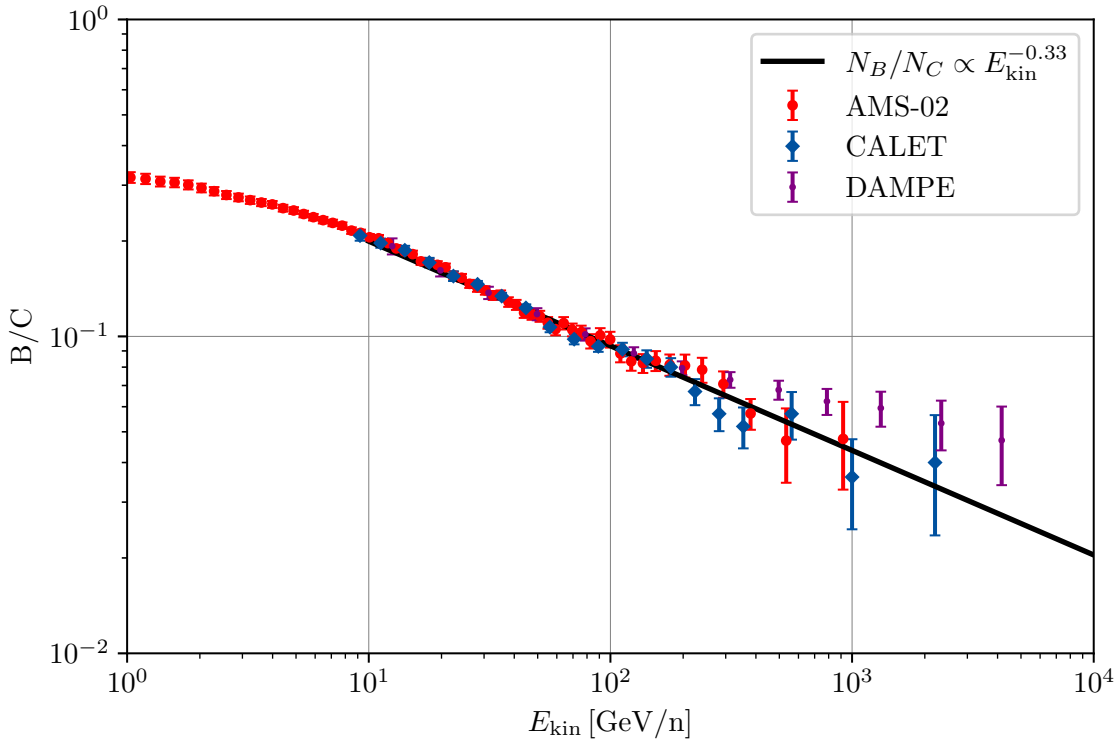

Figure 1.3: B/C ratio as measured by AMS-02 [9], CALET [7] and DAMPE [46] as a function of kinetic energy E_{kin} in GeV per nucleon. The black line indicates a scaling with $\delta \approx -0.33$, which is predicted for Kolmogorov power spectrum. The normalisation is degenerate in n_{gas} and τ_{esc}.

The ratio according to Eq. 1.1 is given by:

$$\frac{N_{^{10}\mathrm{Be}}}{N_{^{9}\mathrm{Be}}} = \frac{\sigma_{\mathrm{prim.}\to{}^{10}\mathrm{Be}}}{\sigma_{\mathrm{prim.}\to{}^{9}\mathrm{Be}}} \frac{\sigma_{^{9}\mathrm{Be}} + \frac{1}{\lambda_{\mathrm{esc}}}}{\sigma_{^{10}\mathrm{Be}} + \frac{1}{\tau_{^{10}\mathrm{Be}}\beta c n_{\mathrm{gas}}} + \frac{1}{\lambda_{\mathrm{esc}}}}. \tag{1.3}$$

The resulting ^{10}Be/^{9}Be as a function of kinetic energy is shown in Fig. 1.4 Together with Eq. 1.2 this breaks the degeneracy and allows determining the average gas density $n_{\mathrm{gas}} = 0.3\,\mathrm{cm}^{-3}$ and escape time $\tau_{\mathrm{esc}} \approx 20\,\mathrm{Myr}$ [162]. Remarkably, the average gas density experienced by the cosmic rays is significantly lower than the gas density in the disk, which indicates that the cosmic rays must spend large amounts of their lifetime in large under-dense regions, the so-called cosmic ray halo. It has to be noted that the integration over the entire galactic volume is not justified for unstable particles with $\tau \leq \tau_{\mathrm{esc}}$, since their propagation distance is limited by the decay time. For a more accurate solution Eq. 5.6 has to be solved.

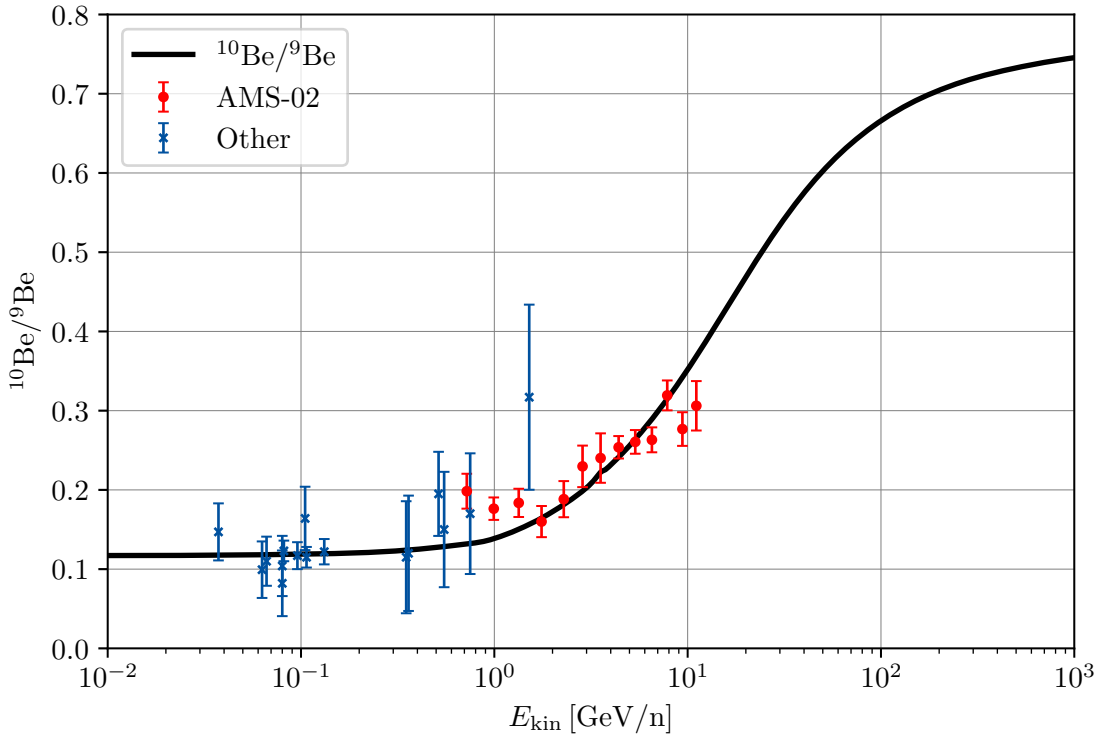

Figure 1.4: ^{10}Be/^{9}Be spectra as a function of kinetic energy per nucleon [40, 82, 83, 111, 138, 139, 158, 217, 219]. The black line indicates the result of a minimal transport model with the spallation cross-sections from [67], which determines the high energy limit. The low and intermediate energy regime is dependent on the escape time τ_{esc} of particles from the Galaxy and the decay time $\tau_{^{10}\mathrm{Be}}$ breaks the degeneracy of n_{gas} and τ_{esc}.

1.2. The Galaxy

Table 1.1: Properties of the different phases of the ISM [75, 76, 182]. T is the temperature of the medium, n the total number density, f_V the Galaxy filling factor, f_i the ionisation fraction and χ the He fraction. The magnetic field in all phases is $B_0 = 5\,\mu$G.

ISM	T [K]	n [cm^{-3}]	f_V	f_i	χ	neutrals	ions
HIM	10^6	10^{-2}	0.5	1	0	-	H^+
WIM	8000	0.35	0.25	0.6-0.9	0.1	H, He	H^+
WNM	8000	0.35	0.25	10^{-2}	0.1	H, He	H^+
CNM	80	35	~ 0	10^{-3}	0.1	H, He	C^+
DiM	50	300	~ 0	10^{-4}	0.1	H_2, He	C^+

Cosmic rays below the ankle are believed to originate in the Galaxy, hence it is necessary to understand the basic galactic properties for accurate models of their transport. Most of the gas and stars are confined to the galactic disk, which has a radius of roughly $R_d = 15$ kpc and a scale height of the order of $h = 100$ pc [143]. The centre is a supermassive black hole of around four million solar masses. It is surrounded by a bulge, spiral arms and potentially a bar structure. The density and state of matter is highly inhomogeneous within the disk. In general one can distinguish up to five different phases of the interstellar medium (ISM), a summary of the basic properties relevant for this thesis is given in Tab. 1.1 [75, 76, 182]. Molecular clouds contain the majority of the mass of the Galaxy while occupying a negligible volume of the disk. The temperature and ionisation fractions in this mostly cold neutral medium (CNM) is low and molecules can form. Stars are created by gravitational collapse of the cores of molecular clouds, containing the diffuse molecular medium (DiM) [90]. The main ionisation agent in these molecular clouds are low energy cosmic rays. This means that they determine the coupling of magnetic fields and the gas which in turn regulates star formation [106, 153, 165, 170].

These clouds are often surrounded by the warm neutral medium (WNM) [76]. Due to the higher temperature and smaller density, there is no gravitational collapse. Similar regions with a larger ionisation fraction are called warm ionised medium (WIM). Both combined make up roughly half of the volume of the Galaxy [75, 76].

Stellar winds and supernovae produce regions of low density and both high temperature and ionisation rate. These hot ionised media (HIM) fill up to 50 % of the disk. One example is the local bubble surrounding the solar system, with roughly 10 % of the average interstellar gas density. It is caused by several supernova explosions in the B1 subgroup of the Pleiades [21].

These media have a distinct influence on cosmic ray propagation. In neutral dense regions low energy cosmic rays lose energy fast by ionisation and pion production, latter is visible in gamma-rays (see Sec. 1.4.2). Additionally, ion-neutral damping efficiently reduces cosmic ray scattering, leading to faster diffusion in the affected regions [36].

Above and below the disk extends the galactic halo, whose exact extent is unknown, but radio signals from synchrotron emission and cosmic ray propagation parameters indicate a height of several kpc. This region contains mostly magnetic fields and only very thin, ionised gas originating from the disk.

1.3. The Standard Model of Cosmic Ray Origin

The identification of the sources of cosmic rays is hindered by their deflection in magnetic fields. However, a variety of basic ideas has been known since the last century. In the following we will shortly explain these.

1.3.1. Supernova Remnant Paradigm

Already in 1934 Baade & Zwicky [16] provided a purely energetic argument for supernova remnants as the sources of the majority of the galactic cosmic rays. The energy density of cosmic rays on Earth is measured to be about $\rho_{CR} = 1\,\mathrm{eV/cm^3}$. The majority of this is contributed by particles with energy of around 1 GeV. Measurements in dense molecular clouds indicate that this energy density should be similar in the entire Galactic disk. The escape time of cosmic rays from the Galactic disk is given by $\tau_{\mathrm{esc,disk}} = \lambda_{\mathrm{esc}}/(c\beta n_{\mathrm{gas,disk}}) \approx 6\,\mathrm{Myr}$. This means the power needed to sustain the observed energy density is given by:

$$P_{\mathrm{CR}} = \frac{\rho_{\mathrm{CR}} V_{\mathrm{disk}}}{\tau_{\mathrm{esc,disk}}} \simeq 3 \cdot 10^{48}\,\mathrm{erg/yr}, \tag{1.4}$$

where the volume of the disk V_{disk} is given by the properties explained in Sec. 1.2.

Supernova explosions occur with a frequency of $f_{\mathrm{SN}} = 0.03\,\mathrm{yr}^{-1}$ with an energy of around $E_{\mathrm{SN}} \approx 10^{51}$ erg. If 10 % of this energy is converted to cosmic rays, it can sustain the observed energy density:

$$P_{\mathrm{SN}} = 0.1 E_{\mathrm{SN}} f_{\mathrm{SN}} \simeq 3 \cdot 10^{48}\,\mathrm{erg/yr}. \tag{1.5}$$

Hence, supernova remnants are the most likely sources of cosmic rays. However, this does not answer how cosmic rays are accelerated.

1.3.2. Fermi Acceleration

One of the first ideas of how cosmic rays are accelerated is by elastic collisions with magnetic scattering centres, called clouds, which travel with a random velocity u. This can be either magnetic mirrors or curved field lines [73]. Then they might gain energy stochastically, a process which is known as second order Fermi acceleration. The basic idea is the following: Due to the proper motion of comic rays they will encounter more clouds moving towards than away from them. In other words, they will experience more head on than tail on collisions. This results in an average net energy gain (ΔE) of

$$\left\langle \frac{\Delta E}{E} \right\rangle \propto \left(\frac{u}{c}\right)^2. \tag{1.6}$$

Due to the quadratic dependence on u/c this is called second order Fermi acceleration [136]. Typically, cosmic rays scatter on alfvénic turbulence. In this case the random velocity is the Alfvén speed as given by Eq. 1.99 and results to 1 km/s. Then $u/c \approx 10^{-5}$ and this process is insufficient to accelerate particles to the highest energies before they can escape their sources [199]. However, if the scattering centres are not randomly oriented but instead converging the probability for a head on collision is increased, then the energy gain is proportional to:

$$\left\langle \frac{\Delta E}{E} \right\rangle \propto \left(\frac{u}{c}\right), \tag{1.7}$$

which is called first order Fermi acceleration [23]. Typical regions where flows converge are shocks, which will be investigated in the next section.

1.3.3. Rankine-Hugoniot Jump Conditions

The maximum speed at which information about density changes can be transmitted in a fluid is the speed of sound c_S in the medium. If the flow velocity is faster than this at the transition to subsonic speeds a shock boundary forms [55]. The width of this region is determined by convective and dissipative effects. For hot astrophysical plasmas it can be regarded as infinitesimal. All quantities before the shock are called upstream and all after the shock downstream. If the magnetic fields are paral-

lel to the shock normal, the condition that the magnetic field has to be divergence free leads to the conservation of magnetic field across the shock [143]. Hence, the shock is purely hydrodynamical.

In this case we can follow the calculations of Fitzpatrick [77], and the conservation equations of fluid mass, momentum and energy in the rest frame of the shock read:

$$\frac{\partial \rho}{\partial t} + \nabla \cdot (\rho \mathbf{v}) = 0, \tag{1.8}$$

$$\frac{\partial \rho \mathbf{v}}{\partial t} + \nabla \cdot \mathbf{T} = 0, \tag{1.9}$$

$$\frac{\partial \mathbf{U}}{\partial t} + \nabla \cdot \mathbf{u} = 0, \tag{1.10}$$

with density ρ, velocity $\mathbf{v}$, stress tensor $\mathbf{T}$, energy tensor $\mathbf{U}$ and total energy density flux density $\mathbf{u}$ as defined in [77]. If the shock radius is larger than the extent of the shock, changes along the shock can be neglected and the problem becomes one dimensional along the shock normal, which we choose to be in z direction without loss of generality. This case is called planar and allows to simplify the equations to:

$$\frac{\mathrm{d}\rho v_z}{\mathrm{d}z} = 0, \qquad \frac{\mathrm{d}T_{zz}}{\mathrm{d}z} = 0, \qquad \frac{\mathrm{d}u_z}{\mathrm{d}z} = 0. \tag{1.11}$$

The total stress tensor $\mathbf{T}$ and the total energy flux $\mathbf{u}$ in z direction are:

$$T_{zz} = \rho v_z^2 + P, \qquad u_z = \frac{1}{2}\rho v_z^3 + \frac{\Gamma}{\Gamma - 1} P v_z, \tag{1.12}$$

where P is the pressure and $\Gamma = \frac{5}{3}$ is the adiabatic index of the plasma, defined by the requirement that the entropy has to be constant:

$$\frac{\mathrm{d}}{\mathrm{d}t}\left(\frac{P}{\rho^\Gamma}\right) = 0. \tag{1.13}$$

Integrating these equations around the shock results in the Rankine-Hugoniot jump conditions [140]

$$\frac{\rho_{\mathrm{down}}}{\rho_{\mathrm{up}}} = r, \qquad \frac{v_{\mathrm{down}}}{v_{\mathrm{up}}} = \frac{1}{r}, \qquad \frac{P_{\mathrm{down}}}{P_{\mathrm{up}}} = R. \tag{1.14}$$

Where r is the compression ratio, R the pressure ratio, M_{up} the Mach number and c_s the sound speed, defined as:

$$r = \frac{(\Gamma + 1) M_{\mathrm{up}}^2}{2 + (\Gamma - 1) M_{\mathrm{up}}^2}, \qquad R = 1 + \Gamma M_{\mathrm{up}}^2 \left(1 - r^{-1}\right), \tag{1.15}$$

$$M_{\mathrm{up}} = \frac{v_{\mathrm{up}}}{c_{s,\mathrm{up}}}, \qquad c_{\mathrm{up}} = \left(\frac{\Gamma p_{\mathrm{up}}}{\rho_{\mathrm{up}}}\right)^{1/2}. \tag{1.16}$$

For a supernova with energy E_{SN} the expansion velocity $u_{\mathrm{sh}} = \sqrt{2E_{\mathrm{SN}}/M_{\mathrm{ej}}}$ of the ejecta of mass M_{ej} is of the order of $u_{\mathrm{sh}} = 10^4\,\mathrm{km/s}$. This is significantly higher than the typical sound speed $c_s = 10 - 100\,\mathrm{km/s}$, hence the Mach number will be large. In this case the shock is called "strong" or "ideal" and the compression ratio is roughly $r \approx 4$. For slower shock speed this ratio changes until at a Mach number of one the shock seizes to exist.

1.3.4. Diffusive Shock Acceleration

Most primary cosmic rays are presumably accelerated from the background plasma via first order Fermi acceleration in shocks. In the rest frame of a shock the upstream material is advected towards the shock with u_{sh}, then according to the jump conditions of Sec. 1.3.3, the downstream plasma moves

away from the shock with $u_{\rm sh}/r$. If the particles are isotropic up- and downstream of the shock, their spectra can be derived from the diffusion-advection equation (see e.g. Eq. 1.47):

$$\frac{\partial f}{\partial t} - \frac{\partial}{\partial z}\kappa\frac{\partial f}{\partial z} + v\frac{\partial f}{\partial z} + \frac{p}{3}\frac{\mathrm{d}v}{\mathrm{d}z}\frac{\partial f}{\partial p} = Q(z,p), \tag{1.17}$$

with absolute value of the momentum p. Particles are being injected at $p_{\rm inj}$ with $Q(z,p) = Q_p(p)\delta(z) = Q_0\delta(p-p_{\rm inj})\delta(z)$. Everywhere but at the shock this can be simplified to:

$$\frac{\partial}{\partial z}\kappa\frac{\partial f}{\partial z} - v\frac{\partial f}{\partial z} = 0, \tag{1.18}$$

where a steady state was assumed.
The general solution to this equation is [57]:

$$f(z,p) = g_0(p)\exp\left(\int_0^z \frac{v}{\kappa(z')}\mathrm{d}z'\right) + g_1(p), \tag{1.19}$$

where g are arbitrary functions of p. Imposing the natural boundary conditions of a spatially independent spectrum far upstream of the shock, $f(z,p) \to f_0(p)$ as $z \to -\infty$, and a finite spectrum downstream $f(z,p) < \infty$ as $z \to \infty$, the solution can be simplified to:

$$f(z,p) = \begin{cases} f_0(p)\exp\left(\int_0^z \frac{v_{\rm up}}{\kappa_{\rm up}(z')}\mathrm{d}z'\right) + f_{\rm up}(p) & z < 0 \\ f_{\rm down}(p) & z \geq 0 \end{cases}, \tag{1.20}$$

if $\int_0^z \mathrm{d}z'/\kappa_\parallel \to \pm\infty$ when $z \to \pm\infty$. This means, a balance between advection and diffusion can only be achieved upstream. In order to connect the functions given in Eq. 1.20 one in principle has to use the full distribution function in pitch-angle $F(z,p,\mu)$ (see [56]). Here the same solution is obtained by demanding Eq. 1.18 to hold at the shock discontinuity as well, which is not a priory valid. Then a weak solution of the equation can be obtained by multiplying with the test function $\int_0^z \frac{\mathrm{d}z'}{\kappa}$ and integrating around an ininitesimal region of size ϵ, which results in:

$$[f]_{-\epsilon}^{+\epsilon} = O(\epsilon). \tag{1.21}$$

This is the continuity condition $f(0^+) = f(0^-) \Rightarrow f_0 + f_{\rm up} = f_{\rm down}$. Because particle transport is determined by magnetic fields and these do not change at the shock if the shock is a parallel shock, there is no immediate effect of the shock on them. The second constant can be determined by using 1 as a test function and repeating the same procedure as above:

$$\left[\kappa\frac{\partial f}{\partial z}\right]_{-\epsilon}^{+\epsilon} + \frac{p}{3}\left[v\frac{\partial f}{\partial p}\right]_{-\epsilon}^{+\epsilon} + [Q(z,p)]_{-\epsilon}^{+\epsilon} = O(\epsilon). \tag{1.22}$$

Evaluating this for f of Eq. 1.20 gives:

$$\frac{p}{3}v_{\rm down}\frac{\partial f_{\rm down}}{\partial p} - \frac{p}{3}v_{\rm up}\frac{\partial}{\partial p}(f_0 + f_{\rm up}) = \kappa\left.\frac{\partial f}{\partial z}\right|_{0^+} - \kappa\left.\frac{\partial f}{\partial z}\right|_{0^-} + Q_p(p), \tag{1.23}$$

$$v_{\rm up}\frac{p}{\gamma_s}\frac{\partial f_{\rm down}}{\partial p} = -v_{\rm up}f_0 + Q_p(p) = -v_{\rm up}(f_{\rm down} - f_{\rm up}) + Q_p(p), \tag{1.24}$$

where the source spectral index is given by $\gamma_s = 3r/(r-1)$.
The general solution of the downstream side is then:

$$f_{\rm down}(p) \equiv \gamma_s p^{-\gamma_s}\int_0^p p'^{\gamma_s - 1} f_{\rm up}(p')\mathrm{d}p' + \frac{\gamma_s}{v_{\rm up}p_{\rm inj}}\left(\frac{p}{p_{\rm inj}}\right)^{-\gamma_s} Q_0, \tag{1.25}$$

where the first term represents all particles injected from upstream infinity and the second one all particles injected by the shock. For a pure injection at the shock, the spectrum will be:

$$f_{\text{down}}(p) \propto \left(\frac{p}{p_{\text{inj}}}\right)^{-\gamma_s} = \left(\frac{p}{p_{\text{inj}}}\right)^{-4}, \tag{1.26}$$

with the latter holding in case of a strong shock. This result is crucial, since it provides a mechanism for particle acceleration true over many orders of magnitude. Due to non-linear feedback effects or deviations of the underlying assumptions of a strong, parallel shock more complex models predict softer spectra [53, 136].

1.3.5. Maximum Energy

The maximum achievable energy is given by the Hillas-Criterion [101], which demands that particles of momentum p and charge q which gyrate around a magnetic field with strength B with Larmor radius r_L are confined in the acceleration region of size R:

$$R \geq r_L \qquad \text{or} \qquad p_{\text{max}} \leq qBR. \tag{1.27}$$

The typical magnetic field strength in the Galaxy is of the order of μG [97] and the typical acceleration regions have sizes of pc scale. The achievable maximum energy in this case is then only TeV and not PeV, as expected by observations of the spectra in Sec. 1.1.1 [133]. This indicates, that the magnetic field has to be increased close to the acceleration sites [183]. How cosmic rays can do so is motivated in Sec. 1.5.3.

1.4. The Cosmic Ray Transport Equation

Instead of using the intensity J, which depends on observational quantities like the volume angle or area, it is convenient to use observation-independent quantities such as the phase space density $f(\mathbf{x}, p, t)$, that is the particles per unit volume in space and momentum or the spectrum differential in momentum or energy $\psi(\mathbf{x}, p, t) = \hat{\psi}(\mathbf{x}, E, t)v$. These quantities are related via:

$$\psi(\mathbf{x}, p, t) = 4\pi p^2 f(\mathbf{x}, p, t). \tag{1.28}$$

The intensity J can be expressed as:

$$J(\mathbf{x}, E, t) = \frac{1}{4\pi}\psi(\mathbf{x}, E, t). \tag{1.29}$$

We will follow the calculations of Mertsch [151] to derive the transport equation of cosmic rays and make additions where we deem them necessary. We start from Liouville's theorem, which implies conservation of phase space density along the particles trajectory [134]:

$$\frac{\mathrm{d}f}{\mathrm{d}t} = \frac{\partial f}{\partial t} + \frac{\mathrm{d}\mathbf{x}}{\mathrm{d}t} \cdot \frac{\partial f}{\partial \mathbf{x}} + \frac{\mathrm{d}\mathbf{p}}{\mathrm{d}t} \cdot \frac{\partial f}{\partial \mathbf{p}} = 0. \tag{1.30}$$

For charged particles in a magnetic field, the momentum change is given by the Lorentz force

$$\frac{\mathrm{d}\mathbf{p}}{\mathrm{d}t} = q\left(\mathbf{E} + \frac{\mathbf{v}}{c} \times \mathbf{B}\right). \tag{1.31}$$

Most of the interstellar matter is a plasma. This means electric fields are efficiently screened out by freely moving charges, leading to $\mathbf{E} = 0$ and electric field fluctuations are significantly smaller

than magnetic ones. Then, Eq. 1.31 can be inserted into Eq. 1.30, which gives the so-called Vlasov equation [214]:

$$\frac{\partial f}{\partial t} + \mathbf{v} \cdot \nabla_x f + q\left(\frac{\mathbf{v}}{c} \times \mathbf{B}\right) \cdot \nabla_p f = 0. \tag{1.32}$$

Collisions of the plasma particles can be accounted for by an additional term on the right-hand side. However, this is not necessary in most astrophysical environments. Magnetic fields in the Galaxy are usually separated into two components, as explained in Sec. 1.5, a large scale homogeneous background field $\mathbf{B_0} = \langle \mathbf{B} \rangle$ and a small-scale turbulent component $\delta\mathbf{B}$ which fulfils $\langle \delta\mathbf{B} \rangle = 0$, where the angled brackets denote the average over an ensemble of magnetic fields. Then we can split Eq. 1.32 into stochastic and deterministic terms for relativistic particles:

$$\frac{\partial f}{\partial t} + c\hat{\mathbf{p}} \cdot \nabla_x f + (\mathbf{p} \times (\mathbf{\Omega} + \omega)) \cdot \nabla_p f = 0, \tag{1.33}$$

with the gyro frequencies $\mathbf{\Omega} = q\mathbf{B_0}/p$ and $\omega = q\delta\mathbf{B}/p$ as well as the identity $c\hat{\mathbf{p}} = \mathbf{v}$. This can be written in terms of Liouville operators:

$$\mathcal{L}_0 = c\hat{\mathbf{p}} \cdot \nabla_x - i\mathbf{\Omega} \cdot \mathbf{L}, \qquad \delta\mathcal{L} = -i\omega \cdot \mathbf{L}, \tag{1.34}$$

where $\mathbf{L} = -i\mathbf{p} \times \nabla_p$. With this the Vlasov equation can be expressed as

$$\frac{\partial f}{\partial t} + \mathcal{L}_0 f + \delta\mathcal{L} f = 0. \tag{1.35}$$

Due to the turbulence of the magnetic field, also the phase space density will become turbulent $f = \langle f \rangle + \delta f$ with $\langle \delta f \rangle = 0$ and $f_0 = \langle f \rangle$. Then the ensemble averaged Vlasov equation reads, see e.g Jokipii [116],

$$\frac{\partial f_0}{\partial t} + \mathcal{L}_0 f_0 = -\langle \delta\mathcal{L}\delta f \rangle . \tag{1.36}$$

This indicates that the local average cosmic ray density changes due to streaming down the density gradient, global rotation around the background magnetic field (l.h.s.) and the ensemble average of the rotations around the turbulent magnetic field (r.h.s.). Substracting Eq. 1.35 from Eq. 1.36 leaves:

$$\frac{\partial \delta f}{\partial t} + \mathcal{L}_0 \delta f + \delta\mathcal{L} f_0 = \delta\mathcal{L}\delta f - \langle \delta\mathcal{L}\delta f \rangle , \tag{1.37}$$

where the difference on the right-hand side is of second order in δf and $\delta\mathbf{B}$. For small perturbations, it can be neglected. Then the formal solution of Eq. 1.37 can be found via the method of characteristics:

$$\delta f = \delta f(t = t_0) + \int_{t_0}^{t} \mathrm{d}t' \left[\delta\mathcal{L} f_0\right]_{P(t')} , \tag{1.38}$$

where the subscript $P(t')$ indicates that the term within the squared brackets has to be evaluated along the unperturbed trajectory of the $\mathcal{L}_0$ operator. If we now substitute Eq. 1.38 into Eq. 1.36 and then write out the Liouville operators explicitly, we obtain:

$$\frac{\partial f_0}{\partial t} + \mathbf{v} \cdot \nabla_x f_0 + q\frac{\mathbf{v} \times \langle \mathbf{B} \rangle}{c} \cdot \nabla_p \langle f \rangle \simeq \int_{t_0}^{t} \mathrm{d}t' \left\langle q\frac{\mathbf{v} \times \delta\mathbf{B}}{c} \cdot \nabla_p \left[q\frac{\mathbf{v} \times \delta\mathbf{B}}{c} \cdot \nabla_p \langle f \rangle \right]_{P(t')} \right\rangle, \tag{1.39}$$

where $\delta f(t = t_0)$ was neglected, since the late time limits we are interested in are independent of the initial perturbations [13, 143, 151]. At this point, it is already apparent that the right-hand side will lead to a diffusion term, since it depends on two momentum derivatives. Additionally, the diffusion tensor has to depend on the two point correlation function of $\delta\mathbf{B}$ integrated along the unperturbed

trajectory $P(t')$. To make further simplifications it is useful to define some properties of the turbulent magnetic field first. The most important one is the two point correlation function:

$$P_{ij} \equiv \left\langle \delta B_i(0) \delta B_j(t) \right\rangle . \tag{1.40}$$

The correlation length L_c of the turbulence in each direction is defined as [151]:

$$\left\langle \delta B^2 \right\rangle L_c \equiv \int_0^\infty \mathrm{d}\Delta r \, \langle \delta B(\mathbf{r}) \delta B(\mathbf{r} + \mathbf{\Delta r}) \rangle \tag{1.41}$$

and the corresponding correlation time τ_c as:

$$\left\langle \delta B^2 \right\rangle \tau_c \equiv \int_0^\infty \mathrm{d}\Delta t \, \langle \delta B(t) \delta B(t + \Delta t) \rangle . \tag{1.42}$$

Then the right-hand side of Eq. 1.39 can be simplified in radial coordinates assuming gyrotropy $\langle f \rangle / \phi = 0$, homogeneous and stationary turbulence as well as a correlation time

$$\frac{\langle f \rangle}{\frac{\partial \langle f \rangle}{\partial t}} \ll \tau_c \ll \Omega^{-1}. \tag{1.43}$$

Then the ensemble averaged Vlasov equation can be written in a Fokker-Planck equation:

$$\frac{\partial \langle f \rangle}{\partial t} + v\mu \frac{\partial \langle f \rangle}{\partial z} = \frac{\partial}{\partial \mu} \left(\kappa_{\mu\mu} \frac{\partial \langle f \rangle}{\partial \mu} \right), \tag{1.44}$$

where $\mu = \cos(\theta)$ with θ being the angle between the direction of motion $\mathbf{p}$ and the background magnetic field $\mathbf{B_0}$, and $\kappa_{\mu\mu}$ is the pitch-angle diffusion coefficient. When the averaged phase space density only varies slowly with time and position, one can derive a spatial diffusion equation along the background magnetic field ($\mathbf{B_0} \parallel \mathbf{z}$) [96]:

$$\frac{\partial \langle f \rangle}{\partial t} - \frac{\partial}{\partial z} \left(\kappa_\parallel \frac{\partial \langle f \rangle}{\partial z} \right) = 0, \tag{1.45}$$

with the parallel diffusion coefficient

$$\kappa_\parallel = \frac{v^2}{8} \int_{-1}^{1} \mathrm{d}\mu \frac{\left(1 - \mu^2\right)^2}{\kappa_{\mu\mu}}. \tag{1.46}$$

This result by itself is already remarkable, since it predicts only diffusion parallel to the background field. Perpendicular diffusion processes exist, but are subdominant in most scenarios, see eg. Kuhlen et al. [130] for more details. If one is only interested in scales above L_c, the random orientation of field lines leads to effective isotropic diffusion with $\kappa = \kappa_\parallel / 3$ [197].

It is convenient to express the comic ray transport equation, which contains particle sources and sinks as well as energy loss processes in addition to diffusion in terms of ψ_j where j denotes an individual particle species [24]:

$$\begin{aligned} \frac{\partial \psi_j}{\partial t} = {} & \nabla \cdot (\kappa \cdot \nabla \psi_j - \mathbf{v} \psi_j) + \frac{\partial}{\partial p} \left(-\dot{p} \psi_j + \frac{p}{3} (\nabla \cdot \mathbf{v}) \psi_j \right) \\ & - \frac{1}{\gamma \tau_j} \psi_j - \psi_j v n_{\mathrm{gas}} \sigma_j + \sum_{k>j} \frac{\psi_k}{\gamma \tau_{k-j}} + \sum_{k>j} \psi_k v n_{\mathrm{gas}} \sigma_{k-j} + Q_j. \end{aligned} \tag{1.47}$$

The first term on the right-hand side describes diffusion with a diffusion tensor κ, which for isotropic diffusion has the form $\kappa_{ij} = \delta_{ij} \kappa$ or for purely parallel diffusion only terms along B_0. This will be further elaborated in Sec. 1.4.3. Advection is accounted for with velocity $\mathbf{v}$. Continuous and adiabatic

energy loss processes are described by the second term, which will be explained further in Sec. 1.4.2. The third and fourth term are particle sinks, namely decay with decay time τ_j and spallation with cross-section σ_j upon interstellar gas of density $n_{\rm gas}$. Equivalently, the next two terms describe the production due to decay and spallation of heavier elements. Finally, the last term describes the injection by primary sources.

1.4.1. The Halo Model

Galactic cosmic ray propagation is often approximated as one dimensional in the direction perpendicular to the disk, since the variation along this axis is significantly stronger than within the disk [89, 168]. Additionally, the Galaxy is nearly symmetric around the disk, hence only one direction has to be solved and symmetry can be imposed. The sources of cosmic rays and most of the gas are assumed to be located within the disk, which has an extension significantly smaller than the halo $h \ll H$, therefore its extension is often approximated as infinitely thin. Additionally, for stable nuclei above a few GeV all involved timescales are significantly smaller than the evolution of the Galaxy, hence a steady state forms and temporal derivatives can be neglected. Under these simplifications the equation describing cosmic ray transport (see Eq. 1.47) can be rewritten as [19]:

$$\frac{\partial}{\partial z}\left(v\psi_j - \kappa\frac{\partial\psi_j}{\partial z}\right) + \frac{\partial}{\partial p}\left[\left(\frac{\mathrm{d}p}{\mathrm{d}t}\right)\psi_j - \frac{p}{3}\frac{dv}{dz}\psi_j\right] + \frac{1}{\gamma\tau_j}\psi_j + 2h\delta(z)\beta c n_{\rm gas}\sigma_j\psi_j = Q_j\,, \tag{1.48}$$

where we have absorbed all source terms into

$$Q_j(p) = 2h\delta(z)Q_{{\rm prim},j}(p) + \sum_{k>j}\frac{\psi_k}{\gamma\tau_{k\to j}} + 2h\delta(z)\beta c n_{\rm gas}\sum_{k>j}\sigma_{k\to j}\psi_k\,, \tag{1.49}$$

with primary source function $Q_{\rm prim,j}(p)$ is the primary source term in the disk.

Since the propagation distance of galactic cosmic rays is long and cosmic rays can be assumed to propagate the entire galactic volume, the diffusion properties represent a global average as measured on Earth and strong local variations still might be possible within the Galaxy. The diffusion process itself is then approximated as isotropic and the tensor reduces to a scalar κ. Additionally, the extent of the galactic halo and the disk are parameters in this model and not explained self-consistently. Despite these constraints, this model has been remarkably successful in fitting the observed spectra. However, recent more precise measurements of spectra on Earth and observations within the Galaxy make extensions necessary (see eg. [80] for a review).

1.4.2. Energy Loss Processes

Depending on the species and energy, cosmic rays loose a significant fraction of their energy during their propagation. In this section we start by discussing energy losses of electrons and positrons at high energies. These are mostly inverse Compton and Synchrotron losses. Due to the screening of electric fields in interstellar plasmas, no bremsstrahlung is emitted. Afterwards, we explain losses of hadrons. In particular Ionisation, Coulomb and Pion-Production losses.

Inverse Compton Losses Electrons and positrons are subject to inverse Compton and synchrotron losses, which limit the distance they travel, especially at TeV energies. Inverse Compton scattering describes the process of a low energy photon scattering upon a high energy electron/positron, where the photon gains energy, which is the inverse of the Compton effect [136]. Seen from the rest frame

$\mathcal{S}'$ of the electron/positron the process resembles the normal Compton scattering. In the classical Thomson regime, where $h\omega' \ll m_e c^2$, the energy loss rate is given by

$$-\left(\frac{\mathrm{d}E}{\mathrm{d}t}\right)' = \sigma_T c U'_{\mathrm{rad}}, \tag{1.50}$$

where $\sigma_T = 8\pi/3r_0^2$, with classical electron radius $r_0 = q_e^2/m_e c^2$ and charge q_e. This is invariant under Lorentz transformation and hence equal to $\mathrm{d}E/\mathrm{d}t$ in the observer frame $\mathcal{S}$. To determine U'_{rad} from a given radiation field U_{rad} in $\mathcal{S}$, the energy $E = h\omega$ needs to be transformed. The relativistic Doppler formula gives:

$$h\omega' = \gamma h\omega\left(1 + \frac{v}{c}\cos(\theta)\right), \tag{1.51}$$

with angle θ between the photon and the electron. Additionally conservation properties of the photon number density and the four-volume element $\mathrm{d}t\mathrm{d}x\mathrm{d}y\mathrm{d}z$ can be used. The energy density at energy E is given by

$$U_{\mathrm{rad}} = N(E)h\omega, \tag{1.52}$$

where $N(E)$ is the number density at E. Within a differential three volume

$$\mathrm{d}N(E) = n(E)\mathrm{d}x\mathrm{d}y\mathrm{d}z \tag{1.53}$$

is conserved under Lorentz transformation. Furthermore, the transformation of the four-volume element using the standard expression (in 2D) reads:

$$\mathrm{d}t\mathrm{d}x = \begin{vmatrix} \frac{\partial t}{\partial t'} & \frac{\partial x}{\partial t'} \\ \frac{\partial t}{\partial x'} & \frac{\partial x}{\partial x'} \end{vmatrix} \mathrm{d}t'\mathrm{d}x'. \tag{1.54}$$

It can be shown that the determinant is unity by using the inverse Lorentz transformation. Hence, the vector is Lorentz invariant. Dividing Eq. 1.53 by $\mathrm{d}t$ and using Eq. 1.54 it is immediately clear that $n(E)/\mathrm{d}t$ is conserved as well. Since energy E and $\mathrm{d}t$ transform identically, also $n(E)/E$ is Lorentz invariant. Thus $n(E)$ also transforms as E, and in combination according to Eq. 1.52 U_{rad} transforms identically to E^2. Assuming an isotropic radiation field, the contribution to the radiation field from the solid angle $\mathrm{d}\Omega$ is:

$$\mathrm{d}U'_{\mathrm{rad}} = U_{\mathrm{rad}}\left(1 + \frac{v}{c}\cos(\theta)\right)^2 \mathrm{d}\Omega. \tag{1.55}$$

Now the integration over the entire sphere results in:

$$U'_{\mathrm{rad}} = \frac{3}{4}U_{\mathrm{rad}}\left(\gamma^2 - \frac{1}{4}\right). \tag{1.56}$$

The energy gain of the photon filed by this process is then:

$$-\left(\frac{\mathrm{d}E}{\mathrm{d}t}\right) = \sigma_T c\frac{3}{4}U_{\mathrm{rad}}\left(\gamma^2 - \frac{1}{4}\right). \tag{1.57}$$

However, the rate at which the energy is removed from the low energy photon field $\sigma_T c U_{\mathrm{rad}}$ has to be subtracted to get the total energy gain of the photon field. Using $\left(\gamma^2 - 1\right) = \left(v^2/c^2\right)\gamma^2$, the final form of the energy loss rate of electrons reads:

$$\frac{\mathrm{d}E}{\mathrm{d}t} = \frac{3}{4}\sigma_T c U_{\mathrm{rad}}\left(\frac{v^2}{c^2}\right)\gamma^2. \tag{1.58}$$

If the energy of the photon in the restframe of the electron is close to the electron mass, the classical Thomson cross-section is not justified and Klein-Nishina first order quantum electrodynamics corrections have to be accounted for [122]. There are several parametrisations of the Klein-Nishina

cross-section available, the full formula can be found in [26]. For the purpose of this thesis it is sufficient to use the approximation [62]:

$$\frac{\sigma_{KN}}{\sigma_T} \approx \frac{45m_e^2/64\pi^2T_i^2}{\left(45m_e^2/64\pi^2T_i^2\right)+\left(E_e^2/m_e^2\right)}. \tag{1.59}$$

However, the energy loss rate derived here is only valid in case the electrons lose a small fraction of their energy in frequent scattering processes. At high energies this approximation is only marginally justified. The impact on inverse Compton γ-ray halos around pulsars has been investigated by John and Linden [114], who found a less pronounced high energy cut off.

Synchrotron Losses Accelerated charged particles emit radiation in the non-relativistic limit according to Larmors law [107]:

$$\frac{\mathrm{d}E}{\mathrm{d}t} = \frac{2q^2a'^2}{3c^2}, \tag{1.60}$$

where a' is the acceleration of the particle in the momentary rest frame S'. In the laboratory frame S this is given by the Lorenz force

$$F_L = \frac{q}{c}\left(\mathbf{E}+\mathbf{v}\times\mathbf{B}\right), \tag{1.61}$$

where q is the charge of the particle, resulting in:

$$a_\parallel = 0, \qquad a_\perp = \frac{qB}{mc\gamma}u_\perp. \tag{1.62}$$

The acceleration in the momentary rest frame is given by:

$$a'_\parallel = \gamma^3 a_\parallel, \qquad a'_\perp = \gamma^2 a_\perp. \tag{1.63}$$

Then the total irradiated power by charged particles in a magnetic field is:

$$\frac{\mathrm{d}E}{\mathrm{d}t} = \frac{2q^2\gamma^4a_\perp^2}{3c^2} = 2\sigma_T c\beta_\perp^2\gamma^2U_B. \tag{1.64}$$

For an isotropically distributed pitch-angle α, the average $\beta_\perp = v_\perp/c$ is given by

$$\langle\beta_\perp^2\rangle = \beta^2\langle\sin(\alpha)^2\rangle = \frac{2}{3}\beta^2. \tag{1.65}$$

Finally, this allows us to write the power emitted by charged particles in a magnetic field via Synchrotron radiation as:

$$\frac{\mathrm{d}E}{\mathrm{d}t} = \frac{4}{3}\sigma_T c\beta^2\gamma^2U_B. \tag{1.66}$$

This result is remarkably similar to the inverse Compton formula, which is not surprising, since the only difference is whether the photon is real or virtual.

Ionisation Losses Protons and heavier charged particles undergo a variety of different interactions when passing through a medium. Electrostatic forces lead to the ionisation and excitation of molecules and atoms, heating up the medium. In contrast to X-rays or other ionising agents, the absorption length of cosmic rays is long. Hence, they are assumed to be responsible for the high ionisation rates observed in dense molecular clouds. The energy losses induced by ionisation above 100 keV are given by [143]:

$$-\left(\frac{\mathrm{d}E}{\mathrm{d}t}\right)_{\mathrm{ion}} \approx 1.82\times10^{-7}Z_{\mathrm{eff}}^2\left(\frac{n_{\mathrm{H}}}{\mathrm{cm}^{-3}}\right)\left[1+0.185\ln(\beta)\theta(\beta-\beta_0)\right]\frac{2\beta^2}{\beta_0^3+2\beta^3}\frac{\mathrm{eV/c}}{\mathrm{s}}, \tag{1.67}$$

where $\beta_0 = 0.01$, θ is the Heaviside function, n_H the number density of hydrogen and

$$Z_{\text{eff}} = Z\left[1 - 1.034\exp\left(-137\beta Z^{-0.688}\right)\right], \tag{1.68}$$

with charge number Z. A typo in [143] is corrected in the prefactor of the logarithm in Eq. 1.67, which is one order of magnitude too small [108].

Coulomb Losses In ionised media, the charged cosmic ray nuclei undergo Coulomb interactions with charges of the ISM. The energy loss rate by this process is given by [143]:

$$-\left(\frac{\mathrm{d}E}{\mathrm{d}t}\right)_{\text{Coulomb}} \approx 3.1\times10^{-7}Z^2\left(\frac{n_e}{\mathrm{cm}^{-3}}\right)\frac{\beta^2}{x_m^3+\beta^3}\frac{\mathrm{eV/c}}{\mathrm{s}}, \tag{1.69}$$

with $x_m = 0.0286\left(T/2\times10^6\,\mathrm{K}\right)$, the electron number density n_e, the particle speed $\beta = v/c$.

Pion-Production Losses In inelastic collision between cosmic ray hadrons and hadrons from the interstellar medium, charged and neutral pions are produced mainly via the channels:

$$\begin{aligned} &p + p \to p + p + \pi^0,\\ &p + p \to p + n + \pi^+,\\ &p + p \to p + p + \pi^+ + \pi^-, \end{aligned} \tag{1.70}$$

which in turn quickly decay via the main channels:

$$\begin{aligned} &\pi^0 \to \gamma + \gamma,\\ &\pi^+ \to \mu^+ + \nu_\mu \quad \text{and} \quad \mu^+ \to e^+ + \overline{\nu}_\mu + \nu_e,\\ &\pi^- \to \mu^- + \overline{\nu}_\mu \quad \text{and} \quad \mu^- \to e^- + \nu_\mu + \overline{\nu}_e. \end{aligned} \tag{1.71}$$

In contrast to the energy loss processes of electrons/positrons, neutrinos are produced here. Hence, the observations of neutrinos from a source is a clear indication of hadronic processes.

The energy loss rate of protons by this mechanism can be approximated by Eq. 34 of Ref. [143]:

$$-\left(\frac{\mathrm{d}p}{\mathrm{d}t}\right)_{\text{pp}} \approx 3.85\times10^{-7}\left(\frac{n_{\text{H}}}{\mathrm{cm}^{-3}}\right)\left(\frac{E}{\mathrm{GeV}}\right)^{1.28}\left(\frac{E}{\mathrm{GeV}}+200\right)^{-0.2}\beta^{-1}\frac{\mathrm{eV/c}}{\mathrm{s}}. \tag{1.72}$$

1.4.3. Quasilinear Diffusion Coefficient in Slab Turbulence

In Sec. 1.4 we have derived that pitch-angle scattering leads to spatial diffusion along the background magnetic field. Now, we want to derive a formula applicable for cosmic rays. The standard approach is the quasilinear theory (QLT) [115]. The main idea of this is to replace the perturbed particle trajectories by the unperturbed ones. We start with the pitch-angle diffusion coefficient, which is given by the Taylor-Green-Kubo formula [93, 128, 201]

$$\kappa_{\mu\mu} = \int_0^\infty \mathrm{d}t\,\langle\dot{\mu}(0)\dot{\mu}(t)\rangle\,, \tag{1.73}$$

where the dots are the derivatives with respect to time. From the equations of motion one finds:

$$\dot{\mu} = \frac{q}{cp}\left(\mathbf{v}\times\mathbf{B}\right)_z = \frac{1}{r_L B_0}\left(v_x\delta\mathbf{B}_y(\mathbf{x}) - v_y\delta\mathbf{B}_x(\mathbf{x})\right) \tag{1.74}$$

and thus

$$\kappa_{\mu\mu} = \frac{1}{r_L^2 B_0^2} \int_0^\infty \mathrm{d}t \left[v_x(t) v_x(0) P_{xx} + v_y(t) v_y(0) P_{yy} \right], \tag{1.75}$$

where the magnetic fields and velocities are evaluated at the unperturbed trajectories. Now, it has become apparent, that the diffusion coefficient depends on the two point correlation function of the magnetic field. The geometry of the turbulence is poorly understood. However, it is often assumed to consist of Alfvén waves [14]. These are low frequency transverse plasma waves that travel along the background magnetic field. Since these are transverse waves, the geometry of the turbulence is the so-called slab turbulence. In this case the correlation function for linear polarised waves is given by

$$P_{i,j}^{\mathrm{slab}} = g(k_\parallel) \frac{\delta(k_\perp)}{k_\perp} \delta_{ij}, \tag{1.76}$$

where $k_\parallel$ and $k_\perp$ are the parallel and perpendicular wave-numbers and g is the turbulence spectrum, which is related to the total turbulence via:

$$\delta B^2 \equiv 4\pi \int_{-\infty}^{\infty} \mathrm{d}\kappa_\parallel g(k_\parallel). \tag{1.77}$$

With this it is possible to show that the pitch-angle diffusion coefficient reads [129]:

$$\kappa_{\mu\mu} = \frac{2\pi^2 \Omega^2 \left(1 - \mu^2\right)}{B_0 v \mu} g\left(k_\parallel = \frac{\Omega}{v\mu}\right), \tag{1.78}$$

with the resonance condition

$$k_\parallel = \frac{\Omega}{v\mu} = \frac{1}{r_L}. \tag{1.79}$$

Hence, particles interact with magnetic waves with a wavelength equal to their Larmor radius. This can be understood intuitively by considering the magnetic field a particle experiences within one Larmor gyration. If the wavelength of the Alfvén wave is equal to the Larmor radius of the particle, the Lorentz force adds up over many gyrations instead of being averaged out. This changes the pitch-angle and ultimately leads to diffusion. For the remainder of this thesis we will use the alfvénic turbulence power spectrum $W(k, t)$, which is normalised via:

$$\frac{\delta B^2}{B_0^2} = \int_{-\infty}^{\infty} \mathrm{d}k W(k). \tag{1.80}$$

Hence, it is related to $g(k) = B_0^2 / 4\pi W(k)$ of Eq. 1.77, where we have omitted the $\parallel$ notation of the wavenumber. If we now evaluate Eq. 1.46 with Eq. 1.78, we find

$$\kappa_\parallel = \frac{4\kappa_{\mathrm{B}}(p)}{\pi k W(k, z, t)}, \tag{1.81}$$

where $\kappa_{\mathrm{B}}(p) = r_{\mathrm{L}}(p) c\beta/3$ is the Bohm diffusion coefficient [156]. The spectral dependence of W will be motivated in Sec. 1.5.1. The approximation of unperturbed trajectories leads to several shortcomings of QLT. The most well-known one is the 90 ° problem[118]. In this case $\kappa_{\mu\mu} \to 0$ for $\mu \to 0$ and the integral in Eq. 1.46 diverges. Additionally, QLT does not account for field line random walk [117].

1.5. Magnetic Fields in the Galaxy

The transport of comic rays is determined by galactic magnetic fields. On large scales they determine particle escape from the Galaxy and deflect ultra-high energy cosmic rays. Its main structure is a spiral disk field, a toroidal halo field and an X-shaped poloidal field [110, 208].

On smaller scales, in resonance with galactic cosmic rays, they determine the amount of scattering and thereby the diffusion of particles as we have shown in Sec. 1.4.3.

1.5.1. Injection of Magnetic Turbulence and Cascade

The precise nature of the turbulence in the galactic disk and the halo is not well known. Within the disk stellar clusters as well as supernova remnants are suspected to inject turbulence. However, the injection scale might vary substantially depending on the region in the disk. Within spiral arms the injection scale L_{inj} is of the order of $1-10$ pc, whereas outside it might reach 100 pc [97]. Subsequently, turbulence cascades to smaller scales until it is dissipated.

For ideal magneto hydrodynamics the magnetic field is frozen into the background plasma. For media where the magnetic energy density is below the kinetic energy density of the plasma, magnetic effects can be ignored and the non-magnetised and incompressible turbulence can be described with the Navier-Stokes equation:

$$\frac{\partial \mathbf{v}}{\partial t} + \mathbf{v} \cdot \nabla \mathbf{v} = -\nabla P + \nu \nabla^2 \mathbf{v} + \mathbf{f}, \tag{1.82}$$

where $\mathbf{v}$ is the velocity field, P the pressure per mass density, ν the kinematic viscosity and $\mathbf{f}$ the force per mass density. Assuming periodicity of the field, this can be rewritten in a spectral balance equation:

$$\frac{\partial E(k,t)}{\partial t} = P(k,t) - \frac{\partial T(k,t)}{\partial k} - D(k,t), \tag{1.83}$$

where $E(k,t) = \frac{\partial \mathcal{E}(k,t)}{\partial t}$ is the power spectrum with cumulative energy density $\mathcal{E}(k,t) = 1/2 \sum_{k'<k} |\tilde{v}(k',t)|^2$, energy injection $P(k,t)$, dissipation $D(k,t) = 2\nu k^2 E(k,t)$, and advection in k by $T(k,t)$. The scales between the injection and dissipation scale are called inertial range.

For homogeneous, isotropic and incompressible hydrodynamic turbulence, so called Kolmogorov turbulence, the spectrum in the inertial range can be derived by purely dimensional arguments [123]. Individual areas of similar vorticity with some degree of coherence are called eddies. For an eddie of size $l = 1/k$ and characteristic velocity $v(k)$, the only characteristic timescale is $\tau_{NL} = (kv(k))$. For a stationary problem, the energy injected at large scales must be dissipated at small scales again, hence the energy transfer rate in between those scales has to be constant. The energy transfer rate ϵ_T must then be

$$\epsilon_T \propto \frac{v^2(k)}{\tau_{NL}} \propto k v^3(k), \tag{1.84}$$

where the first proportionality is given by the cascading power and the second one by the characteristic timescale. The resulting kinetic energy on smaller scales than k is then

$$v^2(k) \propto \left(\epsilon_T k^{-1}\right)^{2/3}, \tag{1.85}$$

which is the well known Kolmogorov law. Since $v^2(k) \propto kE(k)$, this can be reformulated as:

$$E(k) = k^{-1} v^2(k) = \epsilon_T^{2/3} k^{-5/3}. \tag{1.86}$$

Remarkably, the spectrum derived in this way resembles closely the electron density power spectrum, which is a tracer for the turbulent power in the interstellar medium [15]. This solution is only true in the parts of the Galaxy where the magnetic energy density can be ignored. In the magnetised case the expected behaviour was derived by Kraichnan and predicts a power law index of $-2/3$ [124]. In both cases, the advection in k in Eq. 1.83 is given by a diffusion term:

$$T(k,t) = \kappa_{kk} \frac{\partial E(k,t)}{\partial k}, \tag{1.87}$$

where κ_{kk} is given by:

$$\kappa_{kk} \propto \begin{cases} k^{7/2} E(k,t)^{1/2} & \text{Kolmogorov} \\ k^2 E(k,t) & \text{Kraichnan.} \end{cases} \tag{1.88}$$

For the alfvénic power spectrum W the proportionality constant of Eq. 1.88 is given by $c_k v_A$, with $c_k = 0.052$ [62].

Along the background magnetic field, the transport equation for W is [58, 119]:

$$\frac{\partial W}{\partial t} - \frac{\partial}{\partial k}\left(\kappa_{kk}\frac{\partial W}{\partial k}\right) + \frac{\partial}{\partial z}\left(v_A W\right) = \left(\Gamma_{\mathrm{CR}} - \Gamma_D\right) W + Q_W, \tag{1.89}$$

where Γ_{CR} is the growth rate of turbulence due to the resonant streaming instability as derived in Sec. 1.5.3 and Γ_D describes damping processes as explained in Sec. 1.5.2. The injection of turbulence at large scales is accounted for by Q_W. For computational reasons we refrain from calculating the injection of turbulence at large scales and dissipation at small scales and instead impose a background turbulence level W_{BG}. Then the external source term in Eq. 1.89 can be neglected and we obtain

$$\frac{\partial W}{\partial t} + \frac{\partial}{\partial k}\left(\kappa_{kk}\frac{\partial W}{\partial k}\right) + \frac{\partial}{\partial z}\left(v_A W\right) = \left(\Gamma_{\mathrm{CR}} - \Gamma_D\right) W + \Gamma_D(W_{\mathrm{BG}}) W_{\mathrm{BG}}. \tag{1.90}$$

1.5.2. Damping Processes for Magnetic Turbulence

Alfvén waves are damped by interactions with the neutral background or interactions with turbulence cascading from larger scales. The most important processes for Alfvén waves in resonance with galactic cosmic rays are ion-neutral, Farmer-Goldreich and non-linear Landau damping. Which mechanism is dominant depends on the phase of the interstellar medium and the wavelength. In the following we will quickly explain the individual terms closely following Jacobs et al. [108].

Ion-Neutral Damping When transversing partially ionised plasmas, the ions of the wave collide with the neutrals of the background. These interactions dampen the wave. Two different regimes have to be distinguished, depending on the collision frequency. In case the collision frequency is much larger than the wave frequency, the neutrals are well coupled and oscillate with the wave [132, 223]. Hence, they have to be accounted for in the calculation of the Alfvén speed. On the other hand, if the wave frequency is much higher than the collision frequency, only the ions will oscillate and the collisions with the neutrals will dampen the wave effectively. In either case the ion-neutral damping is dominant for media with more than $\sim 10\,\%$ neutrals [182].

For elastic ion-neutral collisions, the dispersion equation for Alfvén waves reads:

$$\omega\left(\omega^2 - \omega_k^2\right) + i\nu_{\mathrm{in}}\left[\left(1+\epsilon\right)\omega^2 - \epsilon\omega_k^2\right] = 0, \tag{1.91}$$

where ω is the frequency of the wave and $\omega_k = k v_{A,i}$ is the wave-vector in units of the inverse Alfvén speed of ions

$$v_{\mathrm{A,i}} = \frac{B}{\sqrt{4\pi\mu m_i n_i}}, \tag{1.92}$$

which determines the coupling of ions and neutrals. Here m_i is the ion mass and n_i the density. The ion-neutral collision frequency ν_{in} is:

$$\nu_{\mathrm{in}} = \frac{m_n}{m_i + m_n}\left\langle \sigma_{\mathrm{mt}} v\right\rangle_{\mathrm{in}} n_n, \tag{1.93}$$

where $\langle \sigma_{\rm mt} v \rangle$ is the collisional rate coefficient [182]. Finally, the ion to neutral mass density ϵ is given by:

$$\epsilon = \frac{m_i n_i}{m_n n_n}. \tag{1.94}$$

Then the ion-neutral damping rate $\Gamma_{\rm in}$ can be obtained by substituting $\omega = \mathcal{R}(\omega) - i\Gamma_{\rm in}$ into Eq. 1.91:

$$\omega_k^2 = \frac{2\Gamma_{\rm in}}{\nu_{\rm in} - 2\Gamma_{\rm in}} \left[(1+\epsilon)\,\nu_{\rm in} - 2\Gamma_{\rm in} \right]^2 . \tag{1.95}$$

If $\epsilon \ll 1$, the damping rate is approximately given by

$$\Gamma_D^{\rm in} \approx \frac{\omega_k^2 \nu_{\rm in}}{2\left[\omega_k^2 + (1+\epsilon)^2 \nu_{\rm in}^2\right]}. \tag{1.96}$$

The Alfvén waves are resonant with cosmic ray particles of $k = 1/r_L$, or expressed in terms of ω_k:

$$\omega_k \approx \frac{eBv_A}{E}. \tag{1.97}$$

Therefore, depending on the energy cosmic rays couple with two different regimes of Alfvén waves, which are investigated in turn.

Efficient coupling $\omega_k \ll \nu_{in}$: For high-energy cosmic rays the resonant wave number is short compared to $\nu_{in}/v_{\rm A}$ and the neutrals are well coupled to the wave. Hence, the Alfvén speed depends on both ions and neutrals,

$$v_{\rm A,n} = \frac{B}{\sqrt{4\pi\mu m_p n}}, \tag{1.98}$$

where $\mu = \sum_s m_s n_s/(m_p n)$ for all species s of the medium. In this limit, the damping rate is $\Gamma_D^{\rm in} \propto E^{-2}$. Hence, ion-neutral damping is inefficient at larger scales in resonance with high energy particles.

Weak coupling $\omega_k \gg \nu_{in}$: Low-energy cosmic rays are resonant with waves of high wave number. In this case the neutrals are unable to follow the movement of the ions and the Alfvén speed depends only on the ions:

$$v_{\rm A,i} = \frac{B}{\sqrt{4\pi\mu m_p n_i}}, \tag{1.99}$$

where $\Gamma_D^{\rm in} \propto$ const. This will increase the Alfvén speed at low energies, compared to higher ones.

For the WIM and the WNM the resulting damping rate as a function of energy is shown in Fig. 1.5. At low energies, the damping rate in both cases is constant at lower energies, where ions and neutrals are weakly coupled. At higher energies, efficient coupling leads to a reduction of the damping $\Gamma \propto E^{-2}$. This causes large scales in resonance with high energy particles to be unaffected by ion-neutral damping. Hence, large scale turbulence can persist in environments with large neutral fractions.

Farmer-Goldreich damping The Alfvén waves also interact with turbulence cascading from larger scales. The turbulent cascade is highly anisotropic elongating perturbations along the magnetic field lines. A wave of initially $\lambda_\perp$ and $\lambda_\parallel$ will suffer an order unity shear after travelling a distance where the field lines spread by $\lambda_\perp$. When waves with $\lambda_\perp$ interact with oppositely directed Alfvén wave packets of the cascade, one wave period in the cascade corresponds to many periods of the wave and the Alfvén wave will experience the wave of the turbulent cascade as background. This leads to the cascade of the wave until the dissipation scale, and ultimately to the dissipation of turbulence. The

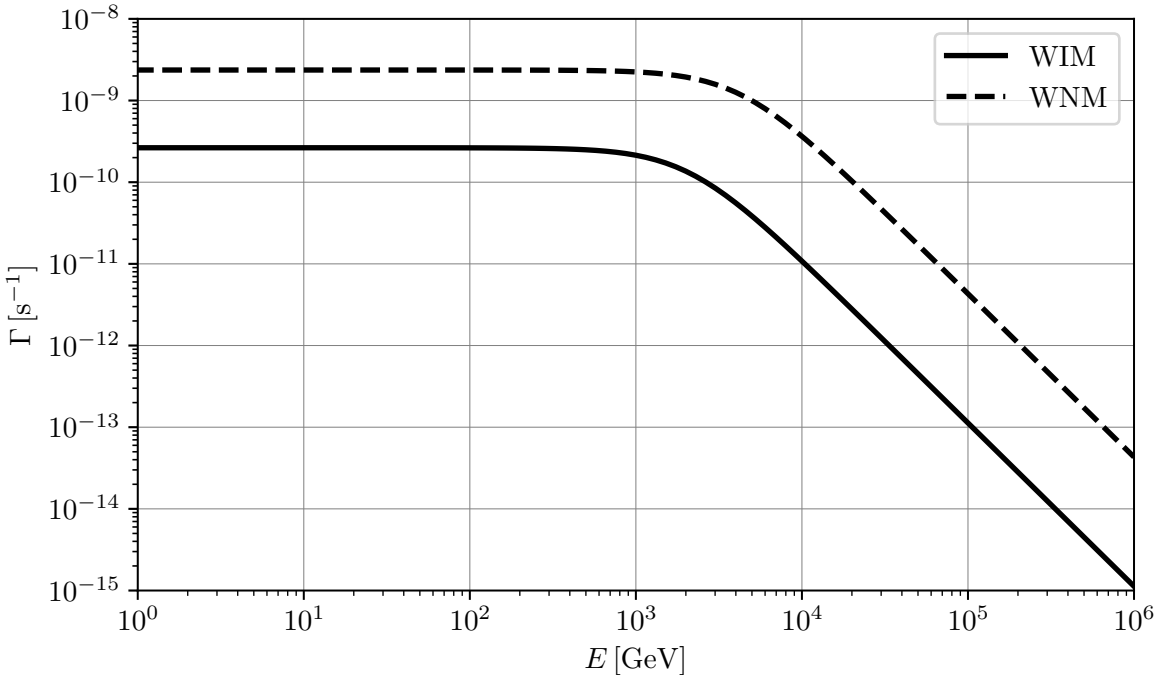

Figure 1.5: Ion-neutral damping rate as a function of resonant energy for the WIM (solid) and WNM (dashed). At high energies in resonance with large scale turbulence the damping rate is $\Gamma \propto E^{-2}$. This causes large scale turbulence to be unaffected by ion-neutral damping.

resulting damping of turbulence is called Farmer-Goldreich damping [72, 218] and its rate is given by:

$$\Gamma_D^{\mathrm{FG}} = \left(\frac{v_{\mathrm{turb}}^3}{L_{\mathrm{inj}} r_{\mathrm{L}} v_{\mathrm{A}}} \right)^{1/2} . \tag{1.100}$$

On the largest scales, given by the size of the injection regions and assumed to be $L_{\mathrm{inj}} = 50\,\mathrm{pc}$, the waves are resonant with high-energy particles. Therefore, the injection velocity v_{turb} is given by $v_{A,n}$, since neutrals are well coupled.

If the fraction of neutrals is appreciable, ion-neutral damping limits the cascade of the external turbulence. The Farmer Goldreich damping in this case has a lower limit in wave length $l_{\mathrm{min}} = 1/k_{\mathrm{min}}$, given by

$$\frac{1}{l_{\mathrm{min}}} = L_{\mathrm{inj}}^{1/2} \left(\frac{2\epsilon\nu_{\mathrm{in}}}{v_{\mathrm{A,n}}} \right)^{3/2} \sqrt{1 + \frac{v_{\mathrm{A,n}}}{2\epsilon\nu_{\mathrm{in}} L_{\mathrm{inj}}}}. \tag{1.101}$$

Non-linear Landau damping In regions of increased turbulence Alfvén waves are likely to interfere and form a beat wave. The modulation frequencies of this superposition are given by the sum and the difference of the individual wave frequencies. If both waves have similar frequencies, the group velocity of the beat v_{gr} can be close to the velocity of thermal background ions v_{pl}. Waves will transfer energy to the plasma if $v_{\mathrm{gr}} > v_{\mathrm{pl}}$ and vice versa. Since there exist more lower energy than higher energy background particles, the net effect is a damping. For a single wave, this is called Landau damping and in the case of a beat wave called non-linear Landau damping. The damping rate is given by [149]

$$\Gamma_D^{\mathrm{NLLD}} = \sqrt{\frac{\pi}{2} \left(\frac{k_B T}{\mu m_p} \right)} \frac{W(k)}{r_{\mathrm{L}}^2(p)}, \tag{1.102}$$

where k_B is the Boltzmann constant, T the temperature of the thermal background and μm_p the effective mass.

1.5.3. Resonant Streaming Instability

Not only large scale astrophysical processes, but also cosmic rays themselves are known to produce magnetic turbulence, upon which they scatter. The two main processes are the resonant streaming instability and the non-resonant streaming instability. The first one has been derived already in the 70s and was applied in the context of cosmic ray escape from the disk, where it leads to so-called self-confinement, meaning there is enough turbulence, that diffusion is subdominant compared to the advection of particles with the background plasma [132, 195]. The latter one produces turbulence modes at non-resonant scales and was derived in 2004 using magneto hydrodynamics [18]. It is thought to be responsible for the high magnetic field observed around the shocks of supernova remnants and explains the maximum energy obtained in diffusive shock acceleration. Instead of following the individual approaches, the following derivation uses a fully kinetic approach, where it can easily be seen that the presence of cosmic rays gives rise to an additional term in the dispersion relation of the plasma. This term leads to a positive imaginary part of the wave frequency and hence a growth rate [125]. It is distinguished between two scenarios, one in which the dominant cosmic ray contribution consists of electron-positron pairs, as is expected around a pulsar and the other one where protons dominate.

Dispersion Relation In order to find small wavelike solutions of the Maxwell equations, one can linearise the equations. From the Fourier-Laplace transformation the Maxwell tensor can be derived, which gives the relation between the first order corrections of the electric field and background quantities. It can be shown that the solutions for the inverse Laplace transformation, which gives the electric field as a function of wavenumber, require the determinant of the Maxwell tensor to vanish. This is called the dispersion relation. For circular polarised waves in the cold plasma limit including cosmic rays the dispersion relation is given by:

$$\frac{c^2k^2}{\omega^2} = 1 + \chi, \tag{1.103}$$

where the response function χ in the test particle regime has the form (see e.g. [125]):

$$\chi = \sum_\alpha \frac{4\pi^2 q_\alpha^2}{\omega} \int_0^\infty \mathrm{d}p \int_{-1}^1 \mathrm{d}\mu \frac{p^2 v(p)(1-\mu^2)}{\omega + kv(p)\mu \pm \Omega_\alpha} \left[\frac{\partial f_\alpha}{\partial p} - \left(\frac{kv(p)}{\omega} + \mu \right) \frac{1}{p} \frac{\partial f_\alpha}{\partial \mu} \right]. \tag{1.104}$$

Here, f_α is the phase space density of the individual plasma components of charge q_α and with gyro frequency $\Omega_\alpha = \Omega_\alpha^*/\gamma$. $v(p)$ is the particle velocity and $\Omega_\alpha^* = q_\alpha B/m_\alpha c$ the cyclotron frequency. The sign in front of the gyro frequency depends on the sign of circular polarisation of the wave. In the frame where the cosmic rays are isotropic, the cold background plasma drifts with:

$$v_d = -\frac{\kappa}{f}\frac{\partial f}{\partial z}, \tag{1.105}$$

where the diffusion coefficient is given by Eq. 1.81. Hence, the distribution function of the background, which compensates the cosmic ray current, reads [4]:

$$f_{BG,e^-,p^+} = \frac{n_i}{2\pi p^2}\delta(p - m_\alpha v_d)\delta(\mu - 1). \tag{1.106}$$

The distribution function of the cosmic rays with number density N_α is given by:

$$f_{CR} = \frac{N_\alpha}{4\pi} g(p), \tag{1.107}$$

where $g(p)$ is the normalised momentum distribution of particles.

Contribution of the Thermal Background The contribution of the background to the dispersion relation can be computed by plugging Eq. 1.106 into Eq. 1.104:

$$\chi_{BG} = \sum_{\alpha,BG} \frac{-4\pi^2 e^2 n_i}{\omega 2\pi} \int_0^\infty \mathrm{d}p \int_{-1}^1 \mathrm{d}\mu \frac{v(p)(1-\mu^2)}{\omega + kv(p)\mu \pm \Omega_\alpha} p^2 \tag{1.108}$$

$$\times \left[\frac{\partial}{\partial p}\delta(p - m_\alpha v_d)\delta(\mu - 1)\frac{1}{p^2} + \left(\frac{kv(p)}{\omega} + \mu\right)\frac{1}{p^3}\frac{\partial}{\partial \mu}\delta(p - m_\alpha v_d)\delta(\mu - 1)\right], \tag{1.109}$$

where all terms proportional to $\delta(\mu - 1)(1 - \mu^2)$ vanish, leaving:

$$\chi_{BG} = \sum_{\alpha,BG} \frac{-2\pi e^2 n_i}{\omega} \int_{-1}^1 \mathrm{d}\mu \frac{v(p)(1-\mu^2)}{\omega + kv(p)\mu \pm \Omega_\alpha} \left(\frac{kv(p)}{\omega} + \mu\right)\frac{\partial}{\partial \mu}\delta(\mu - 1). \tag{1.110}$$

Now, the property of the delta distribution $\int \delta^{(n)}(x) f(x)\mathrm{d}x = (-1)^n \int \delta(x) f^{(n)}\mathrm{d}x$, where (n) denotes the nth derivative can be used together with $v(p) = p/m$ in the non-relativistic limit to arrive at:

$$\chi_{BG} = \sum_{\alpha,BG} \frac{2\pi e^2 n_i}{\omega}\frac{v_d}{m_\alpha v_d} \int_{-1}^1 \mathrm{d}\mu \left(\frac{\partial}{\partial \mu}\frac{(1-\mu^2)}{\omega + kv_d\mu \pm \Omega_\alpha}\left(\frac{kv_d}{\omega} + \mu\right)\right)\delta(\mu - 1) \tag{1.111}$$

$$= \sum_{\alpha,BG} \frac{2\pi e^2 n_i}{\omega m_\alpha} \int_{-1}^1 \mathrm{d}\mu \left(\frac{-2\mu\left(\frac{kv(p)}{\omega} + \mu\right) + (1-\mu^2)}{\omega + kv_d\mu \pm \Omega_\alpha} - \frac{(1-\mu^2)\left(\frac{kv_d}{\omega} + \mu\right)kv_d}{(\omega + kv_d\mu \pm \Omega_\alpha)^2}\right)\delta(\mu - 1) \tag{1.112}$$

$$= \sum_{\alpha,BG} -\frac{4\pi e^2 n_i}{\omega m_\alpha} \int_{-1}^1 \mathrm{d}\mu \frac{\mu\left(\frac{kv(p)}{\omega} + \mu\right)}{\omega + kv_d\mu \pm \Omega_\alpha}\delta(\mu - 1), \tag{1.113}$$

where again terms proportional to $\delta(\mu - 1)(1 - \mu^2)$ vanish. Evaluating the integral gives:

$$\chi_{BG} = \sum_{\alpha,BG} \frac{-4\pi e^2 n_i}{\omega m_\alpha}\frac{\frac{kv_d}{\omega} + 1}{\omega + kv_d \pm \Omega_\alpha} = \sum_{\alpha,BG} \frac{-4\pi e^2 n_i}{\omega^2 m_\alpha}\frac{kv_d + \omega}{\omega + kv_d \pm \Omega_\alpha}. \tag{1.114}$$

Focusing on low frequency waves, namely waves such that $\omega + kv_d \ll \Omega_i^* \ll |\Omega_e^*|$, this can be further simplified expanding around $\tilde{\omega}/\Omega_\alpha^* \ll 1$, where $\tilde{\omega} = \omega + kv_d$:

$$\chi_{BG} = \sum_{\alpha,BG} \frac{-4\pi e^2 n_i}{\omega^2 m_\alpha}\frac{1}{1 \pm \left(\frac{\tilde{\omega}}{\Omega_\alpha}\right)^{-1}} \tag{1.115}$$

$$= \sum_{\alpha,BG} \frac{-4\pi e^2 n_i}{\omega^2 m_\alpha}\left(\pm\frac{\tilde{\omega}}{\Omega_\alpha} - \left(\frac{\tilde{\omega}}{\Omega_\alpha}\right)^2\right) + O\left(\left(\frac{\tilde{\omega}}{\Omega_\alpha}\right)^3\right). \tag{1.116}$$

Since $m_e\Omega_e = -m_p\Omega_p$, the first order terms cancel, resulting in the contribution of the background to the response function of the form:

$$\chi_{BG} = \frac{4\pi e^2 n_i}{\omega^2}\left(\frac{\tilde{\omega}^2}{m_e\Omega_e^2} + \frac{\tilde{\omega}^2}{m_p\Omega_p^2}\right) \tag{1.117}$$

$$= \frac{4\pi e^2 n_i}{\omega^2 m_p}\frac{\tilde{\omega}}{\Omega_p}^2\left(1 + \frac{m_e}{m_p}\right) \tag{1.118}$$

$$\approx \frac{4\pi e^2 n_i}{\omega^2 m_p}\frac{\tilde{\omega}}{\Omega_p}^2 \tag{1.119}$$

$$= \frac{c^2}{v_A^2}\frac{\tilde{\omega}^2}{\omega^2}. \tag{1.120}$$

In the absence of a cosmic ray gradient, when $v_d = 0$, this reduces to the cold plasma limit.

Contribution of the Cosmic Rays The contribution of cosmic rays is given by:

$$\chi_{CR} = \sum_{\alpha} \frac{4\pi^2 q_\alpha^2 N_\alpha}{4\pi\omega} \int_0^\infty \mathrm{d}p p^2 v(p) \frac{\partial}{\partial p} g(p) \int_{-1}^{1} \mathrm{d}\mu \frac{1-\mu^2}{\omega + kv(p)\mu \pm \Omega_\alpha}. \tag{1.121}$$

Due to the pole in the denominator, the calculation of the angular part needs to be done carefully. The Sokhotski-Plemelj theorem in real form (also known as Kramers-Kroning relation [127]) states:

$$\lim_{\epsilon\to 0} \int_a^b \frac{f(x)}{x \pm i\epsilon} \mathrm{d}x = \mp i\pi \int_a^b f(x)\delta(x)\mathrm{d}x + \mathcal{P}\int_a^b \frac{f(x)}{x}\mathrm{d}x, \tag{1.122}$$

where $\mathcal{P}$ denotes the Cauchy-Principal value defined as:

$$\mathcal{P}\int_a^b g(x) = \lim_{\epsilon\to 0}\left(\int_a^{c-\epsilon} g(x)\mathrm{d}x + \int_{c+\epsilon}^b g(x)\mathrm{d}x\right), \tag{1.123}$$

where c is a pole of $g(x)$. Therefore, the pitch-angle integral part of Eq. 1.121 can be written as:

$$\int_{-1}^{1} \mathrm{d}\mu \frac{1-\mu^2}{\omega + kv(p)\mu \pm \Omega_\alpha} = \frac{1}{kv(p)} \lim_{\epsilon\to 0} \int_{-1}^{1} \mathrm{d}\mu \frac{1-\mu^2}{\mu + \frac{\omega}{kv(p)} \pm \frac{\Omega_\alpha}{kv(p)} + i\epsilon} \tag{1.124}$$

$$= -i\frac{\pi}{kv(p)} \int_{-1}^{1} \mathrm{d}\mu \left(1-\mu^2\right)\delta\left(\mu - \left(\frac{\omega}{kv(p)} \pm \frac{\Omega_\alpha}{kv(p)}\right)\right) + \frac{1}{kv(p)}\mathcal{P}\int_{-1}^{1} \mathrm{d}\mu \frac{1-\mu^2}{\omega + kv(p)\mu \pm \Omega_\alpha} \tag{1.125}$$

$$= -i\frac{\pi}{kv(p)}\left(1 - \left(\frac{\omega}{kv(p)} \pm \frac{\Omega_\alpha}{kv(p)}\right)^2\right) + \frac{1}{kv(p)}\mathcal{P}\int_{-1}^{1} \mathrm{d}\mu \frac{1-\mu^2}{\omega + kv(p)\mu \pm \Omega_\alpha}. \tag{1.126}$$

Assuming, as for the background plasma, that $\omega \ll |\Omega_\alpha|$:

$$\int_{-1}^{1} \mathrm{d}\mu \frac{1-\mu^2}{\omega + kv(p)\mu \pm \Omega_\alpha} = -i\frac{\pi}{kv(p)}\left(1 - \left(\frac{\Omega_\alpha}{kv(p)}\right)^2\right) + \frac{1}{kv(p)}\mathcal{P}\int_{-1}^{1} \mathrm{d}\mu \frac{1-\mu^2}{kv(p)\mu \pm \Omega_\alpha}. \tag{1.127}$$

The Principal value is antisymmetric under charge exchange (as is the case for electrons and positrons) since replacing $\mu = -\nu$ gives:

$$\int_{-1}^{1} \mathrm{d}\mu \frac{1-\mu^2}{kv(p)\mu \pm \Omega_\alpha} = -\int_{1}^{-1} \mathrm{d}\nu \frac{1-\nu^2}{-kv(p)\nu \pm \Omega_\alpha} = -\int_{-1}^{1} \mathrm{d}\nu \frac{1-\nu^2}{kv(p)\nu \mp \Omega_\alpha}, \tag{1.128}$$

identical to an exchange of charge; $\Omega_{e^-} = -\Omega_{e^+}$. Therefore, the sum of electrons and positrons cancel out and the term vanishes. The case for protons, where the terms do not cancel gives rise to the non-resonant streaming instability [18]. Combining Eq. 1.121 and the symmetric part of Eq. 1.127 results in the contribution of cosmic-rays to the dispersion relation:

$$\chi_{CR} = -i\sum_{\alpha} \frac{\pi^2 N_\alpha q_\alpha^2}{\omega k} \int_0^\infty \mathrm{d}p p^2 \left(1 - \left(\frac{\Omega_\alpha}{kv(p)}\right)^2\right) \frac{\partial}{\partial p} g(p). \tag{1.129}$$

Using the simplification $\omega \ll |\Omega_\alpha|$ in the delta function in Eq. 1.126 gives a condition on the minimum momentum of a particle to interact with a wave of wave-number k:

$$|\mu| < 1, \qquad v(p) \geq \frac{\Omega_\alpha}{k} = \frac{\Omega_\alpha^*}{\gamma k} \Rightarrow p = \gamma m_\alpha v(p) \geq m_\alpha \frac{\Omega_\alpha^*}{k} = p_{\min}(k) \tag{1.130}$$

Expressed with this $p_{\min}$, Eq. 1.129 reads:

$$\chi_{CR} = -i\sum_{\alpha} \frac{\pi^2 N_\alpha q_\alpha^2}{\omega k} \int_0^\infty \mathrm{d}p \left(p^2 - p_{\min}^2\right) \frac{\partial}{\partial p} g(p). \tag{1.131}$$

Now that the individual contributions of the background Eq. 1.120 and the cosmic-rays Eq. 1.131 are known, the dispersion relation can be written as:

$$\frac{c^2k^2}{\omega^2} = 1 + \frac{c^2}{v_A^2}\frac{\tilde{\omega}^2}{\omega^2} - i\sum_\alpha \frac{\pi^2 N_\alpha q_\alpha^2}{\omega k}\int_0^\infty \mathrm{d}p\left(p^2 - p_{\min}^2\right)\frac{\partial}{\partial p}g(p) \tag{1.132}$$

Neglecting the 1 from the displacement current and multiplying by $\omega^2 v_A^2/c^2$ gives:

$$k^2v_A^2 = \tilde{\omega}^2 - i\sum_\alpha \frac{v_A^2\pi^2\omega N_\alpha q_\alpha^2}{c^2 k}\int_0^\infty \mathrm{d}p\left(p^2 - p_{\min}^2\right)\frac{\partial}{\partial p}g(p) \tag{1.133}$$

$$= \tilde{\omega}^2 - i(\tilde{\omega} - kv_d)\sum_\alpha \frac{N_\alpha Z_\alpha}{n_i}\Omega_i^* I_2(k), \tag{1.134}$$

where the definitions of the Alfvén speed $v_A = B/(4\pi m_i n_i)^{1/2}$, the cyclotron frequency of the medium of $\Omega_i^* = q_i B/m_i c$ and the minimum momentum $p_{\min} = m_\alpha\Omega_\alpha^*/k$ were used. The momentum dependence is given by:

$$I_2(k) = \frac{\pi}{4}p_{\min}(k)\int_{p_{\min}}^\infty \mathrm{d}p\left(p^2 - p_{\min}^2\right)\frac{\partial}{\partial p}g(p). \tag{1.135}$$

Here, the focus is on low frequency waves upon which the cosmic-rays can resonantly scatter. Therefore, it is assumed that $v_\phi = \tilde{\omega}/k \ll v_d$, which sets the condition $\tilde{\omega}_R \ll kv_d$. As seen later, this corresponds to $v_A \ll v_d$ in the test-particle case. Then Eq. 1.134 simplifies to:

$$k^2v_A^2 = \tilde{\omega}^2 + i\sum_\alpha \overbrace{kv_d\frac{N_\alpha Z_\alpha}{n_i}\Omega_i^*}^{\sigma} I_2(k). \tag{1.136}$$

We can now identify the real and imaginary part of $\tilde{\omega}$:

$$\tilde{\omega}^2 = \underbrace{\tilde{\omega}_R^2 - \tilde{\omega}_I^2}_{k^2v_A^2} + i\underbrace{2\tilde{\omega}_R\tilde{\omega}_I}_{\sum_\alpha \sigma I_2(k)} = k^2v_A^2 - i\sum_\alpha \sigma I_2(k), \tag{1.137}$$

by comparing coefficients. The solution of the arising quadratic equations give:

$$\tilde{\omega}_R = -\frac{\sum_\alpha \sigma I_2(k)}{2\tilde{\omega}_I} \tag{1.138}$$

$$\tilde{\omega}_I^2 = \frac{1}{2}k^2v_A^2\left(-1 + \sqrt{1 + \left(\frac{\sum_\alpha \sigma I_2(k)}{k^2v_A^2}\right)^2}\right) \tag{1.139}$$

$$= \frac{1}{4}k^2v_A^2\left(\frac{\sum_\alpha \sigma I_2(k)}{k^2v_A^2}\right)^2 + O\left(\frac{\sum_\alpha \sigma I_2(k)}{k^2v_A^2}\right)^4, \tag{1.140}$$

which can be approximated as:

$$\tilde{\omega}_I \approx \frac{1}{2}\frac{\sum_\alpha \sigma I_2(k)}{kv_A}. \tag{1.141}$$

To derive the growth rate, one needs to assume a momentum distribution of cosmic rays. Identical to [62], it is chosen to be:

$$g(p) = \frac{\delta - 3}{p_0^3}\left(\frac{p}{p_0}\right)^{-\delta}\theta(p - p_0)\theta(p_{\max} - p), \tag{1.142}$$

which is normalised since:

$$\int_{p_0}^{p_{\max}} \frac{\delta-3}{p_0^3}\left(\frac{p}{p_0}\right)^{-\delta} \mathrm{d}p = -\left(\frac{p}{p_0}^{3-\delta}\right)\Big|_{p_0}^{p_{\max}} = 1-\left(\frac{p_{\max}}{p_0}\right)^{3-\delta} \approx 1, \tag{1.143}$$

if $p_{\max} \gg p_0$ and $\alpha > 3$.

Substituting $s = p/p_{\min} = kr_{L_0}p/p_0$, $I_2(k)$ reads:

$$I_2(k) = \frac{\pi}{4}p_{\min}^3 \int_1^\infty (s^2-1)\frac{\partial}{\partial s}g(s)\mathrm{d}s \tag{1.144}$$

$$= \frac{\pi}{4}\frac{p_0}{kr_{L_0}}^3 \left[(s^2-1)g(s)\Big|_1^\infty\right] - \int_1^\infty 2sg(s)\mathrm{d}s \tag{1.145}$$

$$= -\frac{\pi}{2}\frac{p_0}{kr_{L_0}}^3 \int_1^\infty \frac{\delta-3}{p_0^3}\left(\frac{s}{kr_{L_0}}\right)^{-\delta}\theta(s-kr_{L_0})s\mathrm{d}s \tag{1.146}$$

$$= \frac{\pi}{2}\frac{\delta-3}{\delta-2}\left[s^{2-\delta}\left(kr_{L_0}\right)^{-\delta}\theta(s-kr_{L_0})\Big|_1^\infty\right] \tag{1.147}$$

$$= \frac{\pi}{2}\frac{\delta-3}{\delta-2}\begin{cases} -\left(kr_{L_0}\right)^{\delta-3} & kr_{L_0} \le 1 \\ -\left(kr_{L_0}\right)^{-1} & kr_{L_0} \ge 1 \end{cases} \tag{1.148}$$

Then, Eq. 1.141 can be written as:

$$\tilde{\omega}_I = -\frac{\pi}{4}\frac{v_d}{v_A}\sum_\alpha \frac{N_\alpha Z_\alpha}{n_i}\Omega_i^*\frac{\delta-3}{\delta-2}\left(kr_{L_0}\right)^{\delta-3}. \tag{1.149}$$

Now, using the resonance condition $kr_{L_0} = p_0/p$, the definition of the drift velocity in Eq. 1.105 and the diffusion coefficient in Eq. 1.46:

$$\tilde{\omega}_I = \frac{1}{3}\sum_\alpha \frac{\frac{\partial f}{\partial z}}{f}\frac{N_\alpha Z_\alpha}{n_i}\Omega_i^*\frac{\delta-3}{\delta-2}\left(\frac{p}{p_0}\right)^{3-\delta}\frac{c\beta r_L}{kW}. \tag{1.150}$$

Additionally, the well known relations for r_L, $U_0 = \delta B^2/8\pi$ and Ω_i^* allow to rewrite:

$$\tilde{\omega}_I = \frac{1}{6}\sum_\alpha \frac{\frac{\partial f}{\partial z}}{f}\frac{N_\alpha}{}\frac{\delta-3}{\delta-2}\left(\frac{p}{p_0}\right)^{3-\delta} p\frac{c\beta}{kWU_0}. \tag{1.151}$$

Now the total number density of cosmic rays is defined as

$$N_\alpha = \int f_\alpha(p)\mathrm{d}p^3 = 4\pi\int p^2 f_\alpha(p)\mathrm{d}p = 4\pi A_\alpha\int p^{2-\delta}\mathrm{d}p = \frac{4\pi}{\delta-3}A_\alpha p_0^{3-\delta} = \frac{4\pi}{\delta-3}f_\alpha\left(\frac{p}{p_0}\right)^\delta p_0^3. \tag{1.152}$$

If this is substituted in Eq. 1.151 one obtains:

$$\tilde{\omega}_I = \frac{2\pi}{3}\frac{v_A c\beta}{kWU_0}\sum_\alpha \frac{p^4\frac{\partial f_\alpha}{\partial z}}{\delta-2}. \tag{1.153}$$

Which gives the growth rate of the amplitude of the wave. The power in those waves is then growing with $\Gamma_{\mathrm{CR}} = 2\tilde{\omega}_I$, which for a spectral index $\delta = 4$ for the cosmic rays is

$$\Gamma_{\mathrm{CR}} = \frac{2\pi}{3}\frac{v_A c\beta}{kWU_0}p^4\sum_\alpha \frac{\partial f_\alpha}{\partial z}. \tag{1.154}$$

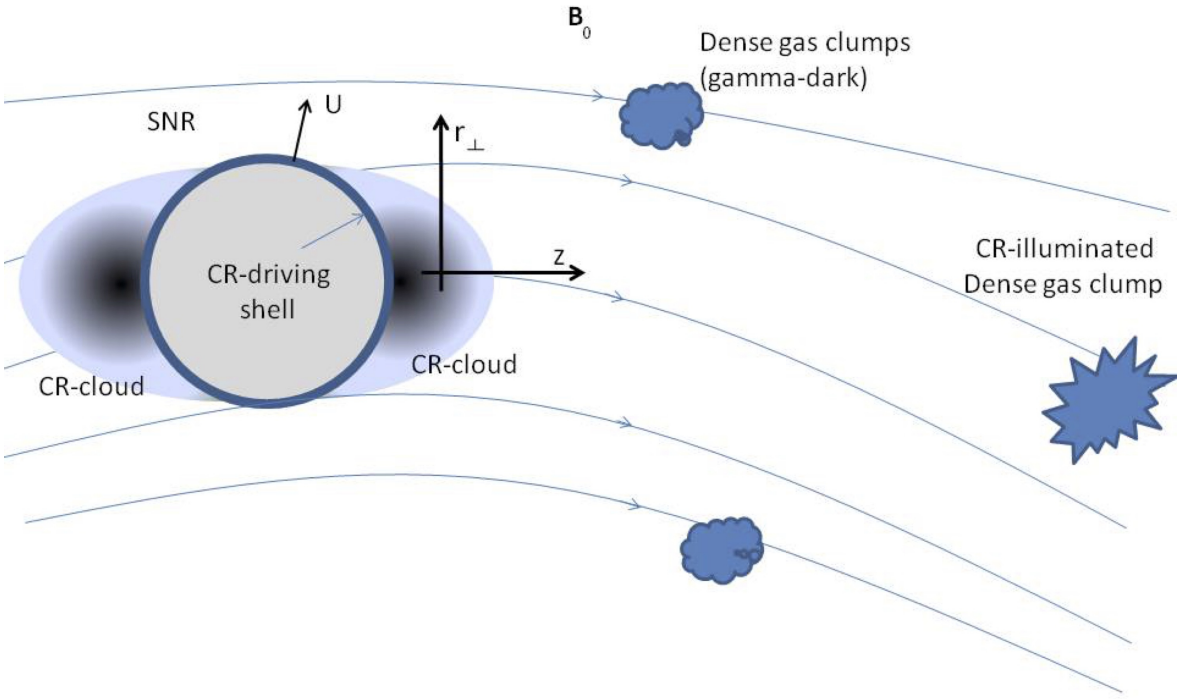

Figure 1.6: Cosmic ray cloud model by Malkov et al. [141]. Cosmic rays initially produced by a supernova remnant are released into the interstellar medium and then propagate along the background magnetic field B_0. Clouds that are magnetically connected with the supernova remnant are illuminated by pion production and clouds not in the direction of the field lines are gamma-ray dark.

This result differs from previously obtained results by a factor of 2 [195]. The reason for this difference is still ongoing work.

1.6. Flux-Tube Approximation

The scales involved in self-consistent modelling of particle acceleration and subsequent propagation vary drastically from sub-parsec scales of the particles gyroradius to galactic distances of several kpc. For small scales particle in cell (PIC) simulations can be used, which track individual particles, but they quickly become computationally unfeasible on larger scales and realistic numbers of particles. On larger scales the transport equation Eq. 1.47 has to be used and the diffusion can be assumed to be isotropic. For self-confinement of cosmic rays around their sources intermediate scales are relevant. In this case the assumption of isotropic diffusion is incorrect. Here, we will motivate the cosmic ray cloud model introduced by Malkov et al. [141] and explain its limitations. The basic setup is given in Fig. 1.6. Instead of modelling particle acceleration by the shock and subsequent escape from the shock, particles are assumed to be injected at escape time t_{esc} with a power law resulting from the acceleration mechanism. The subsequent propagation is determined by the diffusion along and perpendicular to the large scale magnetic field. Propagation along the magnetic field line is well understood. Initially particles gyrate ballistically around the field lines followed by the resonant pitch-angle scattering as derived in Sec. 1.4.3. This leads to spatial diffusion along the large scale magnetic field [96]. Perpendicular transport has proven to be significantly more complicated, but is generally believed to be a combination of particle propagation along the field lines and transport of the field lines themselves [191].

For Kolmogorov turbulence the correlation length L_c directly relates to the maximum scale L_{max} at which turbulence is initially injected via $L_c = L_{\mathrm{max}}/5$. Typical injection sites are astrophysical processes such as supernova remnants, which reach maximum extensions of up to 100 pc. However,

estimates for the correlation length vary by up to two orders of magnitude from 1 pc to 100 pc [97]. Lower values are expected in the spiral arms and higher ones in the surrounding regions.

At scales much larger than L_c field lines are highly tangled. In this case the large scale average diffusion coefficient is isotropic due to the random orientation of the field lines with a value which is $1/3$ of the parallel one [197]. This is the case in the large scale transport models that where introduced in Sec. 1.4.1 and Sec. 1.2 and the reason, why the diffusion coefficient can be reduced to a scalar in the 1D case.

For distances smaller than L_c from the source Malkov et al. [141] argue, that perpendicular transport can be completely neglected and particles propagate along the field line. Then the perpendicular extent is given by the size of the source R_s. This is called the flux-tube. At a distance L_c from the source, field lines start to diverge quickly, leading to a fast transition to 3D diffusion. The particles which where previously confined by the flux-tube to 1D then rapidly spread out, and the boundary can be approximated by a free escape boundary. So in summary, particles are injected by the source of radius R_s and then propagate in 1D along the large scale magnetic field up to the coherence length L_c, where they escape.

The validity of the flux-tube approximation depends on several factors. The first one comes from the fact that the field lines within the source region need to be parallel. This is fulfilled for $R_s \ll L_c$.

Additionally, the approximation of a tube is only justified if transport perpendicular to the field lines and the spread of field lines can be neglected. Both phenomena have been investigated by Kuhlen et al. [130], who performed test particle simulations for particles in isotropic Kolmogorov turbulence. In order to capture the scales of cosmic ray gyroradii for resonant pitch-angle scattering up to the scales of turbulent injection they need to cover 6 orders of magnitude. This is not possible by using models of magneto hydrodynamic turbulence due to computational limitations, but instead achieved by a nested grid approach (see e.g. Mertsch [151]). They derive a simplified analytical model to fit their simulation results. Initially, particles are confined to the magnetic field lines and gyrate around them in a ballistic motion, later resonant pitch-angle scattering leads to diffusion parallel to the field lines. The field lines themselves disperse ballistically before also entering a diffusive regime. They also allow for a subdiffusive period in field line transport. Once the particle displacement in the vertical direction exceeds a correlation length, particles decouple from the field lines and start to diffuse [190].

We use the simulations of Kuhlen et al. [130] in order to determine the spread of field lines initially confined within a source of extent d within a given vertical distance from the source z. The extent reached at $z = L_c$ depends on the turbulence level

$$\eta = \frac{\delta B^2}{B_0^2 + \delta B^2}. \tag{1.155}$$

We calculate the ensemble mean over 20 field realisations. The ensemble mean of the mean perpendicular distance to the z-axis is given by

$$\overline{\Delta r} = \langle \langle \Delta r \rangle_{\text{real.}} \rangle_{\text{ens.}}, \tag{1.156}$$

where Δr is the distance to the x-axis, and the indices mark the ensemble and realisation average. This corresponds to the mean distance of the centre of the flux-tube to the axis. The ensemble mean of the standard deviation of the field lines

$$\sigma(\Delta r) = \langle \sigma_{\text{real.}}(\Delta r) \rangle_{\text{ens.}}, \tag{1.157}$$

where σ is the standard deviation which corresponds to the extent of the flux-tube.

For a magnetic field with turbulence level of $\eta = 0.5$ a the radial extent Δr as a function of distance to the source along the background magnetic field z is shown in Fig. 1.7. The field lines are marked in grey. The extent of the flux-tube is given by $\sigma(\Delta r)$ and is shown as blue shaded region which

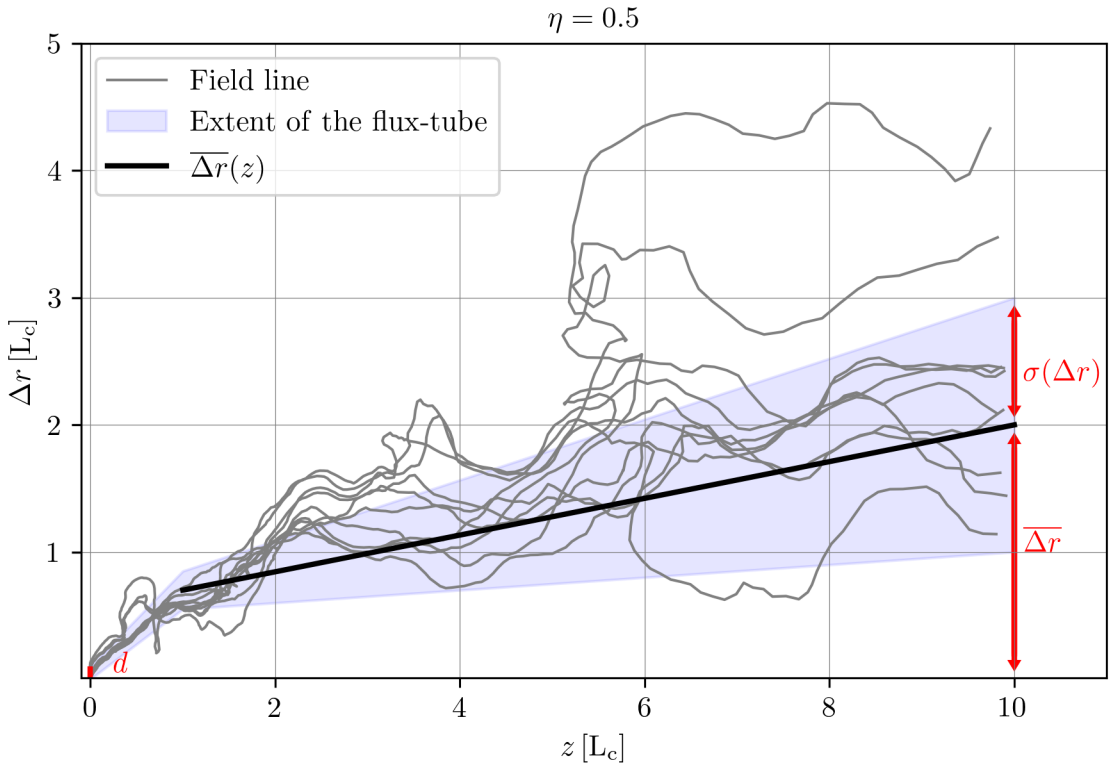

Figure 1.7: Perpendicular distance Δr of field lines as a function of distance to the source along the background magnetic field z. The grey lines indicate individual field lines. The blue shaded region marks the flux-tube, which is centered at $\overline{\Delta r}$ (black line and lower right red arrows) and extends $\sigma(\Delta r)$ (upper right red arrows). The source extent d is marked with the red bar in the lower left corner.

is centred at $\overline{\Delta r}$, indicated as black line. The red arrows on the left mark the centre and extent at $z = 10\,\mathrm{L_c}$. The red bar in the lower left corner indicates the source extent. We choose $\eta = 0.5$ since it corresponds to the turbulence level expected in the Galaxy [97]. As we show in Sec. A, $\sigma(\Delta r)$ is at least of the size of the source d, and increases linearly with roughly $\approx 0.1\,\mathrm{z}$. Hence, the validity of the flux-tube approximation is given only for $d \approx 0.1z$. For larger z the tube can be approximated as a cone with opening angle arctan(0.1) for a turbulence level of $\eta = 0.5$. This is valid as long as the perpendicular distance $\overline{\Delta r}$ is smaller than L_c. At larger distances particles decouple from the field lines and start to diffuse in 3D [130]. Hence, in combination with the condition on the extent of the source, the flux-tube approximation is valid for:

$$R_s \ll L_c \qquad \text{and} \qquad 0.1 L_c \leq R_s. \tag{1.158}$$

However, if the second condition is not fulfilled, it is possible to extend this to a cone-shaped model.

2. Computational Methods

The partial, nonlinear, coupled differential equations describing the transport of comic rays (Eq. 1.47) and the turbulent power spectrum (Eq. 1.89) cannot be solved analytically in their full complexity. Therefore, within this work they are solved numerically using finite differences with second order accurate central differences in all dimensions except time. We use a non-uniform grid which contains two spatial dimensions u and v and one momentum dimension p, denoted with indices i, j and l respectively. The fourth dimension is time, t, with index τ. The procedure follows the explanation in Press et al. [176].

2.1. Grids

Due to the power law dependence of the cosmic ray spectrum in momentum, the momentum grid is always chosen to be logarithmic to resolve small momenta adequately:

$$p_l = p_{\mathrm{min}} \exp\{(j \cdot \Delta \ln p)\} \qquad l = 0, ..., q\,, \tag{2.1}$$

with step size $\Delta \ln p$. Both the scattering of cosmic rays upon turbulence and the production of turbulent waves by the resonant streaming-instability, happens in resonance $r_L \sim 1/k$. Hence, it is convenient to define the wave-number grid in k by this condition. The spatial grid is equal for both the transport equation of particles and waves. Even though it is in principle possible to choose non-uniform grids in regions with larger spatial gradient, for the purposes of this thesis we use equidistant grids, which will be specified within the relevant sections. In general, it has the following form:

$$u_i = u_{\mathrm{min}} + \Delta u \cdot i, \qquad i = 0, ..., n\,, \tag{2.2}$$

for i smaller than the grid size n.

2.2. Finite Differences

Starting from some initial conditions, the solution is obtained by advancing small time steps $\Delta\tau$. It is convenient to transform the equations into the form

$$\frac{\partial f}{\partial t} = \mathcal{L} f + S, \tag{2.3}$$

where the time derivative on the left-hand side of Eq. 2.3 is written using the forward Euler method:

$$\frac{\partial f}{\partial t} = \frac{f_i^{\tau+1} - f_i^{\tau}}{\Delta t}. \tag{2.4}$$

This method is per se only first order accurate in time, but has the advantage that it is possible to write unknown quantities at $\tau + 1$ in terms of known quantities at τ. The operator $\mathcal{L}$ potentially contains second order derivatives with respect to u, v and p. On a uniform grid the derivatives can be expressed as central derivatives, which use the point i in question as well as the two neighbouring points $i \pm 1$:

$$\frac{\partial f}{\partial u} = \frac{f_{i+1}^{\tau} - f_{i-1}^{\tau}}{2\Delta u}, \qquad \frac{\partial^2 f}{\partial u^2} = \frac{f_{i-1}^{\tau} - 2 f_i^{\tau} + f_{i+1}^{\tau}}{(\Delta u)^2}, \tag{2.5}$$

where we have taken the u dimension as example, but the same holds for v and p respectively. This can be derived from the Taylor expansion of the function (see e.g. [121]). The second order accurate central difference scheme for a non-uniform grid is given by [176]:

$$\frac{\partial f}{\partial u} = -\underbrace{\frac{u_{i+1}-u_i}{(u_i-u_{i-1})\,(u_{i+1}-u_{i-1})}}_{\equiv(\Delta u_{i-1})^{-1}} f_{i-1}^{\tau} + \underbrace{\frac{u_{i+1}-2u_i+u_{i-1}}{(u_{i+1}-u_i)\,(u_i-u_{i-1})}}_{\equiv(\Delta u_i)^{-1}} f_i^{\tau} + \underbrace{\frac{u_i-u_{i-1}}{(u_{i+1}-u_i)\,(u_{i+1}-u_{i-1})}}_{\equiv(\Delta u_{i+1})^{-1}} f_{i+1}^{\tau} \tag{2.6}$$

$$\frac{\partial^2 f}{\partial u^2} = \underbrace{\frac{2}{(u_i-u_{i-1})\,(u_{i+1}-u_{i-1})}}_{\equiv(\Delta u_{i-1})^{-2}} f_{i-1}^{\tau} - \underbrace{\frac{2}{(u_{i+1}-u_i)\,(u_i-u_{i-1})}}_{\equiv(\Delta u_i)^{-2}} f_i^{\tau} + \underbrace{\frac{2}{(u_{i+1}-u_i)\,(u_{i+1}-u_{i-1})}}_{\equiv(\Delta u_{i+1})^{-2}} f_{i+1}^{\tau}. \tag{2.7}$$

Now there are two options when to evaluate the right-hand side of Eq. 2.3, τ or $\tau+1$ the first case is called explicit, since all terms on the right are known explicitly and the second one implicit, since the terms are only defined via the equation. It is straight forward to implement the explicit case, but this has the disadvantage that the iteration time steps are bounded by the Courant–Friedrichs–Lewy stability condition. This encodes that information travelling faster than $\Delta u/\Delta t$ is lost, since not only the next neighbours $i \pm 1$ of the evaluated point i, but also points at larger distances contribute and this is not captured in the central difference schemes. Instead, one can evaluate the derivatives at time $\tau+1$, this results in a system of equations, which couple all i. This system is unconditionally stable, since information can be transferred throughout the entire grid, but it is only first order accurate in time [176]. Here, a semi-implicit Crank-Nicolson (CN) [43] scheme is used, which combines both implicit and explicit methods. This means we will evaluate the solution weighted with one half at τ and $\tau+1$. This has the advantage of being second order accurate in time while being unconditionally stable in problems without boundary conditions. If the equation is only one dimensional, meaning $\mathcal{L}$ contains only derivatives wrt. one dimension, the CN scheme results in a tridiagonal matrix, which can be efficiently solved using the Thomas algorithm [202]. For an equation of the form

$$\frac{\partial f}{\partial t} = c_{uu}\frac{\partial^2 f}{\partial u^2} + c_u\frac{\partial f}{\partial u}, \tag{2.8}$$

the CN scheme can be written as

$$\begin{aligned}
\frac{f_i^{\tau+1}-f_i^{\tau}}{\Delta t} &= \frac{c_{uu}}{2}\left(\frac{\partial^2 f_i^{\tau+1}}{\partial u^2} + \frac{\partial^2 f_i^{\tau}}{\partial u^2}\right) - \frac{c_u}{2}\left(\frac{\partial f_i^{\tau+1}}{\partial u} + \frac{\partial f_i^{\tau}}{\partial u}\right) \\
&= \frac{c_{uu}}{2}\left(\frac{f_{i-1}^{\tau+1}}{(\Delta u_{i-1})^2} - \frac{f_i^{\tau+1}}{(\Delta u_i)^2} + \frac{f_{i+1}^{\tau+1}}{(\Delta u_{i+1})^2} + \frac{f_{i-1}^{\tau}}{(\Delta u_{i-1})^2} - \frac{f_i^{\tau}}{(\Delta u_i)^2} + \frac{f_{i+1}^{\tau}}{(\Delta u_{i+1})^2}\right) \\
&\quad + \frac{c_u}{2}\left(-\frac{f_{i-1}^{\tau+1}}{(\Delta u_{i-1})^1} + \frac{f_i^{\tau+1}}{(\Delta u_i)^1} + \frac{f_{i+1}^{\tau+1}}{(\Delta u_{i+1})^1} - \frac{f_{i-1}^{\tau}}{(\Delta u_{i-1})^1} + \frac{f_i^{\tau}}{(\Delta u_i)^1} + \frac{f_{i+1}^{\tau}}{(\Delta u_{i+1})^1}\right).
\end{aligned} \tag{2.9}$$

This equation contains three unknowns, namely the $f^{\tau+1}$ at $i, i\pm1$. For a grid of size $n+1$, this results in $n+1$ equations. We continue by placing the unknown terms at $\tau+1$ on the left and the known quantities on the right and then combine all prefactors for the same f_i. Then the equations can be written in the following form

$$A_i f_{i+1}^{\tau+1} + B_i f_i^{\tau+1} + C_i f_{i-1}^{\tau+1} = P_i f_{i+1}^{\tau} + Q_i f_i^{\tau} + R_i f_{i-1}^{\tau}. \tag{2.10}$$

The system of equations can then be written in matrix form:

$$\begin{pmatrix} B_0 & C_0 & 0 & \cdots & 0 & 0 & 0 \\ A_1 & B_1 & C_1 & \cdots & 0 & 0 & 0 \\ 0 & A_2 & B_2 & \cdots & 0 & 0 & 0 \\ \vdots & \vdots & \vdots & \ddots & \vdots & \vdots & \vdots \\ 0 & 0 & 0 & \cdots & B_{n-2} & C_{n-2} & 0 \\ 0 & 0 & 0 & \cdots & A_{n-1} & B_{n-1} & C_{n-1} \\ 0 & 0 & 0 & \cdots & 0 & A_n & B_n \end{pmatrix} \begin{pmatrix} f_0^{\tau+1} \\ f_1^{\tau+1} \\ f_2^{\tau+1} \\ \vdots \\ f_{n-2}^{\tau+1} \\ f_{n-1}^{\tau+1} \\ f_n^{\tau+1} \end{pmatrix}$$

$$= \begin{pmatrix} Q_0 & R_0 & 0 & \cdots & 0 & 0 & 0 \\ P_1 & Q_1 & R_1 & \dots & 0 & 0 & 0 \\ 0 & P_2 & Q_2 & \dots & 0 & 0 & 0 \\ \vdots & \vdots & \vdots & \ddots & \vdots & \vdots & \vdots \\ 0 & 0 & 0 & \cdots & Q_{n-2} & R_{n-2} & 0 \\ 0 & 0 & 0 & \dots & P_{n-1} & Q_{n-1} & R_{n-1} \\ 0 & 0 & 0 & \dots & 0 & P_n & Q_n \end{pmatrix} \begin{pmatrix} f_0^{\tau} \\ f_1^{\tau} \\ f_2^{\tau} \\ \vdots \\ f_{n-2}^{\tau} \\ f_{n-1}^{\tau} \\ f_n^{\tau} \end{pmatrix} := \begin{pmatrix} D_0 \\ D_1 \\ D_2 \\ \vdots \\ D_{n-2} \\ D_{n-1} \\ D_n \end{pmatrix}, \tag{2.11}$$

with

$$\begin{aligned} A_i &= -\frac{c_{uu}}{2(\Delta u_{i-1})^2} + \frac{c_u}{2(\Delta u_{i-1})^1} \\ B_i &= \frac{1}{\Delta t} + \frac{c_{uu}}{2(\Delta u_i)^2} - \frac{c_u}{2(\Delta u_i)^1} \\ C_i &= -\frac{c_{uu}}{2(\Delta u_{i+1})^2} - \frac{c_u}{2(\Delta u_{i+1})^1} \\ P_i &= -A_i \\ Q_i &= \frac{2}{\Delta t} - B_i \\ R_i &= -C_i. \end{aligned} \tag{2.12}$$

Eq. 2.10 contains the terms A_0 and C_n, even though they do not appear in the matrix and would require the off-grid elements f_{-1} and f_{n+1}. The same is true for P_0 and R_n. These values for f have to be given by the boundary conditions. These depend on the underlying physical problem.

To remain as general as possible, here a combination of Dirichlet and von Neumann boundary conditions are used. Derivatives are written as first order, meaning they only depend on two i. Then the f_i outside the simulation domain can be determined by:

$$f_{-1} = G_0 f_0 + H_0 \qquad f_{n+1} = G_n f_n + H_n, \tag{2.13}$$

and equivalently for both the other boundaries. Then the matrix equation above has to be modified to:

$$\begin{pmatrix} (G_0A_0+B_0) & C_0 & 0 & \cdots & 0 & 0 & 0 \\ A_1 & B_1 & C_1 & \cdots & 0 & 0 & 0 \\ 0 & A_2 & B_2 & \cdots & 0 & 0 & 0 \\ \vdots & \vdots & \vdots & \ddots & \vdots & \vdots & \vdots \\ 0 & 0 & 0 & \cdots & B_{n-2} & C_{n-2} & 0 \\ 0 & 0 & 0 & \cdots & A_{n-1} & B_{n-1} & C_{n-1} \\ 0 & 0 & 0 & \cdots & 0 & A_n & (B_n+G_nC_n) \end{pmatrix} \begin{pmatrix} f_0^{\tau+1} \\ f_1^{\tau+1} \\ f_2^{\tau+1} \\ \vdots \\ f_{n-2}^{\tau+1} \\ f_{n-1}^{\tau+1} \\ f_n^{\tau+1} \end{pmatrix}$$

$$= \begin{pmatrix} (G_0P_0+Q_0) & R_0 & 0 & \cdots & 0 & 0 & 0 \\ P_1 & Q_1 & R_1 & \ldots & 0 & 0 & 0 \\ 0 & P_2 & Q_2 & \ldots & 0 & 0 & 0 \\ \vdots & \vdots & \vdots & \ddots & \vdots & \vdots & \vdots \\ 0 & 0 & 0 & \cdots & Q_{n-2} & R_{n-2} & 0 \\ 0 & 0 & 0 & \ldots & P_{n-1} & Q_{n-1} & R_{n-1} \\ 0 & 0 & 0 & \ldots & 0 & P_n & (Q_n+G_nR_n) \end{pmatrix} \begin{pmatrix} f_0^{\tau} \\ f_1^{\tau} \\ f_2^{\tau} \\ \vdots \\ f_{n-2}^{\tau} \\ f_{n-1}^{\tau} \\ f_n^{\tau} \end{pmatrix} + \begin{pmatrix} H_0(P_0-A_0) \\ 0 \\ 0 \\ \vdots \\ 0 \\ 0 \\ H_n(P_n-A_n) \end{pmatrix}, \tag{2.14}$$

where we again denote the right-hand side as D. This gives a tridiagonal matrix equation which is solved by the Thomas Algorithm [203]. One starts from the first row and divides by the item on the diagonal. The element replacing C_i is X_i and the one replacing D_i is Y_i. Then this row is used to eliminate the A_{i+1} in the next one by substituting $f_i(f_{i+1})$. Afterwards, one again divides by the diagonal element. This process is continued until the last row, which is reduced to a simple uncoupled equation:

$$\begin{aligned} i=0: \qquad & X_0 = \frac{C_0}{G_0A_0+B_0}; \qquad Y_0 = \frac{D_0}{B_0}, \\ 0<i<n: \qquad & X_i = \frac{C_i}{B_i - A_iX_{i-1}}; \qquad Y_i = \frac{D_i - A_iY_{i-1}}{B_i - A_iX_{i-1}}, \\ i=n: \qquad & X_n = 0; \qquad Y_n = \frac{D_n - A_nY_{n-1}}{B_n + G_nC_n - A_nX_{n-1}}, \end{aligned} \tag{2.15}$$

where everything on the right is once again called D_i. Finally, back-substitution gives the solution of the matrix equation:

$$\begin{aligned} i=n: \qquad & f_n = Y_n, \\ i<n: \qquad & f_i = Y_i - X_if_{i+1}. \end{aligned} \tag{2.16}$$

This makes it possible to solve continuous uncoupled one-dimensional partial differential equations.

2.3. Locally One Dimensional Method

In higher dimensions, the resulting matrix will still be sparse but not tridiagonal. In order to preserve the simple form of the matrix the equations are split into parts, each of the form of Eq. 2.3, where $\mathcal{L}$ contains only derivatives of one dimension. For example the cosmic ray transport equation, which can be expressed as:

$$\frac{\partial f}{\partial t} = c_{uu}\frac{\partial^2 f}{\partial u^2} + c_u\frac{\partial f}{\partial u} + c_p\frac{\partial f}{\partial p} + c_0 f + S, \tag{2.17}$$

is split into two equations

$$\frac{\partial f}{\partial t} = c_{uu}\frac{\partial^2 f}{\partial u^2} + c_u\frac{\partial f}{\partial u} \tag{2.18}$$

$$\frac{\partial f}{\partial t} = c_p\frac{\partial f}{\partial p} + c_0 f + S. \tag{2.19}$$

These are solved iteratively, where the result of one equation is used as starting point of the other one. For small enough time steps Δt this will give a good approximation of the solution to the complete equation. However, this procedure is unable to treat mixed derivatives, hence these terms cannot be dealt with in the procedure described here.

2.3.1. Coupling

The transport equations for the particles and waves are coupled by the diffusion coefficient and the cosmic ray streaming-instability. This makes it necessary to couple both equations. Numerically this is achieved by alternately calculating small timesteps in each equation and then using the result of f in $\Gamma_{\mathrm{CR}}(f)$ and adequately W in $\kappa(W)$. This mean that W in the equation for f and f in the equation for W are given explicitly. Hence, the combination is not strictly speaking a Crank-Nicolson scheme anymore and the numerical stability of this procedure is not unconditionally given. In fact, this together with the fact that the coupling is not linear makes it difficult to determine a stability criterion, since this might change during the calculation. The only way to ensure accurate results is to choose a small enough time step.

2.3.2. Linearisation of the Cascade

In Eq. 1.90, there is a non-linear cascade term, which cannot be solved with the scheme above. Should $W(k)$ be power law with negative spectral index, the cascade can be approximated as a damping term:

$$\frac{\partial}{\partial k}\left(\kappa_{kk}(W)\frac{\partial W}{\partial k}\right) = \frac{\kappa_{kk}(W)W}{k^2}, \tag{2.20}$$

as long as the cascade time is smaller than the diffusion and loss timescale. As shown in Evoli et al. [64] this is not always justified. Here, we will instead use the linearisation method explained in Numerical Recipes [176, p. 1047ff] to linearise the damping term. We define $f(W) = W^{1/2}$ and obtain for Eq. 1.81:

$$\kappa_{kk}(W) = c_k v_A k^{7/2} W^{1/2} = c_k v_A k^{7/2} f(W). \tag{2.21}$$

Then the substitution of W is:

$$dZ \equiv f(W)dW \Rightarrow Z = \int dW f(W) = \frac{2}{3}W^{3/2}. \tag{2.22}$$

Now, the diffusion term can be rewritten in terms of the new variable Z:

$$\frac{\partial}{\partial k}\left(\kappa_{kk}\frac{\partial}{\partial k}(W)\right) = c_k v_A\frac{\partial}{\partial k}\left(k^{7/2}\frac{dZ}{dW}\frac{\partial}{\partial k}(W)\right) = c_k v_A\frac{\partial}{\partial k}\left(k^{7/2}\frac{\partial}{\partial k}(Z)\right) \tag{2.23}$$

$$= \frac{7}{2}c_k v_A k^{5/2}\frac{\partial}{\partial k}(Z) + c_k v_A k^{7/2}\frac{\partial^2}{\partial k^2}(Z). \tag{2.24}$$

This converts the diffusion into a first and a second order derivative. Both terms are now linear in Z. Expanding Z in a Taylor series around W^τ up to first order, a linear relation for W is obtained:

$$Z_l^{\tau+1} = Z\left(W_l^{\tau+1}\right) = Z\left(W_l^\tau\right) + \left(W_l^{\tau+1} - W_l^\tau\right)\left.\frac{dZ}{dW}\right|_{j,\tau} \tag{2.25}$$

For the derivatives in k, the same notation is used as in section Sec. 2.2, with z and k exchanged and i and l correspondingly. In the CN scheme, the second order derivative with respect to k can be expressed as

$$\begin{aligned}\frac{\partial^2 Z}{\partial k^2} = &(\Delta k_{l-1})^{-2}\left(Z^\tau_{l-1} + \frac{1}{2}\left(W^{\tau+1}_{l-1} - W^\tau_{l-1}\right) f^\tau_{l-1}\right)\\ &- (\Delta k_l)^{-2}\left(Z^\tau_l + \frac{1}{2}\left(W^{\tau+1}_l - W^\tau_l\right) f^\tau_l\right)\\ &+ (\Delta k_{l+1})^{-2}\left(Z^\tau_{l+1} + \frac{1}{2}\left(W^{\tau+1}_{l+1} - W^\tau_{l+1}\right) f^\tau_{l+1}\right).\end{aligned} \tag{2.26}$$

Equivalently to the second order derivative, the first order derivative in k is then given by:

$$\begin{aligned}\frac{\partial Z}{\partial k} = &-(\Delta k_{l-1})^{-1}\left(Z^\tau_{l-1} + \frac{1}{2}\left(W^{\tau+1}_{l-1} - W^\tau_{l-1}\right) f^\tau_{l-1}\right)\\ &+ (\Delta k_l)^{-1}\left(Z^\tau_l + \frac{1}{2}\left(W^{\tau+1}_l - W^\tau_l\right) f^\tau_l\right)\\ &+ (\Delta k_{l+1})^{-1}\left(Z^\tau_{l+1} + \frac{1}{2}\left(W^{\tau+1}_{l+1} - W^\tau_{l+1}\right) f^\tau_{l+1}\right).\end{aligned} \tag{2.27}$$

If these derivatives are then substituted into Eq. 2.24, the k part of the transport equation for the Alfvén waves is given by:

$$\begin{aligned}&\left[-\frac{1}{2}c_k v_A k_l^{5/2}\left(-\frac{7}{2}(\Delta k_{l-1})^{-1} + k(\Delta k_{l-1})^{-2}\right) f^n_{l-1}\right] W^{\tau+1}_{l-1}\\ &+\left[\frac{1}{\Delta t} - \frac{1}{2}c_k v_A k_l^{5/2}\left(\frac{7}{2}(\Delta k_l)^{-1} - k(\Delta k_l)^{-2}\right) f^\tau_l\right] W^{\tau+1}_l\\ &+\left[-\frac{1}{2}c_k v_A k_l^{5/2}\left(\frac{7}{2}(\Delta k_{l+1})^{-1} + k(\Delta k_{l+1})^{-2}\right) f^\tau_{l+1}\right] W^{\tau+1}_{l+1}\\ &\qquad =\\ &\left[-\frac{1}{2}c_k v_A k_l^{5/2}\left(\frac{7}{2}(\Delta k_{l-1})^{-1} - k(\Delta k_{l-1})^{-2}\right) f^\tau_{l-1}\right] W^\tau_{l-1}\\ &+\left[\frac{1}{\Delta t} - -\frac{1}{2}c_k v_A k_l^{5/2}\left(-\frac{7}{2}(\Delta k_l)^{-1} - k(\Delta k_l)^{-2}\right) f^n_l\right] W^\tau_l\\ &+\left[-\frac{1}{2}c_k v_A k_l^{5/2}\left(\frac{7}{2}(\Delta k_{l+1})^{-1} + k(\Delta k_{l+1})^{-2}\right) f^\tau_{l+1}\right] W^\tau_{l+1}\\ &+\left[c_k v_A k_l^{5/2}\left(-\frac{7}{2}(\Delta k_{l-1})^{-1} + k(\Delta k_{l-1})^{-2}\right)\right] Z^\tau_{l-1}\\ &+\left[c_k v_A k_l^{5/2}\left(\frac{7}{2}(\Delta k_l)^{-1} - k(\Delta k_l)^{-2}\right)\right] Z^\tau_l\\ &+\left[c_k v_A k_l^{5/2}\left(\frac{7}{2}(\Delta k_{l+1})^{-1} + k(\Delta k_{l+1})^{-2}\right)\right] Z^\tau_{l+1}\\ &+\left(\tilde{\Gamma}_{CR}\right)^\tau_l,\end{aligned} \tag{2.28}$$

where we ignored the damping terms. In the usual notation the terms on the left are referred to as A, B, C, the first three on the right as P, Q, R. The last four terms, which are not proportional to any W are implemented as source terms. Here $\tilde{\Gamma}_{CR} = \Gamma_{CR} W^\tau_l$ is independent of W^τ_l.

3. Propagation of Cosmic Rays Around Supernova Remnants

The most likely source candidates for the bulk of galactic cosmic rays are supernova remnants because of their energy budget and their possibility for diffusive shock acceleration (see. eg. Sec. 1.3.4 and Sec. 1.3.1). Recent measurements of gamma-rays show evidence for hadronic acceleration in a number of sources [5, 112]. However, the acceleration itself, the escape from the acceleration region and subsequent transport need to be understood better. In the last couple of years it has become increasingly clear, that the turbulence produced by cosmic rays is not only important for their acceleration to the highest energies [18, 222], but also for the transport in the vicinity of the sources [30, 47, 141, 156, 157]. The overdensity near the source leads to a spatial gradient that gives rise to the resonant streaming instability, as motivated in Sec. 1.5.3. Turbulence produced this way then reduces propagation of particles, leading to self-confinement. Cases where the cosmic ray density is low enough to ignore the non-linear feedback are called test-particle cases.

A self-consistent modelling of cosmic ray acceleration and subsequent propagation is complicated by the huge hierarchy of scales involved. The smallest relevant scales at the shock are of the order of the particle's gyro radius, which need to be simulated by computationally expensive particle-in-cell (PIC) simulations. The global transport in the Galaxy happens on kpc scales and is done by solving transport equations. The escape and subsequent propagation happens on intermediate scales, where PIC simulations are too expensive, but not all assumptions made in deriving the transport equation are justified.

In order to focus on the near source transport Malkov et al. [141] introduced the concept of a cosmic ray cloud. Particles are assumed to be accelerated to some power law by the shock and confined homogeneously downstream of the shock until some escape time. Then they are released and diffuse along the background magnetic field lines while they produce turbulence via the resonant streaming instability. The simplest setup with negligible damping was solved analytically by Malkov et al. [141]. Subsequent work by Nava et al. [156, 157] included additional damping processes of turbulence and a large variety of interstellar medium phases. Additionally, they estimated the escape time of high energy particles. D'Angelo et al. [47] calculated the grammage obtained in the near source region and the contribution to the diffuse gamma ray flux [48]. Most recently, Brahimi et al. [30] included effects of inhomogeneous media and Recchia et al. [182] refined the coupling of ions and neutrals in partially ionised media, especially relevant at low energies.

The studies mentioned before focus on energies above 10 GeV, but the peak of the cosmic ray energy density is at lower energies. Thus, self confinement could be stronger at lower energies, leading to larger source grammage. Precise measurements at these energies have been limited in the past by the influence of the solar wind, which modifies the spectra. However, the Voyager probes have left the solar system and for the first time provided data from the local interstellar space, which is unaffected by solar modulation [45, 126]. These data cannot be obtained by a straight extrapolation of AMS-02 data, after correction for the solar influence, but an additional break in the standard model of cosmic ray transport is needed at around 100 MeV [22, 27, 28, 161, 213]. Phan et al. [172] showed, that this break is a result of the stochastic nature of the cosmic ray sources. Usually this can be ignored in transport models, since the typical distance between sources is smaller than the length particles can diffuse within the lifetime of the source, which leads to many sources contributing to the flux and thereby a smearing effect of individual sources. For low energy hadronic cosmic rays this is not given, since the diffusion distance scales with E^{δ}, where $\delta > 0$ and energy losses become important, reducing the distance particles travel before they loose energy. Then the median flux of an ensemble of source realisations is sufficiently able to reproduce the spectra without the need for an additional break.

Cosmic rays of low energies are able to penetrate the interior of dense molecular clouds and act as the main ionisation agent, since other processes like X-rays are efficiently shielded. Thereby they determine not only the chemistry, but also the coupling of magnetic fields and the gas. This is crucial since efficient coupling can prevent gravitational collapse and hence star formation [106, 153, 166,

170]. Supernova remnants are not proven to be the main source of low energy cosmic rays, but submillimeter and infrared observations of molecular clouds in their vicinity indicate the presence of these particles (see e.g. analyses of clouds around supernova remnants IC443, W51, and W28 [34, 105, 171, 209]).

The ionisation rate inferred from the spectrum of cosmic rays observed by Voyager underpredicts measurements by one or two orders of magnitude. This indicates that the local spectra of MeV cosmic rays are not representative of the entire Galaxy. Instead, aforementioned stochastic effects in combination with the correlation of cloud and source positions are needed to reconcile the naive extrapolation and the measurements [173]. These models do not consider effects of cosmic ray self-confinement.

Answering the above questions requires a better modelling of the near source transport of low energy cosmic rays including the streaming-instability. Straight up extrapolation of the methods used at higher energies is not possible, since energy losses become important. These cannot be incorporated in current models due to the numerical methods used. Here we will propose an extended framework which is able to include energy losses as well as the turbulent cascade which allows us to model the self-confinement of cosmic rays below 10 GeV.

The remainder of this section follows our recent publication Jacobs et al. [108] and is structured as follows: In Sec. 3.1 we motivate the required transport equation in the cosmic ray cloud model. Then we shortly review a model for the evolution of a supernova remnant in Sec. 3.2 before discussing the initial and boundary conditions in Sec. 3.3. Afterwards we present the results in Sec. 3.4.

3.1. Transport Equation for Cosmic Rays around Supernova Remnants

Here we will use the cosmic ray cloud model introduced by Malkov et al. [141] to simplify the transport around the supernova remnant to a flux tube as explained in Sec. 1.6. This is possible because we want to focus on distances from the source which are of the order of the correlation length, assumed to be $L_c = 100\,\mathrm{pc}$. This is typically the case for inter-arm regions with smaller values found in the spiral arms [97]. The typical size of the supernova remnant is a few parsec to 10s of parsec, which is significantly smaller than the correlation length. Hence, magnetic field lines will be nearly parallel. In magnetic fields with the turbulence level expected in the interstellar medium of around $\eta = 0.5$ (see Eq. 1.155), field lines initially closer than $0.1\,\mathrm{L_c}$ do not significantly extend within L_c (see Sec. 1.6). Since the perpendicular displacement is smaller than L_c, particles remain confined to the field lines. Hence, it is justified to assume 1D propagation in a flux tube.

The propagation of cosmic ray protons in a 1D flux tube is described by the usual transport equation [24, 115]

$$\frac{\partial f}{\partial t} + v_\mathrm{A}\frac{\partial f}{\partial z} - \frac{\partial}{\partial z}\left[\kappa(z,p,t)\frac{\partial f}{\partial z}\right] - \frac{dv_\mathrm{A}}{dz}\frac{p}{3}\frac{\partial f}{\partial p} + \frac{1}{p^2}\frac{\partial}{\partial p}\left[p^2\left(\frac{\mathrm{d}p}{\mathrm{d}t}\right)f\right] = Q_p(z,p,t)\,, \tag{3.1}$$

where $f = f(z,p,t)$ is the phase space density of protons. The second term on the left-hand side of Eq. 3.1 describes advection at the (local) Alfvén speed v_A, which is not only a function of the magnetic field and the gas density, but also energy-dependent due to the coupling explained in Sec. 1.5.2. The third term accounts for diffusion with the parallel diffusion coefficient $\kappa(z,p,t)$, which depends on the turbulence power spectrum, as was introduced in Sec. 1.4.3. Momentum losses by adiabatic expansion are accounted for by the fourth term and energy loss processes due to ionisation, pion production and Coulomb scattering by the last term (see Sec. 1.4.2). The term $Q_p(z,p,t)$ on the right-hand side describes sources of CRs.

The diffusion of cosmic ray along the magnetic field lines is mediated by resonant scattering upon turbulence with spectral power $W = W(z,k,t)$ (see Sec. 1.4.3). The main scattering centres are Alfvén

waves with a wave number k in resonance with the Larmor radius of cosmic rays r_{L}, that is $r_{\mathrm{L}}(p) = 1/k$. Then the diffusion coefficient depends on W as given by Eq. 1.81:

$$\kappa(p, z, t) = \frac{\kappa_{\mathrm{B}}(p) 4/\pi}{kW(k, z, t)}, \tag{3.2}$$

where $\kappa_{\mathrm{B}}(p) = r_{\mathrm{L}}(p)c\beta/3$ is the Bohm diffusion coefficient. This couples Eq. 3.1 to the transport equation for the turbulence spectral power:

$$\frac{\partial W}{\partial t} + \frac{\partial}{\partial z}(v_{\mathrm{A}} W) = (\Gamma_{\mathrm{CR}}(f) - \Gamma_D(W))\, W + \Gamma_D(W_{\mathrm{BG}}) W_{\mathrm{BG}} + \frac{\partial}{\partial k}\left[\kappa_{kk}(W)\frac{\partial W}{\partial k}\right]. \tag{3.3}$$

Here, $\Gamma_{\mathrm{CR}}(f)$ describes the growth of turbulence due to the resonant streaming instability given by

$$\Gamma_{\mathrm{CR}}(f) = -\frac{4\pi}{3}\frac{c\,|v_{\mathrm{A}}|}{kW(k)U_0}\beta(p)p^4\frac{\partial f}{\partial z}, \tag{3.4}$$

where U_0 is the background magnetic field energy density (see also Sec. 1.5.3). Γ_D are damping terms as explained in Sec. 1.5.2. The diffusion in wave-number κ_{kk} accounts for the cascade of turbulence described in Sec. 1.5.1. In the absence of a CR gradient, the turbulence level has to retain the average ISM value. Since the continuous injection at large scales and dissipation at small scales are neglected in this work, this requires the introduction of the background compensating term $\Gamma_D(W_{BG})W_{BG}$.

3.2. Supernova Remnant Evolution

The evolution of a supernova remnant is determined by the surrounding medium and more crucially the type of progenitor star, this is illustrated in the below, where we follow the arguments of Longair [136]. If a molecular cloud collapses under its own gravity the pressure and temperature in its core eventually passes the threshold for nuclear fusion of Hydrogen into Helium. Pressure produced this way balances the gravity and as long as there is Hydrogen in the core a balance is maintained. The evolution once the Hydrogen supply in the core is exhausted depends on the mass of the star. Should it be large enough, the gravitational collapse leads to pressure and temperature which is sufficient to burn heavier elements. This is a process that can repeat up to Fe, which is inert and hence does not produce energy under fusion. The individual burning phases have a rising temperature dependence, leading to faster and more violent burning processes. Additionally, the shells surrounding the core might burn lighter elements once the conditions are sufficient. This happens rather explosively since the shell is rapidly expanded by the burning, leading to a drop in temperature and pressure which stops fusion again. During these phases the star ejects large amounts of material of its outer layers into the interstellar medium. Once the mass is not sufficient to induce fusion of heavier elements, the reaction stops and the star collapses. For masses of the core smaller than the Chandrasekhar limit the degeneracy pressure of the electrons counteracts the gravitation leading to the formation of a white dwarf. Above this limit the star collapses into a neutron star, where the balance is provided by neutron degeneracy pressure. During this a core collapse supernova explosion is produced. Several models exist ranging from electron capture to the rebounce of infalling material on the neutron star surface [98]. What all these have in common is that the kinetic energy released is of the order of 10^{51} erg and the surrounding medium has been altered by the winds of the progenitor stars. In contrast, a white dwarf within a binary system can accrete mass from its companion until the Chandrasekhar limit is reached and then collapse. Due to the lack of strong stellar winds and the uniform mass these explosions are of identical magnitude, and their luminosity can be used to determine cosmic distances [39]. The explosion then enters the surrounding medium at speeds initially surpassing the sound speed, creating a shock. In the following we will explain the different phases of the shock evolution on a simple analytical model, which will be necessary to obtain the initial conditions of the cloud model and check its validity.

Initially the mass of the shock is larger than the swept up mass of the surrounding medium. In this case the shock expands freely with a fixed velocity. From dimensional arguments it follows that:

$$E_{SN} = 1/2 M_e v_e^2 \qquad v_e = \left(\frac{2E_{SN}}{M_e}\right)^{1/2}, \tag{3.5}$$

where M_e is the ejected mass and E_{SN} the kinetic energy of the supernova. For typical values of the interstellar medium this is significantly larger than the sound speed [55].

The end of the free expansion is reached at time $t_{FE} = \frac{R_{FE}}{v_e}$, when the swept up mass equals the ejecta-mass, which is given by $M_{\text{swept}} = \frac{4\pi}{3} R_{\text{FE}}^3 \rho$ for a homogeneous medium of density ρ. The shock radius at this time is given by $R_{\text{FE}} = \left(\frac{3M_e}{4\pi\rho}\right)^{1/3}$.

Afterwards the hot supernova remnant expands adiabatically in the Sedov-Taylor phase, which can be modelled as the expansion of a point like source that injects energy into a homogeneous cold medium. In this case one can find a self-similar solution [55]. In this case the radius can be described by [206]

$$R_{\text{SNR}}(t) = 0.5 \left(\frac{E_{51}}{n}\right)^{1/5} \left(1 - \frac{0.009 M_{\text{e},\odot}^{5/6}}{E_{51} n^{1/3} t_{\text{kyr}}}\right)^{2/5} t_{\text{kyr}}^{2/5} \,\text{pc}, \tag{3.6}$$

where E_{51} is the supernova energy in 10^{51} erg, n the ISM number density in $1\,\text{cm}^{-3}$, $M_{\text{ej},\odot}$ the ejecta mass in units of solar masses and t_{kyr} the supernova age in *kyr*. The end of this phase is reached when cooling processes in the outer shells of the supernova remnant cannot be neglected anymore, which happens at [38],

$$t_{\text{rad}} \approx 14 \times E_{51}^{3/14} n^{-4/7} \,\text{kyr}\,. \tag{3.7}$$

Then the hotter inner part pushes the cooler outer layers further outwards, creating a cold and dense layer of gas near the shock. This causes the shock to slow down and increases turbulent damping processes ultimately leading to the dissipation of the shock and release of particles confined downstream. Due to the cold material being pushed by the hot part, this is called Snowplow phase [55].

3.3. Initial and Boundary Conditions in the Cosmic Ray Cloud Model

Initially the cosmic rays are accelerated by the shock, around which instabilities like the non-resonant streaming instability decrease diffusion to the Bohm value κ_B. If the diffusion distance κ_B / v_s is larger than some fraction of the shock radius particles can decouple from the shock and escape. For cosmic rays with energies above 10 GeV this was estimated by Nava et al. [156]. They calculated the half-time of a cosmic ray cloud, half of the particles have left the initial source region as a function of the size of the region and energy of the particles. Then the escape time was defined by the intersection of this function with the supernova remnant radius as function of time [207]. Particles at energies below 10 GeV, are only released when the shock dissipates at the onset of the Snowplow phase. Then the increase in density leads to more efficient damping of turbulence and the increase of the diffusion coefficient. This happens faster than the subsequent propagation, which allows to model the injection of particles as a step-like initial condition

$$f(z,p) = \begin{cases} f_0(p) & \text{if } z \le R_{\text{SNR}}(t_{\text{rad}}), \\ 0 & \text{if } z > R_{\text{SNR}}(t_{\text{rad}}). \end{cases} \tag{3.8}$$

The radius a of the flux tube is given by the condition that the cylindrical volume initially filled by the cosmic rays has to be equal to that of the sphere, resulting in $a = \sqrt{6} R_{\text{SNR}}(t_{\text{rad}})/3$. Due to the diffusive shock acceleration at the shock the momentum dependence is given by a power law with a spectral index of $\alpha = 4.2$, which is slightly different from the result of Sec. 1.3.4 due to non-linear

effects in the shock acceleration. The overall normalisation is given by the requirement motivated in Sec. 1.3.1 that $\xi_{\mathrm{CR}} \simeq 10\,\%$ of the kinetic energy of the supernova is converted into cosmic rays:

$$\xi_{\mathrm{CR}} E_{\mathrm{SNR}} = \int_{p_{\mathrm{min}}}^{p_{\mathrm{max}}} \mathrm{d}p \int_0^{L_c} \mathrm{d}z \pi a^2 4\pi p^2 E_{\mathrm{kin}} f(z, p), \tag{3.9}$$

where the the kinetic energy is given by:

$$E_{\mathrm{kin}} = \left(\sqrt{\left(\frac{p}{m_p \mathrm{c}}\right)^2 + 1} - 1 \right) m_p c^2. \tag{3.10}$$

This results in

$$f_0(p) = \frac{\xi_{\mathrm{CR}} E_{\mathrm{SNR}}}{8\pi^2 a^2 R_{\mathrm{SNR}}(t_{\mathrm{rad}}) \Lambda (m_p \mathrm{c})^3 m_p \mathrm{c}^2} \left(\frac{p}{m_p \mathrm{c}}\right)^{-\alpha}, \tag{3.11}$$

where Λ is a normalisation function,

$$\Lambda = \int_{p_{\mathrm{min}}}^{p_{\mathrm{max}}} \left(\frac{p}{m_p \mathrm{c}}\right)^{2-\alpha} \left[\sqrt{\left(\frac{p}{m_p \mathrm{c}}\right)^2 + 1} - 1 \right] \frac{\mathrm{d}p}{m_p \mathrm{c}}. \tag{3.12}$$

The upper limit in momentum is given by the maximum which is archievable in this accelerator and given by $p_{\mathrm{max}} = 5\,\mathrm{PeV/c}$ ($E_{\mathrm{max}} \simeq 5\,\mathrm{PeV}$). The lower limit is given by $p_{\mathrm{min}} = 0.1\,\mathrm{GeV/c}$ ($E_{\mathrm{min}} \simeq 5\,\mathrm{MeV}$).

The turbulence is assumed to be the same everywhere initially and follows the background turbulence spectrum. The normalisation is given by the results of cosmic ray ratios, as explained in Sec. 1.1.3. These indicate a value of $\kappa_0(10\,\mathrm{GeV/c}) = 0.03\,\mathrm{pc}^2/\mathrm{yr}$. Theoretical models predict either a Kolmogorov or a Kraichnan turbulence spectrum in the interstellar medium (see 1.5.1), which results in a momentum dependence of the diffusion coefficient given by

$$\kappa_0(p) = \left. \frac{\kappa_{\mathrm{B}}(p) 4/\pi}{k W_{\mathrm{BG}}(k)} \right|_{k=1/r_L(p)}. \tag{3.13}$$

For Kraichnan turbulence this results in

$$\kappa_0(p) = 0.03 \frac{\mathrm{pc}^2}{\mathrm{yr}} \left(\frac{p}{10\,\mathrm{GeV/c}}\right)^{1/2} \beta \tag{3.14}$$

and for Kolmogorov:

$$\kappa_0(p) = 0.03 \frac{\mathrm{pc}^2}{\mathrm{yr}} \left(\frac{p}{10\,\mathrm{GeV/c}}\right)^{1/3} \beta. \tag{3.15}$$

Within the supernova remnant the turbulence level should be significantly increased by instabilities at the shock, but as shown by [156], this has a negligible impact on the calculations and is therefore omitted here.

The flux tube is symmetric with respect to the position of the supernova remnant. Hence, it is sufficient to consider only one side. The advection velocity is pointed in z direction outwards. In order to have a smooth transition as $z \to 0$ the advection velocity is reduced to zero there. In this case the phase space density is symmetric, leading to $\partial_z f|_{z=0} = 0$, which corresponds to a no-flux boundary condition for the phase space density f. At the end of the flux tube, defined as L_c we assume a sudden transition to 3D diffusion leading to the quick suppression of the phase space density. This is modelled as a free escape boundary condition. As we have shown in Sec. 1.6, this overestimates the transition, but as long as we want to focus on smaller distances, the effects of the approximation are negligible.

At high energies, energy losses for protons are negligible meaning $t_{\mathrm{loss}} \gg t_{\mathrm{diff}}$, leading to a power law spectrum. Therefore, for maximal energies below the cut-off, the upper boundary in momentum assumes a continuation of the power law. Since we do not consider any energy gain processes, a lower boundary in momentum is not necessary.

As for the turbulence power spectrum W, the same zero flux boundary condition applies at $z = 0$, again for symmetry reasons. Since we can safely assume to retain the background value outside the region of interest, the continuation of the turbulent power spectrum at small and large k is enforced, the same at $z = L_c$.

3.4. Results at Low Energy

In the following we use the model described above to calculate the non-linear transport of cosmic rays around supernova remnants. We focus on the warm ionised medium (WIM) and warm neutral medium (WNM), which are expected to fill 25 % of the galactic disk each(see Sec. 1.2). We do not consider any of the denser and colder phases, since their filling fraction is low and the large neutral fraction will lead to strong damping, hence we expect to obtain the test-particle results in these cases. The hot ionised medium (HIM) is not considered either. The release time of low energy particles, which is given by Eq. 3.7, gives $t_{\mathrm{rad}} = 200\,\mathrm{kyr}$. Then Eq. 3.6 results in a shock radius of $R_{\mathrm{SNR}}(t_{\mathrm{rad}}) = 104\,\mathrm{pc}$. This results in a cosmic ray density diluted by a factor of 10 compared to the other media. In this case the trend towards lower energies already observed in Recchia et al. [180] continues, and no suppression can be achieved. Additionally, the flux tube assumption is not justified since $R_s \approx L_c$. Both for the WIM and WNM the low energy particles are released after 26 kyr at a supernova remnant radius of 23 pc, hence the flux tube approximation is valid. We show the results for Kraichnan turbulence below and afterwards present the results for Kolmogorov turbulence, where the impact of non-linearities is lower. All times are given with respect to the release time.

3.4.1. Spatial Distribution

The spatial distribution of the cosmic ray energy density and the suppression of the diffusion coefficient at different times at an energy of 0.1 GeV is shown in Fig. 3.1. The upper panels show the cosmic ray phase space density f multiplied by p^4 to get the differential energy density. The dashed lines mark the test-particle solution, which is the solution without back-reaction of the magnetic field, meaning the turbulence level is equal to the background $W = W_{\mathrm{BG}}$. The solid lines mark the non-linear solution. In the lower panel the diffusion coefficient with respect to its background value κ/κ_0 is shown. The right side shows the solution within the WNM and the left side the one within the WIM. The same but for 1 GeV is shown in the appendix in Fig. A.3.

For the WIM, the particles are initially confined behind the shock with a step-like initial condition. For propagation times smaller than the growth time of turbulence t_{growth} they still resemble the test-particle result, which is an error function. Since the growth rate depends on the spatial derivative, the suppression of the diffusion coefficient is Gaussian at these times. This can be seen by the blue lines indicating the 10 kyr solution. At later times the non-linearity will cause deviations from this simple shape. The suppression of the diffusion coefficient slows down the propagation of the particles, which preserves the strong gradient at the boundary for longer compared to the test particle results. Therefore, the cosmic rays are confined near the source for longer and the preservation of the gradient enhances the streaming instability creating turbulence also at later times. The maximum of the turbulence is reached once the streaming instability is balanced by the turbulent cascade and the damping processes. Due to the smoothing of the gradient at the edge of the cloud with time, the growth rate of turbulence is reduced continuously. Since this process is lasting significantly longer than the growth and damping time of turbulence, the turbulence at any given time is freshly produced and represents the current balance between growth and damping. This continues until the turbulence level is reduced to the background value. In contrast to previous results at higher energies [157], the

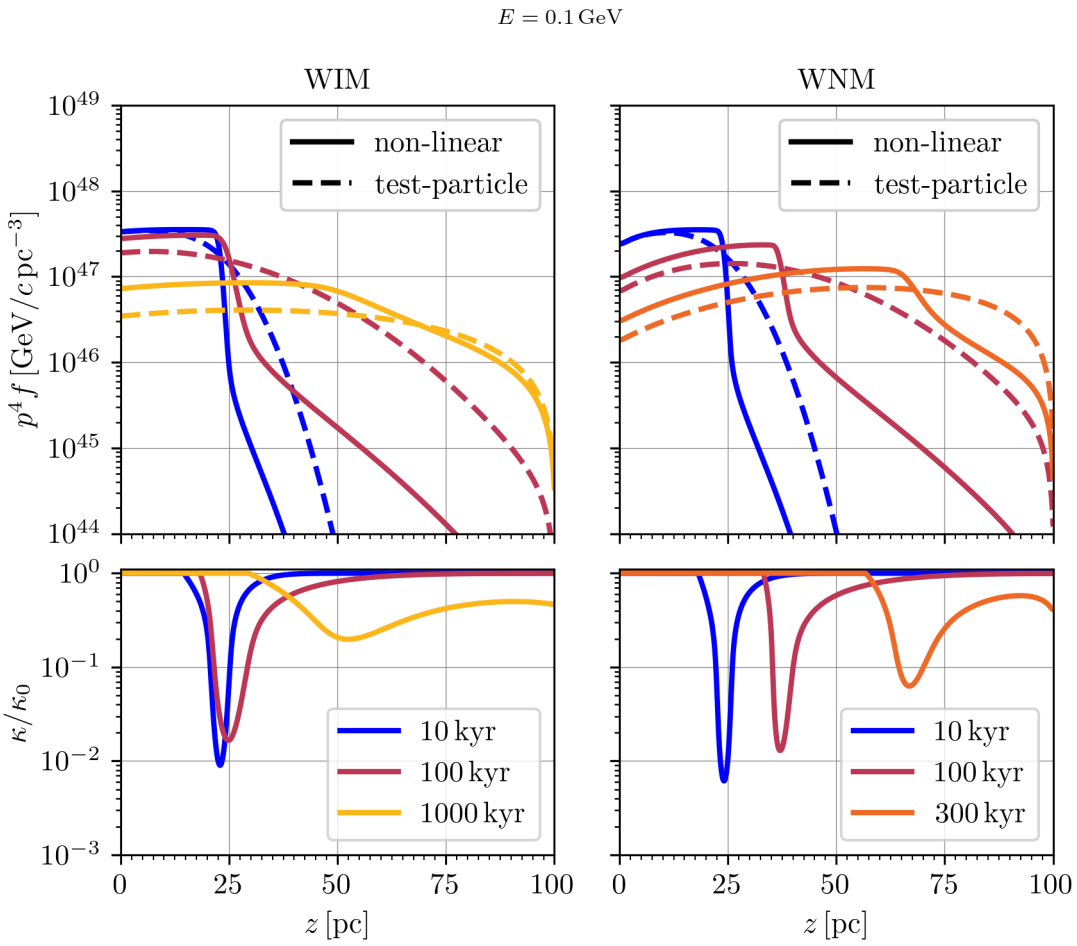

Figure 3.1: Time evolution of the spatial distribution of a CR cloud with $\alpha = 4.2$ at 0.1 GeV in the WIM (left) and WNM (right). z is the distance from the supernova. Particles are released when the radius of the supernova remnant is 23 pc, which is reached 26 kyr after the supernova explosion. All times shown here refer to this release time. The upper panels show the CR energy density $p^4 f$ with the test-particle solution marked in dashed lines and the non-linear results marked in solid lines. The lower panels show the corresponding diffusion coefficient κ normalised to the background coefficient κ_0.

suppression for particles at around 100 MeV lasts more than 1 Myr and reaches two orders of magnitude at early times, which lasts for several 100 kyr. The free escape boundary at $z = L_c$ causes a large gradient in the energy density, leading to a suppression of the diffusion coefficient in this region. The boundary condition is, as discussed in Sec. 1.6, an oversimplification. In a more realistic setup the particles would not freely escape, but slowly start to diffuse in 3D. Since we expect this effect to have little impact on our overall conclusions, we deem this inaccuracy to be tolerable.

In the WNM the Alfvén speed is one order of magnitude larger than in the WIM. This is due to the weak coupling of ions and neutrals (see Sec. 1.5.2) at low energies. This leads to a faster advection of turbulence and particles, which is non-negligible at low energies. Furthermore, the streaming instability is increased as well as the turbulent cascade due to the dependence of both on v_A. Meanwhile, the larger neutral number density increases the ion neutral damping rate. Inside the supernova remnant the larger advection speed compared to the WIM depletes the phase space density close to the inner boundary. This leads to a positive gradient in the differential energy density. Strictly speaking this would lead to backwards propagating waves being excited by the streaming instability, but here we have neglected this effect since the gradients are small and the impact on the propagation is expected to be negligible. The suppression of the diffusion coefficient proceeds in a similar way to the WIM

case. We find an initial suppression of the diffusion coefficient by more than two orders of magnitude. This indicates that the balance between streaming instability and damping, even though both are different due to the change in v_A and neutral fraction, is achieved at similar turbulence levels. Due to the increased advection speed the gradient and phase space density and therefore suppressed diffusion is propagating outwards significantly faster. After around 400 kyr the gradient reaches the outer boundary and leaves the simulation region. Hence, the time limiting factor in this case is the Alfvén speed. Similar to the WIM case, the particle gradient at the boundary, is overestimated by the free escape condition. Due to the increased streaming instability the effect is even more pronounced in the WNM.

3.4.2. Spectral Dependence

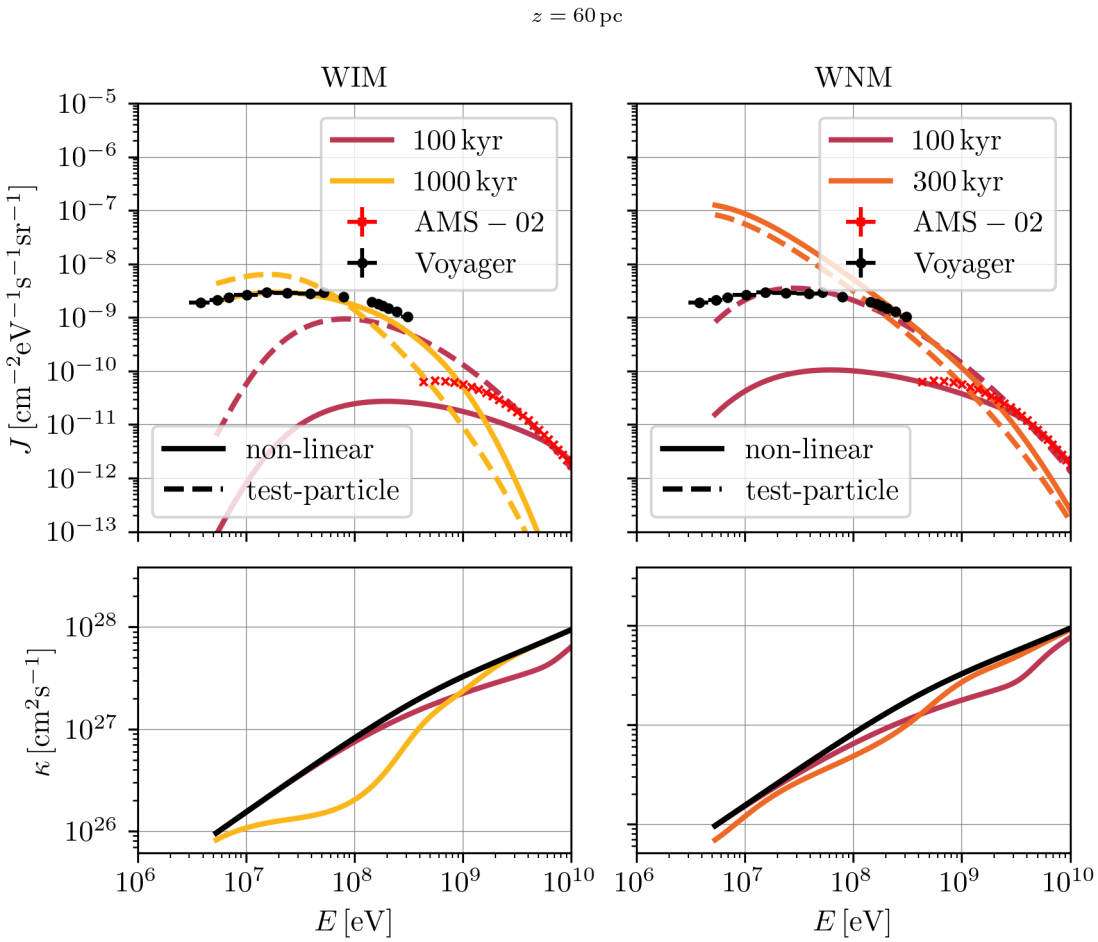

Figure 3.2: CR spectra at a distance of 60 pc from the supernova with initial spectral index $\alpha = 4.2$. The upper panels show the intensity J and the lower ones the diffusion coefficient κ, both as a function of kinetic energy E. Dashed lines mark the test-particle solution and solid ones the non-linear results. Both for the WIM (left) and the WNM (right) the spectra are flattened compared to the test-particle result below a few GeV, similar to the observations by Voyager 1 shown as black dots for reference. The red crosses mark the data points by AMS-02, which are affected by solar modulation at low energies.

Due to the energy dependence of the suppression of the diffusion coefficient we also expect the spectrum of particles to change. This can be of particular importance for our understanding of the Voyager 1 data [126], which have a harder spectral index than predicted by standard cosmic ray propagation models. Here we want to investigate if non-linear effects can contribute to this effect.

In Fig. 3.2 we show our results as a function of kinetic energy E, for a distance of 60 pc from the source along the background magnetic field for both the WIM and WNM. The test-particle solution is shown in dashed lines, the result of the non-linear calculation in solid lines. In the top panels, we show the proton intensities J. The black dots mark the intensity measured by Voyager 1 [45], while the red crosses mark the AMS-02 data [8]. In the bottom panels the corresponding diffusion coefficient κ is shown. The coloured lines show the non-linear result at different times, the black line corresponds to the ISM value. Both for the WIM (left panels) and the WNM (right panels) a flattening of the proton spectrum at lower energies is visible. The spectrum at energies in between $10 - 300$ MeV is generally flatter than in the test particle solution, as favoured by Voyager data. At early times the suppression of the diffusion coefficient at distances smaller than 60 pc reduces the overall flux. Due to the faster propagation of higher energetic particles they reach the observation point earlier. This also means the diffusion coefficient in this region is decreased. So in the non-linear solution the density of high energy particles is enlarged close to the source and the overall spectrum flatter at larger energies. In contrast, at low energies the suppression of the diffusion coefficient leads to a sharp drop. This behaviour is visible in both the WIM and WNM. At later times low energy particles reach 60 pc increasing the density. Since the advection is larger in the WNM, at around 300 kyr the particles will have been advected to 60 pc causing the test-particle and non-linear solutions to agree well. Generally, at higher energies and later times the test-particle and non-linear solutions agree well due to the lower impact of the suppression. At 10 GeV our simulations agree with previous results [156, 157, 180].

It is tempting to combine the results shown in the left panel of Fig. 3.2 in order to explain Voyager and AMS-02 data simultaneously by two sources. However, this scenario requires highly fine-tuned parameters both in age, distance and field line geometry. The likelihood of such a realisation is a priori unclear. For instance, assuming a constant source rate one would expect ten times the amount of older sources to contribute. What would be required instead is a full stochastic model that allows to quantify the likelihood of such a scenario. This is similar to the case for high energy electrons [150] where the diffusion loss time is smaller than the typical distance of sources to the inverse Compton losses. A similar statistical model that uses the test-particle case has been investigated by Phan et al. [172]. We leave the implementation of our results into their model to future work.

For a Kolmogorov turbulence spectrum with the same normalisation fixed at 10 GeV as in the Kraichnan case, the diffusion coefficient is larger due to the lower energy dependence (compare Eq. 3.14 and Eq. 3.15). Therefore, the cosmic rays diffuse faster, which reduces their gradient faster as well and leads to a lower and shorter growth rate. This also reflects in the spectra shown in Fig. 3.3, which is identical in nomenclature to Fig. 3.2, but at a distance of 50 pc and for Kolmogorov turbulence. Again a flattening of the spectra at energies around 10 MeV is observed, but it lasts shorter than for Kraichnan turbulence. Due to the lower energy dependence, the suppression of the diffusion coefficient is of similar magnitude over a large energy range. At high energies fast diffusion reduces the gradient quickly and the test-particle solution is retained, as found in previous studies [157].

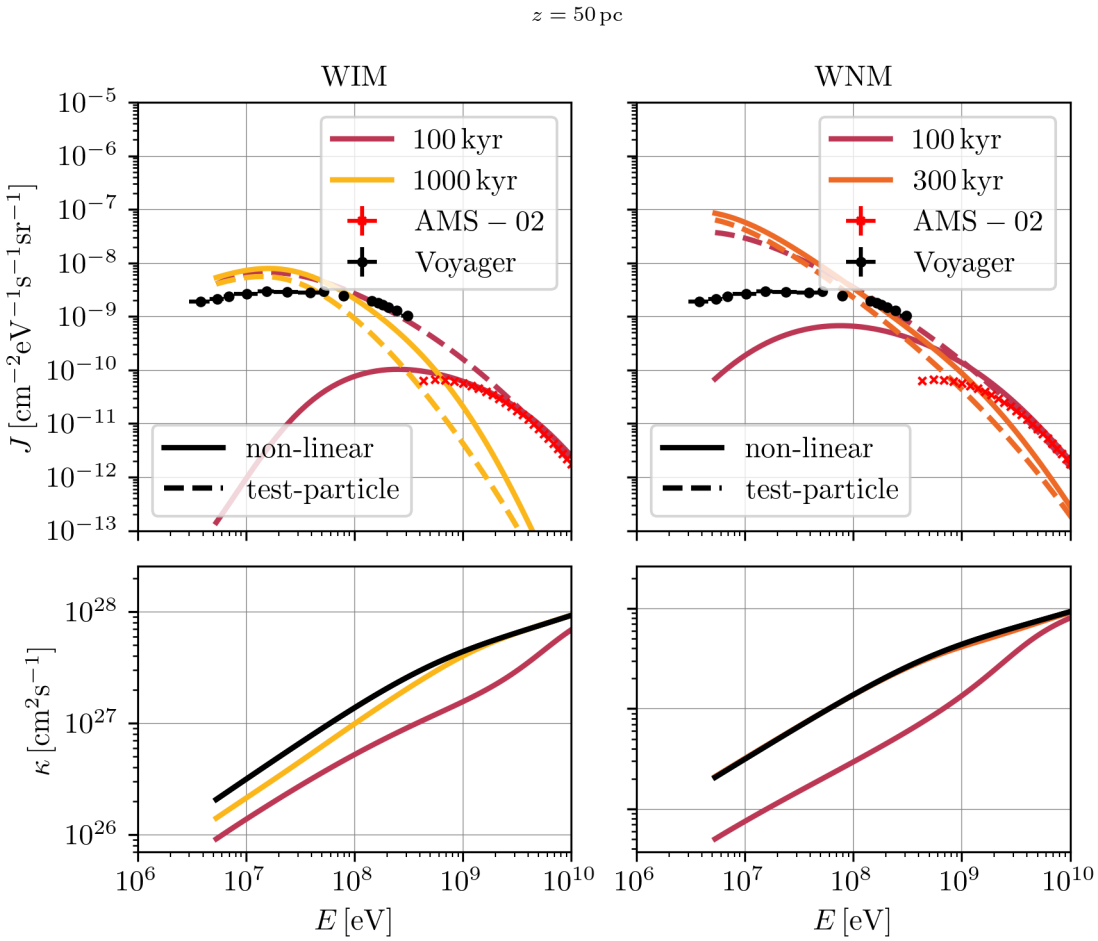

Figure 3.3: CR spectra at a distance of 50 pc from the supernova with initial spectral index $\alpha = 4.2$ and Kolmogorov turbulence. The upper panels show the intensity J and the lower ones the diffusion coefficient κ, both as a function of kinetic energy E. Dashed lines mark the test-particle solution and solid ones the non-linear results. Both for the WIM (left) and the WNM (right) the spectra are flattened compared to the test-particle result below a few GeV. In contrast to the case with Kraichnan turbulence, the smaller energy dependence of the diffusion coefficient causes the suppression to be more equally distributed with energy. Additionally, the suppression lasts shorter. The red crosses mark the data points by AMS-02, which are affected by solar modulation at low energies.

3.4.3. Diffusion Coefficient

The difference between the test-particle results and our non-linear results is the back-reaction of the diffusion coefficient. In order to understand the influence of the suppression of the diffusion coefficient on the cosmic ray spectra it is important to gain a better understanding of its spatial and temporal evolution. For an energy of 100 MeV the diffusion coefficient with respect to its background value is shown for Kraichnan turbulence in Fig. 3.4, where the left panel is again for the WIM and the right one for the WNM. The white arrows indicate the Alfvén speed. Initially the cosmic rays are confined within the supernova remnant with a strong gradient at the edge. This gives rise to the suppression at around 23 pc in both the WIM and WNM cases. The growth stops once the damping and cascade processes balance the instability, which happens on timescales which are significantly shorter than the advection or diffusion timescales and are therefore not visible in the plot. Over time the region of the strongest gradient in cosmic rays is advected outwards with the same Alfvén speed as the turbulence is. During this time diffusion reduces the gradient in phase space density, which leads to a lower balance between production and damping of turbulence. This gradually reduces the turbulence

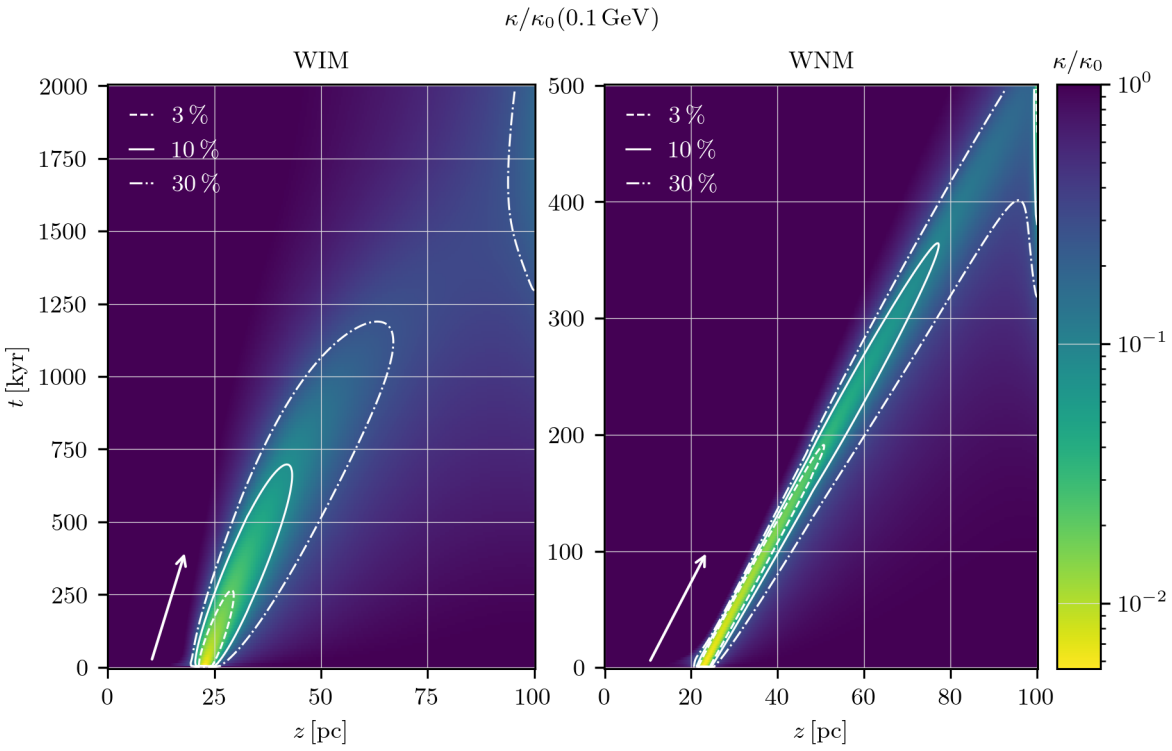

Figure 3.4: Diffusion coefficient κ with respect to its background value κ_0 as a function of time and space at 100 MeV. The left panel shows the WIM case and the right one the WNM case. The contour lines mark different suppression values and the white arrows the local Alfvén speed. In both cases the suppression is the strongest around the edge of the cosmic ray cloud, where the gradient in phase space density is highest. Over time both the particles and the turbulence propagates outwards. The suppression at the boundary is a result of the transition from 1D to 3D, which is over-estimated here due to the free escape boundary.

while the suppression region is advected outwards. Due to the weak coupling of ions and neutrals at low energies the Alfvén speed in the WNM is a factor of 5 larger than in the WIM. This causes the maximum suppression time to be limited by the advection timescale $t_{\mathrm{adv}} = (L_c - R_{\mathrm{SNR}})/v_{\mathrm{A}} \approx 500\,\mathrm{kyr}$. Hence, the suppression zone is advected out of the simulation area before the cosmic ray gradient has subsided enough to reach the background turbulence level. In the WIM the cosmic ray gradient is smoothed out after around 1.5 Myr, which is shorter than the advection time of 2.5 Myr. Therefore, turbulence has subsided before reaching the boundary. The suppression of the diffusion coefficient at the boundary visible again here is a result of the unrealistic transition from 1D to 3D turbulence as explained above.

For Kolmogorov turbulence the resulting spatial and temporal evolution is shown in Fig. 3.5. As in the Kraichnan case, the strongest region of turbulence is initially achieved at the supernova remnant edge. Due to the larger diffusion coefficient the gradient of cosmic rays is spread out faster. This leads to a larger spatial extent of the suppression region, but also a shorter duration. In the WIM the turbulence lasts up to 400 kyr and in the WNM up to 200 kyr. Hence, in both cases the suppression zones do not reach the boundary and the effect on particle propagation over long time scales is lower.

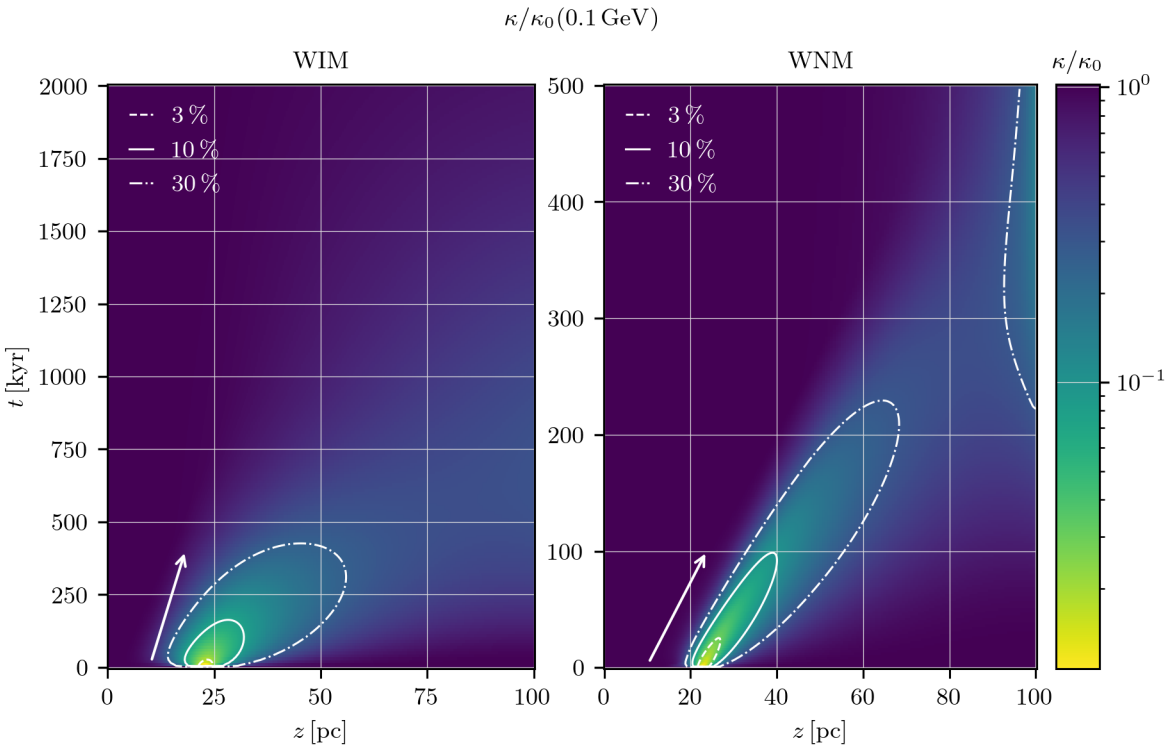

Figure 3.5: Diffusion coefficient κ with respect to its background value κ_0 as a function of time and space at 100 MeV. The left panel shows the WIM case and the right one the WNM case. The contour lines mark different suppression values and the white arrows the local Alfvén speed. In both cases the suppression is the strongest around the edge of the cosmic ray cloud, where the gradient in phase space density is highest. Over time both the particles and the turbulence propagate outwards. The suppression at the boundary is a result of the transition from 1D to 3D, which is over-estimated here due to the free escape boundary.

3.4.4. Grammage

One of the most important and powerful mechanisms to obtain information of galactic cosmic ray propagation is the grammage of particles. As introduced in Sec. 1.1.3, this is the amount of matter traversed during propagation. This can be measured by secondary-to-primary ratios and together with unstable-to-stable secondary ratios allows to both determine the height of the magnetic halo surrounding the galactic disk and the average diffusion coefficient (see e.g. Sec. 5). If comic rays accumulate a significant amount of grammage in or near their sources, this has to be accounted for in models, which usually assume uniform propagation. At low energies the impact was neglected before, since the uncertainties of available data where larger than the expected effects of source grammage. However, the new data by the Voyager probes [126], which are outside the solar sphere of influence, provide data with unprecedented precision. It is therefore necessary to precisely determine the grammage accumulated in the near source region. Since the steaming instability increases the time particles spend in these regions, the non-linear model presented here might affect the estimates. To quantify the grammage accumulated in the flux tube we follow the approach of D'Angelo et al. [48] and incorporate the changes necessary at low energies, in particular energy losses. We start by defining the grammage of a single particle of momentum p and time t as

$$X_{1\mathrm{p}}(p,t) = \int_0^t \rho v_0(p,t')\mathrm{d}t', \tag{3.16}$$

where ρ is the mass density, t propagation time t, and $v_0 = v_0(p,t)$ is the initial speed of particles escaping the simulation region at time t with momentum p. Due to the energy losses, the velocity is

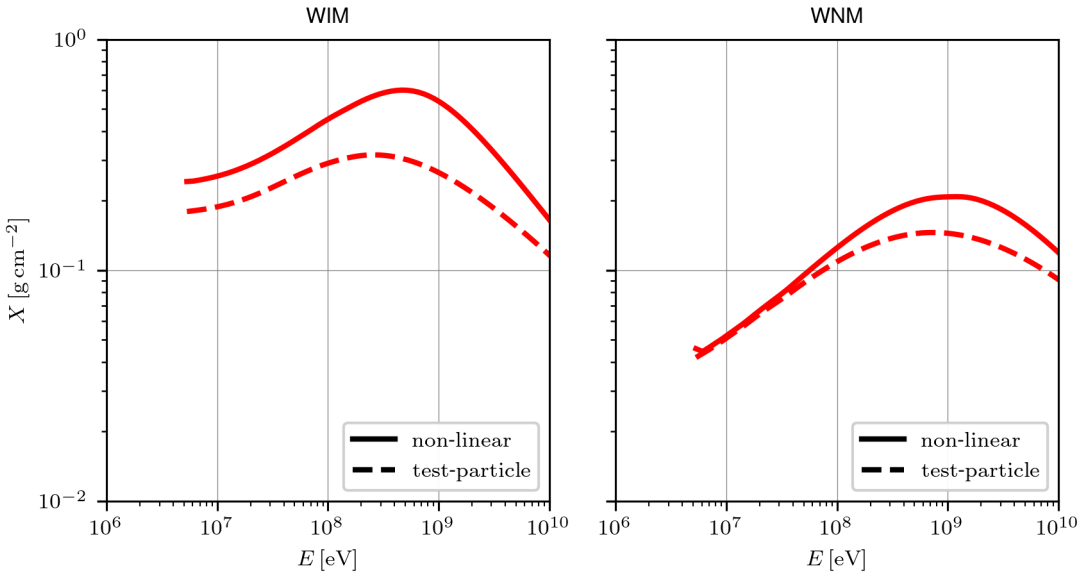

Figure 3.6: Grammage X accumulated within the simulation domain as a function of kinetic energy E. Left panel: WIM, right panel: WNM. The test-particle solution is marked with a dashed line and the result of the non-linear computation with a solid line. At 10 GeV the grammage agrees with the results of [182]. For WIM the grammage at low energies is increased by up to a factor of 3. For the WNM the increase is smaller.

time dependent. The initial speed of the particle can be obtained from the solution of the following equation:

$$t = -\int_{p_0}^{p} \frac{\mathrm{d}p'}{(\mathrm{d}p'/\mathrm{d}t)}. \tag{3.17}$$

To calculate the flux of escaping particles Eq. 3.1 is integrated over z between 0 and L_c for $t \neq 0$ resulting in

$$\frac{\partial N_{in}(p,t)}{\partial t} + \frac{1}{p^2}\frac{\partial}{\partial p}\left[p^2\left(\frac{\mathrm{d}p}{\mathrm{d}t}\right)N_{in}(p,t)\right] + \left[v_A(z)f(p,z,t) - D(z,p,t)\frac{\partial f(p,z,t)}{\partial z}\right]_{z=0}^{z=L_c} = 0, \tag{3.18}$$

where

$$N_{in}(E,t) = \int_0^{L_c} f(E,z,t)\mathrm{d}z. \tag{3.19}$$

The change of particles contained in the flux-tube is due to transport in space and momentum. Since particles which loose energy are still able to contribute to the flux at lower energies, only the flux in space is relevant here. At the inner boundary $z = 0$, where the advection speed is zero, and we impose reflecting boundary conditions $\partial f(p,z,t)/\partial z = 0$ there is no flux of particles. At the outer boundary $z = L_c$, where we impose a free escape boundary condition $f(p, z = L_c, t) = 0$ to mimic the transition to 3D the escape flux is given by:

$$\Phi(p,t) = -D(p,z,t)\left.\frac{\partial f(p,z,t)}{\partial z}\right|_{z=L}. \tag{3.20}$$

To obtain the average grammage of a particle escaping the source region this flux has to be weighted with the individual grammage and normalised:

$$\langle X(p)\rangle = \frac{\int_0^\infty \Phi(p,t)X_{1p}(p,t)\mathrm{d}t}{\int_0^\infty \Phi(p,t)\mathrm{d}t}. \tag{3.21}$$

The results of this calculation for Kraichnan turbulence are shown in Fig. 3.6 as a function of kinetic energy, where the left panel shows the results for the WIM and the right one for the WNM. Again solid lines mark the results of the non-linear calculation and dotted lines indicate the test-particle solution. The inhibited diffusion contains particles for longer, leading to a maximum increase of the grammage accumulated in this region of a factor of 3 to around 0.6 gcm^{-2}, which is significantly lower than the galactic grammage of 10 gcm^{-2} at 10 GeV, but due to the small uncertainties, this correction can be significant for precision models, as long as it is the dominant modelling uncertainty.

At low energies the diffusion time $t_D = \frac{(L_c - R_{SNR})^2}{2D}$ becomes larger than the advection time $t_A = \frac{L_c - R_{SNR}}{v_A} = 2.5$ Myr and particles are advected to the boundary, which is an energy independent process. For the WIM this is at around a few 10 MeV and for the WNM around 100 MeV. Within this range the energy losses are $\propto E^{-1/2}$. This leads to the particles spending a shorter amount of time at lower energies. Since the particle velocity also drops with energy the grammage accumulated in this region becomes lower. In the WIM, this low energy grammage is negligible and the energy dependence of the grammage at low energies is a result of the different initial energies. Due to the energy loss time being lower at smaller energies, the initial energies of particles becomes closer. Hence, the grammage becomes energy independent. In the WNM the residence time of particles in the near source region is significantly shorter than in the WIM and advection is the dominant transport process. In this case the slope is given by the drop in velocity and thereby identical to the energy dependence of the single particle grammage $X_{1,p} \propto v \propto E^{1/2}$. Due to advection being dominant, the non-linear and test-particle solutions agree well. Curiously the same slope is obtained in the WIM for particles at energies below a few 100 MeV. Here the grammage accumulated is not yet negligible and advection is still important, creating similar conditions to those in the WNM. At high energies the single particle grammage becomes energy independent as $v \approx c$. Thus, the energy dependence of the source grammage is purely a result of the escape. Due to diffusion dominating over advection the limiting timescale is $t_D \propto E^{-1/2}$. Hence, the grammage has the same proportionality. For both the WIM and WNM at 10 GeV the solutions of Recchia et al. [180] and D'Angelo et al. [48] are recovered.

3.4.5. Ionisation Rate in a Molecular Cloud

Observations of the ionistion rate in molecular clouds around supernova remnants show an increase of a factor 100 compared to isolated clouds [209]. Since the main ionisation agent are cosmic rays below 1 GeV, this acts as a tracer of these low energetic particles. One of these examples is the supernova remnant W28 around which a suppressed diffusion can be inferred [79]. Here, we want to modify our setup in order to incorporate a molecular cloud at a distance similar to the parameters inferred from W28 and show that our self-consistent model can help to explain the high ionisation rate. We adopt the fiducial parameters of Vaupré et al. [209] for a cloud which is 5 pc ahead of the shock radius $R_{\mathrm{SNR}}(t_{\mathrm{rad}}) = 10$ pc, namely a size of $d_{\mathrm{cl}} = 10$ pc, a hydrogen number density $n = 1000\,\mathrm{cm}^{-3}$, a temperature of $T = 10$ K, an ionistaion fraction of $f_{\mathrm{ion}} = 10^{-7}$ and a helium fraction of $f_{\mathrm{He}} = 0.1$. The density of the surrounding medium is assumed to be $n = 4\,\mathrm{cm}^{-3}$. The transition of the ISM background values to the aforementioned ones within the cloud is modeled as a combination of hyperbolic tangents [31]:

$$g(z) = 1 - \left(\frac{1}{2}\left(1 + \tanh\left(-\frac{z - z_{\mathrm{end-cl}}}{s_{\mathrm{cl}}}\right)\right)\frac{1}{2}\left(1 + \tanh\left(\frac{z - z_{\mathrm{start-cl}}}{s_{\mathrm{cl}}}\right)\right)\right), \tag{3.22}$$

where $z_{\mathrm{start-cl}}$ and $z_{\mathrm{end-cl}}$ are the beginning and the end of the cloud and $s_{\mathrm{cl}} = 1.5$ pc is a parameter that describes the steepness of the transition. The initial conditions for particles released from the supernova remnant are identical to those defined in Sec. 3.3, with the addition that comic rays of higher energies than 10 GeV escape the supernova remnant at earlier times when the half-time of the cloud is equal to the age of the remnant according to Nava et al. [156]. Since ion neutral damping is extremely efficient within the cloud, no turbulent magnetic field is expected and particles are assumed to propagate ballistically. This is mimicked in the transport equation by choosing a turbulence level

which gives $\kappa = c \cdot d_{\mathrm{cl}}$ [153, 170]. In our model of stationary background turbulence this is necessary. However, in principle one should model the injection of turbulence on large scales and dissipation on small scales and derive the turbulence level self-consistently. Furthermore, Eq. 3.1 is not able to capture the ballistic motion of particles.

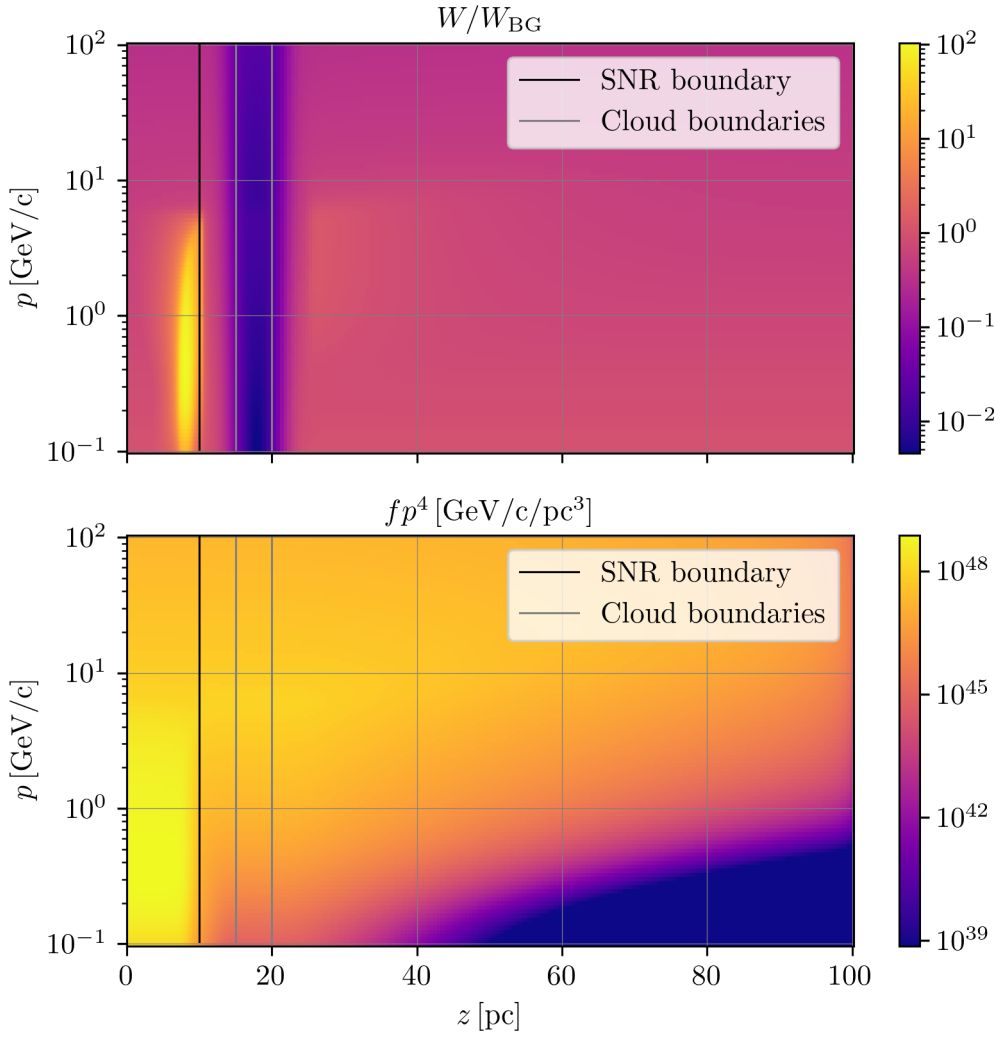

Figure 3.7: Spatial and spectral dependence of the turbulent power spectrum normalised to the background W_{BG} in the top panel and the phase space density f multiplied by p^4 in the bottom panel 40 kyr after the supernova explosion. The particles are initially confined in the supernova remnant of size 10 pc before they escape and propagate into the cloud, which is located at 15 pc and extends for 10 pc. The streaming-instability leads to a longer confinement of particles at low energies, which is indicted by the bright yellow region in the lower plot. In the same panel, the cutoff due to diffusion at larger distances is visible by the drop in phase space density.

In this simplified model, the turbulent power spectrum normalised to the background W/W_{BG} is shown in the top panel of Fig. 3.7 and the phase space density f multiplied by p^4 in the bottom panel, both at 40 kyr after the supernova explosion, which is believed to be the age of W28. Particles below 10 GeV are released after around 6 kyr and higher energy particles earlier [156]. Due to the smaller diffusion coefficient at lower energies, the gradient is also larger which leads to a stronger streaming-instability and consequently to a larger suppression of the diffusion coefficient at the edge of the

cloud. This is indicated by the bright yellow region in the upper panel. As a result, particles below 10 GeV/c are confined within the supernova remnant. The effect of the cloud is seen by the sharp cut-off of the increased turbulence zone towards the cloud, which is a result of the increase in ion-neutral damping. Within the cloud, the fast transport of particles and ion-neutral damping prevent any significant increase in turbulence and the effect of the streaming instability within or on the side opposite of the supernova is negligible.

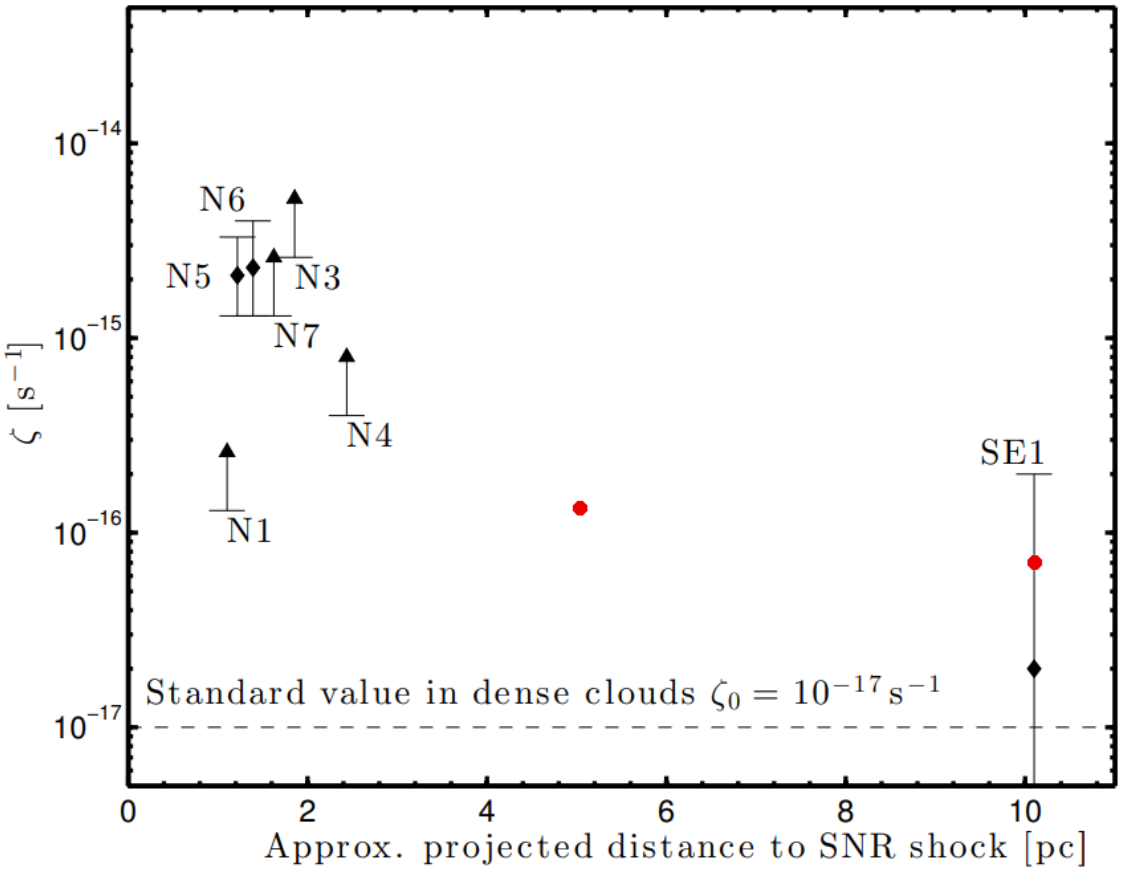

Figure 3.8: Ionisation rate in molecular clouds as measured by Vaupré et al. [209] as function of distance from the shock. The red dots mark the results of the non-linear calculation with the parameters given by Vaupré et al. [209].

Next we want to investigate the ionisation rate ζ for cosmic ray protons, which is given by [165]:

$$\zeta_p(H_2) = \int_I^{E_{\max}} f_p(E) v \left[1 + \phi_p(E)\right] \sigma^p_{\mathrm{ion}}(E) \mathrm{d}E + \int_0^{E_{\max}} f_p(E) v \sigma_{\mathrm{ec}}(E) dE, \tag{3.23}$$

where f_p is the spectrum of cosmic ray protons, σ^p_{ion} is the ionisation cross-section and σ_{ec} the electron capture cross-section. The average secondary production per primary ionisation is given by ϕ_p and the ionisation potential of H_2 is taken to be $I \simeq 15.426\,\mathrm{eV}$. The results of the calculation are indicated as red dots in Fig. 3.8, where we overplot the figure made by Vaupré et al. [209]. The computed ionisation rate in the centre of the cloud is $\zeta = 1.4 \cdot 10^{-16}\,\mathrm{s}^{-1}$, which is one order of magnitude lower than for clouds observed at less than 3 pc form the source, but one order of magnitude above the background value [209]. For a distance of 10 pc between the edge of the supernova remnant and the cloud the ionisation rate is $\zeta = 7.1 \cdot 10^{-17}\,\mathrm{s}^{-1}$, which is a factor of seven above the background and in agreement with the measurements. This shows that with fiducial parameters and a simplified treatment of turbulence it is possible to bring ionistaion rates in agreement with measurements.

4. TeV γ-ray Halos Around Pulsar Wind Nebulae

At 10 GeV the positron fraction exceeds expectations from secondary production by classical cosmic ray transport models [6, 10]. This means a source of primary positrons has to exist, which could either indicate the presence of dark matter or an astrophysical source of primary positrons. Here we will focus on a potential astrophysical source, namely pulsars. Interest in these objects has been increased since the HAWC collaboration detected extended TeV γ-ray emission around the Geminga pulsar in 2017 [2]. The cause of this emission is inverse Compton scattering from high energy electrons and positrons. This confirms the hypothesis that pulsars are primary sources of these particles [12, 92]. However, the spatial extent of the emission is smaller and the intensity larger than expected from the naive expectation, which is the extrapolation of the diffusion coefficient measured by hadronic cosmic ray ratios at GeV to TeV energies in simple 3D isotropic models [2]. Instead, a two order of magnitude smaller value is needed. Ten similar objects have been observed by LHAASO and HAWC [69] leading to the assumption that this should be a common phenomenon. Whether pulsars can explain the positron excess depends on the properties of particle diffusion [142]. Additionally, the TeV-halos are a novel probe of our understanding of particle propagation within (at least parts of) the Galaxy.

In the following we will discuss the nature of the positron excess in Sec. 4.1, motivate why pulsars emit electron positron pairs in Sec. 4.2. Afterwards we show the HAWC observations in Sec. 4.3 and the LHAASO obseravtions in Sec. 4.4. Then we investigate several models that explain the HAWC observations in Sec. 4.5. We start by describing the basic modeling of particle spectra and γ-ray emission in Sec. 4.5.1. Then we discuss two zone transport in Sec. 4.5.2, investigate ballistic transport effects in Sec. 4.5.3. Afterwards we investigate self-confinement in Sec. 4.5.4. We highlight constrains from test-particle simulations in Sec. 4.5.5 and give further ideas in Sec. 4.5.6. Implications and possible explanations of LHAASO data shown at the ICRC 2023 [35] are discussed in Sec. 4.6.

4.1. Positron Excess

All of the visible matter in our universe consists of baryons and not antibaryons. The reason for this symmetry breaking is unclear, but Andrei Sakharov formulated three conditions which needed to be fulfilled in the early Universe to create the asymmetry: (1) Violation of the Baryon number, (2) charge and charge-parity symmetry violation and (3) out of thermal equilibrium reactions [185]. Most theories for the non-visible matter, called dark matter, predict annihilation into standard model particles, creating a matter antimatter pair. Therefore, any measurement of antiparticle fluxes are vital for our understanding of the evolution of the universe and the nature of dark matter. One particular of these is the positron flux, which has been measured by a variety of experiments [6, 10]. Positrons are expected to be produced by spallation reactions of comic rays in the interstellar medium [196]. In principle one has to consider the interaction of cosmic ray nuclei with H and He targets. But since the number density of protons dominates for both, we will use their reaction as example. At energies below about 3 GeV the main production channel for positrons is the Delta resonance, which decays into pions:

$$p + p \rightarrow p + \Delta^+ \rightarrow \begin{cases} p + \pi^0 \\ n + \pi^+ \end{cases} . \tag{4.1}$$

Subsequently, the charged pions decay into muons, which in turn decay into positrons.

$$\pi^+ \rightarrow \mu^+ + \nu_\mu \rightarrow e^+ + \nu_e + \nu_\mu + \bar{\nu}_\mu \tag{4.2}$$

At higher energies either direct production channels for pions or for kaons additionally contribute [61]. Electrons in contrast to positrons are accelerated in sources within the Galaxy and are therefore primary particles with a secondary contribution of around 4 %. Unlike hadronic comic rays these particles suffer major energy losses at TeV and GeV energies due to Synchrotron and inverse Compton losses, as explained in Sec. 1.4.2. Hence, we can follow the argumentation of Evoli and Dupletsa

[60] in order to calculate the flux. Then Eq. 1.48, which describes the transport in the Galaxy, can be simplified for leptons to:

$$-\frac{\partial}{\partial z}\left[\kappa\frac{\partial f_l}{\partial z}\right] = Q_l(E)\delta(z) - \frac{1}{E^2}\frac{\partial}{\partial E}\left[\left(\frac{\mathrm{d}E}{\mathrm{d}t}\right)E^2 f_l\right]. \tag{4.3}$$

If we approximate the energy losses as catastrophic, the equation simplifies to:

$$-\frac{\partial}{\partial z}\left[\kappa\frac{\partial f_l}{\partial z}\right] = Q_l(E)\delta(z) - \frac{f_l}{\tau_{\mathrm{loss}}}, \tag{4.4}$$

where $t_E = E/\left(\mathrm{d}E/\mathrm{d}t\right) \propto E^{-1}$ is the energy loss time. We now want to focus on the limit where energy losses dominate the transport ($\tau_{\mathrm{loss}} \ll \tau_{\mathrm{esc}}$). Then the solution in the disk for electrons injected by sources with $Q_e \propto E^{-\gamma_e}$ is given by:

$$f_e = \frac{Q_e(E)\tau_{\mathrm{loss}}}{\sqrt{\kappa(E)\tau_{\mathrm{loss}}}} \propto E^{-\gamma_e-\frac{1+\delta}{2}}, \tag{4.5}$$

where δ is the spectral index of the diffusion coefficient. Therefore, energy losses soften the spectrum by $(1-\delta)/2$. A positron typically carries a fraction $\alpha_p \approx 5\,\%$ of the kinetic energy of the parent proton:

$$E = \alpha_p E_p. \tag{4.6}$$

Then the production rate of positrons in the interstellar medium is given by

$$Q_{e^+}\mathrm{d}E = f_p(E_p)2c\sigma_{pp}h_d n_d \mathrm{d}E_p, \tag{4.7}$$

where we have assumed a energy independent production cross-section as indicated by recent measurements [120, 163]. The flux of protons is proportional to $f_p(E) \propto E^{-\gamma_p-\delta}$, as is true for other primaries. Then the solution in the loss dominated regime is:

$$f_{e^+}(E) = f_p\left(\frac{E}{\alpha_p}\right)\frac{2c\sigma_{pp}n_d h_d}{\alpha_p}\frac{\tau_{\mathrm{loss}}}{\sqrt{\tau_{\mathrm{loss}}\kappa}} \propto E^{-\gamma_p-\frac{1+3\delta}{2}}. \tag{4.8}$$

Now we can calculate the positron fraction, which is defined as the ratio of positron to electron plus positron flux. Since electrons are usually more abundant than positrons, it is sufficient to look at the first oder in (f_{e^+}/f_{e^-}):

$$\frac{f_{e^+}}{f_{e^-}+f_{e^+}} \approx \frac{f_{e^+}}{f_{e^-}} \propto E^{-\gamma_p+\gamma_e-\delta}. \tag{4.9}$$

This ratio is only rising with energy if $\gamma_e > \gamma_p + \delta$, which is contrary to observations. The positron fraction as a function of kinetic energy as measured by AMS-02 [10] is shown in Fig. 4.1. In contrast to the prediction of Eq. 4.9, the fraction is rising above 10 GeV. This is called the positron excess. Its origin has to be a source of primary positrons. It is tempting to propose a dark matter model which annihilates into electron-positron pairs and has the correct spectral shape to explain the signal [104]. However, first alternative explanations within the standard model of particle physics have to be excluded. These range from drastic changes to the standard model of Galactic particle propagation [135] over secondary positrons produced in supernova remnants [25] to electron-positron pair production in pulsars [142].

Due to recent observations of γ-rays around pulsars, which indicate the presence of positrons and electrons, they are of particular interest in recent years. We will explain what pulsars are and how they create electron-positron pairs in the next section.

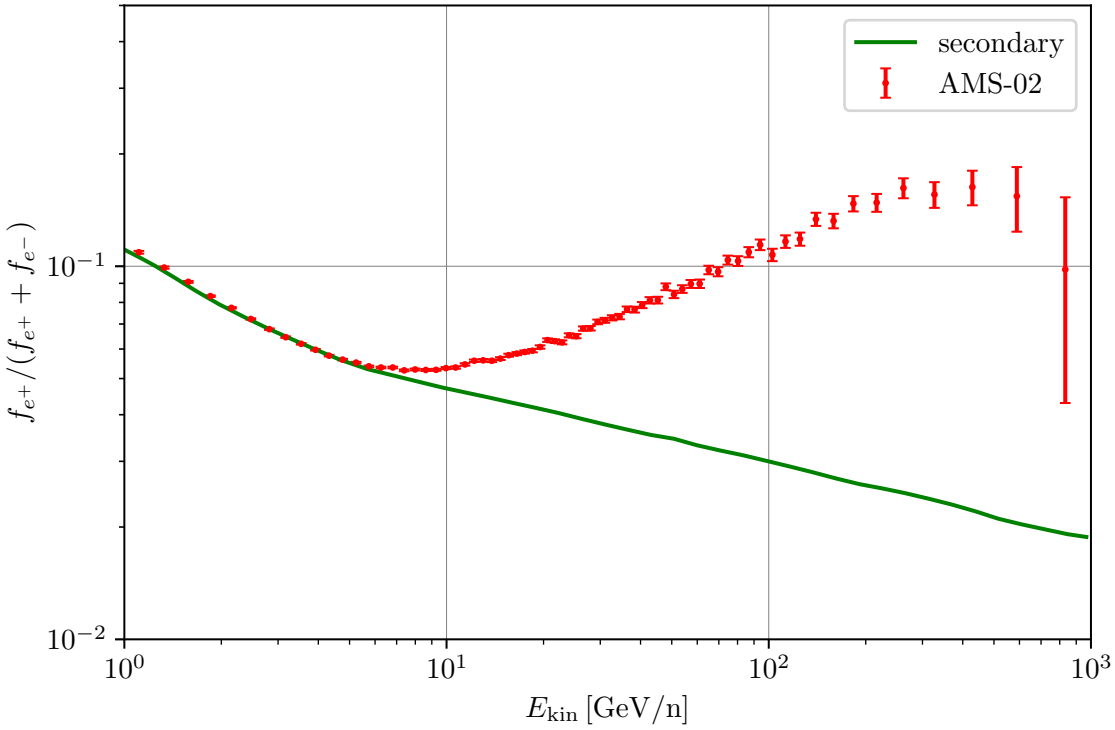

Figure 4.1: Positron-ratio $\frac{f_{e^+}}{f_{e^-}+f_{e^+}}$ as a function of kinetic energy as measured by AMS-02 [10]. The green line indicates the expectation from the propagation of cosmic ray secondaries [10]. The raise of the ratio above 10 GeV is called the positron excess.

4.2. Pulsars and $e^{+/-}$ Emission

Pulsars have been discovered on the 28th of November 1967 by Jocelyn Bell Burnell [100] who measured their periodic emission of radio pulses. These objects are neutron stars with a mass between the Chandrasekhar limit of $1.4\,\mathrm{M}_\odot$, which is the mass at which the electron degeneracy pressure is unable to couter gravity and the Tolman-Oppenheimer-Volkoff limit of $3\,\mathrm{M}_\odot$, where the neutron degeneracy pressure cannot counteract gravity anymore [160]. They are the collapsed cores of massive stars with a size of around 10 km [32]. Since both the angular momentum and magnetic flux are conserved in the collapse, the rotation period can be as low as $\tau_R = 1$ ms and the magnetic fields reach $B = 10^{13}$ G. If the spin and the magnetic axes are not aligned, the neutron star is a spinning dipole, which looses energy due to magnetic braking. The energy loss rate is called spindown-luminosity and given by

$$L_{\mathrm{spin}}(t) = L_{\mathrm{spin}}(0)\,(1 + t/\tau_s)^{-b}\,, \tag{4.10}$$

where b is the magnetic braking index, which is 2 for an ideal dipole in vacuum and τ_s is the spindown timescale. Additionally, the strong magnetic fields confine particles to field lines and inhibit any perpendicular motion on scales larger than r_L. The temporal variation induces an electric field, which at the surface of the neutron star is stronger than gravitational forces and thereby extracts electric charges. This creates a magnetosphere of corotating charges that effectively screen the Lorentz force. At the light cylinder $R_c \equiv c\tau_R/2\pi$, the co-rotation velocity of particles exceeds the speed of light and field lines cannot be closed anymore. This bounds the magnetosphere and causes the field lines near the magnetic poles to be open and due to the potential difference at the pulsars surface and infinity particles are accelerated along them. Charged particles which travel along the field lines emit Synchrotron radiation at radio energies. If the magnetic axis aligns with the line of sight to earth, periodic radio pulses like the ones observed by Bell are produced.

High energy electron positron pairs are expected to be produced in the regions where no effective shielding of the electric field is possible. One region is located at the magnetic poles of the pulsar, where field lines are open and particles have to either escape from the neutron star or fall back to the surface [49, 184]. Another region is near the boundary of the magnetosphere [155]. If the electric field parallel to the magnetic field line becomes sufficiently large, electron-positron pairs are produced and accelerated along the magnetic field. Their bremsstrahlung in turn is large enough to create further pairs and a cascade develops [95]. If these particles collide with the surrounding material a pulsar wind nebula (PWN) is formed, which has a typical size of 1 pc. The non-thermal particles emit Synchrotron radiation making this region visible in radio to γ-rays [81]. Hence, pulsars are a primary source for positrons and potential candidates to explain the positron excess.

One of the closest PWNe is Geminga at a distance of $d_G = 250\,\mathrm{pc}$ with an age of roughly $t_{\mathrm{age}} = 340\,\mathrm{kyr}$ [64]. Its spin-down luminosity is measured at $L_{\mathrm{spin}}(t_{\mathrm{age}}) = 2 \cdot 10^{34}\,\mathrm{erg/s}$ with a spin-down timescale of $\tau_s = 9\,\mathrm{kyr}$ and a braking index close to 2 [210]. Its proper motion is perpendicular to the line of sight with a velocity of $v_S = 200\,\mathrm{km/s}$, resulting in a displacement of around 70 pc from its birthplace. Due to its age a parenting supernova remnant has not been identified and it is unclear whether Geminga is still inside it or not. First Milagro [1] and later HAWC [3] observed extended γ-ray emission in a region of $2\,^\circ$ or roughly 10 pc around Geminga. This is the result of inverse Compton scattering of TeV electrons [3]. At GeV energies Fermi-LAT [52] detected emission extending up to $20\,^\circ$, which is not perfectly spatially coincident with the pulsar, but trailing behind it. All of these observations confirm that pulsars are sources of primary electrons and positrons. Whether they are able to explain the positron excess primarily depends on how these particles propagate to earth.

4.3. HAWC Observation

The HAWC collaboration detected extended γ-ray emission around Geminga in 2017 [3] and later that year published the surface brightness [2]. Their significance map for emission between 1 TeV and 50 TeV is shown in Fig. 4.2 with white lines indicating the $5\,\sigma$, $7\,\sigma$ and $10\,\sigma$ contours. The extension of the $5\,\sigma$ contours is around $5\,^\circ$, which at the distance of Geminga corresponds to a diameter of $d_{\mathrm{halo}} = 25\,\mathrm{pc}$. The emission region at smaller declinations and larger right ascensions is another TeV-halo around the Monogem pulsar. If this additional emission is accounted for, the asymmetry of the emission region is at most a factor of 2. For this reason they provide the surface brightness as a function of the distance to the pulsar and average over azimuthal angle, assuming a distance of 250 pc. This is shown Fig. 4.3, where the red lines indicate the best fit model with uncertainty and the black points are the data. The diffusion coefficient $\kappa(100\,\mathrm{TeV}) = 4.5^{+1.2}_{-1.2} \cdot 10^{27}\,\mathrm{cm}^2/\mathrm{s}$ of their best fit model is roughly a factor 100 smaller than typically inferred from hadronic ratios (see again Sec. 1.1.3). In fact, with the B/C diffusion coefficient the extent of the halo would increase by a factor of 10, which would reduce the surface brightness by a factor 100, which would prevent the detection by HAWC. Since the interaction of particles with turbulence only depends on their energy and charge, also the diffusion coefficient for hadrons will be reduced. Under the assumption this region of suppressed diffusion extends to earth the HAWC collaboration calculated the positron flux at earth. They found that the contribution to the positron flux at earth is negligible, since particles typically diffuse $d \approx \kappa t_E \approx 10\,\mathrm{pc}$ before loosing their energy.

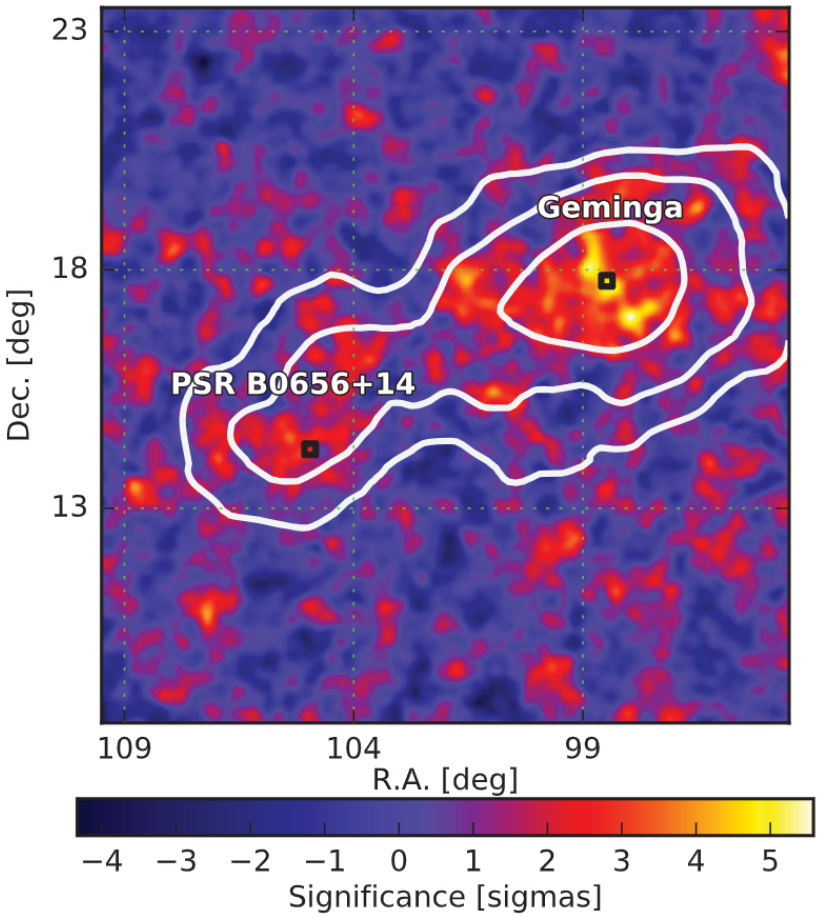

Figure 4.2: Significance map of γ-ray emission around Geminga by HAWC [2]. The white lines indicate the $5\,\sigma$, $7\,\sigma$ and $10\,\sigma$ contours.

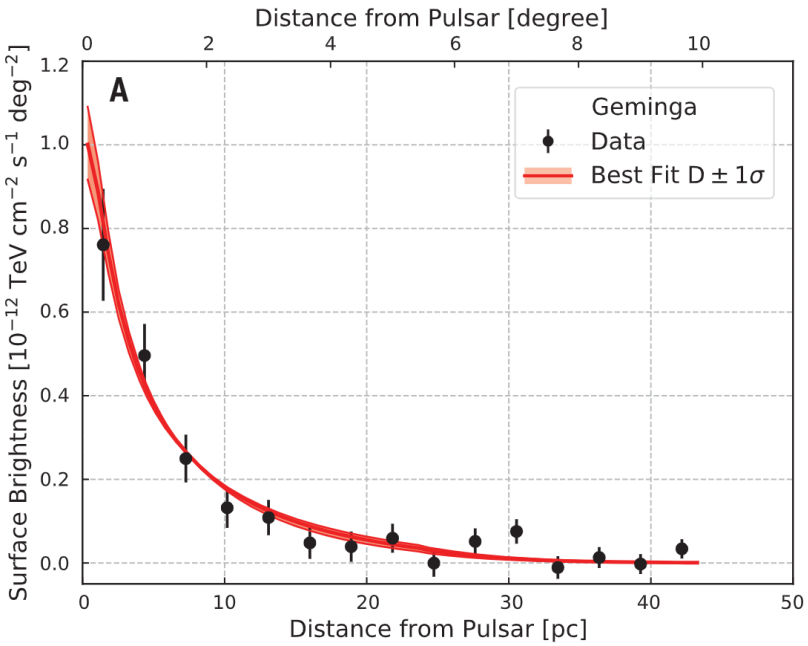

Figure 4.3: Surface Brightness around Geminga by HAWC [2] as a function of angular distance and physical distance under the assumption of a distance to Geminga of 250 pc. The black dots mark the measurements and the red line indicates the best fit model of Abeysekara et al. [2] with $1\,\sigma$ uncertainties.

4.4. LHAASO Observation

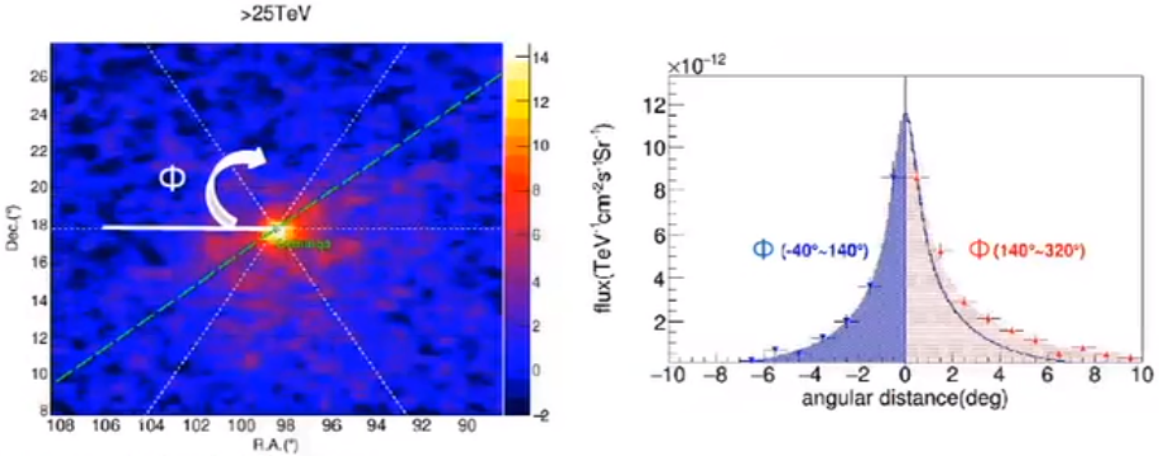

Figure 4.4: Right: Preliminary test statistics map of γ-ray emission above 25 TeV around Geminga by LHAASO [35]. The Green dots mark the position of Geminga and the white markings indicate the azimuthal angle. The dotted green line indicates the separation between the two half spheres with the largest difference in surface brightness according to LHAASO. Left: Surface brightness of Geminga as measured by LHAASO as function of distance to the pulsar. Blue values at negative angles indicate the average within an angle of $\phi = -40 - 140\,^\circ$ and red values on positive angular distances correspond to the average over $\phi = 140 - 320\,^\circ$. The blue line displays a spherically symmetric solution and indicates that the surface brightness found in the two regions is asymmetric.

During the ICRC 2023 the LHAASO collaboration presented their observations of Geminga, which have not been published [35]. The significance map of γ-ray emission above 25 TeV is shown on the left-hand side of Fig. 4.4, where the colours indicate the test statistics and the position of Geminga is marked in green. The surface brightness is calculated as an average over the polar angle ϕ, indicated by the white line and arrow. Instead of calculating the average over the entire circle, they consider two half circles and systematically search for the largest difference between the surface brightnesses. The line dividing the half-circles with the largest difference is indicated with a green dashed line. The corresponding surface brightnesses are shown in the right-hand side of Fig. 4.4 as a function of angular distance from the source. Negative values indicate the solution obtained between $\phi = -40 - 140\,^\circ$ in blue and positive ones the solution between $\phi = 140 - 320\,^\circ$ in red. The blue lines indicate a spherically symmetric solution, which clearly shows that the surface brightness is asymmetric. We investigate possible explanations in Sec. 4.6

4.5. Current Models

In order to explain the observations by HAWC and LHAASO a large variety of models have been suggested. We dedicate the subsequent sections to a detailed study of the current models. The main criteria we expect the models to fulfil are that they produce the radial dependence of the surface brightness, the symmetry of the observations and are also self-consistent. We start in Sec. 4.5.1 by explaining the modeling of the emission with a 3D isotropic diffusion coefficient and use this section to explain how the steps necessary to get from the phase space density of e^+, e^- to the surface brightness. Then we introduce a two zone model in Sec. 4.5.2 with suppressed diffusion close to the pulsar and the galactic average obtained in by hadronic cosmic ray ratios everywhere else, called "3D iso.". Whether ballistic transport close to the source, where the diffusion approximation is not justified, can explain the observations is discussed in Sec. 4.5.3 and denoted as "ballistic". We continue by investigating the effect of the resonant streaming instability in the flux-tube approximation in 3D isotropic diffusion, called "res. SI. 1D" and "res. SI. 3D". Finally, we discuss testparticle simulations

Table 4.1: Overview of the existing theoretical models, see text for explanations. If the model is unable to explain a condition, it is marked with a X, if it is unclear a ? is used and in case it can explain the condition a ✓is used.

	3D iso.	ballistic	res. SI. 1D	res. SI. 3D	external
radial dependence	✓	X?	X	X	✓
symmetry	✓	?	X	✓	✓
self-consistent	X	✓	✓	✓	?

in Sec. 4.5.5, which for typical turbulence in the galaxy give diffusion coefficients below that infered from cosmic ray ratios and motivate possible explanations in Sec. 4.5.6, called "external". In Tab. 4.1 we give a short summary of our findings.

4.5.1. Basic Modeling of particle and γ-ray emission

The quantity measured by water Cherenkov detectors is the surface brightness. This is the density per time of photons produced by inverse Compton scattering directed to earth integrated along the line of sight. In order to model this quantity we have to proceed in three steps:

1. Calculate the flux of electrons and positrons emitted from the pulsar.
2. Compute the photon flux produced by inverse Compton scattering.
3. Integrate the flux along the line of sight.

e^+/e^--Flux We start by computing the flux of electrons and positrons from the pulsar. After being produced in the gaps of the pulsar magnetosphere, they can be further accelerated by the relativistic pulsar wind termination shock. In contrast to supernova remnants, the acceleration mechanism is not simple diffusive shock acceleration, but will differ due to the high velocity of the shock, the different geometry and high magnetic fields. For this reason the spectral index of the source γ_e will be a free parameter in the following. Then the energy dependence of the source is:

$$Q_E(E) = \left(\frac{E}{E_n}\right)^{-\gamma_e} \exp\left(-\frac{E}{E_c}\right), \tag{4.11}$$

where $E_c = 10^3$ TeV is the cutoff energy caused by the maximum energy obtainable in the PWN and $E_n = 1$ GeV the normalisation of the power law. The normalisation and time dependence of the source is given by the assumption that a fraction α of the spin-down luminosity of the pulsar is converted into electrons and positrons. With this assumption the total energy converted into e^+/e^- pairs is given by

$$E_{\mathrm{tot}} = \alpha \int_0^\infty \mathrm{d}t L_{\mathrm{spin}}(t), \tag{4.12}$$

and the source term Q has to fulfil the condition

$$E_{\mathrm{tot}} = \int \mathrm{d}t_0 \int \mathrm{d}r_0^3 \int_{E_1}^\infty \mathrm{d}E_0 E_0 Q(\mathbf{r}_0, E_0, t_0), \tag{4.13}$$

where the minimum energy is set to $E_1 = 0.1$ GeV.

In the diffusion approximation the energy spectrum $\psi = 4\pi p^2 f$ of electrons/positrons which propagate with isotropic and homogeneous diffusion coefficient κ is given by (see Eq. 1.47):

$$\frac{\partial \psi(\mathbf{r}, t, E)}{\partial t} - \kappa \nabla^2 \psi(\mathbf{r}, t, E) + \frac{\partial}{\partial E}\left(\frac{\mathrm{d}E}{\mathrm{d}t}\psi(\mathbf{r}, t, E)\right) = Q(\mathbf{r}, t, E). \tag{4.14}$$

The solution of this equation, the so called Syrovatskii solution, is obtained by finding the corresponding Green's function G, which is the solution for a δ-distribution in all coordinates [198]. The coordinates of the δ distribution are denoted tith a subscript 0. When we substitute with the energy-loss time τ and diffusion-loss distance (squared) l^2:

$$\tau(E, E_0) \equiv \int_{E_0}^{E} \frac{\mathrm{d}E'}{\left(\frac{\mathrm{d}E'}{\mathrm{d}t}\right)} \text{ and } l^2(E, E_0) \equiv \int_{E_0}^{E} \mathrm{d}E' \frac{\kappa(E')}{\left(\frac{\mathrm{d}E'}{\mathrm{d}t}\right)} \tag{4.15}$$

the equation reduces to a simple heat equation. After re-substituting the corresponding Green's function is given by:

$$G(\mathbf{r}, E, t; \mathbf{r}_0, E_0, t_0) = \frac{1}{\left(\frac{\mathrm{d}E}{\mathrm{d}t}\right)} \left(4\pi l^2\right)^{-3/2} \exp\left[-\frac{(\mathbf{r} - \mathbf{r_0})^2}{4l^2}\right] \delta\left(t - t_0 - \tau\right). \tag{4.16}$$

The solution of Eq. 4.14 is obtained by convoluting with the source:

$$\psi(\mathbf{r}, E, t) = \int \mathrm{d}t_0 \int \mathrm{d}^3 r_0 \int \mathrm{d}E_0 G(\mathbf{r}, E, t; \mathbf{r}_0, E_0, t_0) Q(\mathbf{r}_0, E_0, t_0). \tag{4.17}$$

For calculations of the flux of positrons on earth at GeV energies the propagation timescale is significantly longer than the spin-down timescale and the particle injection can be modelled as burst-like. Additionally, the extent of the PWN of 1 pc is negligible compared to the size of the halo or distance to earth and can be assumed to be point like. This simplifies the source term to:

$$Q_{\mathrm{burst}}(\mathbf{r}_0, t_0, E_0) = \delta(\mathbf{r}_0 - \mathbf{r}_S)\delta(t_0 - t_S) Q_{\mathrm{burst}}(E_0) \text{ with } Q_{\mathrm{burst}}(E_0) = Q_{0,\mathrm{burst}} Q_E(E_0), \tag{4.18}$$

where the normalisation $Q_{0,\mathrm{burst}}$ is given by Eq. 4.13. In this case the solution of the transport equation can be written down analytically:

$$\psi(\mathbf{r}, t, E) = \frac{\left(\frac{\mathrm{d}E_S}{\mathrm{d}t}\right)}{\left(\frac{\mathrm{d}E}{\mathrm{d}t}\right)} \left(4\pi l^2(E, E_S)\right)^{-3/2} \exp\left(-\frac{(\mathbf{r} - \mathbf{r}_S)^2}{4l^2(E, E_S)}\right) Q_{\mathrm{burst}}(E_S), \tag{4.19}$$

where $E_S(t, E; t_S)$ is the initial energy at time t_S of a particle which has energy E at time t, which can be obtained by $t - t_S = \tau(E, E_S)$.

In contrast, the assumption of a burst like injection is not justified for the TeV particles which produce the halo, since the age of the pulsar is larger than the energy loss time $t_{\mathrm{age}} \gg t_E$. Hence, the time-dependent source term is given by:

$$Q_{\mathrm{cont}}(\mathbf{r}_0, t_0, E_0) = \delta(\mathbf{r}_0 - \mathbf{r}_S) Q_{\mathrm{cont}}(t_0, E_0) \text{ with } Q_{\mathrm{cont}}(t_0, E_0) = Q_{0,\mathrm{cont}} \alpha L_{\mathrm{spin}}(t_0) Q_E(E_0), \tag{4.20}$$

where the normalisation $Q_{0,\mathrm{cont}}$ is obtained once again by Eq. 4.13 and the largest injection time is $t_0 = t$. Under this assumption the energy density can be written as:

$$\psi(\mathbf{r}, t, E) = \int_0^t \mathrm{d}t_0 \frac{\left(\frac{\mathrm{d}E_S(t_0)}{\mathrm{d}t}\right)}{\left(\frac{\mathrm{d}E}{\mathrm{d}t}\right)} \left(4\pi l^2(E, E_S(t_0))\right)^{-3/2} \exp\left(-\frac{(\mathbf{r} - \mathbf{r}_S)^2}{4l^2(E, E_S(t_0))}\right) Q_{\mathrm{cont}}(t_0, E_S(t_0)), \tag{4.21}$$

where $E_S(t, E; t_0)$ is the initial energy at time t_0 of a particle which has energy E at time t, which can be obtained by $t - t_0 = \tau(E, E_S(t_0))$.

For lower energies the diffusion loss length $\sqrt{l^2}$ becomes comparable to the displacement of the source within one energy loss time $t_E v_S$ and the proper motion of the source has to be accounted for: $r'_S = r_S + v_S t_0$.

Table 4.2: Temperatures T and energy densities U of the interstellar radiation field [65, 103]. Each component is modeled as a grey body spectrum, which in the case of the Cosmic Microwave Background (CMB) reduces to a black body spectrum.

	CMB	IR	STAR	UV
T [K]	2.76	20	5000	10000
U [eV/cm^3]	0.26	0.6	0.6	0.1

The flux at earth is related to the phase space density via

$$\psi_e(\mathbf{r}, t, E) = \frac{c}{4\pi}\psi(\mathbf{r} = \mathbf{r}_{\text{Earth}}, t, E). \tag{4.22}$$

In the following sections we will discuss the results obtained with this approximation as well as its limitations.

γ-ray emission When the electrons and positrons inverse Compton scatter with the photons of the interstellar radiation field (ISRF) they will transfer a large part of their energy. The power emitted into photons of energy E_γ via inverse Compton scattering of electrons or positrons of energy E is given by [26]

$$\mathcal{P}^{\text{IC}}(E, E_\gamma) = \frac{3\sigma_T c m_e^2 c^4}{4E^2} \int_{\frac{m_e c^2}{4E}}^1 \mathrm{d}q \frac{\mathrm{d}N}{\mathrm{d}\epsilon}(\epsilon(q)) \left(1 - \frac{m_e^2 c^4}{4qE^2(1-\tilde{\epsilon})}\right) \left[2q\log(q) + q + 1 - 2q^2 + \frac{\tilde{\epsilon}(1-q)}{2-2\tilde{\epsilon}}\right], \tag{4.23}$$

where $\frac{\mathrm{d}N}{\mathrm{d}\epsilon}(\epsilon(q))$ is the ISRF spectrum of which one photon has energy ϵ and

$$q = \frac{\tilde{\epsilon}}{\Gamma_\epsilon(1-\tilde{\epsilon})},\ \Gamma_\epsilon = \frac{4\epsilon E}{m_e^2 c^4},\ \tilde{\epsilon} = \frac{E_\gamma}{E}. \tag{4.24}$$

We model the ISRF as a combination of several grey body spectra with temperatures and energy densities employed by Evoli et al. [62], Hooper et al. [103] (see Tab. 4.2).

Due to negligible variation within the region of interest spatial variations can be neglected.

The ratio $\mathcal{P}/\mathcal{P}_{\max}$ as a function of initial e^+, e^- and final γ-ray energy E, E_γ is shown in Fig. 4.5. At energies above 100 TeV a e^+, e^- produces a γ-ray of the same energy, while at lower energies the photons only obtain a fraction of the energy. Hence, observations in the Fermi-LAT energy range of 8 GeV up to 1 TeV [142] still trace TeV leptons.

The volume emissivity spectrum of the inverse Compton emission of a spectrum of incident leptons is obtained by calculating the convolution

$$\mathcal{E}(\mathbf{r}, t, E) = \int_{m_e c^2}^\infty \mathrm{d}E \mathcal{P}^{\text{IC}}(E, E_\gamma) f(\mathbf{r}, t, E)/4\pi, \tag{4.25}$$

where we have assumed isotropic emission due to the isotropic distribution of the e^+, e^-.

Line of Sight Integration The flux measured at earth is the superposition of the entire emission along the line of sight and of the entire source region:

$$\frac{\mathrm{d}\psi^{\text{IC}}}{\mathrm{d}\theta \mathrm{d}\phi} = \int_0^\infty \mathrm{d}s \mathcal{E}(s, t, E), \tag{4.26}$$

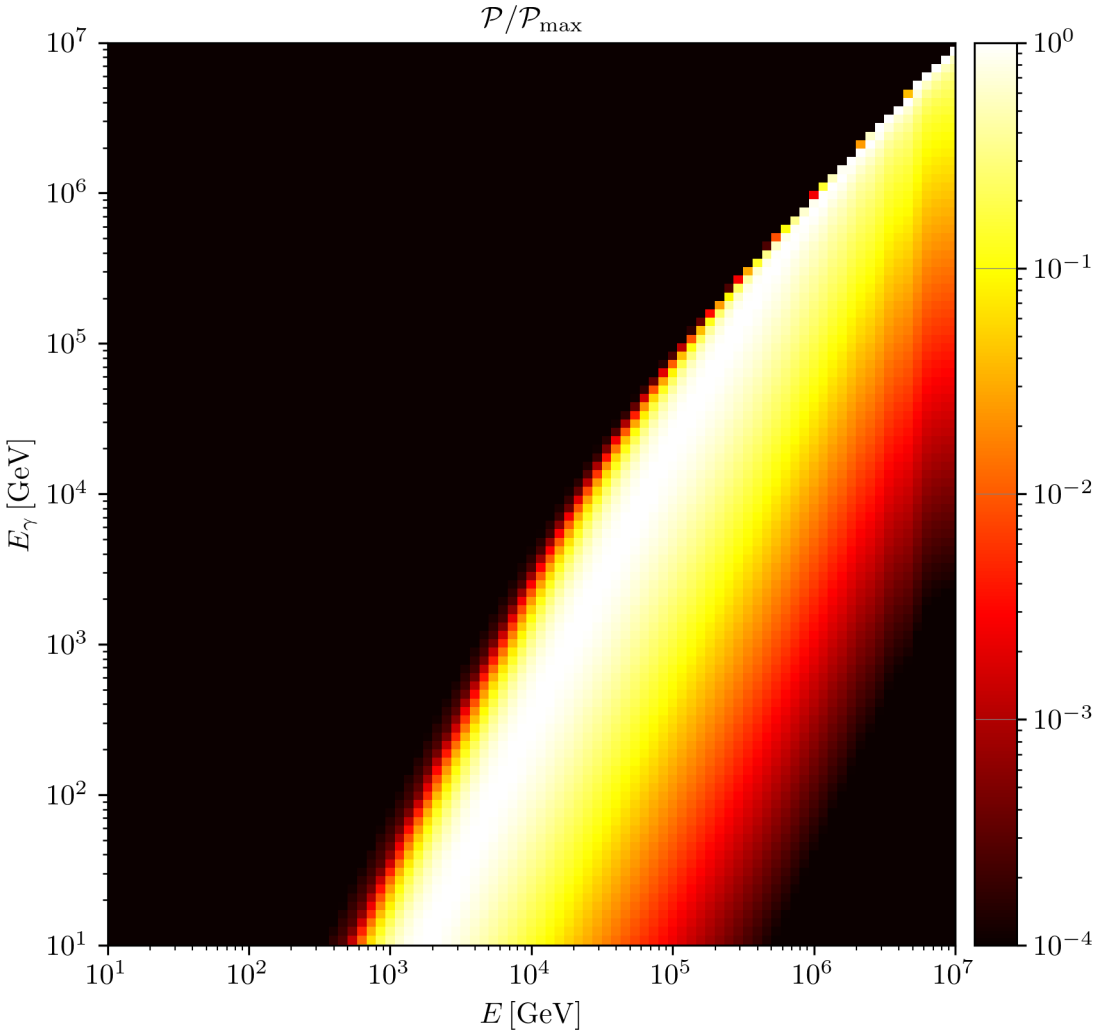

Figure 4.5: Ratio $\mathcal{P}/\mathcal{P}_{\max}$ between the inverse Compton power $\mathcal{P}$ and its maximum $\mathcal{P}_{\max}$ as a function of e^+, e^- energy E and γ-ray energy E_γ. At high energies the photons carry the entire energy of the electron while at lower energies the photons only obtain small fraction of the initial e^+, e^- energy.

where we have to convert the spatial coordinate $\mathbf{r}$ into radial coordinates centred at the observer with the north pole directed towards the centre of the source. Then radius is given by s, the polar angle θ describes the angular distance to the centre of the source and the azimuthal angle is denoted as ϕ. To obtain the entire flux of a source we have to integrate over the entire source solid angle $\Delta\Omega$:

$$\psi^{\mathrm{IC}} = \int_{\Delta\Omega} \mathrm{d}\Omega \frac{\mathrm{d}\psi^{\mathrm{IC}}}{\mathrm{d}\theta \mathrm{d}\phi}. \tag{4.27}$$

The surface brightness SB is defined as the flux from a polar angle averaged over the azimutal angle

$$\mathrm{SB} = \left\langle \frac{\mathrm{d}\psi^{\mathrm{IC}}}{\mathrm{d}\theta \mathrm{d}\phi} \right\rangle_\phi = \int_0^{2\pi} \mathrm{d}\phi \frac{\mathrm{d}\psi^{\mathrm{IC}}}{\mathrm{d}\theta \mathrm{d}\phi} / 2\pi. \tag{4.28}$$

This is the quantity provided by most experiments.

4.5.2. Two Zone Model

If we extrapolate the galactic average diffusion coefficient obtained from B/C to TeV energies and compare to the observations around Geminga we observe a difference of two orders of magnitude. Consequently, the extent of the suppression zones cannot fill the entire Galaxy without contradicting B/C data, or the extrapolation is not valid. The question of how large the suppression zones can be in case we can extrapolate will be answered in Sec. 5. In fact the assumption made by HAWC, that the suppressed diffusion zone extends to earth, has been proven incorrect. Hooper and Linden [102] argued that the electrons observed by HESS at TeV energies would have to come from sources within one energy loss length of 10 pc. However, even though these sources should be bright in γ-rays none have been observed. Additionally, the sum of all known electron sources and a statistical simulation for the unknown ones is able to reproduce the electron flux with the galactic average diffusion coefficient. Hence, they concluded that the region around Geminga must be highly localised and cannot extend to earth. This indicates the inhomogeneity of the diffusion coefficient with a suppression region around the pulsar and the galactic average everywhere else. In this case, called the two zone model, the isotropic diffusion coefficient is given by [70, 200]:

$$\kappa(r) = \begin{cases} \kappa_0 \left(\frac{E}{1\,\mathrm{GeV}}\right)^{\delta} & \text{for } 0 < r < r_b \\ \kappa_2 \left(\frac{E}{1\,\mathrm{GeV}}\right)^{\delta} & \text{for } r \leq r_b \end{cases} , \tag{4.29}$$

where r_b is the boundary of the low diffusion region. The solution of Eq. 4.14 with this diffusion coefficient has been found numerically by Fang et al. [70] and analytically by Osipov et al. [164], who corrected mistakes of previous analytic solutions of Tang and Piran [200]. With this approach it is possible to still fit HAWC data while at the same time not contradicting e^- measurements. The surface

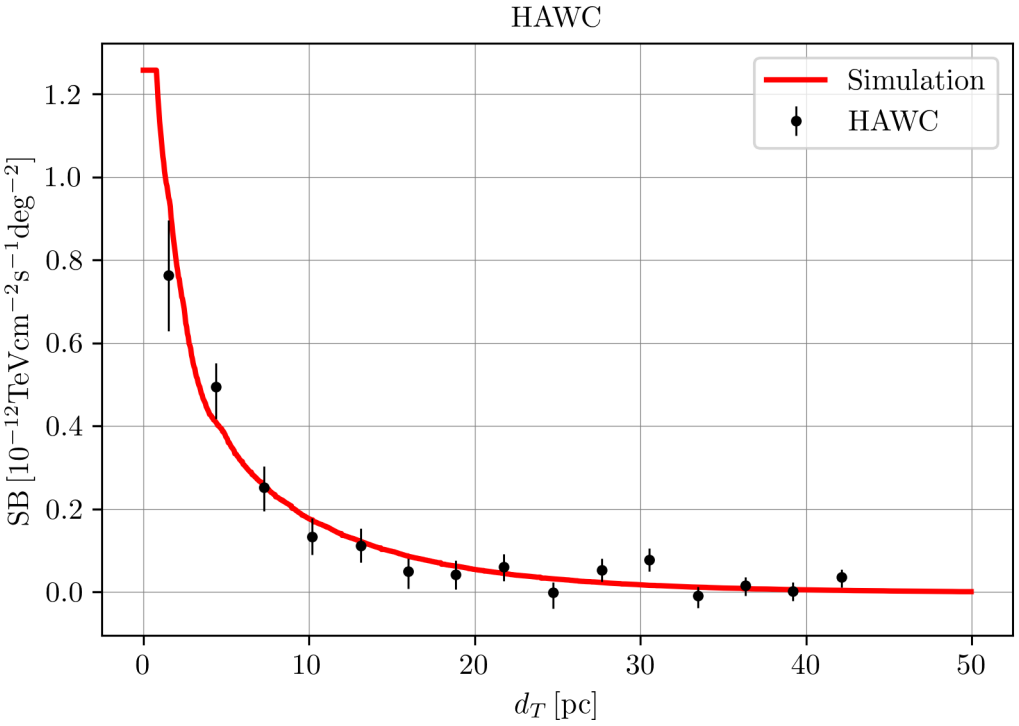

Figure 4.6: Two-zone solution for the Surface Brightness around Geminga as measured by HAWC [2] as a function of distance d_T under the assumption of a distance to Geminga of 250 pc. The black dots mark the measurements and the red line indicates the best fit model of Di Mauro et al. [52]. The plateau at small distances is a result of the finite spatial resolution.

brightness as a function of distance to the pulsar d_T for the best fit values found by Di Mauro et al. [52]

in the two zone model is shown in Fig. 4.6, where the black points mark the measurements by HAWC and the red solid line is the model best fit. The spectral index of the electrons is degenerate with the injection efficiency, since the energy interval observed by HAWC and LHAASO is from $5 - 50$ TeV and above 25 TeV, respectively corresponding to 100 TeV initial state e^+, e^-. For this reason the flux of positrons at AMS-02 energies is poorly constrained and thereby its contribution to the positron excess. To resolve the uncertainty Di Mauro et al. [52] investigated Fermi-LAT data at $E_\gamma > 8$ GeV, since the incident electrons and positrons which produce this emission are of TeV energies. In fact, they obtain a harder spectral index of $\gamma_e = 1.9$ compared to previous fits to TeV data. Here, the fraction of energy lost in each scattering is small and energy losses can be approximated as continuous and these particles will be of the energy relevant for the positron excess when they reach earth. To calculate the combined contribution to the positron excess Manconi et al. [142] accounted for all known pulsars of the ATNF catalogue as well as a simulation of the unknown pulsars from a statistical model. They find that with typical parameters the positron excess can potentially be explained purely by pulsars with a two-zone diffusion model. It has to be noted that the effect on the escape spectrum from the source was neglected, and the flux was calculated using the faulty solution of Tang and Piran [200]. Improvements have been made by Schroer et al. [188], but no fully conclusive model exists as of now.

Diffusion Approximation The particle transport models we have utilised above relies on a variety of underlying assumptions. The first of these is that the propagation of particles is diffusive. This is true only at times larger than a scattering time and therefore at distances larger than the scattering length of particles. For cosmic rays the dominant diffusion process is believed to be resonant scattering, for transport parallel to the background magnetic field, as derived in Sec. 1.4.3. Hence, the length scale at which particles become diffusive is the parallel mean free path $l_\parallel = \kappa 3/c$, which corresponds to a timescale of $\tau_\parallel = l_\parallel/c$. At times $t < \tau_\parallel$ the distance travelled diffusively $r_{\rm diff} = \sqrt{\kappa t}$ is larger than by ballistic transport $r_{\rm ball} = tc$, which clearly indicates the breakdown of the approximation. The transition between the two regimes is called quasi-ballistic. In this case costly numerical simulations that solve the Vlasov equation (see Eq. 1.32) are required to gain further insight [151]. A model where this transition is neglected and the ballistic and diffusive solution are directly matched is discussed in Sec. 4.5.3. The second assumption is that particles diffuse isotropically. This is actually quite surprising, since the diffusion coefficient derived in Sec. 1.4.3 is for transport parallel to the magnetic field lines while the diffusion tensor is highly anisotropic. In fact, the approximation of an isotropic diffusion coefficient for Galactic cosmic ray transport is only valid since the distances are significantly larger that the correlation length of the magnetic field $R_d \gg H \gg L_c$. In this case particles have decoupled from their original filed lines and the field lines themselves have diffused [190]. However, the extent of the γ-ray halos is around 25 pc, which is comparable to the correlation length $L_c = 1 - 100$ pc. Hence, for the typical interstellar turbulence level diffusion will be anisotropic on these scales. We will discuss the implications of this in Sec. 4.5.4.

Diffusion Origin Furthermore, the diffusion models can describe the turbulence around the pulsar, but do not give a self-consistent explanation why the diffusion properties are so vastly different from the rest of the Galaxy. The radial symmetry of the two-zone model also relies on the underlying assumption that the turbulence is symmetric around the pulsar. This can only be fulfilled if the source of turbulence is originating from the pulsar. Additionally, it raises the question if TeV-γ-ray halos are a universal or at least common phenomenon. The most likely mechanism in this case is the streaming instability of the electron positron pairs, which was derived in Sec. 1.5.3. Due to the charge neutrality of the pairs, only the resonant part of the instability is triggered. This process and its limitations will be further investigated in Sec. 4.5.4. It could also be the case that the turbulence is produced by an external mechanism. In this case the symmetry assumption has to be broken at some distance. Additionally, the halos should be a less frequent occurrence since they depend on the probability of a pulsar being in one of these zones. The most obvious explanation is if the pulsar is within its parent supernova. For Geminga the shock of its parent supernova will have dissipated according to

Eq. 3.7 after $t_{\rm rad} \approx 30\,\mathrm{kyr} < t_{\rm age} = 340\,\mathrm{kyr}$. Hence, observations are difficult making it impossible to determine if Geminga is still inside. Furthermore, the pulsar has moved 70 pc since its creation, which requires a large extent of the supernova remnant. If turbulent damping is neglected, Fang et al. [71] showed that it is possible to create the halos by turbulence injected from the supernova. However, this assumption is strong and requires significant fine-tuning of the geometry.

4.5.3. Ballistic-Diffusion Model

Particles travel on balistic trajectories on distances shorter than the parallel mean free path $l_\parallel$ given by [181]:

$$l_\parallel(1\,\mathrm{GeV}) \approx 0.3 \frac{\kappa(1\,\mathrm{GeV})}{10^{28}\,\mathrm{cm}^2/\mathrm{s}}\,\mathrm{pc}. \tag{4.30}$$

For the 100 TeV particles relevant for the TeV-halo and the diffusion coefficient inferred from cosmic-ray ratios of $\kappa(1\,\mathrm{GeV}) \sim 10^{28}\,\mathrm{cm}^2/\mathrm{s}$ the mean free path is $l_\parallel \approx 100\,\mathrm{pc}$ which similar to the size of the halo $d_{\rm halo}$. Hence, the diffusion approximation is not justified in this case and particles travel ballistically. This setup was investigated by Recchia et al. [181] in the absence of a large scale background magnetic field. They assumed spherically symmetric ballistic transport at distances smaller than $l_\parallel$ and matched this solution with a model of isotropic diffusion at larger distances. In the ballistic regime the Inverse Compton γ-rays are emitted primarily along the direction of momentum, leading to a point like source. To model the quasi-ballistic regime they used a small angle diffusion approximation and calculated the photon emission from this anisotropic distribution. From Eq. 4.30 it is apparent, that if diffusion is suppressed by two orders of magnitude also the mean free path will be reduced by this amount. Then $l_\parallel \approx 1\,\mathrm{pc} \ll d_{\rm halo}$ which means the ballistic phase can be neglected and the purely diffusive solution is recovered. Within this model they find that the χ^2 as a function of diffusion coefficient has two minima. The first at a diffusion coefficient reduced by two to three orders of magnitude, which reaches $\chi^2 = 5$. The second one is found at the diffusion coefficient inferred from cosmic ray data and reaches $\chi^2 = 25$. They concluded that a suppressed diffusion coefficient is not necessary to explain the TeV-halos. We believe this conclusion to be flawed for a number of reasons. The most obvious is the better fit with a suppression and the second one is that they require conversion efficiencies above 100 %. Additionally, the assumption of spherical symmetry in the ballistic regime is only justified if there is no large effective background magnetic field on scales larger than the Larmor radius $B_{\rm eff} = B_0 \left(1 + \int_{k_0}^{1/r_L} \mathrm{d}k' W(k')\right)^{1/2}$, where B_0 is the large scale magnetic field. Otherwise, particles would gyrate around the effective magnetic field with $r_L = \frac{p}{qB_{\rm eff}} < l_\parallel$ leading to axisymmetric geometry. For typical values of B_0 of several μG, the Larmor radius of 100 TeV particles is of the order of 0.1 pc. It is unclear why there should not be a background magnetic field and no large scale turbulence in this region. So the conditions required in order to explain the TeV-halos with a ballistic transport phase and an unsuppressed diffusion coefficient are far from normal, but instead need a very fine-tuned parameter set. Phenomenological models like the above have to be treated very carefully and require the necessary understanding of particle propagation. We instead suggest to use test-particle simulations as baseline to develop a phenomenological approach. Advances in this direction have been made by López-Coto and Giacinti [137] and will be discussed in Sec. 4.5.5. In summary, suppressed diffusion remains necessary to explain the TeV-halos.

4.5.4. Self Confinement

Now that we have established that there has to be a region of suppressed diffusion to explain the TeV-halos, we want to investigate its origin. Unlike for the pulsar wind nebula itself, where turbulence is produced at the relativistic wind termination shock, no explanation for the increased level of turbulence in the halo is known. Two different scenarios have been investigated. The first is external turbulence e.g. injected by the SNR [71] and the second is self-generation by cosmic rays via the streaming instability. The latter is a well known theory that predicts suppressed diffusion

around SNRs, where the gradient in particle density gives rise to the resonant part of the instability [30, 108, 141, 156, 157], as is investigated in Sec. 3. Additionally, the charged current of particles escaping from the shock triggers the non-resonant part of the instability [18, 178, 186, 187], which exhibits growth rate well in excess of the resonant instability. A pulsar produces e^+, e^- pairs as motivated in Sec. 4.2 and is therefore not expected to have any charged current that is able to excite the non-resonant streaming instability. However, at large energies there could be charge separated currents [159] but whether they are strong enough to excite necessary turbulence is questionable. The excitation of the resonant streaming instability was first proposed by Evoli et al. [65] and later continued by Mukhopadhyay and Linden [154]. In the following we will explain their model and provide some extension. Furthermore, we will discuss its limitations and assumptions.

Two extreme cases for the particle propagation are spherically symmetric propagation in 3D and propagation along the background magnetic field in 1D in a flux tube as motivated in Sec. 1.6. We will discuss the validity of both approximations later. First we want to reproduce the results of Evoli et al. [65] and Mukhopadhyay and Linden [154] in the flux tube approximation. They assume a correlation length (and thereby length of the flux tube) of $L_c = 100\,\mathrm{pc}$, which is on the upper edge of possible values [97]. The radius R is given by the extent of the source $\sigma = 1\,\mathrm{pc}$, which is modelled as a Gaussian. Particles are assumed to be accelerated to a power law at the relativistic pulsar wind termination shock with spectral indices as hard as $\gamma \simeq 3.5$ and a cut-off energy of E_c. The time dependent normalisation is again given by the spin down luminosity of the pulsar. Since we are interested in high energies $E \approx pc$ and the source term in 1D and 3D can be written as:

$$Q_e^{1D}(z,t,p) = Q_0 L(t) \left(\frac{p}{mc}\right)^{-\gamma} \exp\left\{\frac{-p}{p_c}\right\} \frac{\exp\left(-z^2/2\sigma^2\right)}{\pi R^2 (2\pi\sigma^2)^{1/2}} \tag{4.31}$$

$$Q_e^{3D}(r,t,p) = Q_0 L(t) \left(\frac{p}{mc}\right)^{-\gamma} \exp\left\{\frac{-p}{p_c}\right\} \frac{\exp\left(-r^2/2\sigma^2\right)}{(2\pi\sigma^2)^{3/2}}. \tag{4.32}$$

The normalisation Q_0 is obtained by Eq. 4.13 with $E_{\mathrm{min}} = 1\,\mathrm{GeV}$ and $E_{\mathrm{max}} = 10\,\mathrm{PeV}$.

1D: In the cylindrically symmetric flux tube the transport equation for electrons and positrons is described by:

$$\frac{\partial f}{\partial t} + u\frac{\partial f}{\partial z} - \frac{\partial}{\partial z}\left[\kappa(z,t,p)\frac{\partial f}{\partial z}\right] - \frac{\mathrm{d}u}{\mathrm{d}z}\frac{p}{3}\frac{\partial f}{\partial p} + \frac{1}{p^2}\frac{\partial}{\partial p}\left[p^2\left(\frac{\mathrm{d}p}{\mathrm{d}t}\right)f\right] = Q_e(z,t,p), \tag{4.33}$$

where we have made the dependence of κ on z, t, p explicit to stress that the diffusion coefficient is not a given constant anymore, but self-consistently determined by resonant pitch angle scattering with magnetic turbulence of spectrum $W(z,t,p)$ (see e.g. Sec. 1.4.3):

$$\kappa(p,z,t) = \frac{\kappa_{\mathrm{B}}(p) 4/\pi}{kW(k,z,t)}, \tag{4.34}$$

where $\kappa_{\mathrm{B}}(p) = r_{\mathrm{L}}(p)c\beta/3$ is the Bohm diffusion coefficient. We neglect the injection of turbulence at large scales and dissipation at small scales but instead assume a constant background level of turbulence. Then the transport equation for turbulence is given in an equal manner to Eq. 3.3:

$$\frac{\partial W}{\partial t} + \frac{\partial}{\partial z}(v_{\mathrm{A}} W) = \left(\Gamma_{\mathrm{CR}}(f) - \Gamma_D(W)\right) W + \Gamma_D(W_{\mathrm{BG}}) W_{\mathrm{BG}} + \frac{\partial}{\partial k}\left[\kappa_{kk}(W)\frac{\partial W}{\partial k}\right], \tag{4.35}$$

where W_{BG} is the background turbulence determined by solving Eq. 4.34 for W and setting $\kappa(1\,\mathrm{GeV/c}) = 0.1\,\mathrm{pc}^2/\mathrm{yr}$. The damping rate Γ_D is given by the processes explained in Sec. 1.5.2. We have assumed that the advection velocity $u = v_A$, since the turbulence is believed to be composed of Alfvén waves. For external turbulence, which is not produced by the streaming-instability this is not clear, but be-

lieved to be a good approximation. It certainly holds for turbulence produced by the resonant streaming instability with rate $\Gamma_{\rm CR}$ as shown in Sec. 1.5.3:

$$\Gamma_{\rm CR} = \frac{2\pi}{3}\frac{v_A c\beta}{kWU_0}p^4\sum_\alpha \frac{\partial f_\alpha}{\partial z}, \tag{4.36}$$

where U_0 is the energy density of the background magnetic field. In difference to previous studies we do not approximate the turbulent cascade as:

$$\frac{\partial}{\partial k}\left[\kappa_{kk}(W)\frac{\partial W}{\partial k}\right] \simeq \frac{\kappa_{kk}}{k^2}W, \tag{4.37}$$

where κ_{kk} is given by Eq. 1.88. As shown by Evoli et al. [65] this is only marginally valid. It has been used in order to avoid non-linear terms in the finite difference scheme. We have shown how the cascade can be linearised in Sec. 2.3.2. We will now adapt the parameters of Mukhopadhyay and Linden [154] and compare to their results, since the code of Evoli et al. [65] contained an incorrect cascading term κ_{kk}. Namely, we adopt $B_0 = 1\,\mu$G, Kolmogorov turbulence, an injection efficiency of $\alpha = 10\,\%$, an injection spectral index of $\gamma_e = 3.5$ and a background diffusion coefficient of $\kappa_{\rm BG} = 3.466 \cdot 10^{28}\,{\rm cm}^2/{\rm s}$.

The diffusion coefficient κ as function of energy is shown in Fig. 4.7. The background is marked with a black solid line, the solution obtained with the cascade with dashed and the one with the cascade approximated as damping with a dashdotted line, respectively. Different colours mark different times after the birth of the pulsar. We obtain the same energy-independent diffusion coefficient below 1 TeV as observed by Mukhopadhyay and Linden [154] for the damping approximation. In contrast, for the full cascade we recover the typical scaling for Kolmogorov turbulence $E^{1/3}$. At pulsar ages up to 100 kyr this is potentially important for the positron excess at 100 GeV, but as indicated in Fig. 4.5, the contribution of these below-TeV particles to the γ-ray emission above 10 GeV is negligible. Hence, at early times this is not important for observations of the TeV-halos. However, as indicated by the bright blue line, at the current age of Geminga, the suppression of the diffusion coefficient is up to three orders of magnitude larger at low energies. So for the correct treatment of the cascade, the self-consistent models predict a suppression of the diffusion coefficient at 10 pc from the source which exceeds three orders of magnitude and lasts for up to 340 kyr at energies below 1 TeV. At energies above 1 TeV, the diffusion coefficient rises rapidly. This is caused by the cut-off of the pulsar spectrum at $E_c = 100\,$TeV. Not only is the streaming-instability not effective, but also less turbulence which cascades from larger scales can contribute. The spatial and temporal dependence of the diffusion coefficient at 10 TeV and 100 TeV, which is within the energy range of electrons responsible for the HAWC and LHAASO γ-ray observations, is shown in Fig. 4.8. At 100 TeV the diffusion coefficient is at most suppressed one order of magnitude and only at distances below 5 pc from the pulsar. The high diffusion coefficient leads to efficient escape of particles and the only large gradient is caused by the morphology of the source. Since this is shorter than the extension of the TeV-halos it is not possible to explain the increased turbulence levels around the pulsar with the resonant-streaming instability at 100 TeV. At 10 TeV the diffusion coefficient is reduced by up to three orders of magnitude at distances closer than 5 pc from the pulsar and around two orders of magnitude everywhere else. This is in stark contrast to 100 TeV and serves as warning, that the streaming instability in the 1D flux tube setup is only just able to create a high turbulence level.

Of course the above calculations only provide the e^+, e^- phase space density and neither the γ-ray emission nor make the line of sight integration necessary to obtain the surface brightness. Hence, the conclusions of Mukhopadhyay and Linden [154] and Evoli et al. [62] that the resonant streaming instability can explain the morphology of the TeV-halos is premature. In fact, when we want to calculate the line of sight integral, we have to determine the relative orientation of the flux tube. If it is oriented perpendicular to the line of sight, we expect to observe a highly axisymmetric structure. Smoothed with the point spread functions of the instruments, this would look like an ellipsoid with axis ratio of

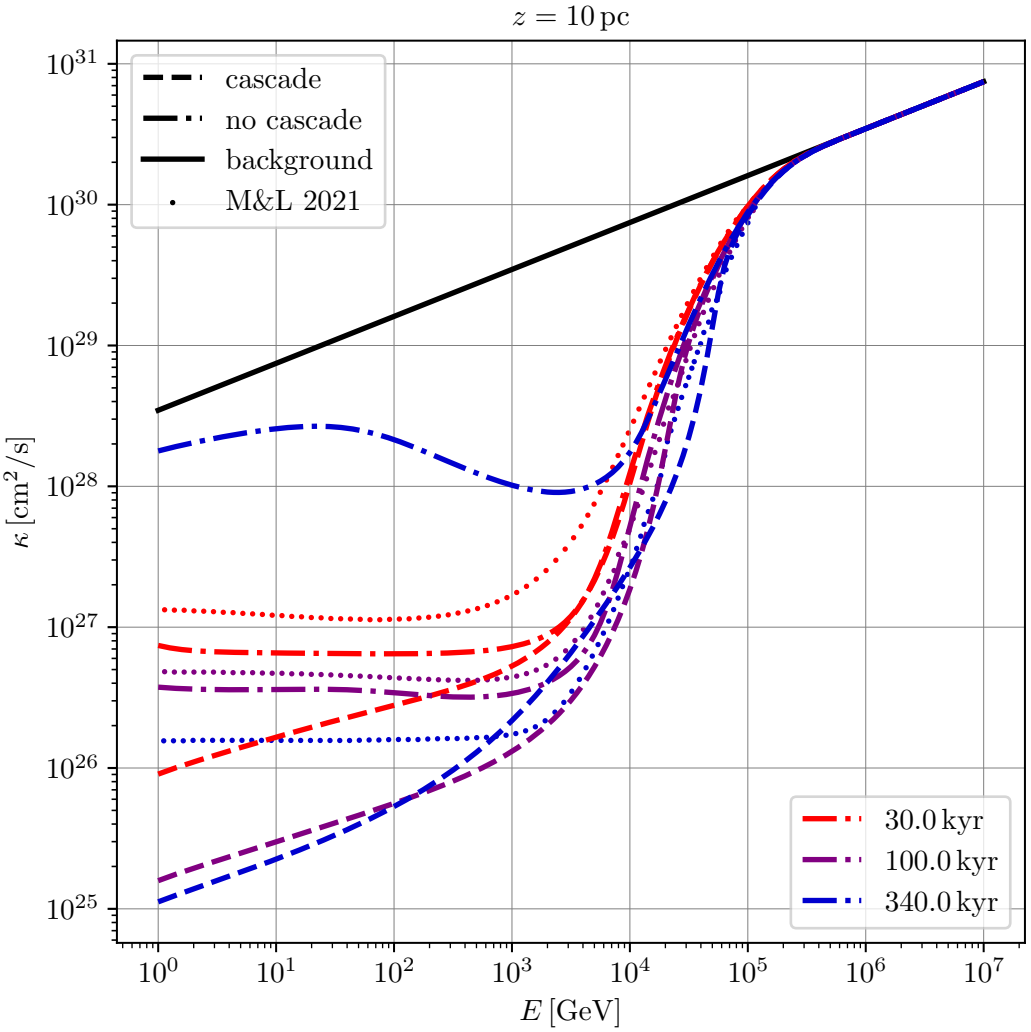

Figure 4.7: Diffusion coefficient κ as a function of energy E at a distance of 10 pc from the pulsar. The solid black line indicates the background value. Dashed lines represent the results of the non-linear computation including a turbulent cascade. The dashdotted lines mark the solution with the damping approximation of the cascade and the dotted lines mark the results of Mukhopadhyay and Linden [154].

$L_C/R = 100$. Due to the symmetry of the observations, which predict an axis ratio of at most 2, this case can be excluded.

Should the local magnetic field be directed towards earth, the gamma ray emission will look symmetric. In this case the angular extend of the emission is caused by the diffusion of particles perpendicular to the magnetic field with $\kappa_\perp$. In a magnetic field of $\eta = 0.5$, the perpendicular diffusion coefficient is given by $\kappa_\parallel \approx 100\kappa_\perp$ [130]. Hence, the angular dependence of the emission is naturally explained by the slower perpendicular diffusion and does not require suppression of the parallel component to be suppressed. The probability that an anisotropic diffusion model produces γ-ray emission which is observed as spherical symmetric was investigated by De La Torre Luque et al. [50]. They calculate the emission from particles diffusing with $\kappa_\perp/\kappa_\parallel = M_A^4$, where the alfvénic mach number is $M_A = \delta B/B_0|_{L_c}$. Then the emission can be calculated as function of the inclination angle ϕ_{incl} between the line of sight and the background magnetic field. The combination of parameters that can

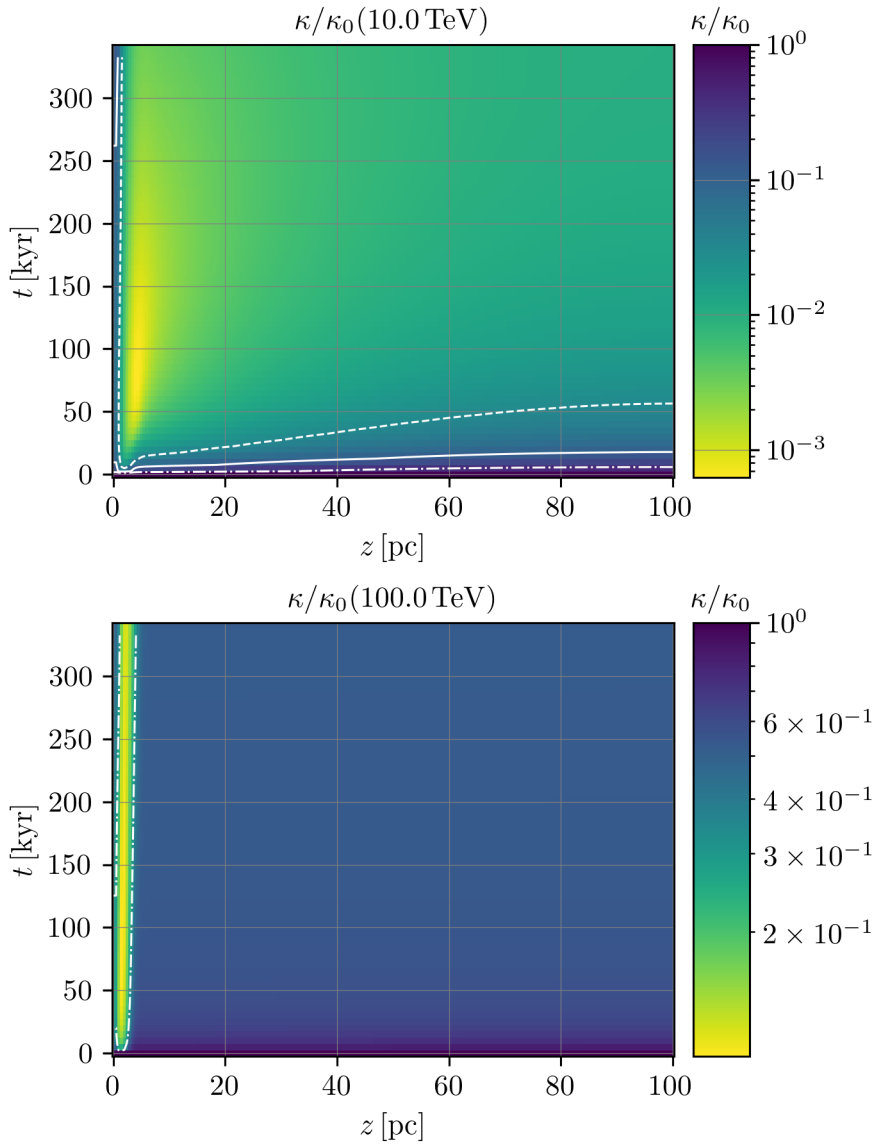

Figure 4.8: Diffusion coefficient κ as a function of distance and age. The top figure shows the results at 10 TeV. Here the diffusion coefficient is suppressed by more than three orders of magnitude over the entire time at close distances to the pulsar. The suppression zone extends up to 100 pc. At the bottom the results for 100 TeV are shown. In contrast to lower energies, the diffusion coefficient is suppressed by one order of magnitude and only within 5 pc of the pulsar.

both explain the extension of the TeV-halos as well as being symmetric, meaning the ratio of major to minor axis is $Z/R < 2$ is very narrow. The inclination angle cannot exceed $\phi_{\mathrm{incl}} = 5\,^\circ$ and $\kappa_\perp/\kappa_\parallel$ has to be in the range of $10^{-3} - 10^{-4}$. The probability of observing a TeV-halo with this inclination angle is $P = [\cos(0\,^\circ) - \cos(5\,^\circ)] \,/\, [\cos(0\,^\circ) - \cos(90\,^\circ)] = 0.004$. These simple geometric estimations highlight, that even though the flux tube approximation can increase the turbulence level significantly it is not able to explain the TeV-halos.

3D: In fact, the flux tube approximation is not justified for a source size of $R_s = 1$ pc and a correlation length of $L_c = 100$ pc for the typical interstellar medium turbulence level of $\eta = 0.5$. The second condition of Eq. 1.6, which demands $0.1 L_c \ll R_s$ is not fulfilled since 10 pc $\gg$ 1 pc. Instead, the model should be expanded to include the divergence of the field lines, if the correlation length is assumed to be 100 pc. However, as discussed in Sec. 1.6, predictions for L_c vary depending on the

position in the Galaxy between 100 pc and 1 pc [97]. In the lower limit of L_c, the field lines around the source and in the halo, which now fulfills $L_c \ll d_{\mathrm{halo}}$, can be assumed to be highly tangled, leading to 3D isotropic diffusion on scale larger than L_c. This will lead to spherical symmetry of the problem and the transport equation can be written as:

$$\frac{\partial f}{\partial t} + u\frac{\partial f}{\partial r} - \frac{1}{r^2}\frac{\partial}{\partial r}\left[r^2\kappa(r,t,p)\frac{\partial f}{\partial r}\right] - \frac{2u}{r}\frac{p}{3}\frac{\partial f}{\partial p} + \frac{1}{p^2}\frac{\partial}{\partial p}\left[p^2\left(\frac{\mathrm{d}p}{\mathrm{d}t}\right)f\right] = Q_e(r,t,p), \tag{4.38}$$

where r is the radius and Q_e is the 3D source function. For the fiducial parameter set the results

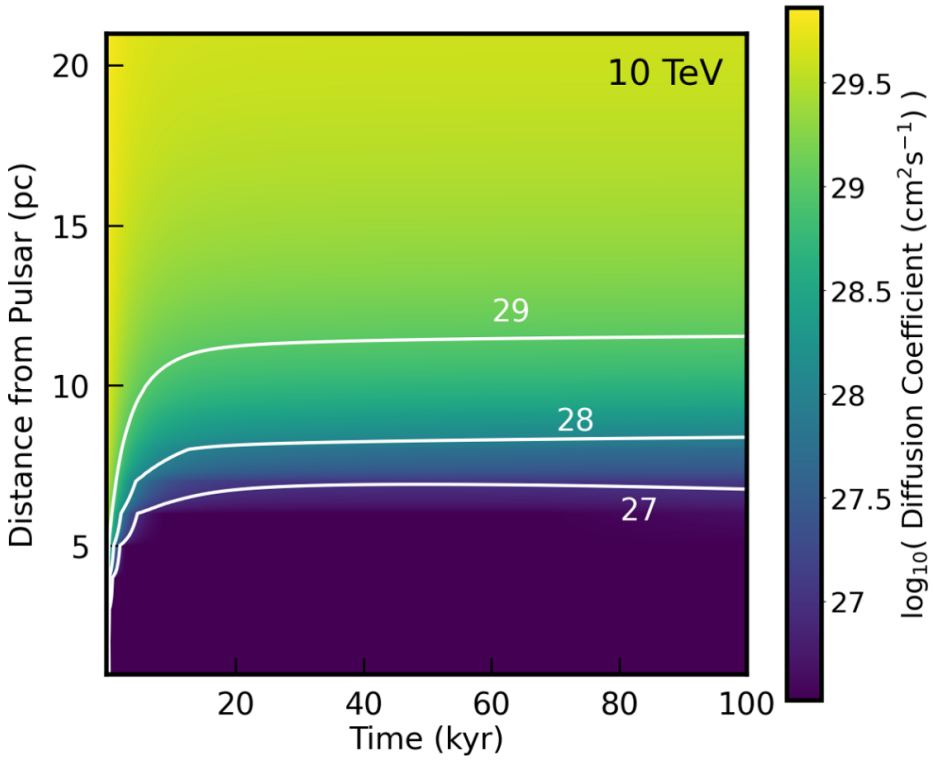

Figure 4.9: Diffusion coefficient κ as a function of distance and time at 10 TeV taken from Mukhopadhyay and Linden [154] for their default parameters with an optimistic injection efficiency of $\alpha = 0.4$. The diffusion coefficient is suppressed by three orders of magnitude only at distances closer than 5 pc from the pulsar for the first 100 kyr of the lifetime. This indicated that the self-confinement in 3D isotropic turbulence is not able to explain the TeV-halos.

without the cascade are shown in Fig. 4.9, which is taken from Mukhopadhyay and Linden [154]. The conversion efficiency is set to $\alpha = 1$. In the tuned parameter set the spectral index is hardened to $\gamma_e = 3.0$, which is in contrast to observations which prefer softer spectra at high energies [68]. Furthermore, the magnetic field is decreased to 0.5 μG and the minimum energy increased to 10 GeV. These assumptions are rather extreme, as they require acceleration mechanisms and efficiencies beyond the most optimistic predictions. The suppression of the diffusion coefficient at 10 TeV for the fiducial model is less than a factor 3, even at distances around 5 pc. For the tuned model this can be increased to more than 2 orders of magnitude at 5 pc and about 1.5 orders at 10 pc. Hence, the streaming instability alone is unable to produce the turbulence required to explain the morphology of the TeV-halos in 3D propagation. Even when including the effect of protons accelerated by the SNR, it is not possible to obtain the suppressed diffusion coefficient needed by the linear models discussed in Sec. 4.5.2 for distances up to 20 pc [154].

Most Optimistic Scenario So neither the flux tube approximation, which is only valid for $L_c > 100\,\mathrm{pc}$, nor isotropic diffusion in the 3D case is able to self-consistently describe the TeV-halos. The underlying problem is that the gradient in cosmic rays, which gives rise to the streaming instability, can only be obtained if the particles are propagating in 1D, but this requires increased turbulence in magnetic fields on scales of the TeV-halo, but this leads to an asymmetry not visible in any of the observed TeV-halos. What remains to be answered is whether it is possible to obtain a sufficient suppression in an intermediate regime, where the magnetic field lines cannot be assumed to be purely parallel, but also not completely random. We estimate this by considering the most optimistic model where we take the results of the 1D flux-tube approach, which predicts the largest suppression of the diffusion coefficient and assume that the Cartesian coordinate z corresponds to a radial coordinate r. We wil call this estimate "most optimistic" in the following. The resulting surface brightness again

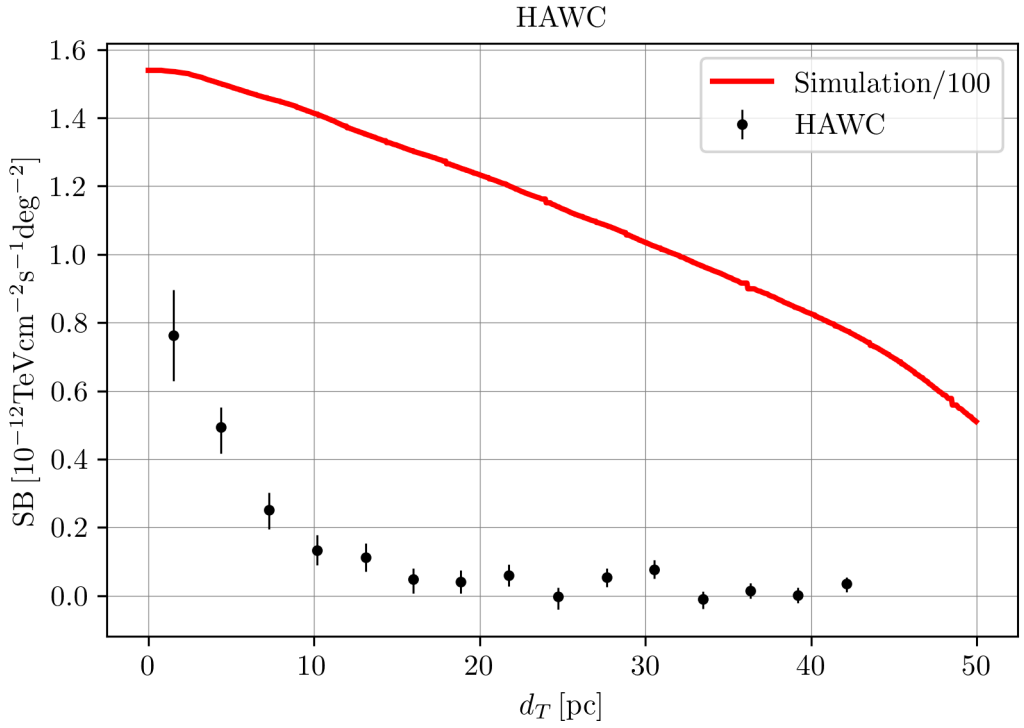

Figure 4.10: Surface brightness of Geminga as a function of distance d_T under the assumption of a distance of 250 pc. The black dots mark the measurements and the red line indicates the result of the "most optimistic" scenario, where we have taken our 1D results with the standard parameters of Mukhopadhyay and Linden [154] and assumed the 1D distance to correspond to a radial coordinate. This gives the most optimistic result in terms of impact of the streaming-instability on the surface brightness, while preserving spherical symmetry.

for the best fit parameters of the Mukhopadhyay and Linden [154] model is shown in Fig. 4.10. The black dots indicate the measurements by HAWC [2] while the red line indicates the "most optimistic" scenario reduced by two orders of magnitude. The reduction is necessary since a large injection efficiency of $\alpha = 10\,\%$ of the spin-down luminosity and a hard spectrum of $\gamma_e = 3.5$ is needed to produce the suppressed diffusion in 1D. In contrast, the phenomenological two-zone models require $\alpha = 1\,\%$ for softer indices of $\gamma_e = 1.8$ [52]. Even worse, the surface brightness predicted in this model is to shallow. This indicates that the suppression caused by the streaming-instability is not large enough to explain the morphology of Geminga as well. This leads to the conclusion, that it is impossible to explain the TeV-halos by turbulence produced with the streaming-instability alone and additional deviations in turbulence level from the extrapolation from hadronic cosmic ray ratios are necessary. We will discuss several interesting effects in the following sections.

4.5.5. Test-Particle Simulations in Artificial Turbulence

All of the currently existing self-confinement models are not able to treat the geometry of the problem self-consistently, which is determined by the background magnetic field and turbulence on scales larger than the Larmor radius of the particles. Instead, they impose a geometry and a fixed background turbulence cascade, which is inferred from the diffusion coefficient in QLT at GeV energies. However, as we have seen in Sec. 4.5.4 the geometry is crucial to determine the cause of the TeV-halos. To tackle this inherent problem, test particle simulations in artificial magnetic fields can help to constrain the properties necessary for the larger field, namely the correlation length L_c, the turbulence level η and the kind of turbulence. In the context of Geminga this was done by López-Coto and Giacinti [137]. They performed test-particle simulations in artificial Kologorov and Kraichnan turbulence without a background magnetic field. For typical turbulent magnetic fields in the galaxy with $B_{\rm rms} = 2 - 5\,\mu$G and coherence length $L_c = 0.1 - 40\,$pc they determined the diffusion coefficient numerically and found values comparable with the values found by isotropic diffusion models [2]. Even without a background magnetic field we expect to recover the scaling of the diffusion coefficient derived in quasi linear theory (see Sec. 1.4.3) at scales smaller than $0.1\,\mathrm{L_c}$ since the large scales provide an effective background field [197]. This leads to the remarkable conclusion that numerical models of particle diffusion with typical turbulence spectra, coherence length L_c and normalisations $B_{\rm rms}$ in the interstellar medium find a diffusion coefficient at GeV energies which is two orders of magnitude lower than that empirically inferred from cosmic ray data [88, 130, 131].

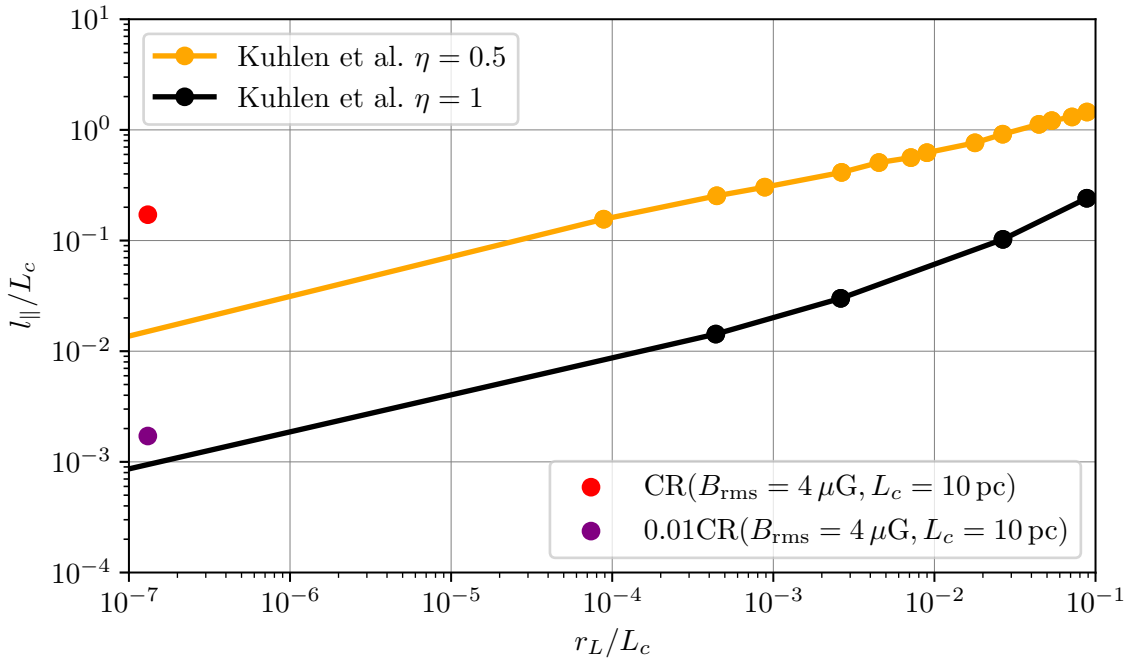

Figure 4.11: Parallel mean free path as a function of Larmor radius. The orange line indicates numerical values found by [131] in artificial turbulence with level $\eta = 0.5$ and the black line the results with $\eta = 1$. The red dot indicates the result of direct cosmic ray measurements of Sec. 5 and galactic magnetic field observations[97], while the purple dot marks 1 % of this result. It is currently unclear what causes the difference between the simulations and the observations.

We show this in Fig. 4.11, where the parallel mean free path $l_\parallel = 3\kappa/c$ as function of Larmor radius is plotted. The red dot marks the value inferred from hadronic cosmic ray ratios as obtained by the null hypothesis in Sec. 5, namely $\kappa(1\,\mathrm{GeV}) = 0.172\,\mathrm{pc}^2/\mathrm{yr}$. Since the exact value of the correlation length in the interstellar medium is unclear, here we assume $L_c = 10\,$pc as average and $B_{\rm rms} = 4\,\mu$G. One percent of this value is marked with the purple dot. The orange line is an interpolation of the results of Kuhlen et al. [130] for $\eta = 0.5$ and the black line indicates the solution without a background magnetic

field extrapolated from Kuhlen et al. [131]. Both simulations predict a scaling of $l_{\parallel}$ as predicted by QLT. This is at first sight surprising, since the theory relies upon the assumption that the turbulent field is smaller than the background field, which is not valid here. However, for scales significantly smaller than the injection scale the larger scales for an effective background magnetic field. Hence, the QLT result is obtained at small enough scales [197]. The normalisation of the simulations and measurements disagree by around one to two orders of magnitude, depending on the precise level of turbulence. This raises the question whether our understanding of particle propagation in the galaxy is fundamentally faulted, or whether the assumptions of the numerical modelling are broken, which has not been answered yet.

For now, we only focus on the fact that the model used by López-Coto and Giacinti [137] predicts a diffusion coefficient which is two orders of magnitude lower than measured from hadronic ratios. They are unable to explain what causes the discrepancy. In this setup they investigate the effect of different L_c on the surface brightness in their figure 3. There it becomes evident, that a correlation length above 5 pc id disfavoured by the symmetry of the observed emission. The best-fit values to

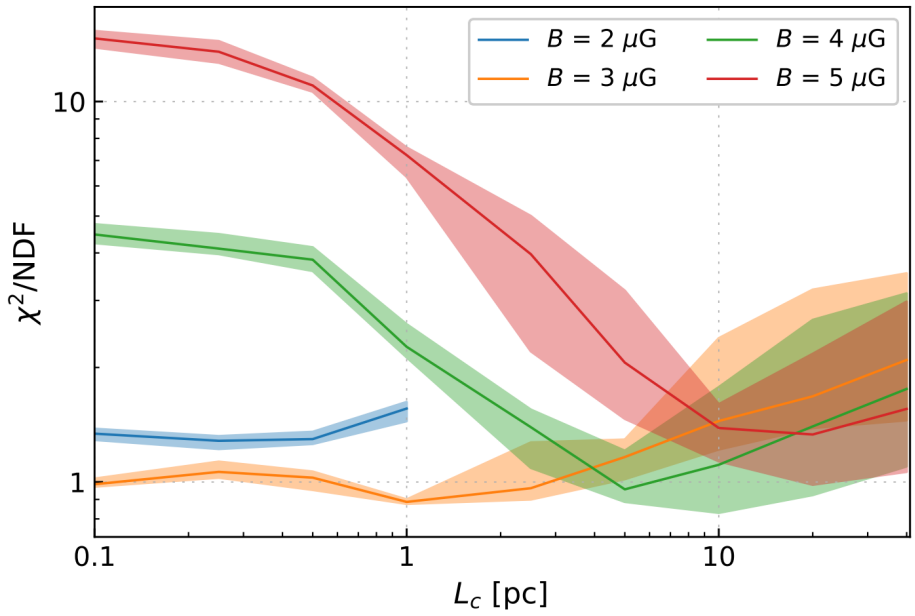

Figure 4.12: χ^2/NDF as a function of L_c for different values of B for a fit to the surface brightness of Geminga taken from [137], where NDF is a constant among all models. The minimum is obtained at $L_c = 1$ pc and $B = 3\,\mu$G. For larger magnetic fields $L_c \approx 10$ pc are preferred. The rise towards higher L_c indicates that correlation length above 10 pc are disfavoured by observations.

the Geminga halos are $B = 3\,\mu$G and $L_c = 1$ pc, as shown in Fig. 4.12. Significantly larger values of L_c for Kolmogorov and Kraichnan turbulence are disfavoured. If a background magnetic field would be included, this would increase the asymmetry. Hence, the properties of the region around Geminga are rather curious. The diffusion coefficient has to be suppressed while the outer scale of turbulence is rather small, in particular smaller than the assumptions in Sec. 4.5.4. In this case the streaming instability should not be effective, and the suppression should be an external feature.

We suggest to extend the model by López-Coto and Giacinti [137] by including a background magnetic field with the expected turbulence levels to draw further conclusions. In principle, these setups have been investigated already in the works of Kuhlen et al. [131]. Even though these are unable to treat the back-reaction of comic rays, they might indicate the properties of the turbulence at scales which are above the maximum resonance scale of particles accelerated by the pulsar.

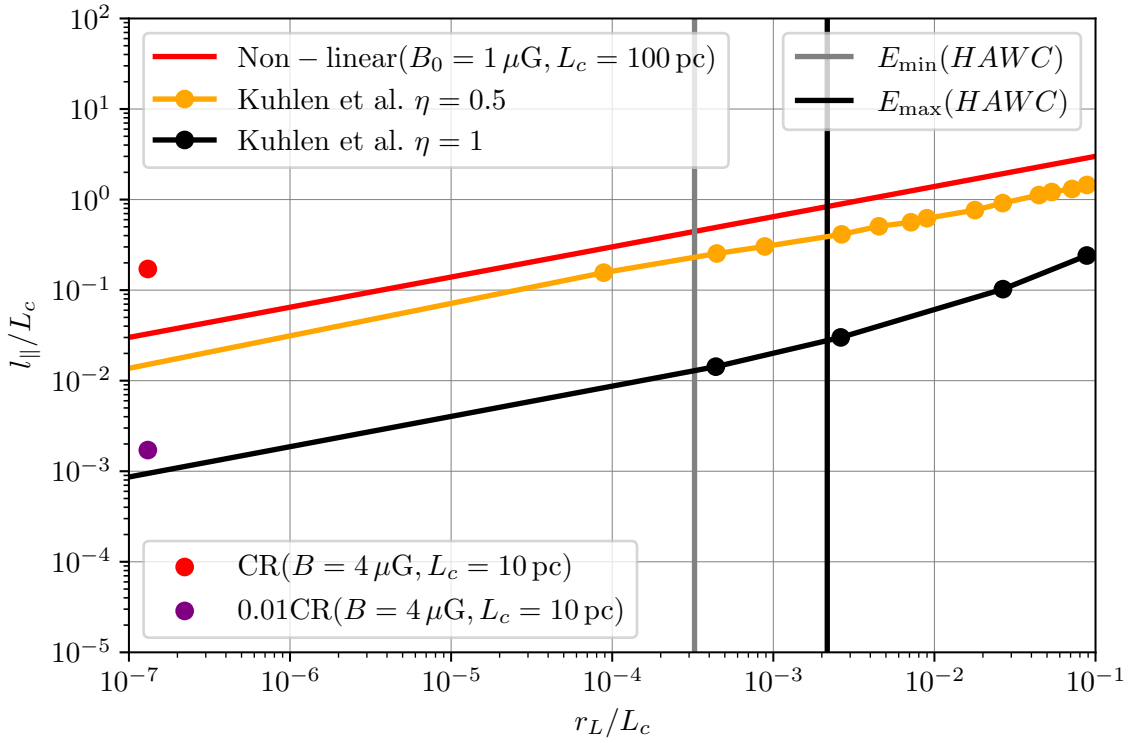

Figure 4.13: Parallel mean free path as a function of Larmor radius. The orange line indicates numerical values found by [131] in artificial turbulence with level $\eta = 0.5$ and the black line the results with $\eta = 1$. The red dot indicates the result of direct cosmic ray measurements as shown in Sec. 5 and galactic magnetic field observations[97], while the purple dot marks 1 % of this result. The red line indicates the results of the non-linear solution in the flux tube approximation. The black and grey lines correspond to the minimum and maximum energies relevant for the HAWC observations with B and L_c identical to the non-linear simulation.

We believe that this approach even without the back-reaction of particles can give further insights. Especially it can be used to determine whether the degree of anisotropy of the diffusion tensor. The two main reasons are that the streaming-instability only affects scales smaller than the injection scale. This can be seen in Fig. 4.13 where we show the impact of the streaming instability in the flux tube approximation on the mean free path as the red line. Vertical lines indicate the minimum and maximum energy of the electrons contributing to the HAWC observations, which can be obtained from Fig. 4.5. At scales $r_g/L_c > 10^{-2}$, the streaming instability has no effect on the mean free path. Within the HAWC range, the streaming instability reduces the mean free path significantly. This highlights, that the larger scales relevant for the effective background magnetic field are unaffected by the streaming instability, and hence it can be expected that the conclusions on L_c drawn by López-Coto and Giacinti [137] hold.

The second reason is that the total turbulence level is dominated by large scales and therefore not significantly affected by the streaming instability. This can be illustrated by defining the effective turbulence level

$$\eta_{\rm eff}(E) = \frac{\delta B^2_{\rm eff}(E)}{\delta B^2_{\rm eff}(E) + B_0^2}. \tag{4.39}$$

For a power spectrum W as defined in Eq. 1.80 $\delta B^2_{\rm eff}(E)$ is given by

$$(\delta B_{\rm eff}(E)/B_0)^2 = \int_{k_0}^{1/r_l(E)} {\rm d}k' k' W(k'). \tag{4.40}$$

For the default parameters of Mukhopadhyay and Linden [154] this is shown in Fig. 4.14 as a function of wave-number for the simulation domain, meaning a maximum energy of 10 PeV.

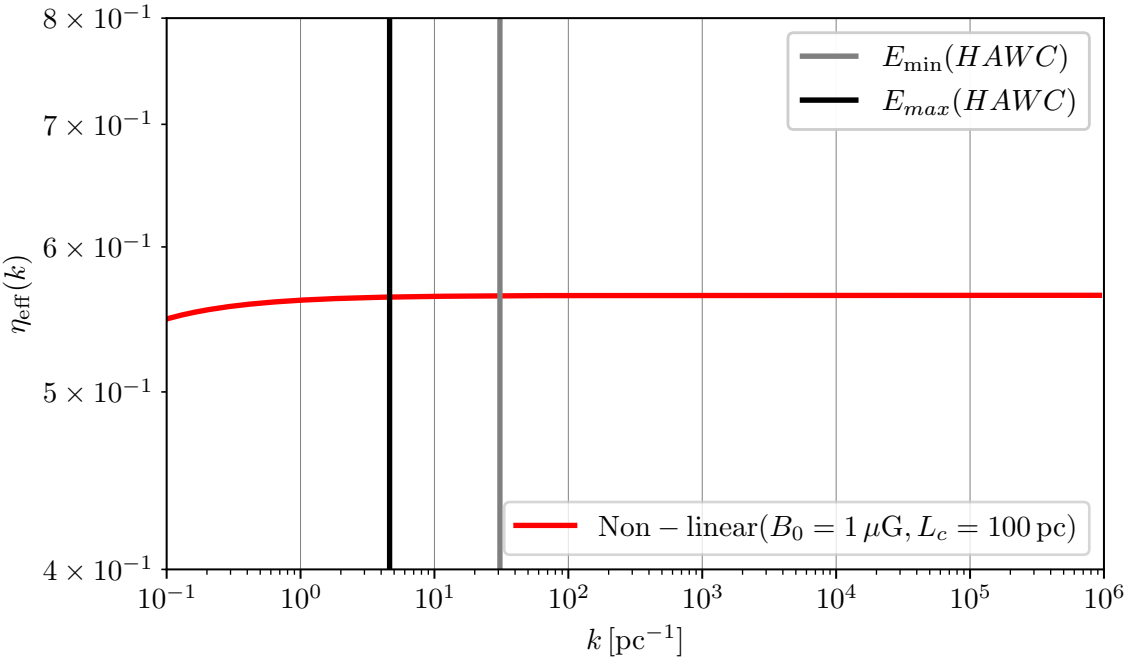

Figure 4.14: Effective turbulence level accumulated from smaller k for the non-linear simulation in flux tube approximation. Between the injection scale and the largest simulated scale (smallest k), a turbulence level of 0.55 is accumulated. Below the scale which is in resonance with the lowest HAWC energy, the effective turbulence level increases to 0.66. This indicates that the majority of the turbulence is accumulated at large scales which is unaffected by the non-linearity.

Since the turbulent magnetic field $\delta B(k) \propto W(k)k \propto k^{-2/3}$, the majority contribution to δB comes from scales above the simulation range reaching a turbulence level of $\eta = 0.55$. Only at scales below the minimum energy of HAWC measurements, the streaming instability raises $\eta_{\rm eff} = 0.66$. Combined with Fig. 4.13 this indicates, that neither L_c nor δB are significantly affected by the streaming instability. This means that the geometry of Geminga has to be explained by external effects.

4.5.6. Effects of Ion-Neutral Damping on the Turbulent Cascade

The test particle simulations discussed in Sec. 4.5.5 all rely on the assumption of a fully developed turbulent cascade. This can be either Kolmogorov or Kraichnan. However, as we have seen in Fig. 4.7, non-linear back-reactions of the particles on the magnetic field can lead to deviations from this uniform power law. While this effect is only relevant at energies below PeV due to the cutoff of the pulsar spectrum, we want to highlight that deviations from ideal MHD turbulence can also change the cascade. In particular the presence of neutrals within the Galactic disk has been used in the past to argue why turbulence might be absent in this region [36]. Here we want to point out, that ion-neutral damping is an energy dependent process, as shown in Fig. 1.5. Depending on the precise ionisation rate, the damping rate is $\Gamma_{\rm IN} \propto E^{-2}$ and hence becomes ineffective at high energies, corresponding to large scales. Since we expect turbulence to be injected at $1 - 100$ pc scales [97], at which the waves are in resonance with $1-100$ PeV particles for 1 μG magnetic fields, the initial cascade develops unaffected by the neutrals. To demonstrate this effect, we consider the cascade of Kolmogorov turbulence described by Eq. 4.41 with an additional injection term:

$$\frac{\partial W}{\partial t} = \left(\Gamma_{\rm CR}(f) - \Gamma_D(W)\right) W + \Gamma_D(W_{\rm BG}) W_{\rm BG} + \frac{\partial}{\partial k}\left[\kappa_{kk}(W)\frac{\partial W}{\partial k}\right] + Q_W(k)\,, \tag{4.41}$$

where $Q_W(k) = \delta(k - k_0)Q_{W,0}$. The injection normalisation is given by the condition, that 10 % of the total energy of a supernova remnant is converted into turbulence equally spread over a spherical region of radius 100 pc within 1 Myr. The injection scale is set to be $k_0 = 1\,\mathrm{pc}$. In identical fashion to Sec. 4.5.4, we again assume a background turbulence level that reproduces the diffusion coefficient obtained from hadronic cosmic ray ratios. We assume the minimum wavenumber to be $k_{\mathrm{min}} = 0.1\,\mathrm{pc}^{-1}$, which is within the expected range[97]. This background is necessary for computational reasons. We have investigated the turbulent power spectrum for the three phases of the interstellar medium with the largest filling factors, namely the HIM with 50 % and the WIM and WNM with 25 % each. The entire properties are provided in Tab. 1.1.

The resulting diffusion coefficient is shown in Fig. 4.15 as a function of energy. In the HIM ion neutral damping is ineffective due to the absence of neutrals and the cascade develops to large k (small scales and energies). After the injection ends at 1 Myr the turbulence decays while retaining a Kolmogorov like power spectrum. For the WIM we can see that the turbulence develops to a Kolmogorov like shape within the first 2 Myr and then decays. Curiously, the ion neutral damping prevents turbulence to cascade to small scales. Instead, the turbulence decays again while keeping the Kologorov-like shape. The trend observed in the WIM continues in the WNM, where the cascade cannot develop to $k > 100\,\mathrm{pc}^{-1}$, which corresponds to scales resonant with particles below 10 TeV. Hence, in the WNM we naturally expect a larger turbulence level at scales in resonance with particles which produce the TeV-halos while we do not expect a suppression at energies which are used to determine the diffusion coefficient from hadronic cosmic ray ratios. Additionally, in media with more neutrals the suppression of the diffusion coefficient lasts longer compared to the HIM. In combination, we would expect parts of the galactic disk filled with low diffusion zones. As we show in Sec. 5, this does not contrast current cosmic ray models. A common feature of this model is that the diffusion coefficient at energies above 10 TeV should be suppressed. This will lead to a more anisotropic Galactic γ-ray emission, which is a feature many models treating the injection of turbulence in the disk have [64].

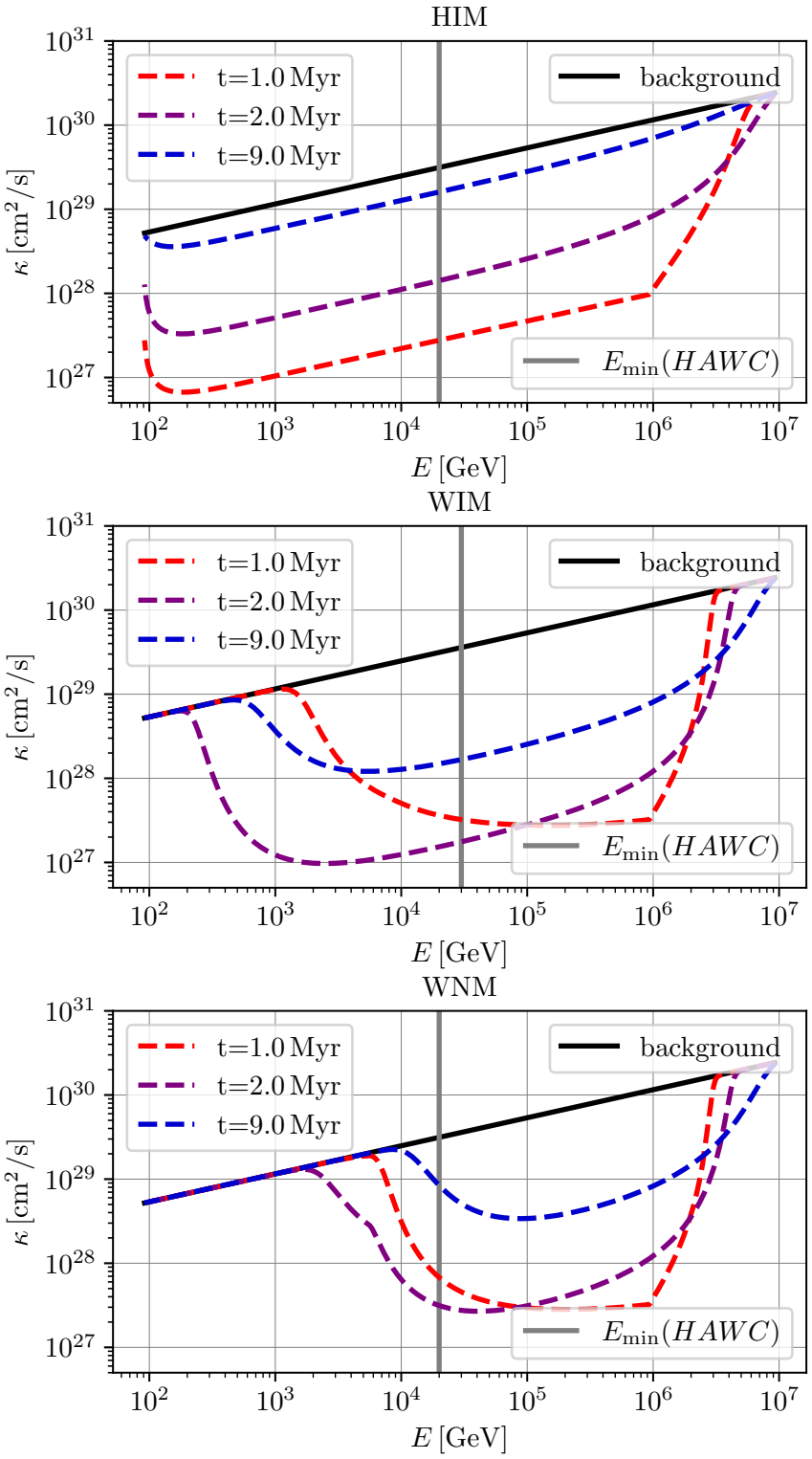

Figure 4.15: Diffusion coefficient κ as a function of resonant energy E, fulfilling $r_L(E) = 1/k$. Turbulence is injected at $k = 1\,\mathrm{pc}^{-1}$ upon a background given by the extrapolation from comic ray observations. The normalisation of the injection is given by the condition that 10 % of the total energy of a supernova remnant is converted into turbulence equally spread over a spherical region of radius 100 pc within 1 Myr. The level of turbulence obtained is two orders of magnitude larger than the background. In phases with more neutrals, turbulence is efficiently damped at small scales in resonance with low energies.

4.6. Explanations for the Asymmetry in LHAASO Observations

The LHAASO observation is rather curious, as the direction of motion of Geminga is roughly $\phi = 50\,^\circ$. In fact, if the energy loss time of particles $t_E \propto 1/E$ is large enough, the motion of the pulsar cannot be neglected anymore since $t_E v_S \geq d_{\mathrm{halo}}$. This will lead to anisotropic halos even in for perfectly isotropic diffusion models.

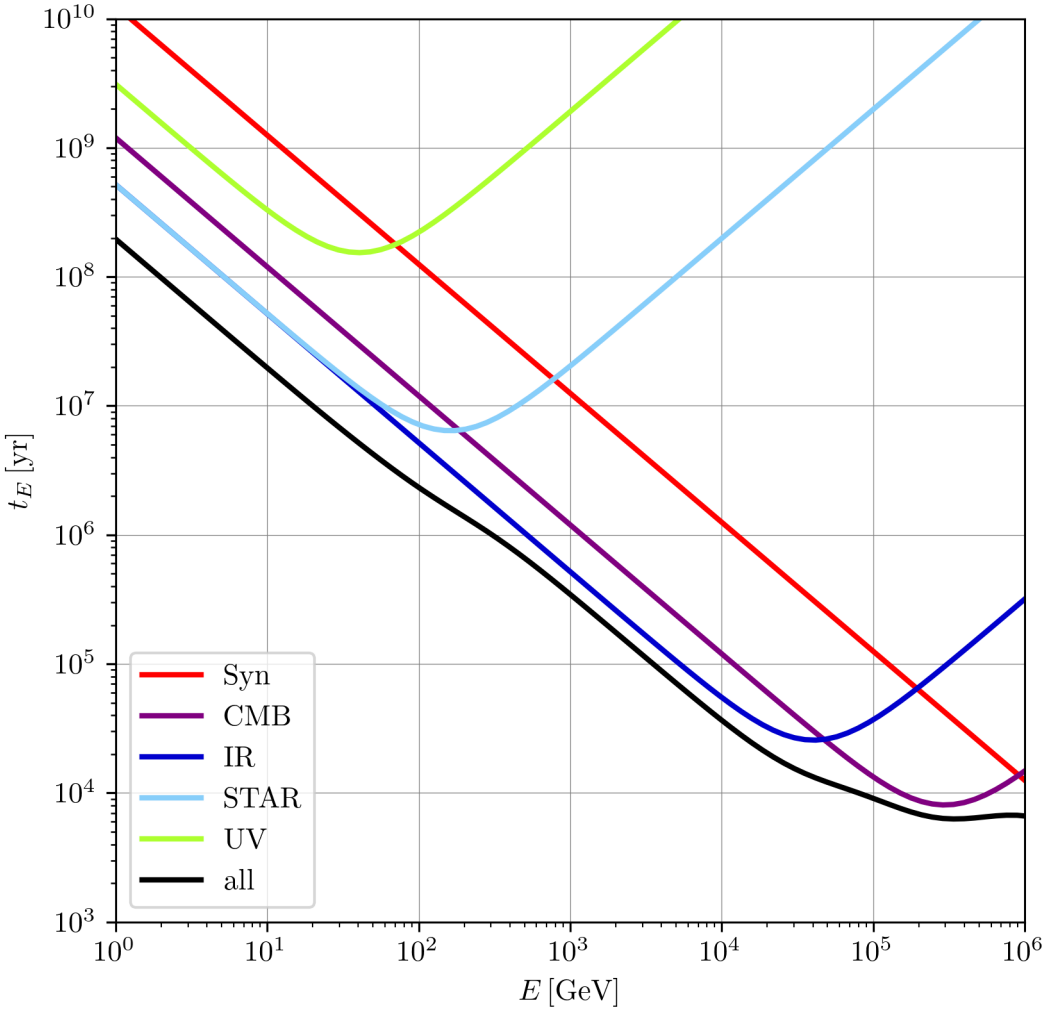

Figure 4.16: Energy loss time $t_E = E/(\mathrm{d}E/\mathrm{d}t)$ for inverse Compton scattering upon different background radiation fields and synchrotron losses as a function of energy. The combined energy loss time is given in black. At energies above a few 10 TeV the dominant loss process is scattering upon CMB photons, which is an irreducible background in the Galaxy. This leads to a minimum $t_E(100\,\mathrm{TeV}) = 10\,\mathrm{kyr}$.

The energy loss times for inverse Compton scattering upon the individual contributions of the photon field as well as the synchrotron losses are shown in Fig. 4.16 as a function of energy. At low energies a large variety of higher energy photon fields contribute, but for higher energies Klein-Nishina [122] corrections suppress the energy losses from high energy photons. Above several TeV, the only contributions come from infrared and Cosmic Microwave Background (CMB) photons. For a weaker magnetic field, the synchrotron loss time will increase, but the scattering upon CMB photons is unavoidable. This leads to an energy loss time of 30 kyr for 10 TeV particles and 10 kyr for 100 TeV

particles. Within this time the pulsar has moved $t_E v_S = 6 - 2\,\mathrm{pc}$ respectively, which corresponds to angles of $1.2 - 0.4\,^\circ$ for a distance to Geminga of 250 pc. The observed asymmetry in Fig. 4.4 is around $1 - 2\,^\circ$. Hence, it seems possible that the proper motion contributes at least partially to the asymmetry.

For a spindown timescale of $\tau_s = 12\,\mathrm{kyr}$, magnetic field $B_0 = 3\,\mu\mathrm{G}$, diffusion coefficient $\kappa(1\,\mathrm{GeV}) = 5 \cdot 10^{25}\,\mathrm{cm}^2/\mathrm{s}$ and total energy emitted into e^+, e^- $E_{\mathrm{tot}} = 7.5 \cdot 10^{46}\,\mathrm{erg}$, the surface brightness (SB) is given in the left of Fig. 4.17. The black dots indicate the measurements of LHAASO. The red line shows the result of the surface brightness in the direction of motion and the blue line indicates the average opposite to the direction of motion. At small angular distances, the solutions disagree due to the averaging procedure. As this area will be dominated by the PWN itself, which is not modelled here, we can safely ignore this. While this setup can reproduce the data in the direction of motion well, it underpredicts the data opposing the direction of motion. This demonstrates that the proper motion cannot be responsible for the observed asymmetry. In fact, this should be expected, since the majority of the contribution to the emission of 25 TeV and above γ-rays is produced by above 100 TeV e^+, e^-, as can be seen in Fig. 4.5. Then the motion of the pulsar within the energy loss time of these particles is at most $0.4\,^\circ$, which is well below the $2\,^\circ$ asymmetry observed by LHAASO. However, artificially increasing v_S by a factor of ten and also increasing $E_{\mathrm{tot}} = 1 \cdot 10^{47}\,\mathrm{erg}$ allows reproducing the measurements of LHAASO, as shown in the fight of Fig. 4.17. Since the proper motion of Geminga is accurately known [33], these parameters are unphysical. Instead, they highlight that especially at lower energies, where t_E is larger, we indeed expect an asymmetry. For GeV energies this was investigated by Di Mauro et al. [52].

Now, that we have shown that the proper motion cannot produce the asymmetry observed by LHAASO, we need an alternative explanation. The LHAASO collaboration suggested a scenario, where Geminga is within its origin supernova remnant of size 92 pc chasing the termination shock, following the model of Fang et al. [71]. Within the supernova remnant the diffusion coefficient is assumed to be $\kappa(100\,\mathrm{TeV}) = 1.7 \cdot 10^{28}\,\mathrm{cm}^2/\mathrm{s}$ and outside $\kappa(100\,\mathrm{TeV}) = 2.9 \cdot 10^{30}\,\mathrm{cm}^2/\mathrm{s}$. A model depiction of this scenario can be seen in the top panel of Fig. 4.18 which is taken from Fang et al. [71]. The grey region is the supernova remnant with the darker region indicating where most turbulence is located. The position of Geminga is marked by a blue square and the surrounding halo is indicated in pink. The proper motion is indicated with a blue arrow. For this setup, the resulting surface brightness is shown in the bottom panel of Fig. 4.18 and can explain the asymmetry. However, this scenario is highly fine-tuned, as it requires a very specific position of the pulsar. Instead, an asymmetry is expected to occur due to asymmetric diffusion, as is elaborated in Sec. 4.5.4. It also needs to be stressed, that the data we have analysed here are preliminary and highly surprising, since HAWC should have been able to detect similar features. This is also the reason we have decided here not to do a finer parameter study and show the residuals. In conclusion, if the detected asymmetry by LHAASO is confirmed in further investigations it cannot be explained by the proper motion of the pulsar alone. Fine-tuned models with a supernova remnant are able to explain the results, but it is far more natural to consider anisotropic diffusion.

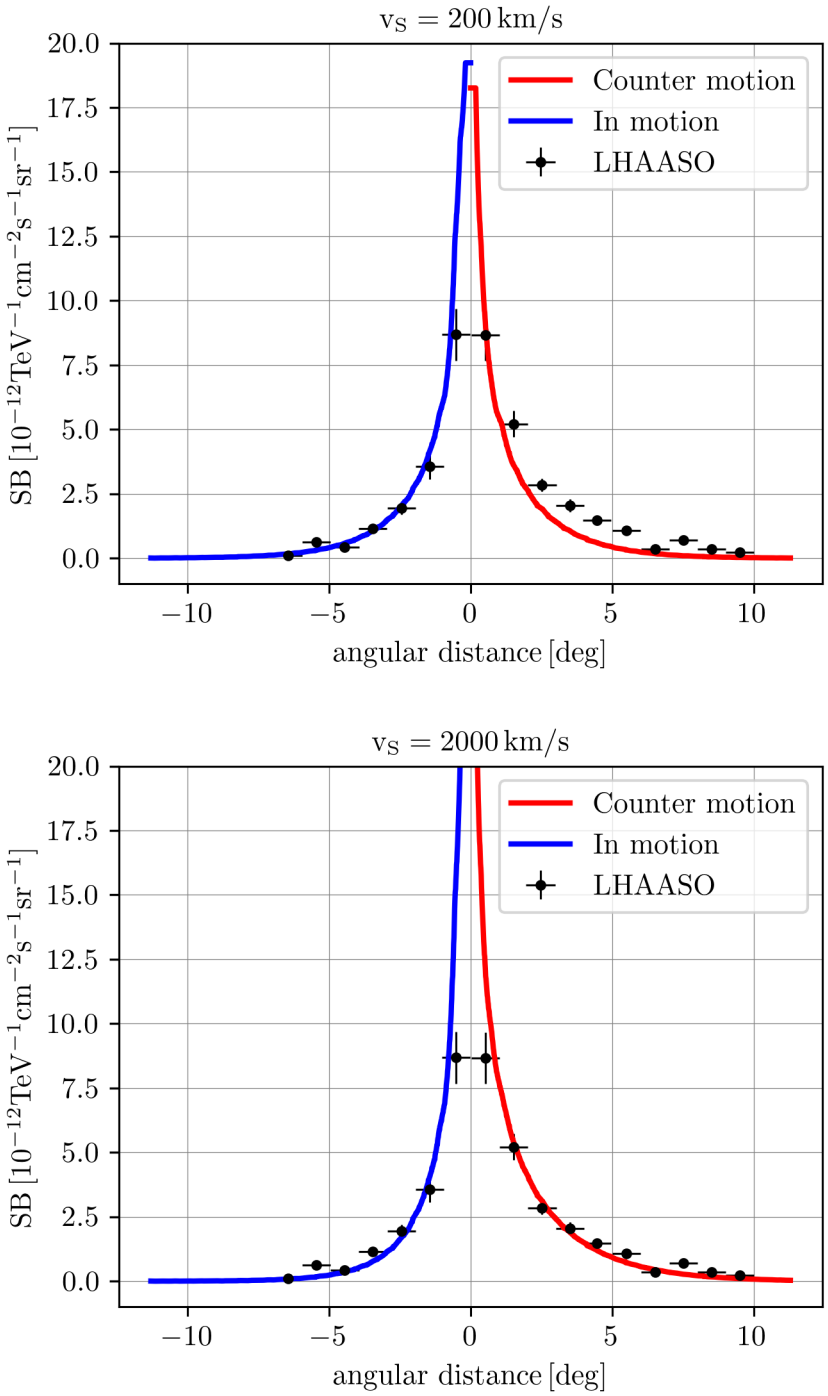

Figure 4.17: Surface brightness of Geminga as a function of angular distance. The black dots indicate the measurements by LHAASO. The red line indicates the average over the half circle in the direction of motion of the pulsar and the blue line in the opposing direction. Top: The proper velocity of the pulsar is $v_S = 200\,\mathrm{km/s}$ and all other parameters are given in the text. With this v_S the observed asymmetry cannot be reproduced by proper motion alone. Bottom: The same parameters as in the text, but increased the proper motion by a factor of 10 to $v_S = 2000\,\mathrm{km/s}$ and increased the total emitted energy to $1 \cdot 10^{47}$ erg. In this unrealistic case the asymmetry could be explained by the proper motion alone.

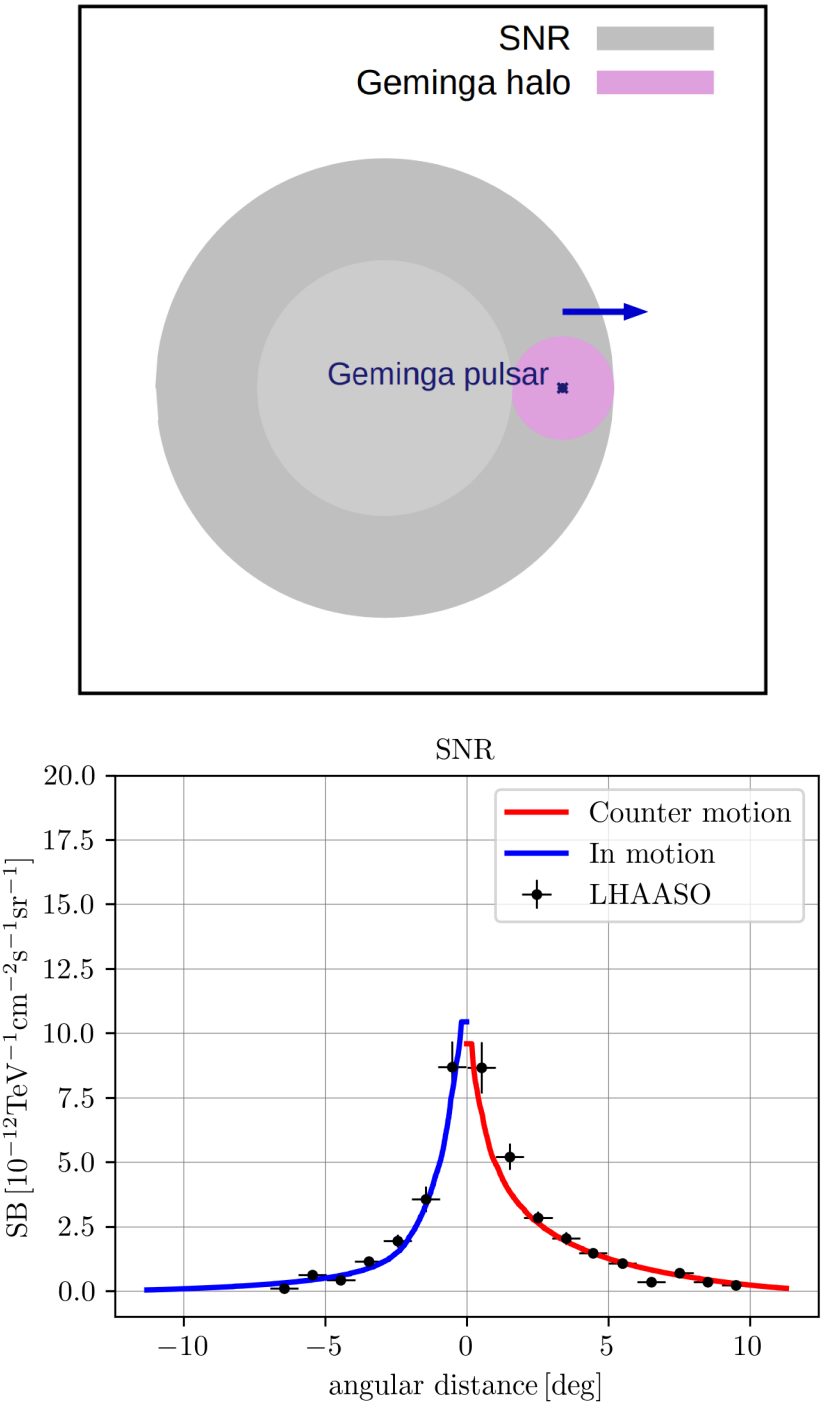

Figure 4.18: Top: Schematic setup of Geminga within a parent supernova remnant from [71]. The supernova is marked in grey with the darker shell indicating a region of increased turbulence. The position of Geminga is marked in blue in the centre of the pink TeV-halo and the direction of motion is indicated with a blue arrow. Bottom: Surface brightness of Geminga as a function of angular distance for the setup in the top figure. The black dots indicate the measurements by LHAASO. The red line indicates the average over the half circle in the direction of motion of the pulsar and the blue line in the opposing direction. This setup, even though its existence is unlikely, can explain the observed values.

5. Impact of Low Diffusion Zones on Galactic Cosmic Ray Propagation

Unlike assumed in the standard paradigm models of cosmic ray transport in the Galaxy (see eg. Sec. 1.4.1), the conditions in the Galaxy are far from homogeneous. In fact, as was shown in Sec. 3 and Sec. 4, there are a large variety of cosmic ray sources in the disk around which the diffusion coefficient is lower than the galactic average by up to three orders of magnitude. An edge-on sketch of the Galaxy in such a scenario is shown in Fig. 5.1 where zones of low diffusion coefficient κ_{low} are randomly distributed within the disk and surrounded by a high diffusion coefficient κ_{high}.

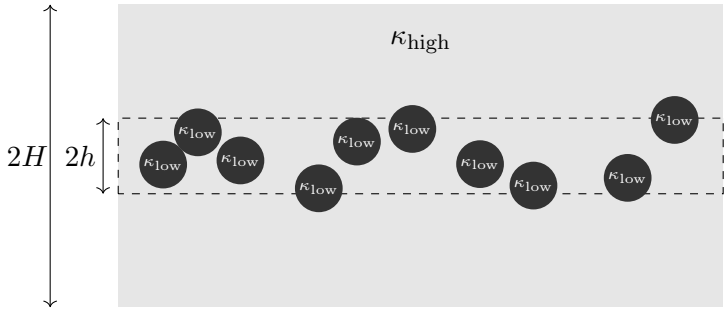

Figure 5.1: Edge-on sketch of the Galaxy with a halo of height H and disk of height h. Zones of low diffusion with κ_{low} are assumed to be distributed randomly within the disk. These zones are surrounded by a high diffusion coefficient κ_{high}.

Whether these zones have an impact on the overall transport parameters has been investigated previously [142, 177]. Low diffusion zones are produced with rate $\mathcal{R}_{\text{bubble}}$ and last for τ_{bubble}, then at any given time $N_{\text{bubbles}} = \mathcal{R}_{\text{bubble}}\tau_{\text{bubble}}$ exist. Each one is assumed to be spherical with radius R_{bubble} and volume V_{bubble}. Then the resulting filling fraction is given by:

$$f \equiv \frac{N_{\text{bubbles}} V_{\text{bubble}}}{V_{\text{disk}}} = \frac{4}{3} \frac{\mathcal{R}_{\text{bubble}} \tau_{\text{bubble}} R_{\text{bubble}}^3}{R_{\text{disk}}^2 h}. \tag{5.1}$$

In case this value is significantly smaller than one, it was neglected in previous works [142, 177].

However, whether this is justified depends on the resulting global averaged diffusion coefficient. How to calculate this average is not a priory clear. Since the residence time in the low diffusion regions is increased, it will not be an arithmetic mean, but since particles can travel around the zones of low diffusion it will not be the harmonic mean either. Jóhannesson et al. [113] tried to estimate the average by adding the propagation times τ. In one dimension particles injected in the centre of a low diffusion zone with κ_l and size z_l embedded in a zone with high diffusion κ_h and size z_h will spend a total time given by

$$\tau \approx \frac{z_l^2}{\kappa_l} + \frac{z_h^2}{\kappa_h} \approx + \frac{z_h^2}{\kappa_{\text{avg}}} \tag{5.2}$$

in both zones. Solved for $\kappa_{\text{avg.}}$ this gives:

$$\kappa_{\text{avg.}} \approx \kappa_h \left[1 + \left(\frac{z_l}{z_h} \right)^2 \frac{\kappa_h}{\kappa_l} \right]^{-1}. \tag{5.3}$$

They embed this into a model of galactic cosmic ray transport, assuming the density of low diffusion zones scales with the source density. Then they compare their model results to cosmic ray data as

listed in their table 1 and conclude that the low diffusion zones have negligible impact on galactic propagation.

Here we will show that they underestimate the average diffusion coefficient and follow our paper Jacobs et al. [109]. Cosmic rays cross the halo many times. Each time a particle enters the disk it has a chance of travelling around the low diffusion zones, which is possible because the zones do not fill the entire disk. This is not accounted for in the 1D simplified approach of Jóhannesson et al. [113]. How to do this accurately will be discussed in Sec. 5.6.

Furthermore, cosmic ray clocks like the $^{10}\mathrm{Be}/^{9}\mathrm{Be}$ ratio do not only break the degeneracy between halo height and diffusion coefficient as shown in Sec. 1.4.1, but also constrain the diffusion coefficient close to the disk, as shown in Sec. 5.3. Hence, they constrain the properties of low diffusion zones, as shown in Sec. 5.5.

5.1. Two-Zone Halo Model

An analytic solution of the galactic transport equation accounting for individual low diffusion zones and in 3D is not feasible. Traditional finite difference methods can in principle solve the transport equation in this case. However, the large dynamic range required to resolve the gradient of the diffusion coefficient at the edge of the bubble and the entire Galaxy makes them unfeasible with modern computing resources. Therefore, a coarse-grained approach is used. Since all potential sources and all observations of low diffusion zones are located within the galactic disk, two distinct zones can be distinguished. The first is the galactic halo of height H, where the average diffusion coefficient κ_{halo} is given by the value around the low diffusion zones κ_{high}. The second is the galactic disk of height h, where the zones of low diffusion coefficient κ_{low} are surrounded by high diffusion regions, which has a coarse grained diffusion efficient of κ_{disk}. This two zone setup is shown in Fig. 5.2.

Figure 5.2: Edge-on sketch of the Galaxy with a halo of height H and disk of height h. Within the halo, the average diffusion coefficient is $\kappa_{\mathrm{halo}} = \kappa_{\mathrm{high}}$ and in the disk, the diffusion coefficient κ_{disk} is given by an average which can be obtained as explained in Sec. 5.6.

In this case the problem can be reduced to one dimension as described in Sec. 1.4.1. The connection between the filling fraction of the low diffusion zones f, the ratio of $\kappa_{\mathrm{low}}/\kappa_{\mathrm{high}}$ and the averaged diffusion coefficient κ_{disk} will be provided in Sec. 5.6. For the galactic transport model, the suppression will be modelled by the scaling factor

$$\kappa_{\mathrm{disk}} = \alpha \kappa_{\mathrm{halo}} \tag{5.4}$$

. The rigidity dependence of the diffusion coefficient is given by a broken power law with two spectral breaks, one at low rigidities ([212]) and one around 300 GV [66]. The latter one is believed to originate from the transition from turbulence injected at large scales and cascading down (see. Sec. 1.5.1) to

turbulence produced via the streaming instability of cosmic rays escaping the disk [66]. The functional form is given by:

$$\kappa(z,\mathcal{R}) = \beta\left(1+\left(\frac{\mathcal{R}}{\mathcal{R}_l}\right)^{-\frac{1}{s_l}}\right)^{s_l(\delta-\delta_l)}\left(\frac{\mathcal{R}}{10\,\mathrm{GV}}\right)^{\delta}\left(1+\left(\frac{\mathcal{R}}{\mathcal{R}_h}\right)^{\frac{1}{s_h}}\right)^{s_h(\delta_h-\delta)}\times\begin{cases}\kappa_{\mathrm{disk}} & z\leq h\ ,\\ \kappa_{\mathrm{halo}} & z>h\ .\end{cases} \tag{5.5}$$

The break parameters at high energies can be determined from primary nuclei [66]: $s_h = 0.5$, $\delta_h = 0.34$, $\mathcal{R}_h = 312\,\mathrm{GV}$ under the assumption that the source spectrum is a pure power law. Since the impact of the softness on the low energy break is small, as shown by [216] it is fixed to $s_l = 0.04$. All other parameters remain as free parameters.

In order to calculate ratios of secondary particles the entire decay and spallation chain starting from some purely primary particles needs to be solved. Here, we use the injection normalisations given by Evoli et al. [67], which extend up to Fe. Then the equation describing the transport of cosmic ray hadrons of species j is given by [19] (see also Eq. 1.48):

$$\frac{\partial}{\partial z}\left(v\psi_j-\kappa(z,\mathcal{R})\frac{\partial\psi_j}{\partial z}\right)+\frac{\partial}{\partial p}\left[\left(\frac{\mathrm{d}p}{\mathrm{d}t}\right)\psi_j-\frac{p}{3}\frac{\mathrm{d}v}{\mathrm{d}z}\psi_j\right]+\frac{1}{\gamma\tau_j}\psi_j+2h\delta(z)\beta cn_{\mathrm{gas}}\sigma_j\psi_j=Q_j(p)\,, \tag{5.6}$$

where ψ_j is the density differential in momentum of cosmic rays of species j. The terms on the left-hand side describe advection, diffusion, (adiabatic) energy losses, decay with boosted decay time $\gamma\tau_j$, and spallation of cosmic rays. The spatial extent of the gas (and hence the energy losses and spallation reactions) is neglected as well as the source distribution, because the vertical extent of the halo is small compared to the disk. However, this is insufficient for the diffusion coefficient since a delta like change in the diffusion coefficient does not affect the solution. The advection speed is directed outwards of the disk $v(z) = \mathrm{sgn}(z)v_c$, leading to $\mathrm{d}v/\mathrm{d}z = 2v_c\delta(z)$ and remains a free parameter in this model. Energy losses for hadrons are completely dominated by hadronic interactions with the background gas, hence the simplification of them occurring in the disk only. Here, only the most important one is accounted for: ionisation loss on the neutral gas

$$\left(\frac{\mathrm{d}p}{\mathrm{d}t}\right)_{j,\mathrm{ion}}=2h\dot{p}_j\delta(z)\,, \tag{5.7}$$

where the formula for $\dot{p}_j$ is given by Mannheim and Schlickeiser [143] and a typo was corrected as explained in Sec. 1.4.2. The right-hand side of Eq. 5.6 contains the source term $Q_j(p)$, which has three parts:

$$Q_j(p)=2h\delta(z)Q_{\mathrm{prim},j}(p)+\sum_{k>j}\frac{\psi_k}{\gamma\tau_{k\to j}}+2h\delta(z)\beta cn_{\mathrm{gas}}\sum_{k>j}\sigma_{k\to j}\psi_k\,. \tag{5.8}$$

The first one describes the injection of primary particles by cosmic ray sources, where the injection mechanism is believed to be diffusive shock acceleration, as explained in Sec. 1.3.4. Due to nonlinear back-reactions, the source spectral index is assumed to be −2.3 [67]. Production by the decay of heavier particles is described in the second term of Eq. 5.8. Furthermore, the last term accounts for the production of secondaries by spallation upon the interstellar gas confined in the disk. The cross-sections for this process are difficult to measure and are currently suffering from large statistical and systematic uncertainties. However, they have a large impact especially on the Beryllium ratio, as we will discuss in detail in Sec. 5.8. For now, we chose the parameterisation provided by Evoli et al. [67]. Then Eq. 5.6 is solved using the following steps:

1. The transport equation is solved in the halo ($h < |z| < H$) with the boundary condition $\psi(H) = 0$.
2. We solve the equation in the disk ($0 \leq z \leq h$) and demand that both the density ψ and its spatial flux be conserved at $|z| = h$.
3. We integrate the transport equation over an infinite volume around $z = 0$ to account for the infinitely thin source distribution there.

In the following we will denote all properties in the halo with an o for outer and in the disk with i for inner.
Starting at (1), the transport equation at $z > 0$ reads:

$$\frac{\partial}{\partial z}\left(v_c\psi_j - \kappa_o\frac{\partial\psi_j}{\partial z}\right) + \frac{1}{\gamma\tau_j}\psi_j = 0\,, \qquad |z| > h, \tag{5.9}$$

$$\frac{\partial}{\partial z}\left(v_c\psi_j - \kappa_i\frac{\partial\psi_j}{\partial z}\right) + \frac{1}{\gamma\tau_j}\psi_j = 0\,, \qquad 0 < |z| < h, \tag{5.10}$$

where we have neglected the decay into species j.
Now we make the ansatz $\psi_j = C\exp(\lambda z)$ and introduce the decay rate $\Gamma_j = \left(\gamma\tau_j\right)^{-1}$. If we substitute this into Eq. 5.9 it results in:

$$\psi_j = \exp\left(\frac{zv_c}{2\kappa_o}\right)\left(A_o\exp\left(\frac{z}{\tilde{z}_o}\right) + B_o\exp\left(-\frac{z}{\tilde{z}_o}\right)\right) \quad \text{with} \quad \frac{1}{\tilde{z}_o} = \sqrt{\left(\frac{v_c}{2\kappa_o}\right)^2 + \frac{\Gamma}{\kappa_o}}. \tag{5.11}$$

Using the boundary condition $\psi(z = H) = 0$ gives:

$$A_o = -B_o\exp\left(-\frac{2H}{\tilde{z}_o}\right). \tag{5.12}$$

Now we can move to step (2). The solution for Eq. 5.10 can be written in a manner analogous to Eq. 5.9 as:

$$\psi_j = \exp\left(\frac{zv_c}{2\kappa_i}\right)\left(A_i\exp\left(\frac{z}{\tilde{z}_i}\right) + B_i\exp\left(-\frac{z}{\tilde{z}_i}\right)\right) \quad \text{with} \quad \frac{1}{\tilde{z}_i} = \sqrt{\left(\frac{v_c}{2\kappa_i}\right)^2 + \frac{\Gamma}{\kappa_i}}. \tag{5.13}$$

Now we match the solutions at $z = h$:

$$\lim_{\epsilon\to 0}\left[\psi_j(h+\epsilon) - \psi_j(h-\epsilon)\right] = 0 \tag{5.14}$$

resulting in:

$$\begin{aligned} & B_o\left[-\exp\left(\frac{h-2H}{\tilde{z}_o}\right) + \exp\left(-\frac{h}{\tilde{z}_o}\right)\right]\exp\left(\frac{hv_c}{2\kappa_o}\right) = \left[A_i\exp\left(\frac{h}{\tilde{z}_i}\right) + B_i\exp\left(-\frac{h}{\tilde{z}_i}\right)\right]\exp\left(\frac{hv_c}{2\kappa_i}\right) \\ \Rightarrow \quad & B_o = \frac{A_i\exp\left(\frac{h}{\tilde{z}_i}\right) + B_i\exp\left(-\frac{h}{\tilde{z}_i}\right)}{-\exp\left(\frac{h-2H}{\tilde{z}_o}\right) + \exp\left(-\frac{h}{\tilde{z}_o}\right)}\exp\left(\frac{hv_c}{2\kappa_i} - \frac{hv_c}{2\kappa_o}\right). \end{aligned} \tag{5.15}$$

If we use the conservation of the flux we get:

$$\lim_{\epsilon\to 0}\left[\left(v_c\psi_j(h+\epsilon) - \kappa_o\left.\frac{\partial\psi_j}{\partial z}\right|_{h+\epsilon}\right) - \left(v_c\psi_j(h-\epsilon) - \kappa_i\left.\frac{\partial\psi_j}{\partial z}\right|_{h-\epsilon}\right)\right] = 0, \tag{5.16}$$

which can be solved for B_o:

$$B_o = \frac{\exp\left(\frac{hv_c}{2\kappa_i} - \frac{hv}{2\kappa_o}\right)\left[\left(\frac{\kappa_i}{\tilde{z}_i} + \frac{v_c}{2}\right)\exp\left(\frac{h}{\tilde{z}_i}\right)A_i + \left(\frac{v_c}{2} - \frac{\kappa_i}{\tilde{z}_i}\right)\exp\left(-\frac{h}{\tilde{z}_i}\right)B_i\right]}{\frac{v_c}{2}\left[\exp\left(-\frac{h}{\tilde{z}_o}\right) - \exp\left(\frac{h-2H}{\tilde{z}_o}\right)\right] - \frac{\kappa_o}{\tilde{z}_o}\left[\exp\left(\frac{h-2H}{\tilde{z}_o}\right) + \exp\left(-\frac{h}{\tilde{z}_o}\right)\right]}. \tag{5.17}$$

If we now eliminate B_o and express A_i in terms of B_i:

$$A_i = -B_i\exp\left(-\frac{2h}{\tilde{z}_i}\right)\left(\frac{2\frac{\kappa_i}{\tilde{z}_i}}{\frac{\kappa_o}{\tilde{z}_o}\tanh^{-1}\left(\frac{h-H}{\tilde{z}_o}\right) - \frac{\kappa_i}{\tilde{z}_i}} + 1\right) \equiv B_i\frac{\gamma_2}{\gamma_1}. \tag{5.18}$$

In order to find B_i we need move to step (3) and integrate Eq. 5.6 over an infinite volume around $z = 0$.
Denoting $\psi_j(z = 0) \equiv \psi_{j,0}$, this gives:

$$\begin{aligned} 2v_c\psi_{j,0} - \kappa_i \left.\frac{\partial}{\partial z}\psi_j\right|_{0-}^{0+} + 2h\beta c n_{\rm gas}\sigma_j\psi_{j,0} + \frac{\partial}{\partial p}\left(2h\dot{p} - \frac{p}{3}\frac{\mathrm{d}v_c}{\mathrm{d}z}\right)\psi_{j,0} \\ = 2hQ_{\rm prim,j}(p) + 2h\beta c n_{\rm gas}\sum_{k>j}\sigma_{k\to j}\psi_k, \end{aligned} \tag{5.19}$$

where the derivative can be computed for the solution for $z > 0$ and the advection velocity is changing sign at the disk.
Then the above equation reads:

$$\begin{aligned} 2v_c\psi_{j,0} - 2\kappa_i \left.\frac{\partial}{\partial z}\psi_j\right|_{0} + 2h\beta c n_{\rm gas}\sigma_j\psi_{j,0} + \frac{\partial}{\partial p}\left(2h\dot{p} - \frac{2pv_c}{3}\right)\psi_{j,0} \\ = 2hQ_{\rm prim,j}(p) + 2h\beta c n_{\rm gas}\sum_{k>j}\sigma_{k\to j}\psi_k, \end{aligned} \tag{5.20}$$

Now we use this equation to calculate B_i. The differential equation that has to be solved is:

$$\begin{aligned} \left[\left(2v_c + 2h\beta c n_{\rm gas}\sigma_j\right)\left(\frac{\gamma_2}{\gamma_1}+1\right) - 2\gamma_i\left(\frac{\gamma_2}{\gamma_1}-1\right) + \frac{\partial}{\partial p}\left(2h\dot{p} - \frac{2pv_c}{3}\right)\left(\frac{\gamma_2}{\gamma_1}+1\right)\right]B_i \\ = 2hQ_{\rm prim,j}(p) + 2h\beta c n_{\rm gas}\sum_{k>j}\sigma_{k\to j}\psi_k, \end{aligned} \tag{5.21}$$

This is done numerically using Scipy's `solve_ivp` function [211].

At low energies the fluxes obtained in this way are altered by solar modulation. Magnetic fields and outgoing winds produced by the sun screen out these particles. In principle, this is a complicated, time-dependent process that depends on a variety of variables. All experiments within the solar system are affected, most notably AMS-02, DAMPE, PAMELA, and CALET. The only direct probes outside the Heliosphere are Voyager 1&2, which entered the local interstellar space (LIS) in 2012 [94]. Instead of employing a full model, here the force field approximation by Gleeson and Axford [91] is used. The modulation potential Φ will vary with time due to different solar activity, so for every measurement, this parameter should be fitted independently. However, this would introduce a large number of additional parameters, because especially for the Beryllium ratios we use a large amount of data measured for more than 50 yr. Instead, here we determine $\Phi = 700\,\mathrm{MeV}$ by fitting to AMS-02 Oxygen data [11]. This will lead to a worse fit than possible in principle, but is necessary to gain any additional information from individual Beryllium ratio measurements.

Overall, the seven free parameters of this model are the five unfixed parameters in the diffusion coefficient, the advection velocity and the halo height. The size of the disk and the gas density are well constrained by observations, here we adopt $h = 100\,\mathrm{pc}$ and $n_{\rm gas} = 1\,\mathrm{cm}^{-3}$ similar to the values from Ferrière [76], Phan et al. [172].

5.2. Data Used

The fluxes obtained by the method explained in the previous section are then used to calculate the B/C ratio, where we make the same assumption for the composition as AMS-02, who assume an isotopic composition of pure ^{12}C as well as a mixture of ^{10}B and ^{11}B [9]. These fluxes are then fitted to recent Voyager 1 data in the LIS [44] and to AMS-02 data [9], in the Heliosphere.

For high energies, the fluxes of stable particles depend on the harmonic average of the diffusion coefficients

$$\begin{aligned} &\psi = \psi\left(w(H, h, \kappa_{\rm disk}, \kappa_{\rm halo})\right) \text{ with} \\ &w(H, h, \kappa_{\rm disk}, \kappa_{\rm halo}) = \frac{H-h}{\kappa_{\rm halo}} + \frac{h}{\kappa_{\rm disk}}, \end{aligned} \tag{5.22}$$

which can be shown to be true in the high energy limit. Therefore, also the B/C ratio has this dependence. High energy electron data indicates that the average diffusion coefficient cannot be suppressed by orders of magnitude in the disk at energies below tens of TeV [102, 177]. Hence, changes in the B/C ratio have to be rather small. Additionally, changes in h/κ_{disk} and H/κ_{halo} are degenerate. In order to break this degeneracy a cosmic ray clock is needed, identically to the one zone model given in Sec. 1.4.1. Here, we chose ^{10}Be/^{9}Be since these elements have similar progenitors and the half lifetime of ^{10}Be is close to the propagation time in the Galaxy. Additionally, the ratio can constrain a suppressed diffusion coefficient close to the disk as shown in the following section.

At energies below $E_{\mathrm{kin}} \approx 1\,\mathrm{GeV/n}$ plenty of data for the Beryllium ratio is available in Connell [40], Garcia-Munoz et al. [82, 83], Lukasiak et al. [138], Lukasiak [139], Nozzoli and Cernetti [158], Wiedenbeck and Greiner [217], Yanasak et al. [219], but no published data is available at higher energies. Here, we use preliminary AMS-02 data [111], which extends up to 10 GeV/n, and also forecast the impact of the first two measurement cycles of HELIX [167] by fitting to mock data. These are generated by taking the parameters of the best fit to all other datasets and generating data points at the energy given in Park et al. [167] with a normal distribution whose mean is given by the model prediction and with a standard deviation given by the error in Park et al. [167].

5.3. Impact of Low Diffusion in the Disk on the Be Ratio

To illustrate some basic features of the Beryllium ratio it is useful to consider the expected behaviour of the one zone model again, which in the leaky box approximation (Eq. 1.3) can be rewritten in terms of characteristic timescales as:

$$\frac{N_{^{10}Be}}{N_{^{9}Be}} = \frac{\sigma_{\mathrm{prim.}\rightarrow{}^{10}Be}}{\sigma_{\mathrm{prim.}\rightarrow{}^{9}Be}} \frac{\frac{1}{\frac{1}{\tau_{\mathrm{in}}}+\frac{1}{\tau_{\mathrm{esc}}}}}{\frac{1}{\tau_{\mathrm{in}}}+\frac{1}{\gamma\tau_{\mathrm{dec}}}+\frac{1}{\tau_{\mathrm{esc}}}}, \tag{5.23}$$

where the inelastic collision timescale is given by $\tau_{\mathrm{in}} = 1/(v n_{\mathrm{gas}} \sigma_{\mathrm{inel}})$, the escape time is $\tau_{\mathrm{esc}} = H^2/\kappa$ and the decay time is τ_{dec}.

At high energies time dilatation causes the ^{10}Be to be practically stable. Then the second term in the denominator is negligible. Additionally, the escape time falls below the inelastic scattering time. Hence, the fraction cancels out, and the high energy limit is solely determined by the production spallation cross-sections [145]. Therefore, the uncertainties in the spallation cross-sections are directly reflected in the ratio [67, 145].

The low energy limit is given by a complex interplay of the diffusion coefficients and the halo height. Due to the non-negligible decay time of ^{10}Be and its production in the disk, the leaky box model is not valid at lower energies. To investigate the effects we show both the B/C and ^{10}Be/^{9}Be ratios in Fig. 5.3 and vary the parameters indicated in the individual title by a factor of two around the default solution. A larger κ_{disk}, corresponding to a larger α, leads to a faster escape of freshly spallated ^{10}Be from the disk, hence reducing the ratio at low energies. In case the diffusion coefficient is reduced more particles are measured.

Similarly, a larger κ_{halo} leads to faster diffusion of particles away from the disk and thereby also reduces the ratio and vice versa. An increase in halo height causes the particles to spend more time in the halo before entering the disk again and thereby leads to a smaller ^{10}Be/^{9}Be ratio. Inversely, for a smaller halo height the ratio is increased.

The transition between the high and low energy limit depends mainly on the properties in the halo. A larger halo increases the escape timescale quadratically, causing the transition to the high energy limit to be at higher energies. A lower diffusion coefficient reduces the timescale only linearly, leading to a transition at higher energies. The diffusion coefficient in the disk is mostly relevant at low energies,

before the particles initially escape the disk, and therefore it has less impact on the transition compared to the one in the halo.

The ratio of H/κ_{halo} is fixed by B/C data. An increase or decrease of both H and κ_{halo} would shift the transition unevenly due to the quadratic and linear dependence. This can be seen when comparing the second and third row of the right column of Fig. 5.3. Hence, this breaks the degeneracy from B/C visible in the left column. Additionally, κ_{disk} shifts the Beryllium ratio up and down at low energies and is therefore also degenerate with the other two parameters.

Even though we have made extensive use of the leaky box approximation above to illustrate the general behaviour, it is important to note that the leaky box model does not precisely hold for unstable isotopes. The reason is that the propagation volume for these particles is not the entire halo, as expected when integrating over the entire volume when deriving the equation, but only a smaller region given by the diffusion loss length $\sqrt{\tau_{\text{dec}}\kappa}$ [61].

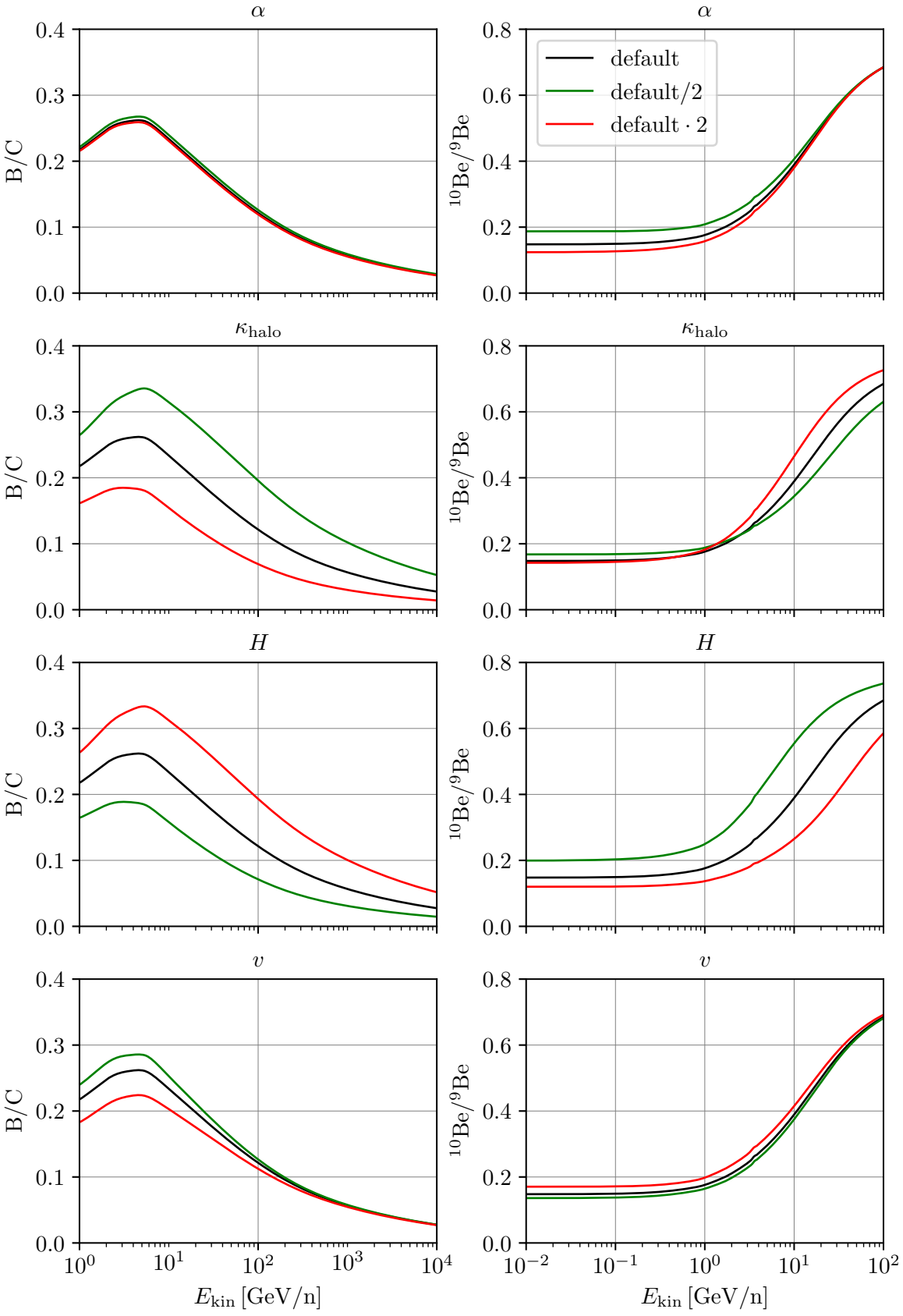

Figure 5.3: B/C and ^{10}Be/^{9}Be as function of kinetic energy. The black line marks the solution for our fiducial set of parameters called "default" and the red and green lines indicate the changes when the parameter given in the individual titles is changed up and down by a factor of two. The top panel in the left column indicates that κ_{disk} has little impact on the B/C ratio and the second and third panels show the degeneracy between H and κ_{halo}. In contrast, the top right panel indicates that the Be-ratio at low energies is sensitive to κ_{disk}. The second and third panels indicate that the degeneracy between H and κ_{halo} is broken.

5.4. Statistical Methods and Models

One of the main aims of this investigation is to show if there is a preference for suppressed diffusion in the disk. This requires us to compare the model with suppression to the one without, the null hypothesis in this study. Additionally, we want to sample the posterior distribution of the individual parameters.

In order to determine the best fit parameters and their posterior we perform a Markov Chain Monte Carlo (MCMC) study with the `emcee` package [78]. We adopt a Gaussian likelihood,

$$-2\ln\left(\mathcal{L}(\theta)\right) = \chi^2(\theta) = \sum_{d,i}\left(\frac{O_{d,i} - O_{d,i}^{(m)}(\theta)}{\sigma_{d,i}}\right)^2, \tag{5.24}$$

where d runs over the observables B/C and ^{10}Be/^{9}Be and i runs over rigidities $\mathcal{R}_i$ for B/C AMS-02 data or kinetic energies $E_{\mathrm{kin},i}$. The errors σ are the systematic and statistical uncertainties summed in quadrature. We have refrained from considering correlated errors (see e.g. Derome et al. [51]), since no official publications exist. Additionally, we expect their impact to be less important for phenomena stretching over larger ranges in rigidity, compared to excesses well localised in rigidity [29]. The priors are chosen uniformly as listed in Tab. 5.1. Then it is straightforward to obtain the posteriors, however, a model comparison in this context is not. Bayesian model comparison requires the evidence - that is the posterior integrated over the phase space - to be known. But in MCMC scans the tails of the posterior are inherently poorly sampled, even though they occupy a large volume in phase space, and hence it is not possible to calculate the evidence accurately (for a detailed explanation see Feroz et al. [74]). Therefore, we resort to the frequentist approach and do model comparisons via the likelihood ratio test. The test assumes that the new parameter α can both be smaller and larger than its value in the null hypothesis. This is however not the case here, since the diffusion coefficient in the disk is assumed to be only smaller than in the default case, leading to $\alpha \leq 1$. If data prefers $\alpha > 1$, the best fit value in our model would correspond to $\alpha = 1$. We will shortly explain the modified calculation given by Cowan et al. [41]. For likelihood $\mathcal{L}$ with nuisance parameters θ the conditional maximum-likelihood - meaning with fixed α - has parameters $\hat{\hat{\theta}}$ and the unconditional one is maximised at $\hat{\alpha}$ and $\hat{\theta}$. In this case the test statistic is given by:

$$q_1 = \begin{cases} -2\ln\frac{\mathcal{L}(\alpha,\hat{\hat{\theta}}(\alpha))}{\mathcal{L}(1,\hat{\hat{\theta}}(1))} & \hat{\alpha} > 1 \\ -2\ln\frac{\mathcal{L}(\alpha,\hat{\hat{\theta}}(\alpha))}{\mathcal{L}(\alpha,\hat{\theta})} & \hat{\alpha} \leq 1 \end{cases}. \tag{5.25}$$

The approximate sampling distribution $f(q_1|\alpha')$ can be calulated under the Wald approximation:

$$q_1 = \frac{(1-\hat{\alpha})^2}{\sigma^2} + O\left(1/\sqrt{N}\right), \tag{5.26}$$

where $\hat{\alpha}$ follows a Gaussian distribution with mean α' and standard deviation σ and N is the sample size. In the limit of large sample sizes this reduces to

$$q_1 = \begin{cases} (1-\hat{\alpha})^2/\sigma^2 & \hat{\alpha} \leq 1, \\ 0 & \hat{\alpha} > 1. \end{cases} \tag{5.27}$$

Table 5.1: Boundaries of the uniform priors on the model parameters. The lower bound on $\mathcal{R}_l$ is chosen to be smaller than the rigidity at which the diffusion timescale becomes smaller than the advection and energy loss timescale.

α	κ_{halo} [pc^2/yr]	H [kpc]	v_c [km/s]	δ	δ_l	$\mathcal{R}_l$ [GV]
$[0, 1]$	$[0.001, 1]$	$[0.1, 20]$	$[0.01, 100]$	$[0, 2]$	$[-4, 4]$	$[2.2, 20]$

The probability density function can then be derived to be a mixture between a delta distribution at $\alpha = 1$ and a chi-square distribution

$$f(q_1, 1) = \frac{1}{2}\delta(q_1) + \frac{1}{2}\frac{1}{\sqrt{2\pi q_1}}\exp\{-q_1/2\}. \tag{5.28}$$

This leads to a cumulative distribution function of

$$F(q_1|1) = \Phi(\sqrt{q_1}) \tag{5.29}$$

where Φ^{-1} is the inverse of the cumulative distribution function of the standard Gaussian. The significance in this case is given by:

$$Z_1 \equiv \Phi^{-1}(1 - p_1) = \sqrt{q_1}. \tag{5.30}$$

We investigate the null hypothesis meaning that there is no suppression in the disk and the full model for different data sets. All of them contain the B/C data from Voyager and AMS-02 as well as all published data on ^{10}Be/^{9}Be. The first setup, referred to as "w/o prelim." reflects our best knowledge as of today. In the second setup "w/ prelim." we also take into account preliminary results from AMS-02 on ^{10}Be/^{9}Be , which extends above 1 GeV. This data is expected to break the degeneracy of H and κ as explained in Sec. 5.3. Additionally, we predict the constraining power of upcoming HELIX data, called "w/ forecast".

5.5. MCMC Scan and Statistical Results

The null hypothesis of the model "w/o prelim." is shown in Fig. 5.4. The lower left triangle displays the 2D marginalised posteriors of all parameter combinations. The dark (bright) regions represent the 68 % (95 %) quantiles. On the diagonal the 1D marginalised posteriors are shown with the 16 % and 84 % quantiles indicated by dashed lines. Both in the 1D and 2D posteriors the best fit values are marked with solid black lines, see also Table 5.2, where we give the χ^2 of the setups as well.

The diffusion coefficient κ_{halo} and the height of the halo H are degenerate, as it is visible in the left uppermost 2D plot, as expected since the low energy ^{10}Be/^{9}Be data does not break the degeneracy. The halo size is around 5 kpc, similar to the values obtained by e.g. Jiahui Wei [111], Maurin et al. [145]. The slope of the diffusion coefficient δ is comparable to the values of Weinrich et al. [216]. A clear correlation between the slope of the diffusion coefficient at intermediate energies (see Eq. 5.5) and the advection velocity occurs, which is a well documented phenomenon for diffusion-advection models, as it is shown in Fig. 2 of Putze et al. [179]. This occurs since at lower energies a larger advection speed can be offset by a larger rigidity dependence of the diffusion coefficient. The spectral index of the diffusion coefficient at low energies is similar to the one at intermediate ones, which leads to the degeneracy shown in the right bottom 2D plot. Overall, these results indicate that the procedure can reproduce previous publications reliably.

The full model, which is shown in the same format in Fig. 5.5, shows the same basic features as the null hypothesis. The additional parameter widens the posterior for all parameters. The degeneracy between the diffusion coefficient and the halo size is still unbroken and even more pronounced than before. The best-fit value for the halo size is $H = 6.3^{+3.5}_{-1.5}$ kpc. All other parameters have similar best fit values as well (see Tab. 5.2). The posterior of the scaling factor α is shown in the leftmost column. Due to the lack of constraining power of the B/C data, highlighted by Eq. 5.22 and the lack of data in the transition region of ^{10}Be/^{9}Be , the suppression of the diffusion coefficient in the disk is nearly unconstrained with $\alpha = 0.5^{+0.3}_{-0.3}$, since it can be compensated for by shifting κ/H. Only for scaling factors below $\alpha = 0.1$, the large increase of H and κ_{halo} needed to fit low energy ^{10}Be/^{9}Be data is disfavoured. Hence, not only electron data [103] at TeV energies, but also nuclei fluxes at GeV energies disfavour suppression of the diffusion coefficient in the disk by more than an order of magnitude.

Table 5.2: Best-fit and median of the setups, the errors are estimated as the distance to the 16 % and 84 % quantiles of the marginalised 1D posteriors respectively.

	Full - w/o prelim.		Full - w/ prelim.		Null - w/ prelim.	
	median	best-fit	median	best-fit	median	best-fit
α	$0.5^{+0.3}_{-0.3}$	0.8	$0.20^{+0.10}_{-0.06}$	0.19	-	-
κ_{halo} [pc^2/yr]	$0.21^{+0.11}_{-0.05}$	0.17	$0.28^{+0.06}_{-0.05}$	0.29	$0.174^{+0.009}_{-0.009}$	0.172
H [kpc]	$6.3^{+3.5}_{-1.5}$	5.1	$8.2^{+1.1}_{-0.9}$	8.2	$6.4^{+0.4}_{-0.4}$	6.2
v_c [km/s]	$4.3^{+1.3}_{-1.5}$	4.3	$4.2^{+1.2}_{-1.3}$	4.2	$6.9^{+0.6}_{-0.7}$	6.5
δ	$0.46^{+0.03}_{-0.02}$	0.46	$0.46^{+0.02}_{-0.02}$	0.45	$0.511^{+0.017}_{-0.016}$	0.506
δ_l	$0.24^{+0.12}_{-0.11}$	0.21	$0.2^{+0.1}_{-0.1}$	0.16	$0.5^{+0.29}_{-0.19}$	0.35
R_l [GV]	$6.5^{+2.6}_{-1.2}$	6.2	$6.1^{+1.9}_{-0.9}$	5.8	$5.0^{+7.0}_{-3.0}$	6.0
χ^2	-	67.7	-	99.6	-	111.9
dof	85	85	98	98	99	99

If we now include preliminary AMS-02 data in the "w/ prelim." model, we expect the degeneracy between diffusion coefficient and halo height to be broken. The corner plot for the null hypothesis is shown in Fig. A.4. The upper left 2D plot indeed shows that the degeneracy does not exist anymore. Consequently, the halo size can be constrained to $H = 6.4^{+0.4}_{-0.4}$ kpc with best fit value $H = 6.2$ kpc. All other parameters are of similar magnitude to the ones obtained in the "w/o prelim." model. In the lower right 2D plot an additional feature becomes visible. In case the break in the diffusion coefficient is at sufficiently low rigidities, the impact on the fitted data will be minimal and hence the allowed range for δ_l increases. This also causes the peak at small R_l in the 1D marginalised posterior. The best fit in this case is achieved with $\chi^2 = 111.9$.

The full model is shown in Fig. 5.6. The first column shows again the posterior as function of α. In contrast to the model without preliminary AMS-02 data, a clear preference for a suppressed diffusion coefficient in the disk can be seen. The mean and quantiles are $\alpha = 0.20^{+0.10}_{-0.06}$ with best fit $\alpha = 0.19$. Both the halo height $H = 8.2^{+1.1}_{-0.9}$ kpc and the diffusion coefficient $\kappa_{\text{halo}} = 0.28^{+0.06}_{-0.05}$ pc^2/yr are slightly larger than in the null hypothesis, since a decreased diffusion coefficient in the disk leads to a preference of larger values for both, as visible in the two upper 2D plots in the left column. This is caused by a more gradual transition to the high energy limit, as preferred by the data. As in the previous figures, the best fit values are located well within the marginalised posteriors. In this case one obtains $\chi^2 = 99.6$.

In addition to the preliminary data, we also want to estimate the constraining power of the upcoming HELIX experiment. Since the mock data in this analysis was produced using the best fit values of the full "w/ prelim." model, existing preferences are expected to increase. However, this is only valid in the limit of large amounts of additional data, which is not the case here. The corner plot for the full model is shown in Fig. A.5. Again a clear preference for $\alpha < 1$ is visible in the left column, with quantiles $\alpha = 0.28^{+0.13}_{-0.09}$ and a best fit value of $\alpha = 0.27$. The difference with respect to the "w/ prelim." model is caused by the statistic effect explained above.

The ^{10}Be/^{9}Be ratio is shown in Fig. 5.7 as a function of kinetic energy for the full model without and with preliminary AMS-02 data (red solid and blue dashed line) and the null hypothesis with preliminary data (green dot-dashed line). The model without preliminary AMS-02 data predicts a transition that is both at too low energies and too steep. If preliminary data is included the full model is preferred compared to the null hypothesis since it is able to flatten the transition. The larger halo size leads to a later transition while the suppressed diffusion in the disk simultaneously increases the low energy ^{10}Be/^{9}Be ratio. Since the high energy limit is determined by the ratio of spallation cross-

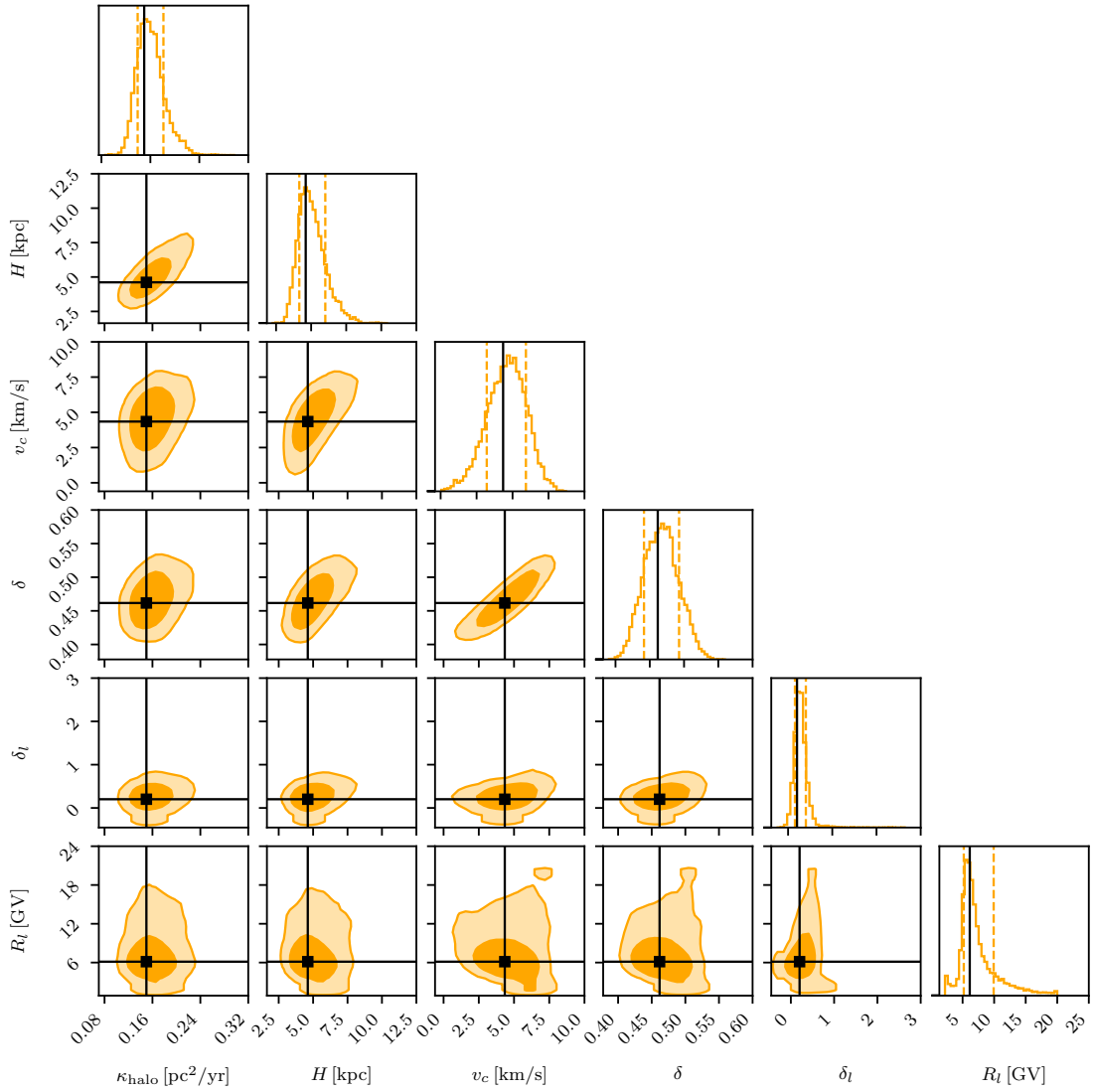

Figure 5.4: Corner plot of the MCMC scan of the null model without preliminary data, “w/o prelim.”. The 2D marginalised posteriors are shown on the lower triangle. The dark/bright orange areas corresponds to the 68 %/95 % quantiles. Similarly, the principal diagonal displays the 1D marginalised posterior with the 16 % and 84 % quantiles marked as orange dashed lines. The black lines indicate the best fit values as listed in Table 5.2.

sections, as explained in Sec. 5.3, this is susceptible to uncertainties in these ratios. The impact is investigated in Sec. 5.8.

In order to compare the models, we now need to investigate the 1D marginalised posteriors and utilise the modified test statistics derived in Sec. 5.4. The marginalised 1D posteriors for the model with and without AMS-02 ^{10}Be/^{9}Be data, as well as a forecast for HELIX data is shown in Fig. 5.8 as a function of α. We used a Gaussian kernel density estimation with a width of 0.1. The posterior for existing data is indicated by the solid red line, the one including preliminary data by the blue dashed line and the forecast in the purple dotted line. For the setup ”w/o prelim.” the posterior is flat and extends to $\alpha = 1$. The cut-off at high alpha is produced by boundary effects of the prior $\alpha \leq 1$ when smoothing with the Gaussian kernel. Values larger than one are unconstrained by our model since the residence time in the disk becomes negligible. Thus, there is no preference for suppressed diffusion in the disk in the setup without preliminary AMS-02 data. If preliminary AMS-02 data is included the

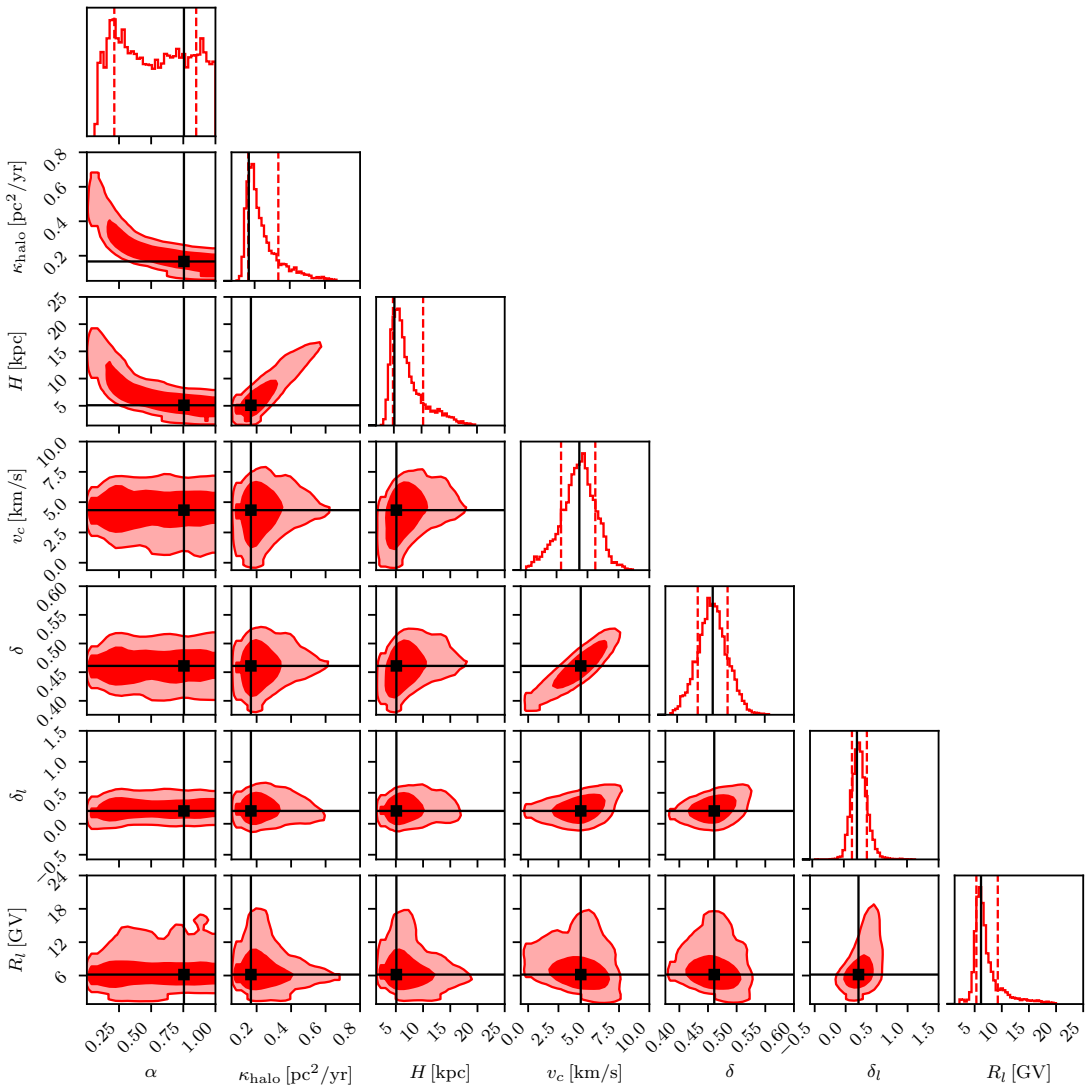

Figure 5.5: Same as Fig. 5.6, but for the full model excluding preliminary data, called "w/o prelim." The extension of the posterior to $\alpha = 1$ indicates that the data cannot constrain α. Furthermore, the ratio of $H/\kappa_{\rm halo}$ is largely unconstrained.

median and quantiles are $\alpha = 0.20^{+0.10}_{-0.06}$ with a best fit value $\alpha = 0.19$. Using the χ^2 listed in Tab. 5.2 the significance can be obtained from the Likelihood ratio by substituting Eq. 5.25 into Eq. 5.30, which in this case results in a preference of $3.5\,\sigma$.

Should the trend continue we predict a detection by $6.8\,\sigma$ with HELIX data. On first sight this seems to contradict what the marginalised posteriors show. However, MCMC scans are good at estimating the median and the nearby quantiles, but bad at sampling the tails of the distribution as explained in Sec. 5.4. Therefore, they cannot be used for model comparison if the null hypothesis is not within the first few quantiles.

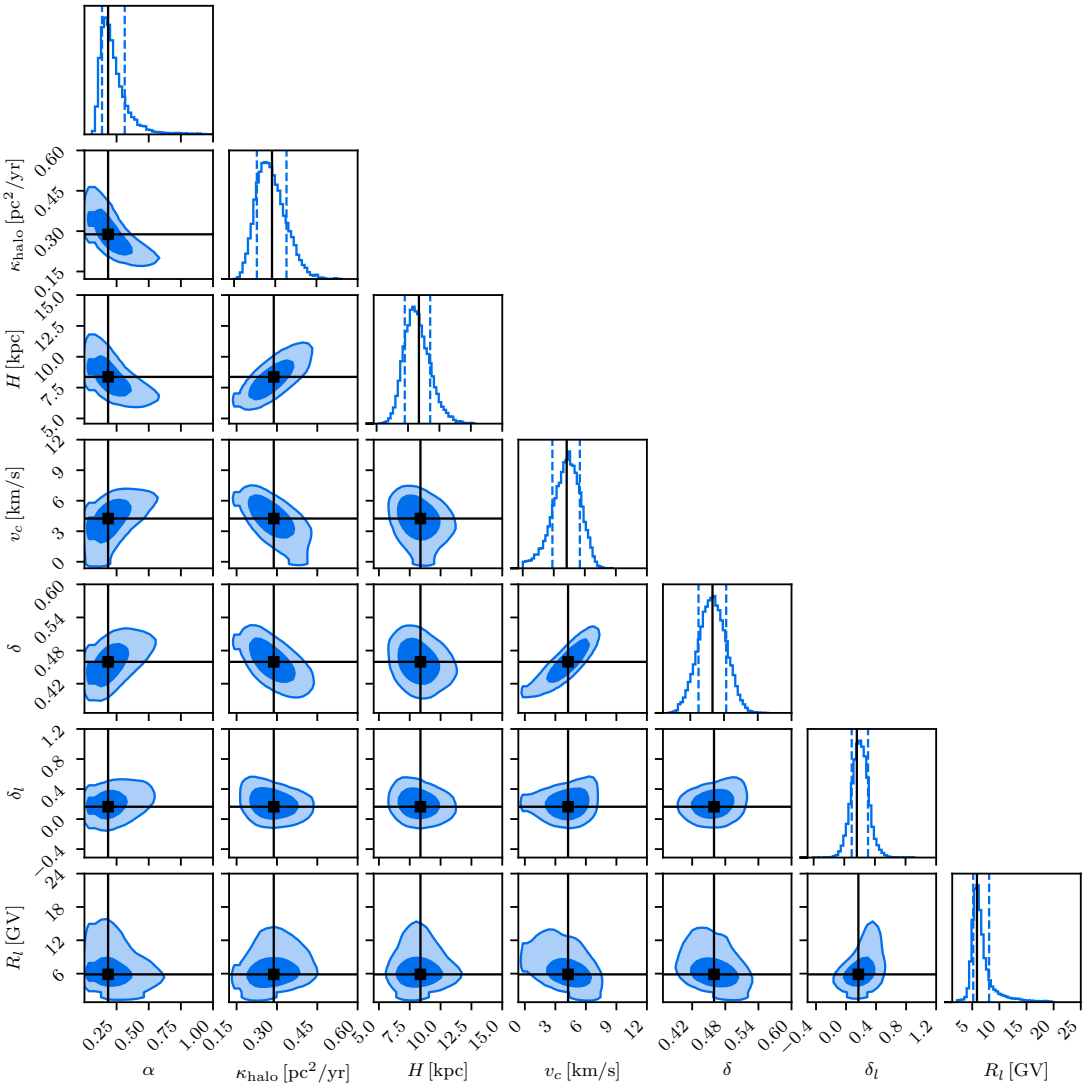

Figure 5.6: Same as Fig. 5.6, but for the full model including preliminary data, called "w/ prelim.". The degeneracy between κ_{halo} and H visible in Fig. 5.6 is broken and α can be constrained to be $\alpha = 0.20^{+0.10}_{-0.06}$.

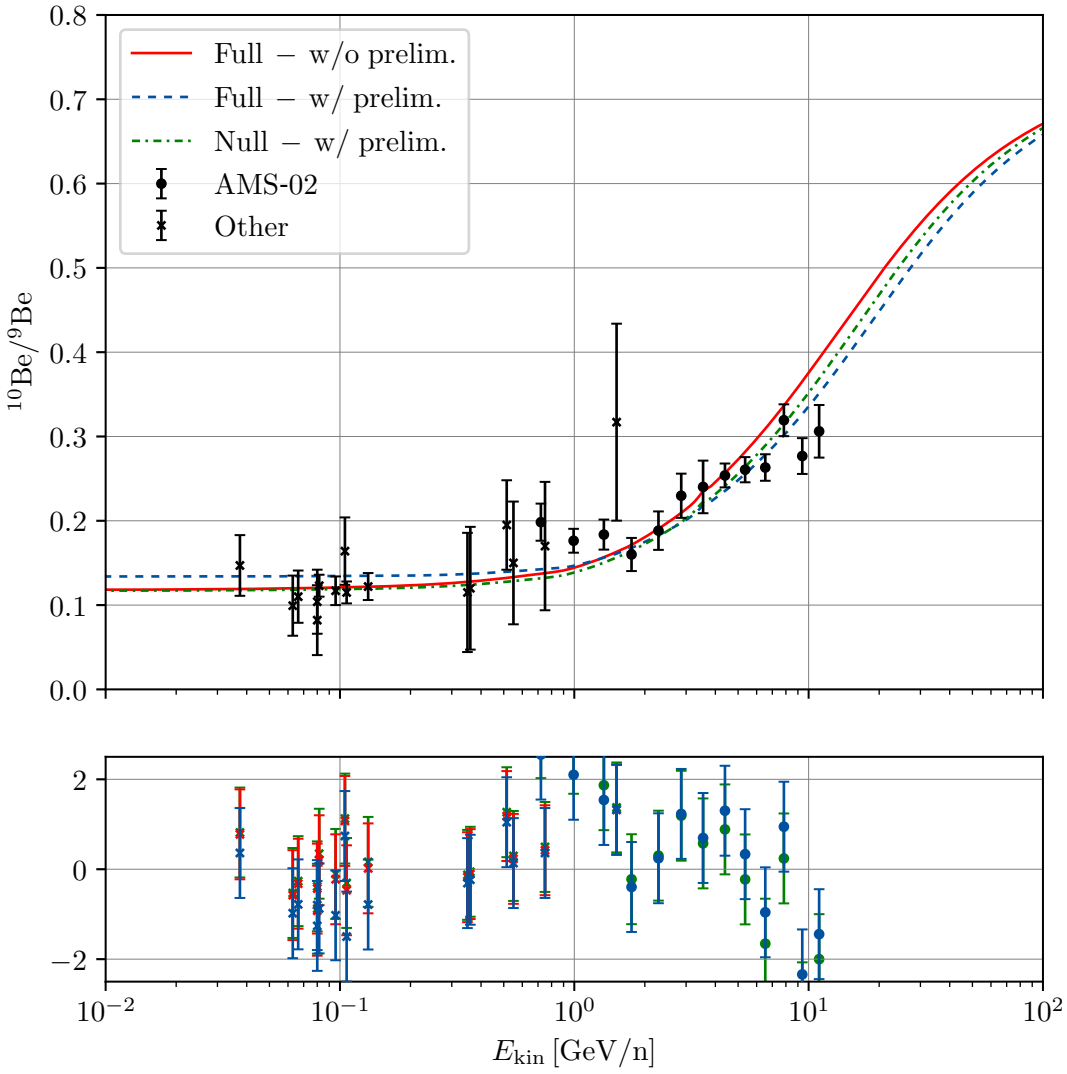

Figure 5.7: Best-fit spectra for the Beryllium ratio to the setups with only existing data (red solid), preliminary AMS-02 data (blue dashed) and the corresponding null hypothesis $\alpha = 1$ (green dot-dashed). The null hypothesis predicts a lower Be ratio at low energies, and a transition to the high energy limit earlier, since the best-fit halo height is smaller (for more details see text). The lower panel is the pull plot.

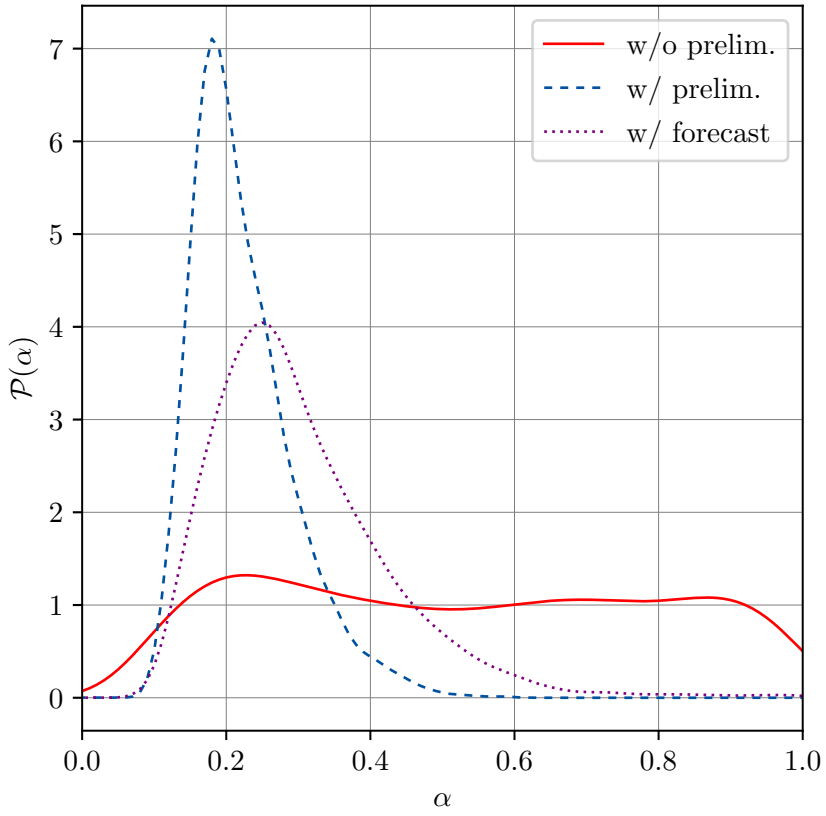

Figure 5.8: Marginalised posterior of the scaling factor α. The setup with existing data only (red solid) shows no preference for a suppression. The setup with preliminary AMS-02 data, "w/ prelim.", allows constraining the scaling factor to around $0.20^{+0.10}_{-0.06}$, with a model preference for $\alpha < 1$ of $3.5\,\sigma$. Upcoming HELIX data will be able to constrain the "w/ prelim." best fit model to $6.8\,\sigma$. Due to different effects the increase in the significance is difficult to estimate from the posterior (see text for details).

5.6. Effective Diffusion Coefficient

The suppressed diffusion coefficient in the disk obtained in the previous section can be interpreted in two different ways. Either the suppression is homogeneous within the disk and produced by some global effect on galaxy scales, or the suppression only exists in smaller localised regions within the disk. Then what is captured by the cosmic ray propagation model is the global average of these small zones with the surrounding high diffusion region. The reason that we think these exist is motivated by observations and models around supernova remnants in Sec. 3 and pulsar wind nebulae in Sec. 4. Due to the vastly different scales involved in these transport processes and their complicated 3D geometry, an analytic solution is not possible and a finite difference scheme is computationally not feasible. Therefore, we (in particular Philipp Mertsch) have calculated the average diffusion coefficient and hence α as a function of $(\kappa_{\rm low}/\kappa_{\rm high})$ and their filling fraction with stochastic differential equations (SDEs). To this end we have modelled the disk as a periodic medium consisting of many identical cubes on a regular cubical grid.

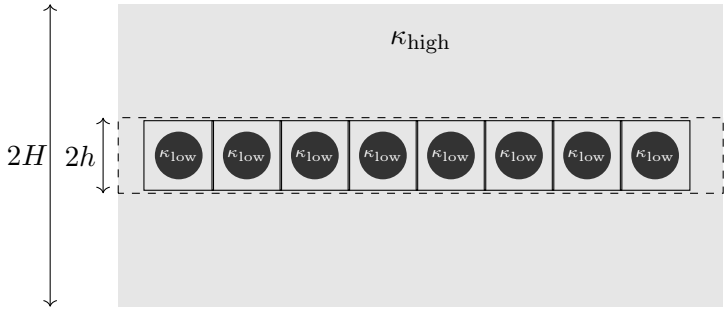

Figure 5.9: Edge-on sketch of the Galaxy with halo of height H and disk of height h. Zones of low diffusion with $\kappa_{\rm low}$ are assumed to be arranged in a regular grid within the disk. These zones are surrounded by a high diffusion coefficient $\kappa_{\rm high}$. The regular ordering is assumed in order to simplify the averaging procedure.

This is shown in Fig. 5.9. Each cube contains a surrounding region with diffusion coefficient $\kappa_{\rm high}$ and embedded spherical, non-overlapping regions with $\kappa_{\rm low}$. We have checked that the exact geometry of the zones has negligible influence on the final results. The sources of cosmic rays are assumed to be uniformly distributed within the cube. The averaged diffusion coefficient in one cell can then be obtained form the mean square displacements of particles,

$$\kappa_{\rm disk} = \lim_{t\to\infty} \frac{1}{2} \frac{{\rm d}\langle(\Delta r)^2\rangle}{{\rm d}t} \,. \tag{5.31}$$

Since it is impossible to take the time limit to infinity, we stop the calculation at the residence time of the particles.

For a face centred cube the setup is shown in Fig. 5.10, where the shaded area corresponds to the low diffusion region, the dots are the source positions, the black line symbolises the track of the particle and the red line notes the mean displacement. We have done this for two values of $(\kappa_{\rm low}/\kappa_{\rm high})$, 10^{-2} and 10^{-3}, and a variety of different filling fractions f and interpolated between them.

The resulting ratio of $\kappa_{\rm disk}/\kappa_{\rm halo}$ is shown in Fig. 5.11 as a function of f. The blue solid line marks the SDE solution for $(\kappa_{\rm low}/\kappa_{\rm high}) = 10^{-3}$ and the orange dashed one the result for 10^{-2}. The results of the arithmetic mean, which overestimates the diffusion coefficient due to the increased residence time in the low diffusion regions is shown for the same two $(\kappa_{\rm low}/\kappa_{\rm high})$ ratios (10^{-2} in red dot-dashed and 10^{-3} in green dotted). To compare with the results of the parameter study of cosmic ray ratios, the 68 % quantiles and the median are given by the grey shaded area and line respectively. The overlapping lines show that the exact value of the ratio $\kappa_{\rm low}/\kappa_{\rm high}$ is not relevant for filling fractions well below

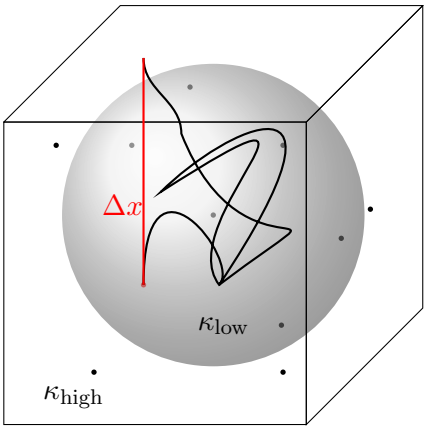

Figure 5.10: Face centred spherical low diffusion zone marked in grey within one of the cubic zones indicated Fig. 5.9. The randomly distributed source positions are marked with black dots and one exemplary particle path is shown as black solid line. The average distance in x, which is used to numerically determine the diffusion coefficient in x direction is marked in red.

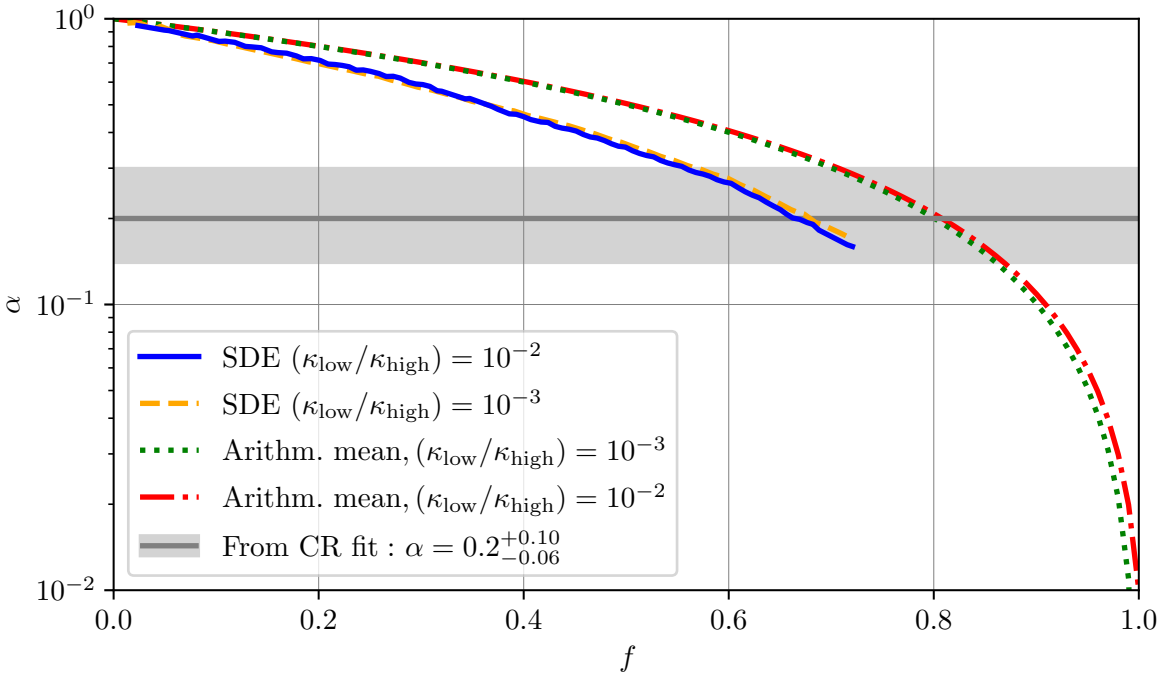

Figure 5.11: Effective diffusion coefficient κ_{disk} from the SDE computation as a function of the volume filling fraction f. The solid blue (dashed orange) line shows κ_{disk} in unit of κ_{high}, assuming a ratio $\kappa_{\mathrm{low}}/\kappa_{\mathrm{high}}$ of 10^{-2} (10^{-3}). The sources of CRs are assumed to be distributed uniformly in the disk. Note that the lines end at the maximum possible filling fraction of $\sim 74\,\%$ for spherical inclusions in a face centered structure. For comparison, the green dotted (red dot-dashed) line shows the arithmetic mean $(\kappa_{\mathrm{low}}/\kappa_{\mathrm{high}})f + (1-f)$ assuming $\kappa_{\mathrm{low}}/\kappa_{\mathrm{high}}$ of 10^{-2} (10^{-3}). The grey line and band highlight the suppression found from the CR fit, $\alpha = 0.2^{+0.10}_{-0.06}$.

one. Hence, in both cases the intersection of the SDE solutions with the median value is achieved at a filling fraction of around $f \approx 2/3$. The end of the SDE lines is at around $f = 0.74$, since this is the highest filling fraction achievable by spherical non-overlapping suppression zones in a face centred structure.

5.7. Interpretation

Having determined that the diffusion coefficient in the disk can be scaled down with respect to the one in the halo by $\alpha = 0.20^{+0.10}_{-0.06}$ and shown that this can be achieved by a filling fraction of $f \approx 2/3$, we can try to determine the physical origin. First, it is useful to rephrase Eq. 5.1 in terms of typical orders of magnitude:

$$f = 0.0048 \left(\frac{\mathcal{R}_{\rm bubble}}{0.03\,{\rm yr}^{-1}}\right)\left(\frac{\tau_{\rm bubble}}{10^5\,{\rm yr}}\right)\left(\frac{R_{\rm bubble}}{0.03\,{\rm kpc}}\right)^3\left(\frac{R_{\rm disk}}{15\,{\rm kpc}}\right)^{-2}\left(\frac{h}{0.1\,{\rm kpc}}\right)^{-1} . \tag{5.32}$$

Both the suppression from supernova remnants and from pulsar wind nebula can last for several hundred kyrs. For typical production rates of $\mathcal{R}_{\rm bubble} = 0.03\,{\rm yr}^{-1}$ and the geometry of the Galaxy given in Sec. 1.2, this results in bubble sizes $R_{\rm bubble} \approx 150\,{\rm pc}$. Interestingly, the high filling fraction is also obtained in Galaxy formation models in order to suppress clump formation in star forming regions of the interstellar medium [189]. Additionally, recent studies of TeV halos indicate a possible extent of the low diffusion region reaching 100 pc [188]. Then a combination of several mechanisms containing the effects of supernova remnants, pulsar wind nebulae and as recently shown also dense molecular clouds [220] can lead to a combined filling fraction of $2/3$ of the Galactic disk. However, the lifetime and the radius of these suppression zones are uncertain and further global effects as well as the uncertainty in the cross-sections might impact the results as well. The latter will be investigated in Sec. 5.8. Recent models that try to self-consistently model the formation of the galactic halo and the observed cosmic ray spectra have been developed [36, 37, 54, 64]. In these cases the halo is created purely by the resonant streaming instability of the cosmic rays [36, 37, 54], or additional large scale injection of turbulence in the disk and subsequent advection into the halo [64]. They predict or argue that the turbulence level in the disk must be reduced by ion neutral damping. This leads to a highly increased diffusion coefficient in contrast to our results. However, none of the models accounts for the highly different phases of the interstellar medium in the disk. In the hot ionised medium, which is believed to fill up to 50 % of the volume of the disk no ion neutral damping will occur. Furthermore, ion-neutral damping will not be effective at larger scales in resonance with larger energies (see e.g. Recchia et al. [182] Fig. 1) even in more ionised regions. Additionally, they do not consider the geometry of the background magnetic field, which could be important in modelling the self-generated turbulence. Given that our results indicate reduced diffusion in the disk it would be interesting to revisit these models with a more realistic approach.

5.8. Cross Sections

For the interpretation of comic ray ratios it is imperative to know the cross-sections of the individual particles with the interstellar medium. These can in principle be obtained from particle collider experiments on Earth up to their maximum achievable energy for the respective projectile. For higher energies one has to rely on extrapolations or theoretical models. Since we are interested in the collision of massive hadrons mostly upon proton targets, reactions are complex and difficult to predict [84]. It is comparatively easy to measure the total inelastic cross-sections because the final state particles do not have to be known. The total inelastic cross-sections relevant for cosmic ray transport can be well described by the formulas and values given by Tripathi et al. [204, 205], which agree with measurements [204, 205].

The spallation cross-sections relevant for secondary production require the final state particles to be known and are therefore not only difficult to model, but also to measure. Outside the cosmic ray community there seems to be little interest and hence funding to do so. However, we will shortly highlight below why they are crucial to improve our understanding of particle propagation in our Galaxy. Actually, with the new ^{10}Be/^{9}Be data, they are the limiting factor in determining the halo height in 1D diffusion models.

Table 5.3: Best fit values of the full model "w/ prelim." for the DRAGON2 and GALPROP `OPT12up22` cross-sections.

	α	κ_{halo} [pc^2/yr]	H [kpc]	v_c [km/s]	δ	δ_l	$\mathcal{R}_l$ [GV]
GALPROP	0.41	0.28	7.0	0.3	0.46	0.26	5.0
DRAGON2	0.19	0.29	8.2	4.2	0.45	0.16	5.8

Sporadic measurements of the spallation cross-sections have already been done in the 1960s[221] and further studies with semi-empirical parametrisations followed in the 1970s to the 1990s [192–194, 215]. All of them suffer from large systematic uncertainties and are done at energies of MeV/n instead of the GeV/n relevant for cosmic rays. Above we have used the parameterisation by DRAGON2 [63] which has been obtained by normalising the results of Silberberg et al. [194], Webber et al. [215] to experimental data. Another parameterisation based on all the work above is used by GALPROP [174] which utilises a comprehensive set of routines to calculate the spallation cross-sections. The most up-to-date model is called `Galp-opt12`. Recent works extended this further, leading to the model `OPT12up22`, which will be used as alternative in the following [85, 87, 146].

5.8.1. Impact of Cross Sections on Low Diffusion Zones

We have repeated the model testing of Sec. 5.5 for the `OPT12up22` cross-sections, which have been kindly provided to us by Yoann Genolini. The best fit ^{10}Be/^{9}Be spectra of the null model "w/ prelim." for both set of cross-sections is shown in Fig. 5.12 as a function of kinetic energy. The solid red line indicates the best fit with DRAGON2 cross-sections as used before, and the dotted blue line marks the best fit of the new `OPT12up22` cross-section set. The high energy limit is reduced from 0.8 to 0.51. This leads naturally to a flatter transition to the high energy limit, which has been accomplished by a suppressed diffusion coefficient in the disk before.

The corner plot of the MCMC scan of the full model with preliminary AMS-02 data is shown in Fig. 5.13. The posterior as a function of α is shown in the left column and extends up to $\alpha = 1$. Hence, due to the flatter transition there is no preference of a suppressed diffusion coefficient in the disk anymore. In fact, a strong suppression by more than one order of magnitude can be excluded. The best fit parameters are provided in Tab. 5.3. For both cases the halo height and most other parameters agree well, the only exception being α.

The overlaid corner plots are shown in Fig Fig. 5.14, where the model with the DRAGON2 cross-sections are marked in blue and the one with the GALPROP cross-sections in red. With the currently available data no mayor discrepancy is visible, except α. However, a variety of 2D plots show minor discrepancies - most pronounced in the δ, v_c plot. Hence, especially for our two zone model, but with better data even in the null hypothesis, the uncertainty in the cross-section could restrict our understanding of Galactic cosmic ray propagation.

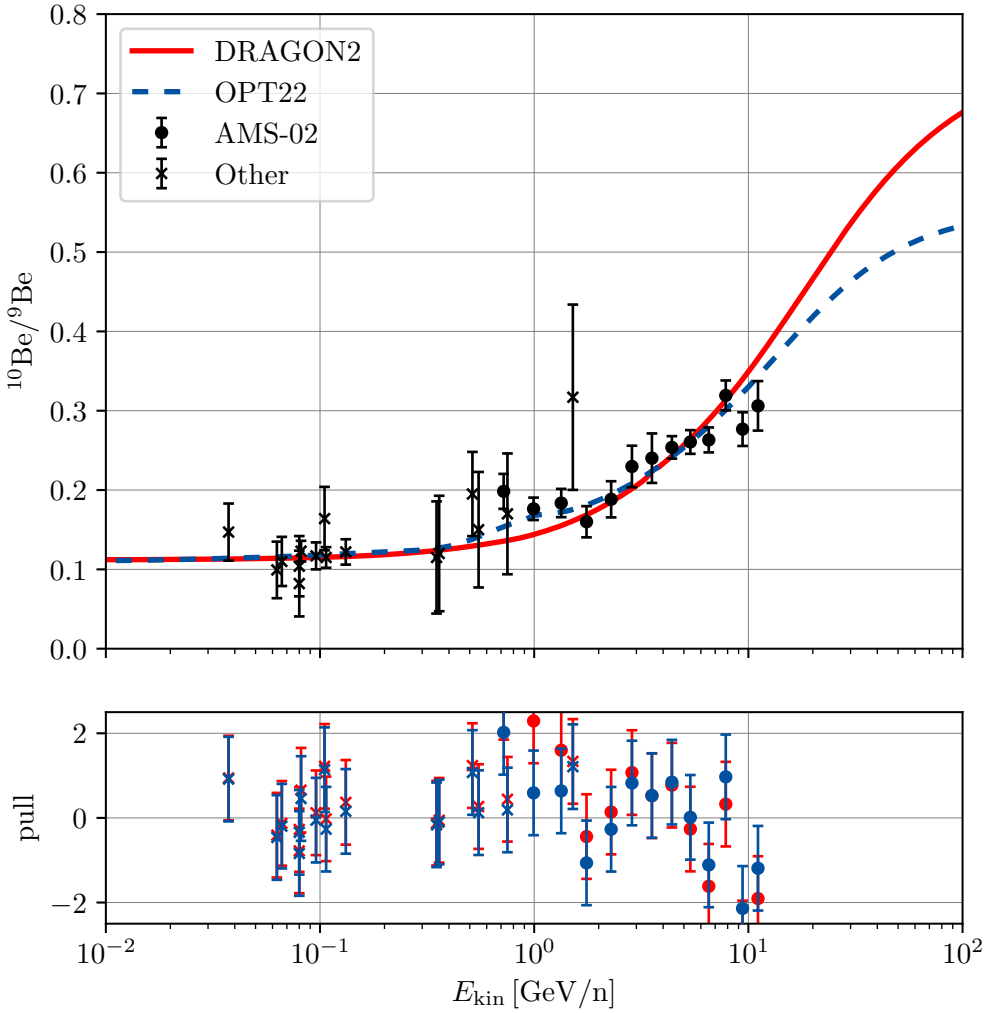

Figure 5.12: Best-fit spectra of the null hypothesis $\alpha = 1$ for the Beryllium ratio for the setup with preliminary AMS-02 data. The red solid line marks the model with the DRAGON2 cross-sections and the blue dashed lines indicates the `OPT12up22` parameterisation. Since the high energy limit for DRAGON2 is 0.8 compared to 0.51 in the `OPT12up22` case, the transition in the latter case is naturally flatter, as preferred by data.

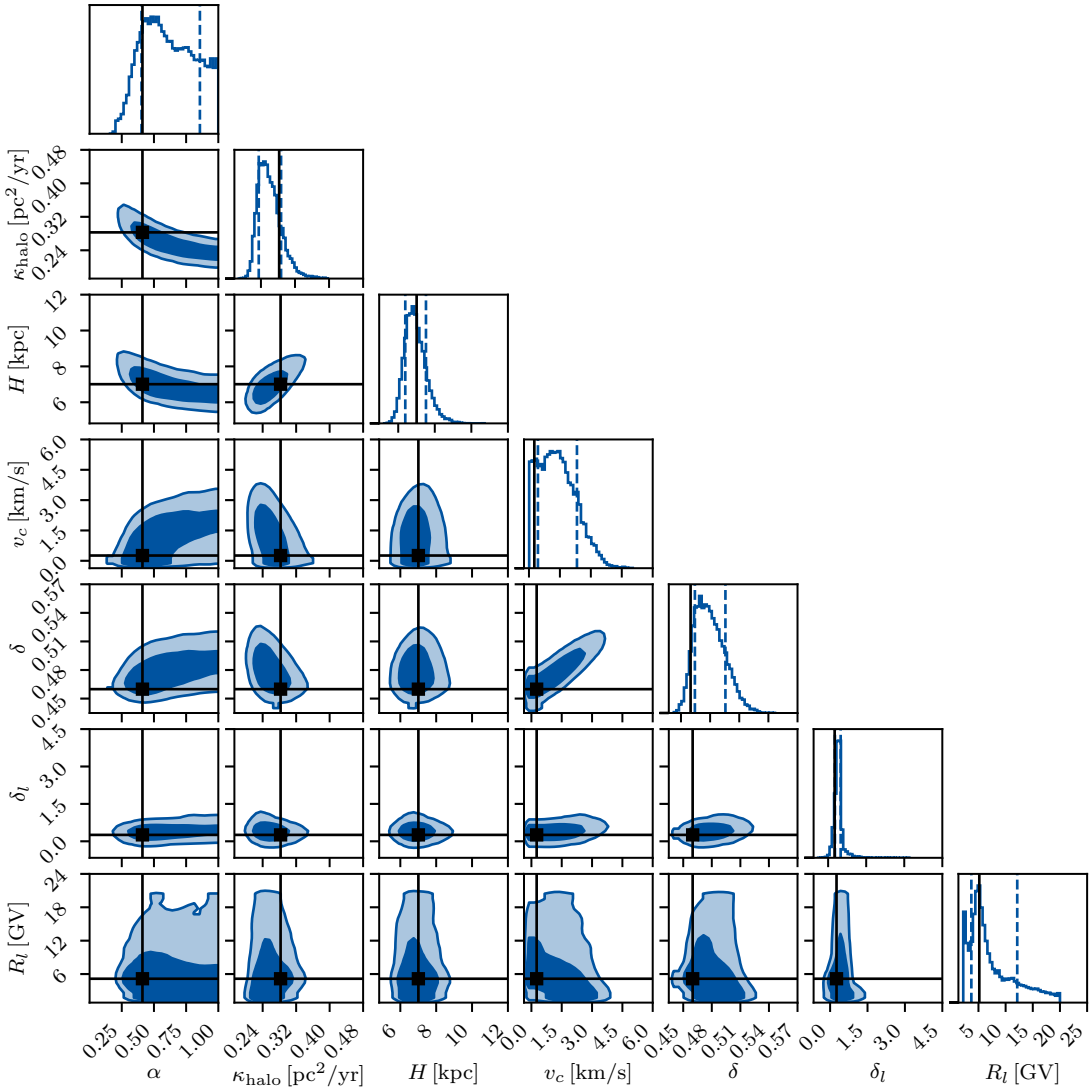

Figure 5.13: Corner plot of the MCMC scan of the full model including preliminary data, "w/ prelim." for the `OPT12up22` cross-section parameterisation. The 2D marginalised posteriors are shown on the lower triangle. The dark/bright blue areas corresponds to the 68 %/95 % quantiles. Similarly, the principal diagonal displays the 1D marginalised posterior with the 16 % and 84 % quantiles marked as blue dashed lines. The black lines indicate the best fit values.

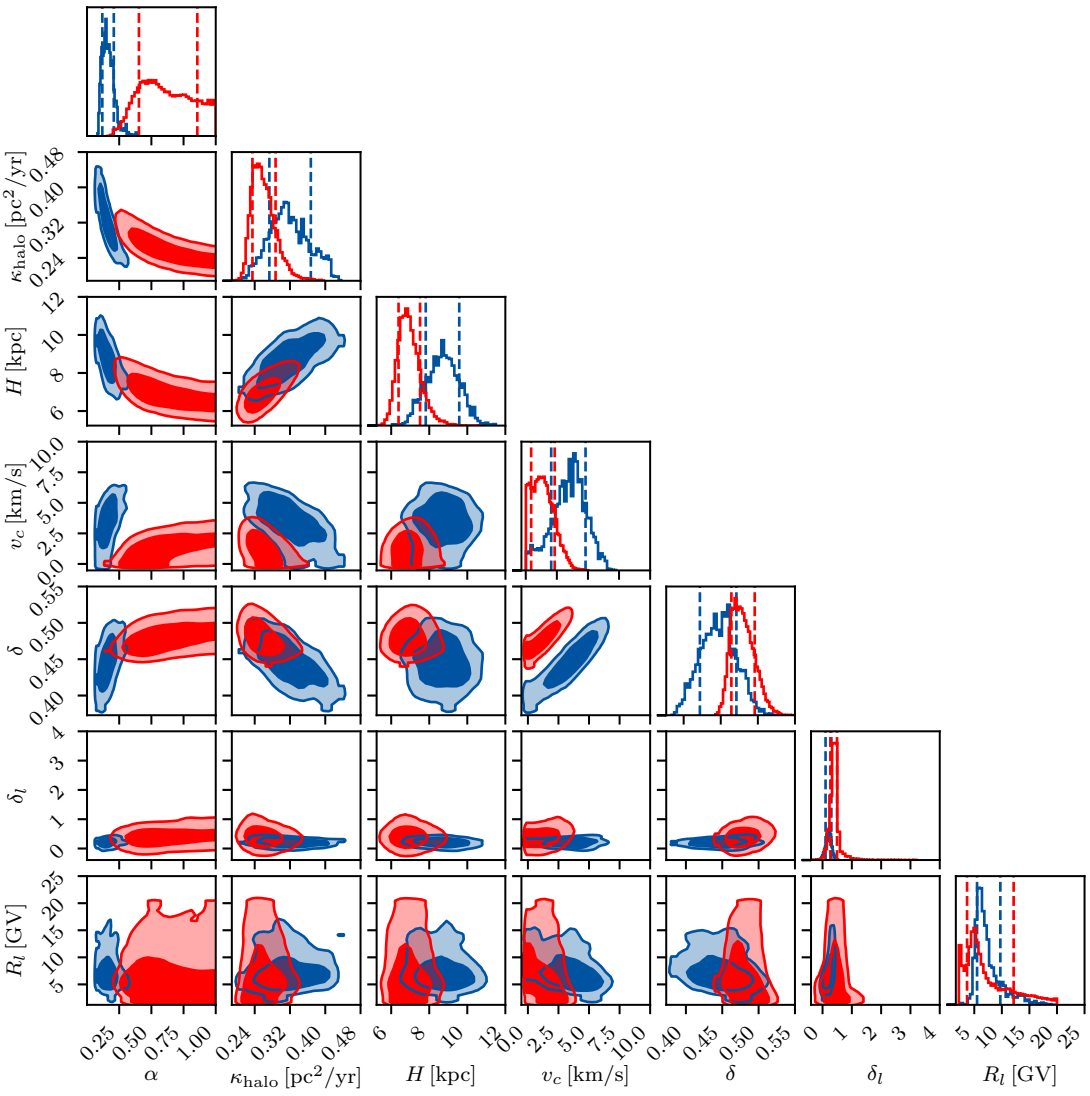

Figure 5.14: Corner plot of the MCMC scan of the full model including preliminary data, "w/ prelim." for the `OPT12up22` cross-section parameterisation (red) and the DRAGON2 cross section (blue).

6. Summary and Conclusions

The fluxes of stable GeV particles observed by direct particle detectors in space are remarkably isotropic. Together with the ratio of secondary to primary particles, which indicates that particles need to on average cross the Galaxy many times before being detected, this proves that particles cannot travel ballistically, but diffuse within the Galaxy. The diffusion is caused by deflection upon magnetic turbulence within the Galaxy. Simple propagation models are capable of reproducing most features of hadronic ratios satisfactory. However, since the particles probe the entire Galaxy, they represent an average. The spatial dependence of the cosmic ray density can indirectly be probed by γ-rays, which balistically propagate from their source regions. Observations around pulsars and supernova remnants, which are suspected sources of comic rays, indicate increased cosmic ray densities. These can only be explained when diffusion is suppressed by more than two orders of magnitude in these regions. Hence, conditions within the Galaxy are far from homogeneous.

In Sec. 1, we have introduced cosmic rays and covered the necessary basics to understand the standard model. We explained the underlying physics of possible extensions like the backreaction of cosmic rays on the magnetic field due to the resonant streaming-instability. Additionally, we utilised magnetic field simulations to provide boundaries for the flux-tube approximation, which is used within this thesis.

Subsequently, we have used the flux-tube approximation and the streaming-instability for a non-linear model of particle propagation around supernova remnants. There we calculate the propagation of particles after they escape from the supernova remnant. We use finite difference equations to compute the coupled, non-linear transport equations for particles and waves. We split the transport equation in several parts, each only containing derivatives with respect to time and one other coordinate. With this scheme we are able to include energy losses and the cascade of turbulence from large to small scales. This allows extending previous models to below 10 GeV, where energy loss processes become important. For fiducial parameters of the supernova remnant, we are able to show that the diffusion coefficient at 100 MeV is suppressed for up to 1 Myr, depending on the phase of the interstellar medium. This causes the particles to be confined in this region for longer. Since the suppression at lower energies lasts longer than at higher ones, the spectrum at late times becomes significantly flatter at low energies than in the test-particle case, where the diffusion coefficient is assumed to be constant. We show that this can contribute to the flattening observed by recent Voyager data collected outside the heliosphere which is not impacted by solar modulation. Additionally, we explain how to calculate the grammage accumulated by particles undergoing energy losses and show that for 1 GeV particles this increase can reach a factor of three compared to the standard expectation. Finally, we indicate how our setup can be used to calculate the propagation into a molecular cloud and provide first estimations of the ionisation rate, which are in agreement with observations around W28 for fiducial parameters.

Around pulsar wind nebulae, γ-ray emission extending up to 10° has been observed by HAWC, LHAASO and Fermi-LAT at energies between GeV and TeV, which seems to be radially symmetric. The cause for the emission is inverse Compton scattering of electorn/positron pairs which have been accelerated by the pulsar and its wind termination shock. This indicates that pulsars are primary sources of positrons and can thereby potentially explain the positron excess observed by AMS-02. However, the radial dependence of the observed emission can only be explained by a diffusion coefficient at TeV, which is more than two orders of magnitude lower than that extrapolated from direct observations at GeV. Due to the short energy loss time of the particles, the existence and extent of these suppressed diffusion zones is crucial to determine whether pulsars can account for the entire excess. We investigated existing models and further possible explanations for the observations in Sec. 4. We reproduced two zone models with isotropic diffusion and showed that they can fit the surface brightness. In order to explain the suppressed diffusion coefficient we investigated the impact of the streaming-instability in a flux tube model and in a spherically symmetric setup. We found that in spherical symmetry the resonant streaming-instability is not able to explain the observed suppression due to the strong spatial gradient. With the flux tube approximation, we did not manage to reproduce

the morphology and normalisation of the emission and we are unable to explain the radial symmetry of observations. Since the flux-tube approximation maximises the impact of the streaming-instability, we concluded that it cannot explain the emission even if the spread of the flux-tube, caused by the extending of magnetic field lines, is considered. All of the above scenarios depend on a predetermined large scale magnetic field geometry as external model parameter. The two most important ones are the turbulence level and correlation length. To determine these we reviewed test-particle approaches in magnetic tubulence. With these it was shown that only a correlation length of around 1 pc can explain the observations for typical magnetic field strength in the Galaxy and Kolmogorov turbulence. We highlighted that these simulations naturally predict a diffusion coefficient significantly below the predictions of hadronic ratios, which is a long-standing problem. Finally, we suggested to consider ion-neutral damping, which efficiently damps turbulence at smaller scales but not larger scales. We demonstrated the effects on the turbulent cascade, and indicated possible ways to constrain this model. With these findings, we conclude that the γ-ray halos around pulsars cannot be explained, but offer a very promising testground for our understanding of particle transport.

In the last two sections we have shown that there are zones of low diffusion around both pulsars and supernova remnants. Whether these zones impact global cosmic ray propagation within the Galaxy depends on the filling fraction of these zones. Since the size of the suppression region is significantly smaller than the size of the Galaxy, the large number of grid points make finite difference methods unfeasible. In order to make computations possible, we developed a two zone model of the Galaxy. Instead of individual low diffusion zones we considered a coarse grained diffusion coefficient in the disk, which is lower than in the halo. We used this model to fit B/C and ^{10}Be/^{9}Be data. The latter do not only break the degeneracy between diffusion coefficient and halo height by B/C data, but also allow to constrain a potential suppression in the disk. Like all secondary cosmic rays, Be is produced in the disk by spallation. When the diffusion coefficient in the disk is smaller, unstable ^{10}Be is confined in the disk for longer, which increases the amount detected on Earth, before it can escape into the Halo and decays there. We have performed Monte Carlo Markov chain scans to determine the posterior parameters space for three different data sets with and without preliminary AMS-02 data and with a forecast for upcoming HELIX data. Without AMS-02 data the degeneracy between halo height and diffusion coefficient cannot be broken and this also prevents the detection of suppressed diffusion in the disk. Including the higher energy data by AMS-02 leads to the preference of a diffusion in the disk, which is a factor of 5 lower than in the halo. We computed the model preference compared to a setup with homogeneous diffusion everywhere by test statistics and find a preference of $3.5\,\sigma$, which can potentially be increased with HELIX data to $6.8\,\sigma$. This result can be interpreted in two ways: Either the diffusion in the entire disk is reduced, or this is an average of low diffusion zones like the ones discussed in the previous sections surrounded by high diffusion zones. We used stochastic differential equations to compute a coarse-grained diffusion coefficient. For a diffusion coefficient suppressed by a factor five this results in a filling fraction of around 66 %. Should this be caused by pulsars or supernova remnants, which as we have show last around 1 Myr, the size of these zones would have to be 150 pc. This is rather large. However, we stressed that this result crucially depends on the parameterisation of the spallation cross-sections we have used, which is the DRAGON2 version. For the GALPROP parameterisation, we have found no preference for suppressed diffusion. This difference is caused by the lower high energy limit of the ^{10}Be/^{9}Be ratio, which leads to a flatter transition as preferred by the data. In the DRAGON2 setup, this was achieved by suppressed diffusion in the disk. Hence, even if the AMS-02 and HELIX data - once available - allow to constrain diffusion in the disk for a fixed spallation cross-section, the large systematic uncertainties in these parameterisations will prevent further conclusions.

Our results highlight that none of the currently existing models can explain the TeV-halos self-consistently. We have highlighted that it remains plausible that the diffusion coefficient around Geminga has to be lower by two orders of magnitude than inferred from direct cosmic ray observations. We have suggested considering the effects of ion-neutral damping in the turbulent cascade in order to explain the TeV-halos. Additionally, they might be able to reconcile test-particle simulations with a

fixed turbulence spectra to the hadronic cosmic ray observations. In the future this can be probed by measuring cosmic ray ratios at energies above 10 TeV. Alternatively, more observations of TeV-halos could indicate whether the effects observed around Geminga - and other pulsar wind nebulae - are a common feature or caused by specific circumstances. Furthermore, the results presented by LHAAS0 at the ICRC 2023 show a curious asymmetry in the direction of motion. Should these results be confirmed, this can be used to study the particle transport around Geminga in unprecedented detail.

New direct detectors in space such as AMS-02, CALET and DAMPE are able to measure cosmic ray ratios more precisely than ever. This has sparked the need for ever more sophisticated theoretical explanations. We have considered one of these, namely a two zone model with reduced diffusion in the disk in Sec. 5. However, we have also highlighted the constraints arising from the lack of proper measurements of spallation cross-sections. In the future these can be measured more precisely by colliders in fixed target experiments such as NA61/SHINE, if proper funding and resources are allocated. Then, more self-consistent models of galactic cosmic ray propagation can enrich our understanding of wave-particle interactions and the Galaxy in general.

With new upcoming experiments and plenty of unanswered questions in astroparticle physics, a lot of progress can be expected in the coming years.

Acknowledgments

First and foremost I would like to thank my supervisor Prof. Philipp Mertsch for providing me the support and freedom to pursue the topics I was interested in. His comprehensive lectures served as an excellent introduction to the field. Thanks to him, I had the opportunity to further expand my knowledge in the amazing schools I was able to participate in. During the last couple of years, he not only provided me the academic skills I need, but also the moral compass on what good scientific research is. His flat hierarchy, easy availability and humour brightened our interactions.

During my PhD I had the pleasure to meet numerous great scientists. In particular, I enjoyed my long discussions with Silvia Manconi, who has always been a role model for me and helped me understand the philosophy of research and life. Minh Vo Hong Phan helped whenever I needed it and discussions with him always provided another point of view that helped me to progress.

The time in the office has been enlighted by many members of the institute, but the ones who had to suffer my presence the most where my office mates Marco Kuhlen, Anton Stall and Laurin Söding. I sincerely thank all of them for all the fruitful discussions and banter. Our beautiful sketches clarified most problems and our calendar enabled me not to forget any birthday. During all of this the common coffee provided the necessary brain power.

Throughout my course of studies, I had the pleasure to make a great number of friends with whom working was not only significantly more fun, but also more productive. It was amazing to have such an environment. In addition, I would like to thank everyone who helped me enjoy my life and develop as a person during my studies, and I am grateful that the list is too long to be written down here. This really provided the distraction I needed.

I am grateful to Lena Rathmann, Lukas Simon, Philipp Fürst and Philipp Mertsch for investing their precious time to proofread the messier versions of this thesis.

Finally, I would like to express my deepest gratitude to my family. Without their support throughout the entire course of my studies I would not have been able to achieve this degree. It is a huge relief to know they always have my back. My girlfriend Lena always provided me a save heaven and believed in me even in times I didn't. For this I am truly grateful. Her support, charm and intelligence brightens my life.

Hanno out.

References

[1] Abdo Abdo, B. Allen, T. Aune et al. Milagro observations of multi-tev emission from galactic sources in the fermi bright source list. *The Astrophysical Journal*, 703, 04 2009. doi: 10.1088/0004-637X/703/2/L185.

[2] A. U. Abeysekara, A. Albert, R. Alfaro et al. Extended gamma-ray sources around pulsars constrain the origin of the positron flux at Earth. *Science*, 358(6365):911–914, November 2017. doi: 10.1126/science.aan4880.

[3] A. U. Abeysekara, A. Albert, R. Alfaro et al. The 2hwc hawc observatory gamma-ray catalog. *The Astrophysical Journal*, 843(1):40, Jun 2017. ISSN 1538-4357. doi: 10.3847/1538-4357/aa7556. URL http://dx.doi.org/10.3847/1538-4357/aa7556.

[4] A. Achterberg. Modification of scattering waves and its importance for shock acceleration. *A&A*, 119(2):274–278, March 1983.

[5] M. Ackermann et al. Detection of the Characteristic Pion-Decay Signature in Supernova Remnants. *Science*, 339:807, 2013. doi: 10.1126/science.1231160.

[6] O. Adriani, G. C. Barbarino, G. A. Bazilevskaya et al. Cosmic-Ray Positron Energy Spectrum Measured by PAMELA. *Phys. Rev. Lett.*, 111(8):081102, August 2013. doi: 10.1103/PhysRevLett.111.081102.

[7] O. Adriani, Y. Akaike, K. Asano et al. Cosmic-Ray Boron Flux Measured from 8.4 GeV /n to 3.8 TeV /n with the Calorimetric Electron Telescope on the International Space Station. *Phys. Rev. Lett.*, 129(25):251103, December 2022. doi: 10.1103/PhysRevLett.129.251103.

[8] M. Aguilar, D. Aisa, B. Alpat et al. Precision Measurement of the Proton Flux in Primary Cosmic Rays from Rigidity 1 GV to 1.8 TV with the Alpha Magnetic Spectrometer on the International Space Station. *Phys. Rev. Lett.*, 114(17):171103, May 2015. doi: 10.1103/PhysRevLett.114.171103.

[9] M. Aguilar, L. Ali Cavasonza, G. Ambrosi et al. Precision Measurement of the Boron to Carbon Flux Ratio in Cosmic Rays from 1.9 GV to 2.6 TV with the Alpha Magnetic Spectrometer on the International Space Station. *Phys. Rev. Lett.*, 117(23):231102, December 2016. doi: 10.1103/PhysRevLett.117.231102.

[10] M. Aguilar, L. Ali Cavasonza, G. Ambrosi et al. Towards Understanding the Origin of Cosmic-Ray Positrons. *Phys. Rev. Lett.*, 122(4):041102, February 2019. doi: 10.1103/PhysRevLett.122.041102.

[11] M. Aguilar, L. Ali Cavasonza, M. S. Allen et al. Properties of Iron Primary Cosmic Rays: Results from the Alpha Magnetic Spectrometer. *Phys. Rev. Lett.*, 126(4):041104, January 2021. doi: 10.1103/PhysRevLett.126.041104.

[12] F. A. Aharonian, A. M. Atoyan, and H. J. Voelk. High energy electrons and positrons in cosmic rays as an indicator of the existence of a nearby cosmic tevatron. *A&A*, 294:L41–L44, February 1995.

[13] Markus Ahlers and Philipp Mertsch. Small-scale Anisotropies of Cosmic Rays from Relative Diffusion. *ApJ*, 815(1):L2, December 2015. doi: 10.1088/2041-8205/815/1/L2.

[14] H. Alfvén. Existence of Electromagnetic-Hydrodynamic Waves. *Nature*, 150(3805):405–406, October 1942. doi: 10.1038/150405d0.

[15] J. W. Armstrong, B. J. Rickett, and S. R. Spangler. Electron Density Power Spectrum in the Local Interstellar Medium. *ApJ*, 443:209, April 1995. doi: 10.1086/175515.

[16] W. Baade and F. Zwicky. Cosmic Rays from Super-novae. *Proceedings of the National Academy of Science*, 20(5):259–263, May 1934. doi: 10.1073/pnas.20.5.259.

[17] A. R. Bell. The acceleration of cosmic rays in shock fronts - I. *MNRAS*, 182:147–156, January 1978. doi: 10.1093/mnras/182.2.147.

[18] A. R. Bell. Turbulent amplification of magnetic field and diffusive shock acceleration of cosmic rays. *MNRAS*, 353(2):550–558, September 2004. doi: 10.1111/j.1365-2966.2004.08097.x.

[19] V. S. Berezinskii, S. V. Bulanov, V. A. Dogiel, and V. S. Ptuskin. *Astrophysics of Cosmic Rays*. North-Holland, Amsterdam, 1990. ISBN 978-0-444-87292-2.

[20] V. S. Berezinsky, S. I. Grigorieva, and B. I. Hnatyk. Extragalactic UHE proton spectrum and prediction for iron-nuclei flux at 10^{8}-10^{9} GeV. *Astroparticle Physics*, 21(6):617–625, September 2004. doi: 10.1016/j.astropartphys.2004.06.004.

[21] T. W. Berghöfer and D. Breitschwerdt. The origin of the young stellar population in the solar neighborhood – A link to the formation of the Local Bubble? *A&A*, 390:299–306, July 2002. doi: 10.1051/0004-6361:20020627.

[22] D. Bisschoff, M. S. Potgieter, and O. P. M. Aslam. New Very Local Interstellar Spectra for Electrons, Positrons, Protons, and Light Cosmic Ray Nuclei. *ApJ*, 878(1):59, June 2019. doi: 10.3847/1538-4357/ab1e4a.

[23] R. D. Blandford and J. P. Ostriker. Particle acceleration by astrophysical shocks. *ApJ*, 221: L29–L32, April 1978. doi: 10.1086/182658.

[24] Roger Blandford and David Eichler. Particle acceleration at astrophysical shocks: A theory of cosmic ray origin. *Phys. Rep.*, 154(1):1–75, October 1987. doi: 10.1016/0370-1573(87)90134-7.

[25] Pasquale Blasi. Origin of the Positron Excess in Cosmic Rays. *Phys. Rev. Lett.*, 103(5):051104, July 2009. doi: 10.1103/PhysRevLett.103.051104.

[26] George R. Blumenthal and Robert J. Gould. Bremsstrahlung, Synchrotron Radiation, and Compton Scattering of High-Energy Electrons Traversing Dilute Gases. *Reviews of Modern Physics*, 42(2):237–271, January 1970. doi: 10.1103/RevModPhys.42.237.

[27] M. J. Boschini, S. Della Torre, M. Gervasi et al. HelMod in the Works: From Direct Observations to the Local Interstellar Spectrum of Cosmic-Ray Electrons. *ApJ*, 854(2):94, February 2018. doi: 10.3847/1538-4357/aaa75e.

[28] M. J. Boschini, S. Della Torre, M. Gervasi et al. Deciphering the Local Interstellar Spectra of Primary Cosmic-Ray Species with HELMOD. *ApJ*, 858(1):61, May 2018. doi: 10.3847/1538-4357/aabc54.

[29] Mathieu Boudaud, Yoann Génolini, Laurent Derome et al. AMS-02 antiprotons' consistency with a secondary astrophysical origin. *Physical Review Research*, 2(2):023022, April 2020. doi: 10.1103/PhysRevResearch.2.023022.

[30] L. Brahimi, A. Marcowith, and V. S. Ptuskin. Nonlinear diffusion of cosmic rays escaping from supernova remnants: Cold partially neutral atomic and molecular phases. *Astronomy and Astrophysics*, 633(36166), 2020. ISSN 14320746. doi: 10.1051/0004-6361/201936166.

[31] Chad Bustard and Ellen G. Zweibel. Cosmic-Ray Transport, Energy Loss, and Influence in the Multiphase Interstellar Medium. *ApJ*, 913(2):106, June 2021. doi: 10.3847/1538-4357/abf64c.

[32] Collin D. Capano, Ingo Tews, Stephanie M. Brown et al. Stringent constraints on neutron-star radii from multimessenger observations and nuclear theory. *Nature Astronomy*, 4:625–632, March 2020. doi: 10.1038/s41550-020-1014-6.

[33] Patrizia A. Caraveo, Giovanni F. Bignami, Roberto Mignani, and Laurence G. Taff. Parallax Observations with the Hubble Space Telescope Yield the Distance to Geminga. *ApJ*, 461:L91, April 1996. doi: 10.1086/310012.

[34] C. Ceccarelli, P. Hily-Blant, T. Montmerle et al. Supernova-enhanced Cosmic-Ray Ionization and Induced Chemistry in a Molecular Cloud of W51C. *ApJ*, 740(1):L4, October 2011. doi: 10.1088/2041-8205/740/1/L4.

[35] Ensheng Chen. Study of particle diffusion around geminga with lhaaso-km2a, August 2023. URL `https://confit.atlas.jp/guide/event/icrc2023/session/3TYM09-17/tables?IDvdeixBZj`.

[36] D. O. Chernyshov, V. A. Dogiel, A. V. Ivlev et al. Formation of the Cosmic-Ray Halo: The Role of Nonlinear Landau Damping. *ApJ*, 937(2):107, October 2022. doi: 10.3847/1538-4357/ac8f42.

[37] D. O. Chernyshov, A. V. Ivlev, and V. A. Dogiel. Secondary cosmic-ray nuclei in the model of Galactic halo with nonlinear Landau damping. *arXiv e-prints*, art. arXiv:2309.04772, September 2023. doi: 10.48550/arXiv.2309.04772.

[38] Denis F. Cioffi, Christopher F. McKee, and Edmund Bertschinger. Dynamics of Radiative Supernova Remnants. *ApJ*, 334:252, November 1988. doi: 10.1086/166834.

[39] S. A. Colgate. Supernovae as a standard candle for cosmology. *ApJ*, 232:404–408, September 1979. doi: 10.1086/157300.

[40] J. J. Connell. Galactic Cosmic-Ray Confinement Time: Ulysses High Energy Telescope Measurements of the Secondary Radionuclide ^{10}Be. *ApJ*, 501(1):L59–L62, July 1998. doi: 10.1086/311437.

[41] Glen Cowan, Kyle Cranmer, Eilam Gross, and Ofer Vitells. Asymptotic formulae for likelihood-based tests of new physics. *European Physical Journal C*, 71:1554, February 2011. doi: 10.1140/epjc/s10052-011-1554-0.

[42] R. Cowsik, Yash Pal, S. N. Tandon, and R. P. Verma. Steady State of Cosmic-Ray Nuclei-Their Spectral Shape and Path Length at Low Energies. *Physical Review*, 158(5):1238–1242, June 1967. doi: 10.1103/PhysRev.158.1238.

[43] J. Crank, P. Nicolson, and D. R. Hartree. A practical method for numerical evaluation of solutions of partial differential equations of the heat-conduction type. *Proceedings of the Cambridge Philosophical Society*, 43(1):50, January 1947. doi: 10.1017/S0305004100023197.

[44] A. C. Cummings, E. C. Stone, B. C. Heikkila et al. Galactic Cosmic Rays in the Local Interstellar Medium: Voyager 1 Observations and Model Results. *ApJ*, 831(1):18, November 2016. doi: 10.3847/0004-637X/831/1/18.

[45] A. C. Cummings, E. C. Stone, B. C. Heikkila et al. Galactic Cosmic Rays in the Local Interstellar Medium: Voyager 1 Observations and Model Results. *ApJ*, 831(1):18, November 2016. doi: 10.3847/0004-637X/831/1/18.

[46] Dampe Collaboration. Detection of spectral hardenings in cosmic-ray boron-to-carbon and boron-to-oxygen flux ratios with DAMPE. *Science Bulletin*, 67(21):2162–2166, November 2022. doi: 10.1016/j.scib.2022.10.002.

[47] Marta D'Angelo, Pasquale Blasi, and Elena Amato. Grammage of cosmic rays around Galactic supernova remnants. *Phys. Rev. D*, 94(8):083003, October 2016. doi: 10.1103/PhysRevD.94.083003.

[48] Marta D'Angelo, Giovanni Morlino, Elena Amato, and Pasquale Blasi. Diffuse gamma-ray emission from self-confined cosmic rays around Galactic sources. *MNRAS*, 474(2):1944–1954, February 2018. doi: 10.1093/mnras/stx2828.

[49] J. K. Daugherty and A. K. Harding. Electromagnetic cascades in pulsars. *The Astrophysical Journal*, 252:337–347, January 1982. doi: 10.1086/159561.

[50] Pedro De La Torre Luque, Ottavio Fornieri, and Tim Linden. Anisotropic diffusion cannot explain TeV halo observations. *Phys. Rev. D*, 106(12):123033, December 2022. doi: 10.1103/PhysRevD.106.123033.

[51] L. Derome, D. Maurin, P. Salati et al. Fitting B/C cosmic-ray data in the AMS-02 era: a cookbook. Model numerical precision, data covariance matrix of errors, cross-section nuisance parameters, and mock data. *A&A*, 627:A158, July 2019. doi: 10.1051/0004-6361/201935717.

[52] Mattia Di Mauro, Silvia Manconi, and Fiorenza Donato. Detection of a γ -ray halo around Geminga with the Fermi-LAT data and implications for the positron flux. *Phys. Rev. D*, 100 (12):123015, December 2019. doi: 10.1103/PhysRevD.100.123015.

[53] Rebecca Diesing and Damiano Caprioli. Steep Cosmic-Ray Spectra with Revised Diffusive Shock Acceleration. *ApJ*, 922(1):1, November 2021. doi: 10.3847/1538-4357/ac22fe.

[54] V. A. Dogiel, A. V. Ivlev, D. O. Chernyshov, and C. M. Ko. Formation of the Cosmic-Ray Halo: Galactic Spectrum of Primary Cosmic Rays. *ApJ*, 903(2):135, November 2020. doi: 10.3847/1538-4357/abba31.

[55] Bruce T. Draine. *Physics of the Interstellar and Intergalactic Medium*. Princeton University Press, Princeton, NJ, 2011. ISBN 978-0-691-12214-4. URL https://press.princeton.edu/books/hardcover/9780691122144/physics-of-the-interstellar-and-intergalactic-medium.

[56] L. O. Drury, P. Duffy, and J. Kirk. Diffusive shock acceleration in dense and incompletely ionised media. 1995.

[57] L O'C Drury. An introduction to the theory of diffusive shock acceleration of energetic particles in tenuous plasmas. *Reports on Progress in Physics*, 46(8):973–1027, aug 1983. doi: 10.1088/0034-4885/46/8/002. URL https://doi.org/10.1088/0034-4885/46/8/002.

[58] J. A. Eilek. Particle reacceleration in radio galaxies. *ApJ*, 230:373–385, June 1979. doi: 10.1086/157093.

[59] Carmelo Evoli. The cosmic-ray energy spectrum, May 2023. URL https://doi.org/10.5281/zenodo.7948212.

[60] Carmelo Evoli and Ulyana Dupletsa. Phenomenological models of Cosmic Ray transport in Galaxies. *arXiv e-prints*, art. arXiv:2309.00298, September 2023. doi: 10.48550/arXiv.2309.00298.

[61] Carmelo Evoli and Ulyana Dupletsa. Phenomenological models of Cosmic Ray transport in Galaxies. *arXiv e-prints*, art. arXiv:2309.00298, September 2023. doi: 10.48550/arXiv.2309.00298.

[62] Carmelo Evoli, Pasquale Blasi, Giovanni Morlino, and Roberto Aloisio. Origin of the Cosmic Ray Galactic Halo Driven by Advected Turbulence and Self-Generated Waves. *Phys. Rev. Lett.*, 121(2):021102, July 2018. doi: 10.1103/PhysRevLett.121.021102.

[63] Carmelo Evoli, Daniele Gaggero, Andrea Vittino et al. Cosmic-ray propagation with DRAGON2: II. Nuclear interactions with the interstellar gas. *J. Cosmology Astropart. Phys.*, 2018(7):006, July 2018. doi: 10.1088/1475-7516/2018/07/006.

[64] Carmelo Evoli, Tim Linden, and Giovanni Morlino. Self-generated cosmic-ray confinement in TeV halos: Implications for TeV γ -ray emission and the positron excess. *Phys. Rev. D*, 98(6): 063017, September 2018. doi: 10.1103/PhysRevD.98.063017.

[65] Carmelo Evoli, Tim Linden, and Giovanni Morlino. Self-generated cosmic-ray confinement in TeV halos: Implications for TeV γ -ray emission and the positron excess. *Phys. Rev. D*, 98(6): 063017, September 2018. doi: 10.1103/PhysRevD.98.063017.

[66] Carmelo Evoli, Roberto Aloisio, and Pasquale Blasi. Galactic cosmic rays after the AMS-02 observations. *Phys. Rev. D*, 99(10):103023, May 2019. doi: 10.1103/PhysRevD.99.103023.

[67] Carmelo Evoli, Giovanni Morlino, Pasquale Blasi, and Roberto Aloisio. AMS-02 beryllium data and its implication for cosmic ray transport. *Phys. Rev. D*, 101(2):023013, January 2020. doi: 10.1103/PhysRevD.101.023013.

[68] Carmelo Evoli, Elena Amato, Pasquale Blasi, and Roberto Aloisio. Galactic factories of cosmic-ray electrons and positrons. *Phys. Rev. D*, 103(8):083010, April 2021. doi: 10.1103/PhysRevD.103.083010.

[69] Kun Fang. Gamma-ray pulsar halos in the galaxy. *Frontiers in Astronomy and Space Sciences*, 9, 10 2022. doi: 10.3389/fspas.2022.1022100.

[70] Kun Fang, Xiao-Jun Bi, Peng-Fei Yin, and Qiang Yuan. Two-zone Diffusion of Electrons and Positrons from Geminga Explains the Positron Anomaly. *ApJ*, 863(1):30, August 2018. doi: 10.3847/1538-4357/aad092.

[71] Kun Fang, Xiao-Jun Bi, and Peng-Fei Yin. Possible origin of the slow-diffusion region around Geminga. *MNRAS*, 488(3):4074–4080, September 2019. doi: 10.1093/mnras/stz1974.

[72] Alison J. Farmer and Peter Goldreich. Wave damping by magnetohydrodynamic turbulence and its effect on cosmic-ray propagation in the interstellar medium. *The Astrophysical Journal*, 604(2):671–674, 04 2004. ISSN 1538-4357. doi: 10.1086/382040. URL `http://dx.doi.org/10.1086/382040`.

[73] Enrico Fermi. On the Origin of the Cosmic Radiation. *Physical Review*, 75(8):1169–1174, April 1949. doi: 10.1103/PhysRev.75.1169.

[74] Farhan Feroz, Michael P. Hobson, Ewan Cameron, and Anthony N. Pettitt. Importance Nested Sampling and the MultiNest Algorithm. *The Open Journal of Astrophysics*, 2(1):10, November 2019. doi: 10.21105/astro.1306.2144.

[75] K. Ferrière. Plasma turbulence in the interstellar medium. *Plasma Physics and Controlled Fusion*, 62(1):014014, January 2020. doi: 10.1088/1361-6587/ab49eb.

[76] Katia M. Ferrière. The interstellar environment of our galaxy. *Reviews of Modern Physics*, 73 (4):1031–1066, October 2001. doi: 10.1103/RevModPhys.73.1031.

[77] R. Fitzpatrick. *Plasma Physics: An Introduction*. Taylor & Francis, 2014. ISBN 9781466594265. URL `https://books.google.de/books?id=0RwbBAAAQBAJ`.

[78] Daniel Foreman-Mackey, Alex Conley, Will Meierjurgen Farr et al. emcee: The MCMC Hammer. Astrophysics Source Code Library, record ascl:1303.002, March 2013.

[79] S. Gabici, S. Casanova, F. A. Aharonian, and G. Rowell. Constraints on the cosmic ray diffusion coefficient in the W28 region from gamma-ray observations. In S. Boissier, M. Heydari-Malayeri, R. Samadi, and D. Valls-Gabaud, editors, *SF2A-2010: Proceedings of the Annual meeting of the French Society of Astronomy and Astrophysics*, page 313, December 2010. doi: 10.48550/arXiv.1009.5291.

[80] Stefano Gabici, Carmelo Evoli, Daniele Gaggero et al. The origin of Galactic cosmic rays: Challenges to the standard paradigm. *International Journal of Modern Physics D*, 28(15): 1930022-339, January 2019. doi: 10.1142/S0218271819300222.

[81] Bryan M. Gaensler and Patrick O. Slane. The evolution and structure of pulsar wind nebulae. *Annual Review of Astronomy and Astrophysics*, 44(1):17–47, Sep 2006. ISSN 1545-4282. doi: 10.1146/annurev.astro.44.051905.092528. URL `http://dx.doi.org/10.1146/annurev.astro.44.051905.092528`.

[82] M. Garcia-Munoz, G. M. Mason, and J. A. Simpson. The age of the galactic cosmic rays derived from the abundance of ^{10}Be. *ApJ*, 217:859–877, November 1977. doi: 10.1086/155632.

[83] M. Garcia-Munoz, J. A. Simpson, and J. P. Wefel. The Propagation Lifetime of Galactic Cosmic Rays Determined from the Measurement of the Beryllium Isotopes. In *International Cosmic Ray Conference*, volume 2 of *International Cosmic Ray Conference*, page 72, January 1981.

[84] Yoann Génolini, David Maurin, Igor V. Moskalenko, and Michael Unger. Current status and desired precision of the isotopic production cross sections relevant to astrophysics of cosmic rays: Li, Be, B, C, and N. *Phys. Rev. C*, 98(3):034611, September 2018. doi: 10.1103/PhysRevC.98.034611.

[85] Yoann Génolini, David Maurin, Igor V. Moskalenko, and Michael Unger. Current status and desired precision of the isotopic production cross sections relevant to astrophysics of cosmic rays: Li, Be, B, C, and N. *Phys. Rev. C*, 98(3):034611, September 2018. doi: 10.1103/PhysRevC.98.034611.

[86] Yoann Génolini, David Maurin, Igor V. Moskalenko, and Michael Unger. Current status and desired accuracy of the isotopic production cross-sections relevant to astrophysics of cosmic rays II. Fluorine to Silicon (and updated LiBeB). *arXiv e-prints*, art. arXiv:2307.06798, July 2023. doi: 10.48550/arXiv.2307.06798.

[87] Yoann Génolini, David Maurin, Igor V. Moskalenko, and Michael Unger. Current status and desired accuracy of the isotopic production cross-sections relevant to astrophysics of cosmic rays II. Fluorine to Silicon (and updated LiBeB). *arXiv e-prints*, art. arXiv:2307.06798, July 2023. doi: 10.48550/arXiv.2307.06798.

[88] G. Giacinti, M. KachelrieSS, and D. V. Semikoz. Reconciling cosmic ray diffusion with Galactic magnetic field models. *J. Cosmology Astropart. Phys.*, 2018(7):051, July 2018. doi: 10.1088/1475-7516/2018/07/051.

[89] V. L. Ginzburg and S. I. Syrovatskii. *The Origin of Cosmic Rays*. Pergamon Press, Oxford, 1964. ISBN 978-0-08-010568-1.

[90] Philipp Girichidis, Stella S. R. Offner, Alexei G. Kritsuk et al. Physical Processes in Star Formation. *Space Sci. Rev.*, 216(4):68, June 2020. doi: 10.1007/s11214-020-00693-8.

[91] L. J. Gleeson and W. I. Axford. Cosmic Rays in the Interplanetary Medium. *ApJ*, 149:L115, September 1967. doi: 10.1086/180070.

[92] D. Grasso, S. Profumo, A. W. Strong et al. On possible interpretations of the high energy electron-positron spectrum measured by the Fermi Large Area Telescope. *Astroparticle Physics*, 32(2):140–151, September 2009. doi: 10.1016/j.astropartphys.2009.07.003.

[93] Melville S. Green. Brownian Motion in a Gas of Noninteracting Molecules. *J. Chem. Phys.*, 19(8):1036–1046, August 1951. doi: 10.1063/1.1748449.

[94] D. A. Gurnett, W. S. Kurth, L. F. Burlaga, and N. F. Ness. In Situ Observations of Interstellar Plasma with Voyager 1. *Science*, 341(6153):1489–1492, September 2013. doi: 10.1126/science.1241681.

[95] Alice Harding. Pulsar polar cap and slot gap models: Confronting fermi data. *Journal of Astronomy and Space Sciences*, 30:145–152, 09 2013. doi: 10.5140/JASS.2013.30.3.145.

[96] K. Hasselmann and G. Wibberenz. A Note on the Parallel Diffusion Coefficient. *ApJ*, 162: 1049, December 1970. doi: 10.1086/150736.

[97] M. Haverkorn, J. C. Brown, B. M. Gaensler, and N. M. McClure-Griffiths. The Outer Scale of Turbulence in the Magnetoionized Galactic Interstellar Medium. *ApJ*, 680(1):362–370, June 2008. doi: 10.1086/587165.

[98] A. Heger, C. L. Fryer, S. E. Woosley et al. How Massive Single Stars End Their Life. *ApJ*, 591(1):288–300, July 2003. doi: 10.1086/375341.

[99] Victor F. Hess. Über Beobachtungen der durchdringenden Strahlung bei sieben Freiballonfahrten. *Phys. Z.*, 13:1084–1091, 1912.

[100] A.R. Hewish, S. Bell, J. Pilkington et al. Observation of a rapidly pulsating radio source. *Nature*, 217, 02 1968. doi: 10.1038/217709a0.

[101] A. M. Hillas. The Origin of Ultra-High-Energy Cosmic Rays. *ARA&A*, 22:425–444, January 1984. doi: 10.1146/annurev.aa.22.090184.002233.

[102] Dan Hooper and Tim Linden. Measuring the local diffusion coefficient with H.E.S.S. observations of very high-energy electrons. *Phys. Rev. D*, 98(8):083009, October 2018. doi: 10.1103/PhysRevD.98.083009.

[103] Dan Hooper, Ilias Cholis, Tim Linden, and Ke Fang. HAWC observations strongly favor pulsar interpretations of the cosmic-ray positron excess. *Phys. Rev. D*, 96(10):103013, November 2017. doi: 10.1103/PhysRevD.96.103013.

[104] Alejandro Ibarra, David Tran, and Christoph Weniger. Decaying dark matter in light of the PAMELA and Fermi LAT data. *J. Cosmology Astropart. Phys.*, 2010(1):009, January 2010. doi: 10.1088/1475-7516/2010/01/009.

[105] Nick Indriolo, Geoffrey A. Blake, Miwa Goto et al. Investigating the Cosmic-ray Ionization Rate Near the Supernova Remnant IC 443 through H^+_3 Observations. *ApJ*, 724(2):1357–1365, December 2010. doi: 10.1088/0004-637X/724/2/1357.

[106] A. V. Ivlev, M. Padovani, D. Galli, and P. Caselli. Interstellar Dust Charging in Dense Molecular Clouds: Cosmic Ray Effects. *ApJ*, 812(2):135, October 2015. doi: 10.1088/0004-637X/812/2/135.

[107] John David Jackson. *Classical Electrodynamics*. John Wiley & Sons, New York, 1962. ISBN 978-0-471-43132-6.

[108] Hanno Jacobs, Philipp Mertsch, and Vo Hong Minh Phan. Self-confinement of low-energy cosmic rays around supernova remnants. *J. Cosmology Astropart. Phys.*, 2022(5):024, May 2022. doi: 10.1088/1475-7516/2022/05/024.

[109] Hanno Jacobs, Philipp Mertsch, and Vo Hong Minh Phan. Unstable cosmic ray nuclei constrain low-diffusion zones in the Galactic disc. *MNRAS*, 526(1):160–174, November 2023. doi: 10.1093/mnras/stad2719.

[110] Ronnie Jansson and Glennys R. Farrar. The Galactic Magnetic Field. *ApJ*, 761(1):L11, December 2012. doi: 10.1088/2041-8205/761/1/L11.

[111] Jiahui Wei. Properties of cosmic beryllium isotopes. URL: https://agenda.infn.it/event/28874/contributions/170166/attachments/93944/128556/ICHEP2022_Be_Isotope.pdf, 7 2022.

[112] T. Jogler and S. Funk. Revealing W51c as a Cosmic ray Source Using Fermi-lat Data. *Astrophys. J.*, 816(2):100, 2016. doi: 10.3847/0004-637X/816/2/100.

[113] Guðlaugur Jóhannesson, Troy A. Porter, and Igor V. Moskalenko. Cosmic-Ray Propagation in Light of the Recent Observation of Geminga. *ApJ*, 879(2):91, July 2019. doi: 10.3847/1538-4357/ab258e.

[114] Isabelle John and Tim Linden. Pulsars do not produce sharp features in the cosmic-ray electron and positron spectra. *Phys. Rev. D*, 107(10):103021, May 2023. doi: 10.1103/PhysRevD.107.103021.

[115] J. R. Jokipii. Cosmic-Ray Propagation. I. Charged Particles in a Random Magnetic Field. *ApJ*, 146:480, November 1966. doi: 10.1086/148912.

[116] J. R. Jokipii. Fokker-Planck Equations for Charged-Particle Transport in Random Fields. *ApJ*, 172:319, March 1972. doi: 10.1086/151349.

[117] J. R. Jokipii, J. Kota, and J. Giacalone. Perpendicular transport in 1- and 2-dimensional shock simulations. *Geophys. Res. Lett.*, 20(17):1759–1761, September 1993. doi: 10.1029/93GL01973.

[118] Frank C. Jones, Thomas B. Kaiser, and Thomas J. Birmingham. New Approach to Cosmic-Ray Diffusion Theory. *Phys. Rev. Lett.*, 31(7):485–487, August 1973. doi: 10.1103/PhysRevLett.31.485.

[119] T. W. Jones. Alfven Wave Transport Effects in the Time Evolution of Parallel Cosmic-Ray–modified Shocks. *ApJ*, 413:619, August 1993. doi: 10.1086/173031.

[120] M. Kachelrieß, I. V. Moskalenko, and S. Ostapchenko. AAfrag: Interpolation routines for Monte Carlo results on secondary production in proton-proton, proton-nucleus and nucleus-nucleus interactions. *Computer Physics Communications*, 245:106846, December 2019. doi: 10.1016/j.cpc.2019.08.001.

[121] Eugenia Kálnay de Rivas. On the Use of Nonuniform Grids in Finite-Difference Equations. *Journal of Computational Physics*, 10(2):202–210, October 1972. doi: 10.1016/0021-9991(72)90060-5.

[122] O. Klein and T. Nishina. Über die Streuung von Strahlung durch freie Elektronen nach der neuen relativistischen Quantendynamik von Dirac. *Zeitschrift fur Physik*, 52(11-12):853–868, November 1929. doi: 10.1007/BF01366453.

[123] A. Kolmogorov. The Local Structure of Turbulence in Incompressible Viscous Fluid for Very Large Reynolds' Numbers. *Akademiia Nauk SSSR Doklady*, 30:301–305, January 1941.

[124] Robert H. Kraichnan. Inertial-Range Spectrum of Hydromagnetic Turbulence. *Physics of Fluids*, 8(7):1385–1387, July 1965. doi: 10.1063/1.1761412.

[125] Nicholas A. Krall and Alvin W. Trivelpiece. Principles of plasma physics. *American Journal of Physics*, 41(12):1380–1381, 1973. doi: 10.1119/1.1987587. URL https://doi.org/10.1119/1.1987587.

[126] S. M. Krimigis, R. B. Decker, E. C. Roelof et al. Search for the Exit: Voyager 1 at Heliosphere's Border with the Galaxy. *Science*, 341(6142):144–147, July 2013. doi: 10.1126/science.1235721.

[127] R. De L. Kronig. On the theory of dispersion of x'rays. *Journal of the Optical Society of America (1917-1983)*, 12(6):547, November 1926.

[128] Ryogo Kubo. Statistical-Mechanical Theory of Irreversible Processes. I. *Journal of the Physical Society of Japan*, 12(6):570–586, June 1957. doi: 10.1143/JPSJ.12.570.

[129] Marco Kuhlen. *Small-scale anisotropies in cosmic ray arrival directions*. PhD thesis, RWTH Aachen U., 2022.

[130] Marco Kuhlen, Vo Hong Minh Phan, and Philipp Mertsch. Field line subdiffusion and cosmic ray perpendicular transport in isotropic turbulence. *arXiv e-prints*, art. arXiv:2211.05882, November 2022. doi: 10.48550/arXiv.2211.05882.

[131] Marco Kuhlen, Vo Hong Minh Phan, and Philipp Mertsch. Diffusion of relativistic charged particles and field lines in isotropic turbulence. *arXiv e-prints*, art. arXiv:2211.05881, November 2022. doi: 10.48550/arXiv.2211.05881.

[132] Russell Kulsrud and William P. Pearce. The Effect of Wave-Particle Interactions on the Propagation of Cosmic Rays. *ApJ*, 156:445, May 1969. doi: 10.1086/149981.

[133] P. O. Lagage and C. J. Cesarsky. The maximum energy of cosmic rays accelerated by supernova shocks. *A&A*, 125:249–257, September 1983.

[134] J. Liouville. Note sur la théorie de la variation des constantes arbitraires. *Journal de Mathématiques Pures et Appliquées*, pages 342–349, 1838. URL `http://eudml.org/doc/234417`.

[135] Paolo Lipari. Spectral shapes of the fluxes of electrons and positrons and the average residence time of cosmic rays in the Galaxy. *Phys. Rev. D*, 99(4):043005, February 2019. doi: 10.1103/PhysRevD.99.043005.

[136] Malcolm S. Longair. *High Energy Astrophysics*. Cambridge University Press, Cambridge, 3rd edition, 2011. ISBN 978-0-521-75696-9. URL `https://www.cambridge.org/core/books/high-energy-astrophysics/30FF321245F2315D6CC22DCA3D98A52A`.

[137] Rubén López-Coto and Gwenael Giacinti. Constraining the properties of the magnetic turbulence in the Geminga region using HAWC γ-ray data. *MNRAS*, 479(4):4526–4534, October 2018. doi: 10.1093/mnras/sty1821.

[138] A. Lukasiak, P. Ferrando, F. B. McDonald, and W. R. Webber. The Isotopic Composition of Cosmic-Ray Beryllium and Its Implication for the Cosmic Ray's Age. *ApJ*, 423:426, March 1994. doi: 10.1086/173818.

[139] Andrew Lukasiak. Voyager Measurements of the Charge and Isotopic Composition of Cosmic Ray Li, Be and B Nuclei and Implications for Their Production in the Galaxy. In *26th International Cosmic Ray Conference (ICRC26), Volume 3*, volume 3 of *International Cosmic Ray Conference*, page 41, August 1999.

[140] W. J. Macquorn Rankine. On the Thermodynamic Theory of Waves of Finite Longitudinal Disturbance. *Philosophical Transactions of the Royal Society of London Series I*, 160:277–288, January 1870.

[141] M. A. Malkov, P. H. Diamond, R. Z. Sagdeev et al. Analytic solution for self-regulated collective escape of cosmic rays from their acceleration sites. *Astrophysical Journal*, 768(1):1–31, 2013. ISSN 15384357. doi: 10.1088/0004-637X/768/1/73.

[142] Silvia Manconi, Mattia Di Mauro, and Fiorenza Donato. Contribution of pulsars to cosmic-ray positrons in light of recent observation of inverse-Compton halos. *Phys. Rev. D*, 102(2):023015, July 2020. doi: 10.1103/PhysRevD.102.023015.

[143] K. Mannheim and R. Schlickeiser. Interactions of cosmic ray nuclei. *A&A*, 286:983–996, 06 1994.

[144] D. Maurin, F. Melot, and R. Taillet. A database of charged cosmic rays. *A&A*, 569:A32, September 2014. doi: 10.1051/0004-6361/201321344.

[145] D. Maurin, E. Ferronato Bueno, and L. Derome. A simple determination of the halo size from ^{10}Be/^{9}Be data. *A&A*, 667:A25, November 2022. doi: 10.1051/0004-6361/202243546.

[146] D. Maurin, E. Ferronato Bueno, Y. Génolini et al. The importance of Fe fragmentation for LiBeB analyses. Is a Li primary source needed to explain AMS-02 data? *A&A*, 668:A7, December 2022. doi: 10.1051/0004-6361/202243446.

[147] David Maurin, Hans Peter Dembinski, Javier Gonzalez et al. Cosmic-Ray Database Update: Ultra-High Energy, Ultra-Heavy, and Antinuclei Cosmic-Ray Data (CRDB v4.0). *Universe*, 6 (8):102, July 2020. doi: 10.3390/universe6080102.

[148] David Maurin, Markus Ahlers, Hans Dembinski et al. A cosmic-ray database update: CRDB v4.1. *European Physical Journal C*, 83(10):971, October 2023. doi: 10.1140/epjc/s10052-023-12092-8.

[149] J. F. McKenzie and R. A. B. Bond. The role of non-linear Landau damping in cosmic ray shock acceleration. *A&A*, 123(1):111–117, June 1983.

[150] Philipp Mertsch. Stochastic cosmic ray sources and the TeV break in the all-electron spectrum. *JCAP*, 11:045, 2018. doi: 10.1088/1475-7516/2018/11/045.

[151] Philipp Mertsch. Test particle simulations of cosmic rays. *Ap&SS*, 365(8):135, August 2020. doi: 10.1007/s10509-020-03832-3.

[152] Philipp Mertsch. The cosmic ray spectrum, October 2023. URL `https://doi.org/10.5281/zenodo.10003566`.

[153] G. Morlino and S. Gabici. Cosmic ray penetration in diffuse clouds. *MNRAS*, 451:L100–L104, July 2015. doi: 10.1093/mnrasl/slv074.

[154] Payel Mukhopadhyay and Tim Linden. Self-generated cosmic-ray turbulence can explain the morphology of TeV halos. *Phys. Rev. D*, 105(12):123008, June 2022. doi: 10.1103/PhysRevD.105.123008.

[155] Alex Muslimov and Alice Harding. Extended acceleration in slot gaps and pulsar high-energy emission. *The Astrophysical Journal*, 588, 01 2003. doi: 10.1086/368162.

[156] L. Nava, S. Gabici, A. Marcowith et al. Non-linear diffusion of cosmic rays escaping from supernova remnants – i. the effect of neutrals. *Monthly Notices of the Royal Astronomical Society*, 461(4):3552–3562, 07 2016. ISSN 1365-2966. doi: 10.1093/mnras/stw1592. URL `http://dx.doi.org/10.1093/mnras/stw1592`.

[157] L Nava, S Recchia, S Gabici et al. Non-linear diffusion of cosmic rays escaping from supernova remnants – ii. hot ionized media. *Monthly Notices of the Royal Astronomical Society*, 484(2):2684–2691, 01 2019. ISSN 1365-2966. doi: 10.1093/mnras/stz137. URL `http://dx.doi.org/10.1093/mnras/stz137`.

[158] Francesco Nozzoli and Cinzia Cernetti. Beryllium Radioactive Isotopes as a Probe to Measure the Residence Time of Cosmic Rays in the Galaxy and Halo Thickness: A "Data-Driven" Approach. *Universe*, 7(6):183, June 2021. doi: 10.3390/universe7060183.

[159] B. Olmi and N. Bucciantini. Full-3D relativistic MHD simulations of bow shock pulsar wind nebulae: emission and polarization. *MNRAS*, 488(4):5690–5701, October 2019. doi: 10.1093/mnras/stz2089.

[160] J. R. Oppenheimer and G. M. Volkoff. On Massive Neutron Cores. *Physical Review*, 55(4): 374–381, February 1939. doi: 10.1103/PhysRev.55.374.

[161] E. Orlando. Imprints of cosmic rays in multifrequency observations of the interstellar emission. *MNRAS*, 475(2):2724–2742, April 2018. doi: 10.1093/mnras/stx3280.

[162] J. Ormes and P. Freier. On the propagation of cosmic rays in the Galaxy. *ApJ*, 222:471–483, June 1978. doi: 10.1086/156160.

[163] Luca Orusa, Mattia Di Mauro, Fiorenza Donato, and Michael Korsmeier. New determination of the production cross section for secondary positrons and electrons in the Galaxy. *Phys. Rev. D*, 105(12):123021, June 2022. doi: 10.1103/PhysRevD.105.123021.

[164] S. M. Osipov, A. M. Bykov, A. E. Petrov, and V. I. Romansky. Energetic positron propagation from pulsars: an analytical two-zone diffusion model. In *Journal of Physics Conference Series*, volume 1697 of *Journal of Physics Conference Series*, page 012009, December 2020. doi: 10.1088/1742-6596/1697/1/012009.

[165] M. Padovani, D. Galli, and A. E. Glassgold. Cosmic-ray ionization of molecular clouds. *A&A*, 501(2):619–631, July 2009. doi: 10.1051/0004-6361/200911794.

[166] M. Padovani, D. Galli, and A. E. Glassgold. Cosmic-ray ionization of molecular clouds. *A&A*, 501(2):619–631, July 2009. doi: 10.1051/0004-6361/200911794.

[167] N. Park, L. Beaufore, R. Mbarek et al. Cosmic-ray Isotope Measurements with HELIX. In *36th International Cosmic Ray Conference (ICRC2019)*, volume 36 of *International Cosmic Ray Conference*, page 121, July 2019. doi: 10.22323/1.358.0121.

[168] E. N. Parker. The passage of energetic charged particles through interplanetary space. *Planet. Space Sci.*, 13(1):9–49, January 1965. doi: 10.1016/0032-0633(65)90131-5.

[169] Particle Data Group, P. A. Zyla, R. M. Barnett et al. Review of Particle Physics. *Progress of Theoretical and Experimental Physics*, 2020(8):083C01, August 2020. doi: 10.1093/ptep/ptaa104.

[170] V. H. M. Phan, G. Morlino, and S. Gabici. What causes the ionization rates observed in diffuse molecular clouds? The role of cosmic ray protons and electrons. *MNRAS*, 480(4):5167–5174, November 2018. doi: 10.1093/mnras/sty2235.

[171] V. H. M. Phan, S. Gabici, G. Morlino et al. Constraining the cosmic ray spectrum in the vicinity of the supernova remnant W28: from sub-GeV to multi-TeV energies. *A&A*, 635:A40, March 2020. doi: 10.1051/0004-6361/201936927.

[172] Vo Hong Minh Phan, Florian Schulze, Philipp Mertsch et al. Stochastic Fluctuations of Low-Energy Cosmic Rays and the Interpretation of Voyager Data. *Phys. Rev. Lett.*, 127(14):141101, October 2021. doi: 10.1103/PhysRevLett.127.141101.

[173] Vo Hong Minh Phan, Sarah Recchia, Philipp Mertsch, and Stefano Gabici. Stochasticity of cosmic rays from supernova remnants and the ionization rates in molecular clouds. *Phys. Rev. D*, 107(12):123006, June 2023. doi: 10.1103/PhysRevD.107.123006.

[174] T. A. Porter, G. Jóhannesson, and I. V. Moskalenko. The GALPROP Cosmic-ray Propagation and Nonthermal Emissions Framework: Release v57. *ApJS*, 262(1):30, September 2022. doi: 10.3847/1538-4365/ac80f6.

[175] Marius S. Potgieter. Solar Modulation of Cosmic Rays. *Living Reviews in Solar Physics*, 10 (1):3, 06 2013. doi: 10.12942/lrsp-2013-3.

[176] W.H. Press, S.A. Teukolsky, W.T. Vetterling, and B.P. Flannery. *Numerical Recipes: The Art of Scientific Computing*. Cambridge University Press, 3 edition, 2007. ISBN 9780521880688. URL http://nr.com/.

[177] Stefano Profumo, Javier Reynoso-Cordova, Nicholas Kaaz, and Maya Silverman. Lessons from HAWC pulsar wind nebulae observations: The diffusion constant is not a constant; pulsars remain the likeliest sources of the anomalous positron fraction; cosmic rays are trapped for long periods of time in pockets of inefficient diffusion. *Phys. Rev. D*, 97(12):123008, June 2018. doi: 10.1103/PhysRevD.97.123008.

[178] V. S. Ptuskin, V. N. Zirakashvili, and A. A. Plesser. Non-linear diffusion of cosmic rays. *Advances in Space Research*, 42(3):486–490, August 2008. doi: 10.1016/j.asr.2007.12.007.

[179] A. Putze, L. Derome, and D. Maurin. A Markov Chain Monte Carlo technique to sample transport and source parameters of Galactic cosmic rays. II. Results for the diffusion model combining B/C and radioactive nuclei. *A&A*, 516:A66, June 2010. doi: 10.1051/0004-6361/201014010.

[180] S. Recchia, S. Gabici, F. A. Aharonian, and J. Vink. Local fading accelerator and the origin of TeV cosmic ray electrons. *Phys. Rev. D*, 99(10):103022, May 2019. doi: 10.1103/PhysRevD.99.103022.

[181] S. Recchia, M. Di Mauro, F. A. Aharonian et al. Do the Geminga, Monogem and PSR J0622+3749 γ -ray halos imply slow diffusion around pulsars? *Phys. Rev. D*, 104(12):123017, December 2021. doi: 10.1103/PhysRevD.104.123017.

[182] S. Recchia, D. Galli, L. Nava et al. Grammage of cosmic rays in the proximity of supernova remnants embedded in a partially ionized medium. *arXiv e-prints*, art. arXiv:2106.04948, June 2021.

[183] B. Reville and A. R. Bell. A filamentation instability for streaming cosmic rays. *MNRAS*, 419 (3):2433–2440, January 2012. doi: 10.1111/j.1365-2966.2011.19892.x.

[184] M. A. Ruderman and P. G. Sutherland. Theory of pulsars: polar gaps, sparks, and coherent microwave radiation. *The Astrophysical Journal*, 196:51–72, February 1975. doi: 10.1086/153393.

[185] A. D. Sakharov. Violation of CP Invariance, C Asymmetry, and Baryon Asymmetry of the Universe. *Soviet Journal of Experimental and Theoretical Physics Letters*, 5:24, January 1967.

[186] B. Schroer, O. Pezzi, D. Caprioli et al. Cosmic-ray generated bubbles around their sources. *MNRAS*, 512(1):233–244, May 2022. doi: 10.1093/mnras/stac466.

[187] Benedikt Schroer, Oreste Pezzi, Damiano Caprioli et al. Dynamical Effects of Cosmic Rays on the Medium Surrounding Their Sources. *ApJ*, 914(1):L13, June 2021. doi: 10.3847/2041-8213/ac02cd.

[188] Benedikt Schroer, Carmelo Evoli, and Pasquale Blasi. TeV halos and the role of pulsar wind nebulae as sources of cosmic-ray positrons. *Phys. Rev. D*, 107(12):123020, June 2023. doi: 10.1103/PhysRevD.107.123020.

[189] Vadim A. Semenov, Andrey V. Kravtsov, and Damiano Caprioli. Cosmic-Ray Diffusion Suppression in Star-forming Regions Inhibits Clump Formation in Gas-rich Galaxies. *ApJ*, 910 (2):126, April 2021. doi: 10.3847/1538-4357/abe2a6.

[190] A. Shalchi. Heuristic Description of Perpendicular Diffusion of Energetic Particles in Astrophysical Plasmas. *ApJ*, 881(2):L27, August 2019. doi: 10.3847/2041-8213/ab379d.

[191] Andreas Shalchi. Perpendicular Transport of Energetic Particles in Magnetic Turbulence. *Space Sci. Rev.*, 216(2):23, February 2020. doi: 10.1007/s11214-020-0644-4.

[192] R. Silberberg and C. H. Tsao. Partial Cross-Sections in High-Energy Nuclear Reactions, and Astrophysical Applications. I. Targets With z <= 28. *ApJS*, 25:315–333, April 1973. doi: 10.1086/190271.

[193] R. Silberberg and C. H. Tsao. Partial Cross-Sections in High-Energy Nuclear Reactions, and Astrophysical Applications. II. Targets Heavier than Nickel. *ApJS*, 25:335–367, April 1973.

[194] R. Silberberg, C. H. Tsao, and A. F. Barghouty. Updated Partial Cross Sections of Proton-Nucleus Reactions. *ApJ*, 501(2):911–919, July 1998. doi: 10.1086/305862.

[195] J. Skilling. Cosmic ray streaming - III. Self-consistent solutions. *MNRAS*, 173:255–269, November 1975. doi: 10.1093/mnras/173.2.255.

[196] Andrew W. Strong and Igor V. Moskalenko. Propagation of Cosmic-Ray Nucleons in the Galaxy. *ApJ*, 509(1):212–228, December 1998. doi: 10.1086/306470.

[197] P. Subedi, W. Sonsrettee, P. Blasi et al. Charged Particle Diffusion in Isotropic Random Magnetic Fields. *ApJ*, 837(2):140, March 2017. doi: 10.3847/1538-4357/aa603a.

[198] S. I. Syrovatskii. The Distribution of Relativistic Electrons in the Galaxy and the Spectrum of Synchrotron Radio Emission. *Soviet Ast.*, 3:22, February 1959.

[199] Joni Tammi and Peter Duffy. Particle-acceleration timescales in TeV blazar flares. In Felix A. Aharonian, Werner Hofmann, and Frank Rieger, editors, *American Institute of Physics Conference Series*, volume 1085 of *American Institute of Physics Conference Series*, pages 475–478, December 2008. doi: 10.1063/1.3076711.

[200] Xiaping Tang and Tsvi Piran. Positron flux and γ-ray emission from Geminga pulsar and pulsar wind nebula. *MNRAS*, 484(3):3491–3501, April 2019. doi: 10.1093/mnras/stz268.

[201] G. I. Taylor. The Motion of a Sphere in a Rotating Liquid. *Proceedings of the Royal Society of London Series A*, 102(715):180–189, November 1922. doi: 10.1098/rspa.1922.0079.

[202] L.H. Thomas. Elliptic Problems in Linear Difference Equations over a Network. *Watson Sc. Comp. Lab. Rep., Columbia University, New York.*, 1949.

[203] L.H. Thomas. Elliptic Problems in Linear Difference Equations over a Network. *Watson Sc. Comp. Lab. Rep., Columbia University, New York.*, 1949.

[204] R. K. Tripathi, Francis A. Cucinotta, and John W. Wilson. Accurate universal parameterization of absorption cross sections. *Nuclear Instruments and Methods in Physics Research B*, 117(4): 347–349, October 1996. doi: 10.1016/0168-583X(96)00331-X.

[205] R. K. Tripathi, John W. Wilson, and Francis A. Cucinotta. Accurate universal parameterization of absorption cross sections II — neutron absorption cross sections. *Nuclear Instruments and Methods in Physics Research B*, 129(1):11–15, June 1997. doi: 10.1016/S0168-583X(97)00121-3.

[206] J. Kelly Truelove and Christopher F. McKee. Evolution of nonradiative supernova remnants. *The Astrophysical Journal Supplement Series*, 120(2):299–326, 02 1999. doi: 10.1086/313176. URL `https://doi.org/10.1086/313176`.

[207] J. Kelly Truelove and Christopher F. McKee. Evolution of Nonradiative Supernova Remnants. *ApJS*, 120(2):299–326, February 1999. doi: 10.1086/313176.

[208] Michael Unger and Glennys Farrar. Progress in the Global Modeling of the Galactic Magnetic Field. In *European Physical Journal Web of Conferences*, volume 210 of *European Physical Journal Web of Conferences*, page 04005, October 2019. doi: 10.1051/epjconf/201921004005.

[209] S. Vaupré, P. Hily-Blant, C. Ceccarelli et al. Cosmic ray induced ionisation of a molecular cloud shocked by the W28 supernova remnant. *Astronomy and Astrophysics*, 568(Aharonian 2013), 2014. ISSN 14320746. doi: 10.1051/0004-6361/201424036.

[210] J. P. W. Verbiest, J. M. Weisberg, A. A. Chael et al. On Pulsar Distance Measurements and Their Uncertainties. *ApJ*, 755(1):39, August 2012. doi: 10.1088/0004-637X/755/1/39.

[211] Pauli Virtanen, Ralf Gommers, Travis E. Oliphant et al. SciPy 1.0: Fundamental Algorithms for Scientific Computing in Python. *Nature Methods*, 17:261–272, 2020. doi: 10.1038/s41592-019-0686-2.

[212] Andrea Vittino, Philipp Mertsch, Henning Gast, and Stefan Schael. Breaks in interstellar spectra of positrons and electrons derived from time-dependent AMS data. *Phys. Rev. D*, 100(4): 043007, August 2019. doi: 10.1103/PhysRevD.100.043007.

[213] Andrea Vittino, Philipp Mertsch, Henning Gast, and Stefan Schael. Breaks in interstellar spectra of positrons and electrons derived from time-dependent ams data. *Physical Review D*, 100(4), 08 2019. ISSN 2470-0029. doi: 10.1103/physrevd.100.043007. URL http://dx.doi.org/10.1103/PhysRevD.100.043007.

[214] A. A. Vlasov. Reviews of Topical Problems: the Vibrational Properties of AN Electron Gas. *Soviet Physics Uspekhi*, 10(6):721–733, June 1968. doi: 10.1070/PU1968v010n06ABEH003709.

[215] W. R. Webber, A. Soutoul, J. C. Kish, and J. M. Rockstroh. Updated Formula for Calculating Partial Cross Sections for Nuclear Reactions of Nuclei with Z <= 28 and E > 150 MeV Nucleon^{-1} in Hydrogen Targets. *ApJS*, 144(1):153–167, January 2003. doi: 10.1086/344051.

[216] N. Weinrich, M. Boudaud, L. Derome et al. Galactic halo size in the light of recent AMS-02 data. *A&A*, 639:A74, July 2020. doi: 10.1051/0004-6361/202038064.

[217] M. E. Wiedenbeck and D. E. Greiner. A cosmic-ray age based on the abundance of Be-10. *ApJ*, 239:L139–L142, August 1980. doi: 10.1086/183310.

[218] Huirong Yan and A. Lazarian. Cosmic-Ray Scattering and Streaming in Compressible Magnetohydrodynamic Turbulence. *ApJ*, 614(2):757–769, October 2004. doi: 10.1086/423733.

[219] N. E. Yanasak, M. E. Wiedenbeck, R. A. Mewaldt et al. Measurement of the Secondary Radionuclides ^{10}Be, ^{26}Al, ^{36}Cl, ^{54}Mn, and ^{14}C and Implications for the Galactic Cosmic-Ray Age. *ApJ*, 563(2):768–792, December 2001. doi: 10.1086/323842.

[220] Rui-zhi Yang, Guang-Xing Li, Emma de Oña Wilhelmi et al. Effective shielding of $\lesssim$10 GeV cosmic rays from dense molecular clumps. *Nature Astronomy*, January 2023. doi: 10.1038/s41550-022-01868-9.

[221] F. Yiou, M. Baril, J. Dufaure de Citres et al. Mass-Spectrometric Measurement of Lithium, Beryllium, and Boron Isotopes Produced in ^{16}O by High-Energy Protons, and Some Astrophysical Implications. *Physical Review*, 166(4):968–974, February 1968. doi: 10.1103/PhysRev.166.968.

[222] V. N. Zirakashvili, V. S. Ptuskin, and H. J. Völk. Modeling bell's nonresonant cosmic-ray instability. *The Astrophysical Journal*, 678(1):255–261, May 2008. ISSN 1538-4357. doi: 10.1086/529579. URL http://dx.doi.org/10.1086/529579.

[223] E. G. Zweibel and J. M. Shull. Confinement of cosmic rays in molecular clouds. *ApJ*, 259: 859–868, August 1982. doi: 10.1086/160220.

A. Appendix

A.1. Flux-Tube

In Sec. 1.6 we have motivated when the flux-tube approximation is justified. Here we show additional results of the magnetic field simulations, which have been used especially in Fig. 1.7. The mean perpendicular distance and standard deviation of field lines according to Eq. 1.156 and Eq. 1.157 as a function of source extent d for a distance of $z = L_c$ and a turbulence level of $\eta = 0.5$ are shown in Fig. A.1. We choose this turbulence level since it corresponds to the one expected in the Galaxy [97]. The solid black line corresponds to the mean distance of the centre of the flux-tube and the dashed black line indicates the extent of the flux-tube. Fainter lines show the individual field realisations. The mean distance of the flux-tube is $0.7\,\mathrm{L_c}$ independently of the source size, so particles are not decoupled from the field line. The extent of the flux-tube shows a slight dependence on the source extent, increasing from $0.05\,\mathrm{L_c}$ at small source extents to about $0.1\,\mathrm{L_c}$ at extends of $0.1\,\mathrm{L_c}$. Hence, for small source extents the expansion of the field lines within $1\,\mathrm{L_c}$ is not negligible, but for extents of $0.1\,\mathrm{L_c}$ it is.

The same as in Fig. A.1, but for $z = 10\,\mathrm{L_c}$ is shown in Fig. A.2. In this case the mean distance of the centre of the flux-tube is around $2\,\mathrm{L_c}$ and its size is $1\,\mathrm{L_c}$ nearly independent of the source extent. This indicates, that the flux-tube is extending linearly with z for $z \geq d$.

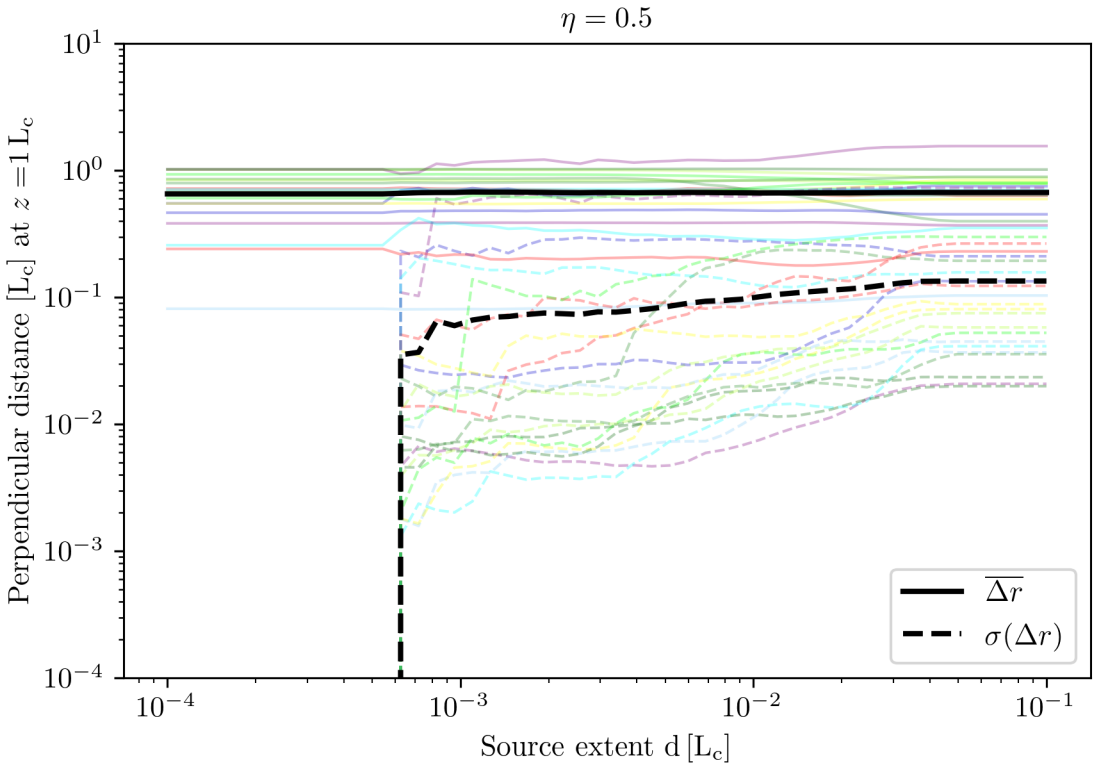

Figure A.1: Mean and standard deviation of field lines at 1 L_c from the source as function of the initial extent d for isotropic turbulence with turbulence level of $\eta = 0.5$. The black lines indicate the mean over all ensembles and the coloured lines indicate the individual realisations. The mean of the standard deviation of field lines is a measure for the spread of a flux-tube. At a distance of 1 L_c this is nearly independently of the source size 0.1 L_c.

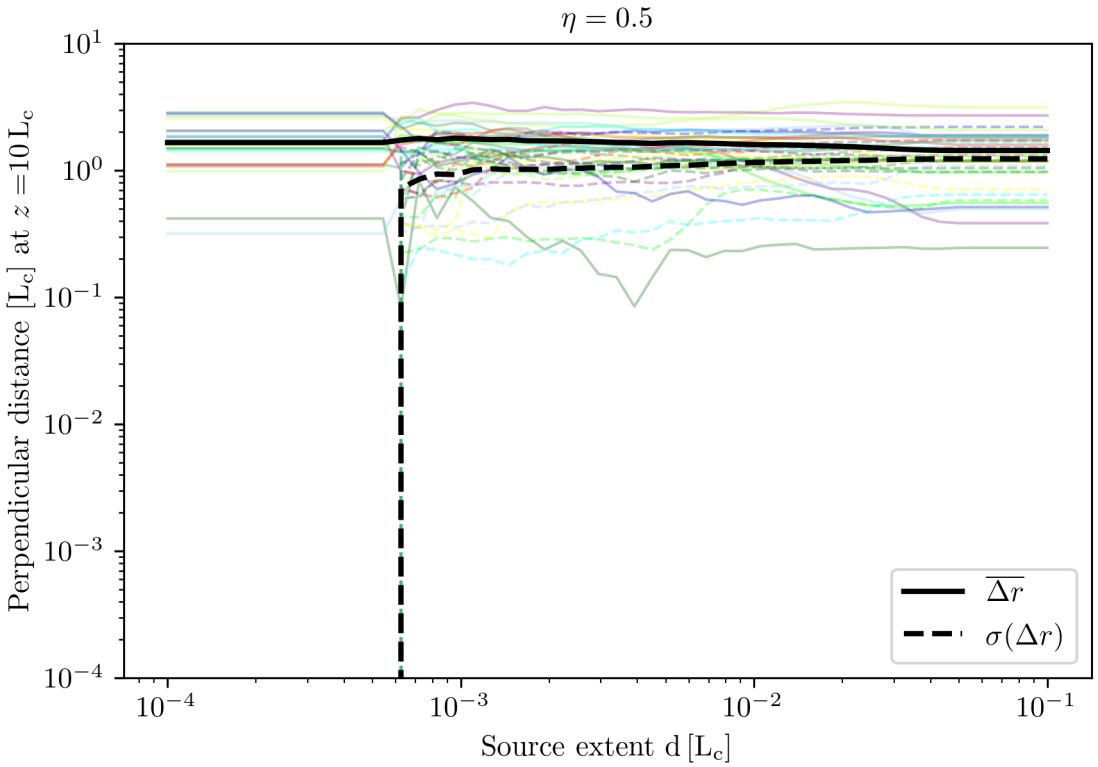

Figure A.2: Mean and standard deviation of field lines at $10\,L_c$ from the source as function of the initial extent d for isotropic turbulence with turbulence level of $\eta = 0.5$. The black lines indicate the mean over all ensembles and the coloured lines indicate the individual realisations. The mean of the standard deviation of field lines is a measure for the spread of a flux-tube. At a distance of $10\,L_c$ this is nearly independently of the source size $1\,L_c$.

A.2. Spatial Dependence of a SNR at 1 GeV

In Sec. 3.4.1 we have presented the spatial dependence of cosmic rays around supernova remnants at 0.1 GeV. Here we additionally show the results at 1 GeV in Fig. A.3.

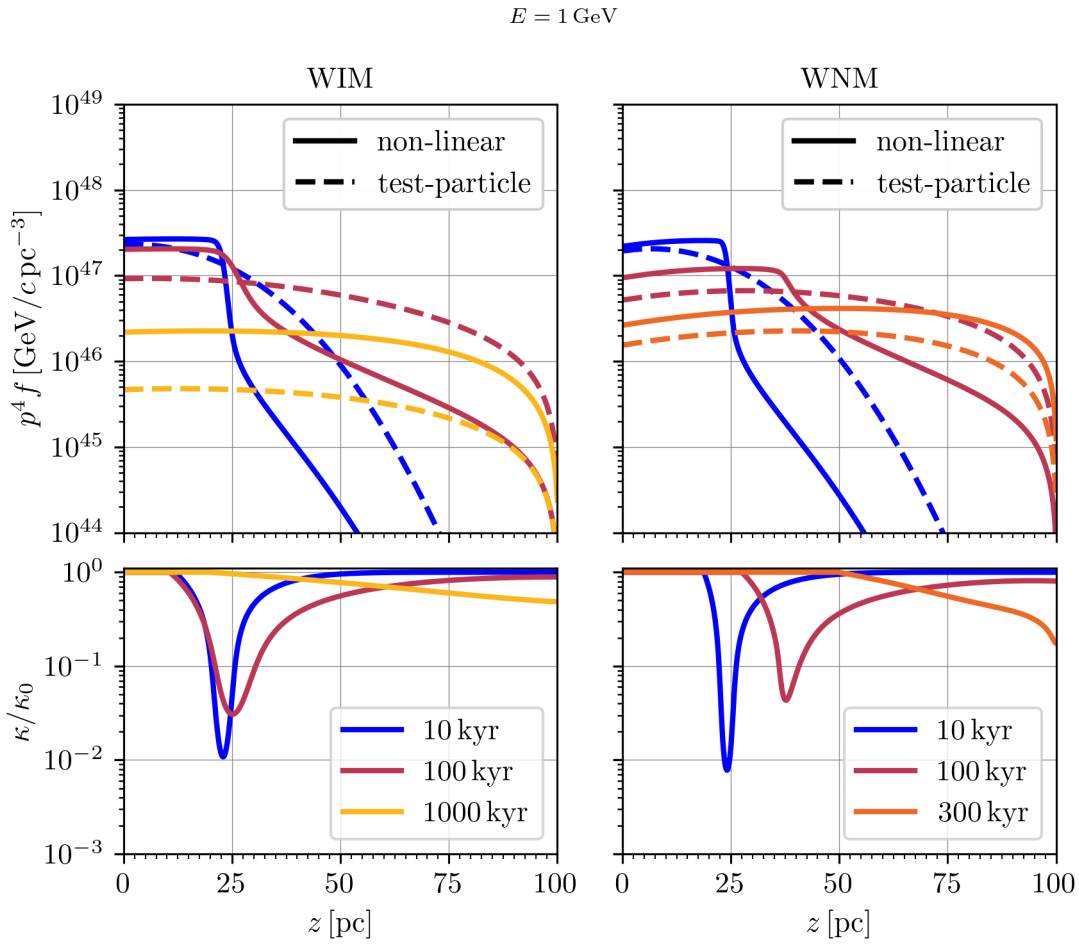

Figure A.3: Time evolution of the spatial distribution of a CR cloud with $\alpha = 4.2$ at 1 GeV in the WIM (left) and WNM (right). z is the distance from the supernova. Particles are released when the radius of the SNR is 23 pc, which is reached 26 kyr after the supernova explosion. All times shown here refer to this release time. The upper panels show the CR energy density $p^4 f$ with the test-particle solution marked in dashed lines and the non-linear results marked in solid lines. The lower panels show the corresponding diffusion coefficient κ normalised to the background coefficient κ_0.

A.3. Corner Plots

In this appendix we present the corner plots for additional setups for the full and null models introduced in Sec. 5.1, which have been mentioned in the text. In Fig. 5.5 the results for the full "w/o prelim." case is shown, in Fig. 5.6 the results for the null "'w/o prelim." case is shown and Fig. 5.6 shows the results for the full "'w/ forecast" case.

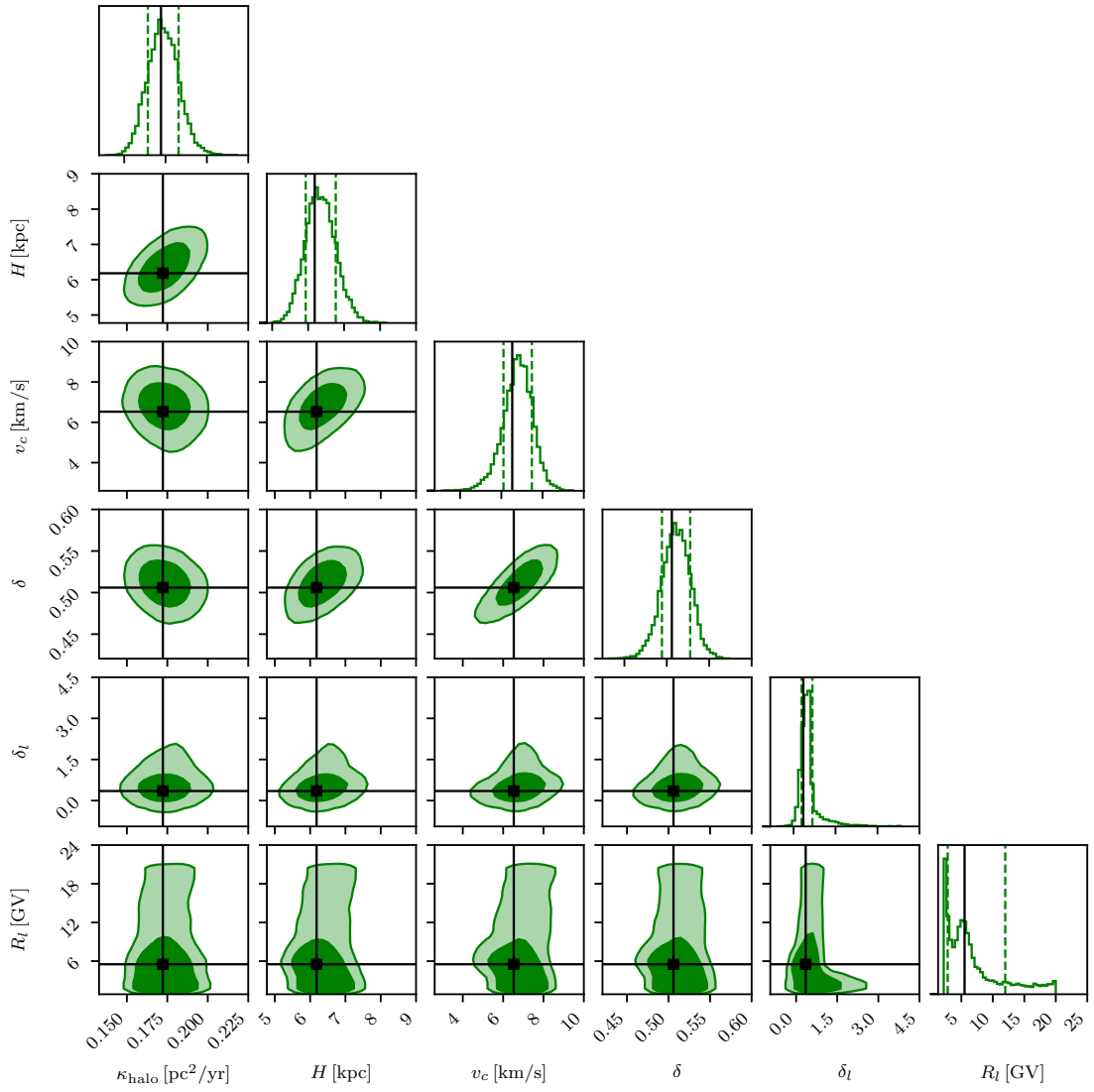

Figure A.4: Same as Fig. 5.6, but for the null model including preliminary AMS-02 data.

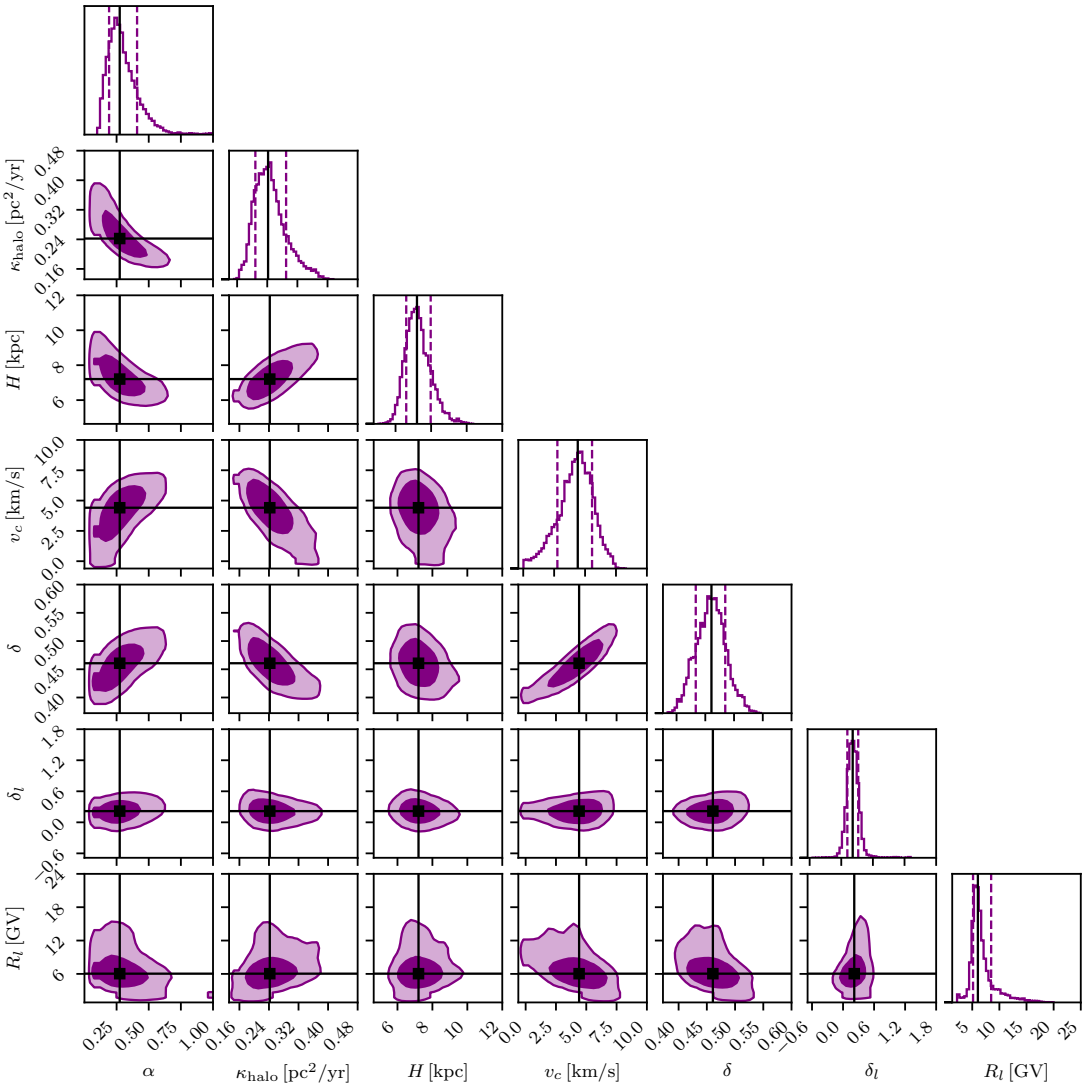

Figure A.5: Same as Fig. 5.6, but for the full model including a forecast of upcoming HELIX data.